Electrical Power Optimisation of Grid-connected Wave Energy Converters using Economic Predictive Control

Adrian C.M. O'Sullivan

NATIONAL UNIVERSITY OF IRELAND, CORK

SCHOOL OF ENGINEERING

Thesis submitted for the degree of Doctor of Philosophy

22 March 2018

Head of School: Prof. William Marnane

Supervisors: Dr Gordon Lightbody
Prof. Anthony Lewis

Research supported by Science Foundation Ireland

Contents

List of Figures

List of Tables

This is to certify that the work I, Adrian C.M. O'Sullivan, am submitting is my own and has not been submitted for another degree, either at University College Cork or elsewhere. All external references and sources are clearly acknowledged and identified within the contents. I have read and understood the regulations of University College Cork concerning plagiarism.

Adrian C.M. O'Sullivan

Acknowledgements

Firstly I would like to thank my supervisor Dr Gordon Lightbody for his high involvement throughout the PhD duration. It was an honour to work with him, the information I gained was invaluable, and I hope to collaborate in the future. I would like to thank Dr Paul Leahy and Dr Wasif Naeem for examining my thesis, their thorough evaluation led to a refined dissertation which was appreciated.

I would like to thank Science Foundation Ireland (SFI), without their financial support, this would not have been possible. I would like to show my gratitude towards the Marine and Renewable Energy Research, Development and Innovation Centre (MaREI), especially Prof. Tony Lewis and Dr Wanan Sheng, where their considerable contributions were valued.

I would like to thank all the staff of the School of Engineering at University College Cork (UCC). This involves Ralph O'Flaherty, Niamh O'Sullivan, Mary O'Leary, and Claudia Cashman for their administrative support and Mick O' Shea, Tim Power, Hillary Mansfield and James Griffiths for their unique skill sets. Many thanks, ye won't believe it until I put my hand on my heart and tell ye that we're through.

I would like to thank my postgraduate comrades for battling through the hard office days, sacrificing years of their lives for the good of man, where recognition is well deserved. Special mention goes towards Donal Murray, Kilian O'Donaghue, Jack Birmingham, Edward O'Dwyer, Diarmaid Hogan, Patrick Xie, Conor O'Shea, Yeny Vazquez-Guitierrez, Alex Jaeger, Robert Ryan, Daniel O'Keefe, Oliwier Melon, Brian Murphy, George O'Mahony, Oksana Semenova, Alison O'Shea and Juan Pablo La Torre. Hours were spent on enjoyable social activities, which I will forever be grateful. I would especially like to thank and apologise to Kevin Davis and Brendan Barry who sat next to me throughout the PhD duration, their company was highly appreciated. Hopefully, my thirst for knowledge was inconsequential towards them.

I would like to thank my friends from my school years where they have supported me from the beginning. I would like to thank my sisters, Audrey and Joyce, and their partners; their encouragement has always been cherished and valued. To my dear Ana, I owe my life to the fragile butterfly effect which generously placed me on the unique pathway to find you. We're at the tippy top of the mountain, but we're really only half way up, so let's climb it together. Finally, I would like to thank my parents John and Caroline O'Sullivan. I can honestly say that without their daily encouragement and genuine support, I would not be where I am today. On days where failure loomed, their inspiration helped me overcome the challenges that seemed insurmountable.

Abstract

This thesis investigates the advanced control algorithms used for optimally extracting energy from a wave-to-wire wave energy converter system. The research focuses on the wave-to-wire system model as a whole, instead of its separate subsystems. This allows maximum exportation of average electrical power onto the grid from a wave energy array, with minimum mechanical and electrical constraint infringement and acceptable power quality.

An economic model predictive control algorithm is first described for a wave-to-DC-link system with a single wave energy converter connected to a simulated linear generator. This work investigates the importance of including the linear generator's resistive losses in the cost function. Linear mechanical and non-linear electrical constraints are introduced into the model predictive control algorithm, where the effects on the average electrical power harvest are presented. A model predictive control algorithm with a field weakening enabled cost function is introduced, where the feasible region is extended for low DC-link voltages. By including a uni-directional power flow constraint into the algorithm, the power exported onto the DC-link bus is guaranteed to be positive.

A detailed analysis of the effect of uncertainty on performance was carried out, where the controller's internal model is mismatched from the simulation model. The results indicate that the high fidelity of the controller's internal model is not required and that a sufficient amount of average electrical power is extractable.

A non-linear model predictive control algorithm is described, where the non-linear viscosity forces are incorporated into the control algorithm - extracting maximum energy from a viscous system. It was shown that given the constraints on the system that the non-linear action of the control algorithm could be approximated, a linear model predictive control algorithm with an estimated viscous term. This produces a computationally inexpensive control algorithm, while maintaining good performance. A move-blocking was also introduced to further reduce the computation expense.

Finally the thesis considers multiple point absorbers in an array and analyses the potential benefits of using either decentralised or centralised model predictive control algorithms. This demonstrated that the performance of a decentralised controller becomes comparable to the centralised controller when linear mechanical constraints are introduced into the viscous hydrodynamic array. However, when an upper power limit is introduced into the control algorithm the advantages of the centralised controller become apparent.

List of Acronyms

AC	Alternating Current
AMPL	A Mathematical Programming Language
AWC	Archimedes Wave Swing
BEM	Boundary Element Method
CFD	Computational Fluid Dynamics
DC	Direct Current
DQ	Direct Quadrature
FOH	First Order Hold
HSVD	Hankel Singular Value Decomposition
HVAC	High Voltage Alternating Current
HVDC	High Voltage Direct Current
IGBT	Insulated Gate Bipolar Transistor
IPOPT	Interior Point Optimiser
JONSWAP	Joint North Sea Wave Project
LFPMG	Longitudinal Flux Permanent Magnet Generator
LPMG	Linear Permanent Magnet Generator
LPV	Linear Parameter Varying
MIMO	Multi Input Multi Output
MPC	Model Predictive Control
NMPC	Non-linear Model Predictive Control
OWC	Oscillating Water Column
PCC	Point of Common Coupling
PI	Proportional Integral
PLL	Phase Lock Loop
PMG	Permanent Magnet Generator
PTO	Power Take Off
PWM	Pulse Width Modulation
QP	Quadratic Programming
SCR	Short Circuit Ratio
SIMO	Single Input Multi Output
SVD	Singular Value Decomposition
SVM	Space Vector Modulation
SVPWM	Space Vector Pulse Width Modulation

TAPMG	Tubular Air-cored Permanent Magnet Generator
UNFCCC	United Nations Framework Convention on Climate Change
VRPMG	Variable Reluctance Permanent Magnet Generator
VSC	Voltage Source Converter
WAMIT	Wave Analysis at Massachusetts Institute of Technology
WEC	Wave Energy Converter
ZOH	Zero Order Hold

Nomenclature

A	WEC's cross sectional area
a	Spectrum amplitudes
$A_b(k)$, $B_b(k)$, $F_b(k)$, $E_b(k)$	The state space matrices of the LPV system
A_c, B_c, F_c	State space continuous hydrodynamic model
$A_c(t)$	Non-linear continuous time state space A_c matrix
$\mathbf{A_c}(t)$, $\mathbf{E_c}(t)$	Non-linear matrices containing a global set of $A_c(t)$ and $E_c(t)$
$\tilde{A}_c(k+i)$	The linearised non-linear $A_c(t)$ for time step $(k+i)$
A_d, B_d, C_d, F_d	Discrete state space matrices
α	Monochromatic excitation wave amplitude
A_r, B_r, C_r, D_r	State space matrices of radiation system
A_{r_j}, B_{r_j}, C_{r_j}, D_{r_j}	The state matrices of the radiation system
A_s	Spectral scale factor
A_w, B_w, C_w, F_w	FOH system with field weakening enabled
A_z, B_z, C_z, F_z	Discrete ZOH state space matrices relating the j^{th} WEC velocity to the total radiation force of the i^{th} WEC
$\mathbf{B_c}(t)$, $\mathbf{F_c}(t)$	Linear matrices containing a global set of $B_c(t)$ and $F_c(t)$
$B_d(s)$	Prony's polynomial numerator
β	Hydrostatic coefficient
b_i	Prony's numerator polynomial coefficients
B_s	Spectral exponential scale factor matrices from all the WEC's in the array
$\tilde{\mathbf{C}_{\mathbf{vis}}}(k+i)$	Non-linear viscosity linearisation points
c_i	Prony's magnitude terms
$C_{qd}(z)$	Controller difference equation for LPMG
C_{dc}	Capacitance of the DC-link
$C_{vis}(t)$	Non-linear viscosity sectional area
$\tilde{C_{vis}}$	Linear viscous coefficient estimate
$\tilde{\mathbf{C}_{\mathbf{vis},98\%}}$	The range of the linear viscous coefficient estimate $\tilde{C_{vis}}$which produces an efficiency higher or equal to 98% using the results found from a LPV NMPC as the 100% efficiency mark
$\mathbb{C}$	A set of complex numbers

C_d	Viscous drag coefficient
δ	Randomised phase
d	WEC separation distance in an array
$\eta(t)$	Free surface wave elevation
$\dot{\eta}(t)$	Free surface velocity of the wave
$e_{a,b,c}(t)$	Three-phase induced electromagnetic field
$E_{d,q}(z)$	Reference error
$\in$	An element of
$E_c(t)$	Non-linear continuous time wave surface velocity component of the hydrodynamic model
$\tilde{E_c}(k+i)$	The linearised non-linear $E_c(t)$ for time step $(k+i)$
F_g	Gravitational force
$F_{PTO}(t)$	External PTO force
$F_{dy}(t)$	Hydrodynamic force of potential flow model
$F_h(t)$	Hydrostatic force of potential flow model and linear model
$F_D(t)$	Diffraction force of potential flow model
$F_R(t)$	Radiation force of potential flow model
$F_{rad}(t)$	Radiation force from a linear model
$F_e(t)$	Excitation force from a linear model
$F_v(t)$	Viscosity force
$F_r(t)$	Radiation convolution integral
f	Frequency
$\bar{\mathbf{F}}_{\mathbf{r}}(\mathbf{s})$	Array of radiation forces in an array
$F_{h_i}(t)$	Hydrostatic force of the i^{th} WEC in the array
$F_{r_i}(t)$	Radiation force of the i^{th} WEC in the array
$F_{e_i}(t)$	Excitation force of the i^{th} WEC in the array
$F_{PTO_i}(t)$	PTO force of the i^{th} WEC in the array
$F_{v_i}(t)$	Viscous force of the i^{th} WEC in the array
$\mathbf{g}$	External source
g	Acceleration due to gravity
$g(t)$	System states of transformed radiation system
$G_{qd}(z)$	System difference equation for LPMG
Γ	The weighted Gamma function of the weighted spectrum
$h_r(t)$	Radiation kernel in the time domain
$h_e(t)$	Excitation kernel in the time domain

$H_e(\omega)$	Excitation frequency response
H_s	Significant wave height
$\mathbf{H_r}(s)$	Radiation kernel global matrix
$h_{r_{i,j}}(t)$	Impulse response of the convolution integral relating the velocity of the j^{th} WEC to the total radiated force of the i^{th} WEC
$\mathbf{H}(t)$	Array of all the wave surface velocity's from all the WEC's matrices from all the WEC's in the array
$i_{d,q}(t)$	Direct, Quadrature current
$i_{d_g,q_g}(t)$	dq0 current on the grid side
$i^*_{dq}(t)$	Generator dq0 current reference
$J_z(k)$	ZOH MPC cost function
$J_f(k)$	FOH MPC cost function
$J_w(k)$	Cost function of MPC with field weakening
$J_i(k)$	The cost function of the i^{th} WEC device
J_T	The global cost function
ξ	Vertical axis
k	Wave number
λ	Wavelength
λ_i	Prony's denominator polynomial coefficients
λ_{fd}	Flux linkage
λ_d	Direct flux linkage
λ_q	Quadrature flux linkage
$\lambda^{'}_{fd}$	Scaled flux linkage
L_s	Series inductance of grid network
L	LPMG inductance
$\mathbf{M}$	WEC mass
m_μ	Added mass
$m_d(k)$	direct control signal
$m_q(k)$	quadrature control signal
M_i	Mass of the i^{th} WEC in the array
$\mathbf{n}$	Normal vector
N_d	Number of discrete frequency intervals
N_{py}	Prony's transfer function system order
N_H	Kung's approximation system order
N_p	Prediction horizon

N_c	The control horizon
N_{wp}	The window parameter
n	Order of radiation state space system
N_r	Amount of control variables negated in the control horizon after the standard control horizon reduction
N_w	Number of WEC's in the array
N_θ	The amount of angles considered
ω	Angular frequency
$\omega(t)$	LPMG electrical rotary speed
ω_n	2_{nd} order damping frequency
$\Omega(\omega)$	Hydrodynamics impedance
$\bar{\Omega}(\omega)$	Hydrodynamics impedance conjugate
p	Pressure field
$P_{dp}(t)$	Dynamic pressure
$\Phi(t)$	Potential flow
$\Phi_I(t)$	Incidental potential flow
$\Phi_D(t)$	Diffraction potential flow
$\Phi_R(t)$	Radiation potential flow
$P_{dy}(t)$	Dynamic Froude-Krylov pressure
$P_{st}(t)$	Static Froude-Krylov pressure
$P_D(t)$	Diffraction pressure
$P_R(t)$	Radiation pressure
p_i	Prony's exponential terms
P	Controllability gramian
$P(t)$	Instantaneous real power
$P_{grid}(t)$	Power exported onto the grid
$P_{gen}(t)$	Power generated from WEC's
$P_{DC}(t)$	Power dissipated on the DC-link
Ψ_g	Grid impedance angle
P_{avg}	Average mechanical power
$P_z(k)$	ZOH discrete average power estimation
$P_f(k)$	FOH average power approximation
$P_e(t)$	Average electrical power
$P_{avge,N_p=160}$	Average power with $N_p = 160$
$P_{avge,N_p=40}$	Average power with $N_p = 40$
P_w	Average power from system with field weakening

ψ	PMG force-current conversion
$P_{e_{tot}}$	Total average electrical power from all the WEc's in the array
P_{e_i}	The average electrical power from the i^{th} WEC device
$\Delta P^2(\omega)$	The power variance factor, measuring how much th average power varies with the wave penetration angle range θ
$\bar{P}$	The average electrical power
$\bar{P}_c$	The average power extracted from an array that is hydro-dynamically coupled
$\bar{P}_d$	The average power extraction from a single WEC which has no surrounding WEC's
P_{local}	The average electrical power extracted from a hydro-dynamically coupled array using decentralised MPC
P_{global}	The average electrical power extracted from a hydro-dynamically coupled array using centralised MPC
P_{MAX}	The global limitation of instantaneous electrical power
$\hat{P}$	The global instantaneous peak electrical power
Q	Observability gramian
$Q(t)$	Reactive power
q	The q factor, which is the ratio of the average power extracted from a coupled array to the average power from isolated WEC's
ρ	Fluid density
R	Stator resistance
R_s	Series resistance of grid network
$r(k+i)$	MPC reference trajectory
$\mathbb{R}$	Set of real numbers
r	Radius of WEC
$S(t)$	Instantaneous submerged wetted surface area
$S(f)$	Spectral density
Σ	Singular values decomposition eigenvalues
S_{sc}	Short circuit level
S_n	Nominal power level
$s(k+i)$	MPC set-point
s	The s parameter, declaring the width of a weighted wave penetration spectrum
t	Time

T_p	Peak spectral period
T_{py}	Sampling period of Prony's approximation
T	Transformation matrix
T_H	Kung's approximation data sampling
τ	Pole pitch
T_{gen}	Current controller sample time
T_{switch}	Switching time of IGBT's
$\theta(t)$	LPMG electrical angle
T_L	Outer controller sample time
T_{set}	set-point settling time
T	Integration time interval
θ	Uni-directional wave excitation penetration angle
θ^*	The centre wave penetration angle
$\mathbf{u}$	Velocity vector
$u_c(t)$	Scaled PTO force
$\hat{u}(k+i\|k)$	future control variables
$u_d(k)$	Discrete scaled PTO force
$u_q(k)$	FOH scaled PTO force
$\mathbf{\Delta \hat{u}}(k)$	Predicted scaled PTO force increments
$U(k)$	System with field weakening input array
$\mathbf{\Delta u_{qm}}(k)$	The reduced array of future control inputs using the move-blocking horizon reduction
$\mathbf{\Delta u_{qh}}(k)$	The reduced array of future control inputs using the standard control horizon reduction
$\mathbf{U_q}(t)$	Array of all the scaled PTO forces from all the WEC's
$u_{q_{max}}$	The scaled PTO force limitation
$v_c(t)$	Scaled excitation force
$V_{dc}(t)$	DC-link voltage
$v_{a,b,c}(t)$	Three-phase average controller voltage
$v_{d,q}(t)$	dq0 voltage on the generation side
$v_{d_g,q_g}(t)$	dq0 voltage on the grid side
$v'_{d_g,q_g}(t)$	dq0 voltages on the grid side at the point of common coupling
V	The line-to-line voltage of $v'_{a,b,c}(t)$
$V(k)$	Reference tracking MPC cost function
$v_d(k)$	Discrete scaled excitation force

$\mathbf{\Delta\hat{v}}(k)$	Predicted scaled wave excitation force increments
$v_f(k)$	FOH scaled excitation force
$\mathbf{V}(t)$	Array of all the scaled excitation forces from all the WEC's
x	Wave displacement delay
$\mathbf{x_r}(t)$	Radiation kernel system state
$\mathbf{x}(t)$	Continuous hydrodynamic state space state matrix
$\mathbf{x}(k)$	Discrete state matrix
$\mathbf{x_z}(k)$	ZOH state matrix
$\mathbf{x_f}(k)$	FOH state space state matrix
$\mathbf{x_w}(k)$	State matrix for FOH MPC field weakening enabled
$\mathbf{x_b}(k)$	The state matrix of the LPMG system
$\mathbf{X}(t)$	Array of all the state matrices in the array
$\mathbf{X_f}(k)$	The array of states from each WEC in the array in the augmented form
$y(k+i)$	MPC output
$y_z(k)$	ZOH system output
$\mathbf{y_f}(k)$	FOH state space system
$\mathbf{y_w}(k)$	Output of system with field weakening
$\mathbf{y_b}(k)$	Output of the LPV system
$z(t)$	WEC heave displacement
$\dot{z}(t)$	WEC velocity
$\ddot{z}(t)$	WEC velocity
$\mathbf{Z}$	z-transform
ζ	2_{nd} order damping factor
Z_s	Series impedance of grid network
ζ	Passive damping control coefficient
$\dot{\mathbf{z}}^*(k+i\|k-1)$	The prediction velocity's across the prediction horizon from the previous discrete time step
$z_i(t)$	Heave displacement of the i^{th} WEC in the array
$\dot{z}_i(t)$	Velocity of the i^{th} WEC in the array
$\ddot{z}_i(t)$	Acceleration of the i^{th} WEC in the array
z_{max}	The heave displacement limitation
$\dot{z}_{max}$	The velocity limitation

List of Publications

Conference Papers

1. O'Sullivan, A. C. M. & Lightbody, G. (2015), 'Wave to Wire Power Maximisation from a Wave Energy Converter', *Proceedings of the 11th European Wave and Tidal Conference EWTEC 2015, Nantes, France*, 1–9.

2. O'Sullivan, A. C. M. & Lightbody, G. (2016 Special Session), 'Predictive control of a wave to wire energy conversion system - The importance of field weakening', *2016 UKACC International Conference on Control, UKACC Control, Belfast, Northern Ireland, 2016*, 1–6.

3. O'Sullivan, A. C. M. & Lightbody, G. (2017 Special Session),'The Effect of Viscosity on the Maximisation of Electrical Power from a Wave Energy Converter under Predictive Control',*The 20th World Congress of the International Federation of Automatic Control, Toulouse, France* , 14698–14704.

4. O'Sullivan, A. C. M. & Lightbody, G. (2017) , 'The Effect of Model Inaccuracy and Move-blocking on the Performance of a Wave-to-wire Wave Energy Converter , under Economic Predictive Control', *The 12th European Wave and Tidal Energy Conference, Cork, Ireland*, 1–10.

Journal Papers

1. O'Sullivan, A. C. M. & Lightbody, G. (2017) , 'Co-design of a wave energy converter using constrained predictive control', *Renewable Energy* **102**, 142–156.

2. O'Sullivan, A. C. M., Sheng, W. & Lightbody, G. (Accepted 2018) , 'An Analysis of the Potential Benefits of Centralised Predictive Control for Optimal Electrical Power Generation from Wave Energy Arrays', *IEEE Transactions on Sustainable Energy*, Accepted, DOI: 10.1109/TSTE.2018.2812749

Chapter 1

Introduction

In 2015, the Paris Agreement introduced by the United Nations Framework Convention on Climate Change (UNFCCC) set targets for each country to reduce their carbon footprint by 2020, in order to reduce the effects of global warming (Savaresi 2016). In (Figueres et al. 2017), a six-goal plan declared the necessary steps to achieve these targets set out in the 2015 Paris Agreement. One goal which is relevant to this thesis stated: *"Renewable energy should make up 30 percent of global electricity supply, and no coal-fired power plants should be commissioned by 2030"*.

Along with the objective of reducing the carbon footprint, there is also the economic incentive for many countries to reduce the fossil fuels imports. In 2014, Ireland had an energy source import dependency of 85% (Dineen et al. 2016); of the imported energy, 97% was from fossil fuels (oil (56%) , natural gas (31%), and coal (10%)). Reducing the dependency on imported energy will essentially reduce the cost of energy.

Nuclear energy emits little CO_2 into the atmosphere. However, the method is liable to rare but devastating faults which can cause dangerous environmental damages (Chino et al. 2011, Buesseler et al. 2011, Hatch et al. 2005). Renewable energy is an attractive substitute for nuclear energy as it is emission-free, environmentally friendly and regenerative (Boyle 1997). Renewable energy can range from geothermal (Barbier 2002), biomass (Field et al. 2008), solar (Foster et al. 2009), hydro (Hoffert et al. 2002), tidal (Rourke et al. 2010) and wind sources. Wind energy is now a mature technology, with a limited number of design choices which are progressively converging to some optimal solution. Wind brings with it problems of intermittency, network stability and curtailment which are a particular challenge to island grids with restricted interconnection, such as Ireland (Dineen et al. 2016).

Ireland as an island country has a large coastline which is conveniently adjacent to the

Atlantic Ocean. Therefore, wave energy resources are abundant, estimated at 21 TWh (Deane et al. 2012). Unlike wind, wave energy has multiple methods of power extraction (Falnes 2007), where these methods fall into the near-shore (Folley & Whittaker 2009*a*) and offshore (Falnes 2007) categories. Offshore devices can potentially take advantage of the interference phenomena present in ocean waves. Coupling multiple wave energy converters (WEC) together in a wave energy farm, constructive interference can become favourable. Hence, a wave energy farm of smaller devices can produce greater average power levels than a single WEC device of equivalent size (Barcelli & Ringwood 2013).

Even though the concept of extracting high levels of energy from an offshore wave farm seems promising, there are issues which present themselves (Cahill & Lewis 2013). These problems are inherited from the infrastructure needed for WEC farms, such as mechanical, hydrodynamical and electrical components (Penalba & Ringwood 2016). There is an economic necessity to optimise the wave-to-grid system as a whole which will substantially minimise the energy cost for the consumer (Leijon et al. 2003). Furthermore, to produce the minimum cost of energy, the average power extracted from the system must be maximised while preventing permanent damage to the system. Control techniques are used to maximise average power extraction while incorporating the system constraints. It is imperative to include control algorithms within the wave-to-grid system; allowing optimum power flow, low maintenance and power quality regulation which is crucial for grid operation (Ringwood et al. 2014).

1.1 The Aims and Scope of this Thesis

The prime objective of this thesis is to analyse the system from wave-to-grid and to show the advantages of implementing model predictive control (MPC). In previous work, research has covered the individual subsystems of the wave-to-grid system without considering the remaining subsystems within the wave-to-grid chain. For economic feasibility, the system from wave-to-grid needs to be considered as a whole. It is imperative that the control algorithm factors in the physical and electrical system constraints while optimising for electrical power to minimise the cost of energy for the consumer. The design and tuning of the controller needs to allow a fast and robust control algorithm; without this analysis, the control scheme can become obsolete in real life application. Utilising smart centralised control algorithms, WEC farms can produce large amounts of average electrical power while maintaining an acceptable power quality which is key to reducing consumer energy costs. Research has covered power

quality issues with the use of energy storage devices, however research on the effects of electrical power aggregation from an array of multiple WECs has been limited.

1.2 A Survey of Existing Work

Research in the area of wave energy has quickly matured in recent years. These research topics range from the excitation wave characteristics, the WEC design, the mechanical infrastructure, the electrical infrastructure, energy storage, the WEC control, the WEC array layout and the WEC array control.

1.2.1 Wave Energy Device Topologies

Multiple WEC device types are currently in development, which allows for different energy extraction methods, where each device type has its own set of advantages and disadvantages. The oscillating water column is a system where air is compressed using the motion of the wave and passes through a turbine (Amundarain et al. 2011). The oscillating water column can be onshore or offshore, where the main advantage of the oscillating water column is the indirect connection that the turbine has with the water, reducing future maintenance. The overtopping WEC uses a reservoir to store the water from the overtopping waves; the stored water is then released through a turbine (Igic et al. 2011). The generated power is advantageously nearly constant due to the constant flow of fluid passing through the turbine from the reservoir. However, with the water directly in contact with the turbine, increased maintenance is inherited. The oscillating wave surge converter is a nearshore hinged WEC device that absorbs the horizontal energy of the oncoming waves; the Aquamarine power oyster is an example (Whittaker & Folley 2012). This system is advantageous not only because it absorbs power, but it also has the potential of shadowing waves from hitting the shoreline which could prevent shoreline erosion. However, the system is highly non-linear and is prone to bio-fouling growth (Tiron et al. 2015), which can restrict the surging motion. A desalination WEC system uses the pressure created from the excitation waves to force ocean salt water through a mesh to create drinking water (Bacelli et al. 2009). Although this system does not directly extract energy, it does take advantage of a natural high-pressure force, which can be used to replace the energy demanding desalination system. The attenuating WEC has a snake-like geometry which operates with multiple degrees of freedom whereby, using actuators, energy is absorbed from the incoming waves (Palha et al. 2010). This device, like the surge device, potentially

could shadow the shoreline from the incoming wave that would cause erosion. However, the system consists of many hydraulic and mechanical mechanisms, which can increase future maintenance. The submerged pressure differential is a seabed bound device that utilises the change in pressure caused by the variable volume of water that is inherited from the waves passing overhead on the water surface; an Archimedes wave swing is an example (de Sousa Prado et al. 2006). This system is aesthetically advantageous since the device is invisible to the public eye. However, a problematic maintenance procedure is also inherited. The point absorber is a simple symmetric device that is insignificant in size when compared with the wavelength of the excitation waves (Antonio 2010). Point absorber WECs are commonly used in research as they are easily modelled using linear wave theory and are well suited for deployment in arrays (Folley et al. 2012), which is the main reason why it is the focus of this thesis.

1.2.2 Wave-to-Grid Infrastructure

Along with hydrodynamic and mechanical design, research has focussed on the difficulties that are related to WEC-to-grid integration (Thorburn et al. 2004). The electrical system includes components such as generators, safety mechanisms, cabling, power converters, the DC-link system, offshore electrical network topologies and whether the network is DC or AC.

1.2.2.1 Power Take Off Topologies

Generator types commonly used are either hydraulic, pneumatic or electrical systems, where each generator is suitable for different applications. A hydraulic generator power take-off (PTO) system can utilise high-pressure accumulators which act as a short-term energy storage, allowing smooth power extraction (Henderson 2006). A hydraulic turbine PTO system creates electrical energy by allowing fluid to pass through the turbine, which is connected to a rotary generator (Stier & Kynard 1986). The fluid in question can be a hydraulic fluid or a direct ocean water source. In the case of the hydraulic fluid system, a group of check valves and a set of low and high-pressure accumulators allow a unidirectional fluid to pass through a turbine; allowing electrical energy conversion. However, it is difficult to control this system actively, causing suboptimal results. A pneumatic turbine PTO system allows bi-directional pressurised airflow through the turbine blades, connecting the turbine to a rotary generator, allowing energy extraction (Gato & Falcão 1988). A direct drive electrical generator is an entirely electrical system which utilises a linear generator, where the translator of

the generator is directly connected to the heaving buoy (Polinder et al. 2004). Linear generators can be longitudinal flux permanent magnet generators (LFPMG) (Danielsson et al. 2005), variable reluctance permanent magnet generators (VRPMG) which are preferred over the LFPMG due to it's higher power density and efficiency (Mellor et al. 2005), or tubular air-cored permanent magnet generators (TAPMG) which have less power density than the LFPMG, but a high power factor (Wang et al. 1999). Linear direct drive electrical generators are advantageous since they can produce substantial PTO force levels without the need for high-pressure hydraulic mechanisms, hence, maintaining the force density of the hydraulic system while reducing the maintenance.

1.2.2.2 Safety Mechanisms

The safety mechanisms for the WEC system include electrical safety components such as a crowbar system (Larsen & Ritter 1998) and mechanical safety equipment such as moorings (Harris et al. 2004). The crowbar system is a shunt device that allows current to bypass the power converters controlling the WEC; this prevents permanent damages occurring to the power converters. The moorings are mechanical anchorage components that prevent the WEC from drifting out of position; this concept is crucial in WEC arrays as it reduces the potential for device collision.

1.2.2.3 Electrical Infrastructure

The choice in power converter, the DC-link system (Schoen et al. 2011), offshore electrical network topology and whether the network is DC or AC are all linked together (López et al. 2013). The cabling for a WEC system is designed differently from standard energy sources, as the cable rating for a wave energy system depends on the thermodynamics caused by instantaneous current fluctuations (Blavette et al. 2015). Power converters come in a range of different topologies (Bimbhra & Kaur 2012). A commonly used AC/DC/AC topology is a back-to-back voltage source converter (VSC) (Friedli et al. 2012). The power rating of the power converter depends on the power extracted from the WEC. If the converter has an insufficient power rating, the WEC can become difficult to control. If the converter is overrated, then the ocean energy extraction system becomes less economical. The DC-link system consists of an energy storage device which enables a constant DC voltage between the two VSCs that are on the generation and grid side. The storage device may consist of a capacitor, battery storage (Nie et al. 2013), flywheel (Cimuca et al. 2006) or supercapacitor (Murray et al. 2012). The offshore electrical network topologies are primarily chosen

by the ratings of the power converters, cabling and DC-link energy storage. As shown in (López et al. 2013), there is a multitude of electrical topologies. The suitability of the topologies depends mainly on maximising the energy absorption while reducing the cost, hence producing an economic system.

With wave-to-grid system design, it is essential to focus on the complete wave-to-grid system as a whole; not to concentrate solely on the average electrical power harvest or the quality of the instantaneous power injected onto the national grid (O'Sullivan et al. 2012). By its nature, power quality issues for wave energy devices are significantly more problematic than for wind turbines, with potentially significant swings in delivered electrical power occurring over seconds (Bizzozero et al. 2016). This is a particular problem for grid integration, especially when the local grid is weak, which is often likely due to the probable remote locations of WEC systems (Santos-Mugica et al. 2010). One approach is to use energy storage such as batteries or super-capacitors to smooth out the power flow onto the local grid (Murray et al. 2017). Likewise, the aggregation of the electrical power from an array of WECs can be utilised to minimise the resulting significant power fluctuations, just by nature of their phase differences, or by active control over the array (Göteman et al. 2015, Sjolte et al. 2012, Molinas et al. 2007).

1.2.3 WEC Array Layout

Ideally, a wave energy array should be designed to maximise the electrical energy harvest from a particular site, depending on the wave direction, the separation distance of the WECs, constructive interference, power variance and non-ideal WEC positioning. Depending on the orientation of the wave energy array, constructive or deconstructive interference can occur (Babarit 2013). Therefore it is necessary to orientate the wave energy array to maximise constructive interference to the wave climate (Xu et al. 2017). This interference phenomenon is caused by the devices interacting with each other through the means of radiated waves caused by the motion of the WECs. As the devices get closer to each other, the interference between each device increases (Balitsky & Ringwood 2014). As the number of devices in the array increases, the number of constructive optimum points available across the range of wave frequency and wave direction angle increases. Furthermore, as the number of WECs in the array increases, the need for an optimum WEC farm layout becomes less essential (Göteman et al. 2014). Hence, as the number of devices grows within the array, the less dependent the average power is on wave direction. Of course, these factors are assuming ideal

conditions where system constraints, electrical layout, non-ideal PTOs, control algorithms and effects caused by multiple degrees of motion are excluded. In (Göteman et al. 2015), the benefit of randomised WEC positioning in an array is demonstrated where power quality improvements are shown. This exhibits an authentic aspect of a real life WEC array operation, where the WEC devices will naturally drift to some degree from their neutral position. Recent investigations have found that the inclusion of control techniques in the layout optimisation stage is essential (Garcia-Rosa et al. 2015), including the control technique, how it is tuned, and the control constraints, as all affect the energy extracted from the array.

1.2.4 WEC Control

1.2.4.1 Classical Control

WEC control techniques initially focussed on classical causal methods such as linear damping, latching, declutching and impedance matching where all of these control techniques have the primary objective to maximise the average power extracted from the incoming excitation wave. Linear damping is the most straightforward method out of the classical group. It involves using a passive damper, which creates a PTO force that is proportional to the velocity of the WEC, hence causing unidirectional power flow at all times. The linear damper needs to be tuned differently for each frequency and does not produce optimum average power. Latching is an active control method that physically locks the WEC into position for an optimised amount of time and is then released, hence causing a forced oscillation of the WEC (Babarit et al. 2004). This method performs well in a frequency spectrum lower than the WECs natural frequency. Declutching operates similarly to latching control (Babarit et al. 2009). Instead of physically locking the WEC into position, the PTO is disengaged for a period. This allows close to maximum average power extraction during excitation waves with frequencies higher than the WECs natural frequency. Both latching and declutching are time domain methods which produce positive results. However, other frequency domain methods produce optimum average power results over a more extensive frequency range. One of the first methods developed was impedance matching control (Budal & Falnes 1977, Costa et al. 2010). This method involves controlling the WECs velocity to have a specific amplitude and phase difference in reference to the excitation wave force. These optimum velocity amplitudes and phases allow maximum average power extraction from the excitation wave. These classical methods produce promising results in terms of energy extraction, however, they typically allow excessive forces

to be generated by the power take-off, resulting in significant power swings which are unacceptable to be exported onto the grid.

1.2.4.2 Optimal Control

Recently, optimal control methods such as bang-bang control, dynamic programming, pseudospectral control and model predictive control (MPC) have been investigated, where these methods can easily incorporate constraints into the control algorithm. Bang-bang control involves an iterative finite-time optimisation which maximises the average power absorbed from the excitation waves over a receding horizon, utilising PTO force acting on the WEC that is restricted to instantaneously switch between two states (Abraham & Kerrigan 2013). This method emulates the control action of a latching classical control method. However, the controller is complex to implement . Dynamic programming was introduced to bypass the convexity issues that may emerge in advanced optimal control systems which rely on convex cost functions (Li et al. 2012). This method produces near optimial results, however, the method is computationally expensive. Pseudospectral control is a frequency domain optimal controller (Genest & Ringwood 2016), where the predicted wave excitation over the receding horizon is decomposed into individual frequency components using the Galerkin method (Cockburn & Shu 1998). Utilising these frequency components, an optimisation produces the optimum PTO force frequency components efficiently, reducing the computational complexity. However, the method is dependent on the number of discrete frequencies preselected within a preselected spectrum window, where problems may arise if the preselected discrete frequencies density and spectrum window are ill-defined. Model predictive control (MPC) is a discrete time model-based predictive controller widely used in industry (Maciejowski 2002), which has been utilised in the wave energy industry (Cretel et al. 2010). With general MPC reference tracking control, a cost function is utilised which is based on the error between the systems reference points and outputs that are extended over a finite prediction horizon. Furthermore, MPC is commonly used in industry because linear and non-linear constraints are easily incorporated into the optimisation (Mayne et al. 2000). By minimising the cost function of the controller, the optimal control inputs over the control horizon are found. These optimum control variables translate to minimising the difference between the reference points and the system outputs over the prediction horizon (Camacho & Alba 2013). However in a generic MPC, it is only the first optimised control input variable that is implemented on the system while the others over the control horizon are neglected; the optimisation process is then repeated at the next time step.

1.2.4.3 Economic Model Predictive Control

In the case of wave energy, economic MPC was initially introduced to maximise the average mechanical power extracted from a point absorber (Li & Belmont 2014, Cretel et al. 2010). Defining the MPC cost function as the average power over the prediction horizon (Hals et al. 2011), the average power is maximised over the prediction horizon. Amending the MPC to use a system model with a first-order hold (FOH) formulation allowed for greater power extraction and a more compact formulation (Cretel et al. 2011). However, with these advanced optimum control techniques, there is a need for an excitation wave prediction over a specified horizon (Li et al. 2012, Fusco & Ringwood 2012, Schoen et al. 2011). The excitation wave prediction can introduce errors into the control algorithms, since the control algorithm depends on a perfect prediction over the finite prediction horizon. In this thesis, the excitation wave prediction is assumed perfect. Therefore the effects of wave prediction error are decoupled from the system performance.

1.2.5 WEC Array Optimum Control

Initially, decentralised control was utilised for WEC arrays, where each device is independently controlled, assuming little or no interaction between the devices. Decentralised control techniques implemented on arrays have employed both optimal methods such as MPC (Oetinger et al. 2014*b*) and standard methods which are independent of an excitation wave prediction such as suboptimal control (Folley & Whittaker 2009*b*) and quiescent control (Belmont 2010). Optimal centralised methods in which the whole array is controlled as one dynamic system, including the inter-device interactions, have included methods such as matrix control (Nambiar et al. 2015), Galerkin control (Barcelli & Ringwood 2013, Bacelli & Ringwood 2015) and MPC (Oetinger et al. 2014*a*). In (Barcelli & Ringwood 2013), a comparison between a decentralised and a centralised control system illustrated the effect of the separation distance between WEC devices in the array. It showed that multiple decentralised control systems are sufficient when the separation distance is over a certain threshold (Bozzi et al. 2017). One fundamental disadvantage of implementing a centralised control system is the computational expense when considering a large array - to amend this problem distributed control is used (Li & Belmont 2014, Mc Namara et al. 2013). Distributed control offers performance which comes close to that obtained with centralised control, by the decomposition of the optimisation problem into local problems with some limited communication between the devices (Mc Namara et al. 2013). Typically, an

iterative MPC method is used which produces an equivalent global solution and which can incorporate global constraints (Diehl et al. 2017).

1.3 Thesis Outline

In Chapter 2, the theoretical background of the wave-to-grid system is described in detail. The hydrodynamics of an object in water is designed using the non-linear potential flow modelling method and also the simplified linear modelling method. Using sea spectrum analysis, irregular unidirectional sea modelling is explained. Using system identification methods, the radiation kernel system for a single WEC and multiple WECs is modelled. The electrical system from wave-to-grid begins with the modelling of the PTO, where the differences between a generic rotary generator and a linear generator are explained. An explanation of the LPMG current controller design and operation is covered, where Park's transformation is utilised to simplify the control. The grid side DC-link voltage control scheme is then analysed, where difficulties such as grid weakness non-linearity and the potential for non-minimum phase behaviour are discussed.

In Chapter 3, the economic model predictive control (MPC) used throughout the remainder of the thesis is introduced. Initially, the classical wave power extraction control algorithm is explained, where the advantages and disadvantages are shown. Including a non-ideal PTO into the system, the effects due to resistive losses are shown when using standard optimum classical control which does not include the losses within the control algorithm. The generic reference tracking MPC is then introduced, where the difference between the reference tracking MPC, and the economic MPC is described. The MPC with the LPMGs resistive losses within the cost function is then introduced. A comparison between an MPC with a piecewise constant input and a piecewise linear input is established, where matters such as high frequency power quality are discussed.

In Chapter 4, field weakening is incorporated into the MPC to combat the issues introduced by the systems electrical restrictions. Initially, the mechanical constraints of the WEC and LPMG are analysed, where the effects of the linear mechanical constraints on the average electrical power extracted are shown. This work investigates the effect of electrical constraints on the feasible region and on the performance of the system. This focuses on the potential benefits of using a high DC link voltage. The formulation of the MPC with field weakening incorporated into the cost function is then explained. Implementing a uni-directional power flow constraint, the advantage of using an MPC

with field weakening during low DC-link voltage levels is shown.

In Chapter 5, the robustness and the efficiency of the control algorithm are analysed. Initially, the robustness of the control algorithm is tested using model mismatch analysis. This includes analysing the performance of the power extraction system while the error between the control model and the system model increases. A non-linear MPC (NMPC) is then introduced to compensate for the non-linear viscous forces present. A linear MPC is then described, where this MPC estimates the non-linear component of the NMPC. A move-blocking control horizon reduction method is then explained, where the advantages of utilising the method are discussed.

In Chapter 6, the advantage of implementing a centralised MPC algorithm on an array of multiple devices is shown. The effects of constructive and destructive interference are analysed by comparing the average electrical power results captured using the centralised control from an array of multiple WEC devices with close device spacing and a substantial device spacing. Introducing linear mechanical constraints and viscous effects into the system and the centralised control algorithm, the effects of the interference phenomena are analysed. Using monochromatic and polychromatic uni-directional excitation waves, a constrained centralised MPC is contrasted against a constrained decentralised MPC. Implementing a power limit constraint on the decentralised and centralised MPC algorithms, the advantage of sharing information between the devices within the array is highlighted.

Chapter 7 focuses on the main contributions for the thesis and the recommendations of the future steps to be taken. Final conclusions and remarks are made.

1.4 Contributions

In Chapter 2, a contribution was made where a full wave-to-grid system was described as a single model, instead of multiple constraint independent subsystems. This contribution included a discussion of the co-design problems in one document, including the hydrodynamic, mechanical and electrical modelling issues.

In Chapter 3, a major contribution was made where the resistive losses from the realistic LPMG were included in the control algorithm. This allowed maximum average electrical power to be extracted from the entire WEC-LPMG system. A contribution was also made, where the high-frequency noise present in a ZOH control algorithm was reduced by merely utilising a FOH PTO input signal.

In Chapter 4, a major contribution was made with the inclusion of the non-linear electrical constraints in the control algorithm, showing how important it is to design the wave-to-DC-link system as a unit, instead of its constituent subsystems. Another major contribution was made by including field weakening in the control algorithms. During periods of low DC-link levels, higher speeds could be allowed by enabling field weakening, due to the significant expansion of the feasible region providing increased average electrical power. A contribution was made where a uni-directional power flow constraint was introduced into the MPC algorithm, restricting the extraction of power from the grid. This power flow constraint enables a stable grid side DC-link voltage controller, which is essential for allowing a fully functioning controller on the generation side.

In Chapter 5, another contribution of this thesis is the accomplished robustness analysis, showing that MPC can still produce an acceptable amount of average electrical power without a perfect match between the MPC internal model and the actual system. A major contribution was made when an LPV NMPC was introduced to tackle the viscous effects that commonly occurred when utilising active control algorithms. Without viscous effects included in the control algorithm, major power losses can occur. A major contribution was made by introducing a linear MPC which approximated the non-linear viscous effects of the LPV NMPC with a linear model, which maintained the controller fidelity while substantially reducing the computational burden. A major contribution was made by incorporating a move-blocking technique into the control algorithm, which reduced the control algorithms computational expense even more by reducing the number of free variables to be calculated across the control horizon.

In Chapter 6, a contribution was made by showing how the performance of the decentralised MPC control system becomes similar to the centralised MPC control algorithm when linear constraints and viscous effects are included in the system. This showed that a centralised MPC algorithm is not essential when optimising for electrical power from an array of hydrodynamically coupled WECs. A major contribution was made by introducing an upper electrical power constraint into the centralised control algorithm. It was shown that a centralised MPC with a global power constraint could outperform a centralised MPC with a set of local power constraints when focusing on average electrical power levels and a better average to peak power ratio. This contribution also impacts on DC-link voltage controller stability issues on the gird side, where the centralised MPC algorithm with a global power constraint reduces the chance of grid side stability issues.

References

Abraham, E. & Kerrigan, E. C. (2013), 'Optimal active control and optimization of a wave energy converter', *IEEE Transactions on Sustainable Energy* **4**, 324–332.

Amundarain, M., Alberdi, M., Garrido, A. J. & Garrido, I. (2011), 'Modeling and simulation of wave energy generation plants: Output power control', *IEEE Transactions on Industrial Electronics* **58**(1), 105–117.

Antonio, F. de. O. (2010), 'Wave energy utilization: A review of the technologies', *Renewable and sustainable energy reviews* **14**(3), 899–918.

Babarit, A. (2013), 'On the park effect in arrays of oscillating wave energy converters', *Renewable Energy* **58**, 68–78.

Babarit, A., Duclos, G. & Clément, A. H. (2004), 'Comparison of latching control strategies for a heaving wave energy device in random sea', *Applied Ocean Research* **26**(5), 227–238.

Babarit, A., Guglielmi, M. & Clément, A. H. (2009), 'Declutching control of a wave energy converter', *Ocean Engineering* **36**(12), 1015–1024.

Bacelli, G., Gilloteaux, J.-C. & Ringwood, J. (2009), A predictive controller for a heaving buoy producing potable water, *in* 'Control Conference (ECC), 2009 European', IEEE, pp. 3755–3760.

Bacelli, G. & Ringwood, J. V. (2015), 'Numerical optimal control of wave energy converters', *IEEE Transactions on Sustainable Energy* **6**(2), 294–302.

Balitsky, P. & Ringwood, J. V. (2014), 'Control-Influenced Layout Optimization of Arrays of Wave Energy Converters', *33rd International Conference on Ocean, Offshore and Arctic Engineering* pp. 1–10.

Barbier, E. (2002), 'Geothermal energy technology and current status: an overview', *Renewable and Sustainable Energy Reviews* **6**(1), 3–65.

Barcelli, G. & Ringwood, J. (2013), 'Constrained control of arrays of wave energy devices', *International Journal of Marine Energy* **3**, 53–69.

Belmont, M. R. (2010), 'Increases in the average power output of wave energy converters using quiescent period predictive control', *Renewable Energy* **35**(12), 2812–2820.

Bimbhra, P. S. & Kaur, S. (2012), *Power electronics*, Vol. 2, Khanna publishers.

Bizzozero, F., Bozzi, S., Gruosso, G., Passoni, G. & Giassi, M. (2016), 'Spatial interactions among oscillating wave energy converters: Electricity production and power quality issues', *Industrial Electronics Society, IECON 2016-42nd Annual Conference of the IEEE* pp. 4235–4240.

Blavette, A., O'Sullivan, D. L., Lewis, T. W. & Egan, M. G. (2015), 'Dimensioning the equipment of a wave farm: Energy storage and cables', *IEEE Transactions on Industry Applications* **51**(3), 2470–2478.

Boyle, G. (1997), *Renewable energy: power for a sustainable future*, Vol. 2, Taylor & Francis.

Bozzi, S., Giassi, M., Miquel, A. M., Antonini, A., Bizzozero, F., Gruosso, G., Archetti, R. & Passoni, G. (2017), 'Wave energy farm design in real wave climates: the Italian offshore', *Energy* **122**, 378–389.

Budal, K. & Falnes, J. (1977), 'Optimum operation of improved wave-power converter', *Marine Science Communications* **3**, 133–150.

Buesseler, K., Aoyama, M. & Fukasawa, M. (2011), 'Impacts of the Fukushima nuclear power plants on marine radioactivity', *Environmental science & technology* **45**(23), 9931–9935.

Cahill, B. G. & Lewis, T. (2013), 'Wave energy resource characterisation of the Atlantic Marine Energy Test Site', *International Journal of Marine Energy* **1**(Supplement C), 3–15.

Camacho, E. F. & Alba, C. B. (2013), *Model predictive control*, Springer Science & Business Media.

Chino, M., Nakayama, H., Nagai, H., Terada, H., Katata, G. & Yamazawa, H. (2011), 'Preliminary estimation of release amounts of 131I and 137Cs accidentally discharged from the Fukushima Daiichi nuclear power plant into the atmosphere', *Journal of nuclear science and technology* **48**(7), 1129–1134.

Cimuca, G. O., Saudemont, C., Robyns, B. & Radulescu, M. M. (2006), 'Control and performance evaluation of a flywheel energy-storage system associated to a variable-speed wind generator', *IEEE Transactions on Industrial Electronics* **53**(4), 1074–1085.

Cockburn, B. & Shu, C.W. (1998), 'The Runge–Kutta discontinuous Galerkin method for conservation laws V: multidimensional systems', *Journal of Computational Physics* **141**(2), 199–224.

Costa, P. R., Garcia-Rosa, P. B. & Estefen, S. F. (2010), 'Phase control strategy for a wave energy hyperbaric converter', *Ocean Engineering* **37**(17), 1483–1490.

Cretel, J. A. M., Lewis, A. W., Lightbody, G. & Thomas, G. P. (2010), 'An Application of Model Predictive Control to a Wave Energy Point Absorber', *Proceedings of the IFAC Conference on Control Applications in Marine Systems* (1980), 1–6.

Cretel, J. A. M., Lightbody, G., Thomas, G. P. & Lewis, A. W. (2011), 'Maximisation of energy capture by a wave-energy point absorber using model predictive control', *IFAC Proceedings Volumes* **44**(1), 3714–3721.

Danielsson, O., Leijon, M. & Sjostedt, E. (2005), 'Detailed study of the magnetic circuit in a longitudinal flux permanent-magnet synchronous linear generator', *IEEE Transactions on Magnetics* **41**(9), 2490–2495.

de Sousa Prado, M. G., Gardner, F., Damen, M. & Polinder, H. (2006), 'Modelling and test results of the Archimedes wave swing', *Proceedings of the Institution of Mechanical Engineers, Part A: Journal of Power and Energy* **220**(8), 855–868.

Deane, J. P., Dalton, G. & Gallachóir, B. P. Ó. (2012), 'Modelling the economic impacts of 500MW of wave power in Ireland', *Energy Policy* **45**, 614–627.

Diehl, M., Keviczky, T., De Schutter, B. & Doan, Dang, M. (2017), 'A Jacobi Decomposotion algorithm for distribuated convex optimisation in distribuated model predicitive control', *120h IFAC World Congress* .

Dineen, D., Howley, M., Holland, M. & Cotter, E. (2016), Energy Security in Ireland: A Statistical Overview 2016, Technical report.

Falnes, J. (2007), 'A review of wave-energy extraction', *Marine Structures* **20**(4), 185–201.

Field, C. B., Campbell, J. E. & Lobell, D. B. (2008), 'Biomass energy: the scale of the potential resource', *Trends in ecology & evolution* **23**(2), 65–72.

Figueres, C., Schellnhuber, H. J., Whiteman, G., Rockström, J., Hobley, A. & Rahmstorf, S. (2017), 'Three years to safeguard our climate', *Nature News* **546**(7660), 593.

Folley, M., Babarit, A., Child, B., Forehand, D., O'Boyle, L., Silverthorne, K., Spinneken, J., Stratigaki, V. & Troch, P. (2012), 'A review of numerical modelling of wave energy converter arrays', *Proceedings of the 31st International Conference on Offshore Mechanics & Arctic Engineering, Rio de Janeiro, Brazil* pp. 10–15.

Folley, M. & Whittaker, T. J. T. (2009*a*), 'Analysis of the nearshore wave energy resource', *Renewable Energy* **34**(7), 1709–1715.

Folley, M. & Whittaker, T. J. T. (2009*b*), 'The effect of sub-optimal control and the spectral wave climate on the performance of wave energy converter arrays', *Applied Ocean Research* **31**(4), 260–266.

Foster, R., Ghassemi, M. & Cota, A. (2009), *Solar energy: renewable energy and the environment*, CRC Press.

Friedli, T., Kolar, J. W., Rodriguez, J. & Wheeler, P. W. (2012), 'Comparative evaluation of three-phase AC–AC matrix converter and voltage DC-link back-to-back converter systems', *IEEE Transactions on industrial electronics* **59**(12), 4487–4510.

Fusco, F. & Ringwood, J. V. (2012), 'A study of the prediction requirements in real-time control of wave energy converters', *IEEE Transactions on Sustainable Energy* **3**(1), 176–184.

Garcia-Rosa, P. B., Bacelli, G. & Ringwood, J. V. (2015), 'Control-informed optimal array layout for wave farms', *IEEE Transactions on Sustainable Energy* **6**(2), 575–582.

Gato, L. M. C. & Falcão, A. F. de. O. (1988), 'Aerodynamics of the Wells turbine', *International Journal of Mechanical Sciences* **30**(6), 383–395.

Genest, R. & Ringwood, J. V. (2016), 'A critical comparison of model-predictive and pseudospectral control for wave energy devices', *Journal of Ocean Engineering and Marine Energy* **2**(4), 485–499.

Göteman, M., Engström, J., Eriksson, M. & Isberg, J. (2015), 'Optimizing wave energy parks with over 1000 interacting point-absorbers using an approximate analytical method', *International Journal of Marine Energy* **10**, 113–126.

Göteman, M., Engström, J., Eriksson, M., Isberg, J. & Leijon, M. (2014), 'Methods

of reducing power fluctuations in wave energy parks', *Journal of Renewable and Sustainable Energy* **6**(4), 43103.

Hals, J., Falnes, J. & Moan, T. (2011), 'Constrained optimal control of a heaving buoy wave-energy converter', *Journal of Offshore Mechanics and Arctic Engineering* **133**(1), 11401.

Harris, R. E., Johanning, L. & Wolfram, J. (2004), 'Mooring systems for wave energy converters: A review of design issues and choices', *Marec2004* .

Hatch, M., Ron, E., Bouville, A., Zablotska, L. & Howe, G. (2005), 'The Chernobyl disaster: cancer following the accident at the Chernobyl nuclear power plant', *Epidemiologic reviews* **27**(1), 56–66.

Henderson, R. (2006), 'Design, simulation, and testing of a novel hydraulic power take-off system for the Pelamis wave energy converter', *Renewable Energy* **31**(2), 271–283.

Hoffert, M. I., Caldeira, K., Benford, G., Criswell, D. R., Green, C., Herzog, H., Jain, A. K., Kheshgi, H. S., Lackner, K. S., Lewis, J. S. & Others (2002), 'Advanced technology paths to global climate stability: energy for a greenhouse planet', *science* **298**(5595), 981–987.

Igic, P., Zhou, Z., Knapp, W., MacEnri, J., Sørensen, H. C. & Friis-Madsen, E. (2011), 'Multi-megawatt offshore wave energy converters–electrical system configuration and generator control strategy', *IET renewable power generation* **5**(1), 10–17.

Larsen, E. V. & Ritter, A. M. (1998), 'Apparatus for protection of power-electronics in series compensating systems'.

Leijon, M., Bernhoff, H., Berg, M. & Ågren, O. (2003), 'Economical considerations of renewable electric energy production—especially development of wave energy', *Renewable Energy* **28**(8), 1201–1209.

Li, G. & Belmont, M. R. (2014), 'Model predictive control of sea wave energy converters–Part II: The case of an array of devices', *Renewable Energy* **68**, 540–549.

Li, G., Weiss, G., Mueller, M., Townley, S. & Belmont, M. R. (2012), 'Wave energy converter control by wave prediction and dynamic programming', *Renewable Energy* **48**, 392–403.

López, I., Andreu, J., Ceballos, S., de Alegr, I. M. & Kortabarria, I. (2013), 'Review

of wave energy technologies and the necessary power-equipment', *Renewable and Sustainable Energy Reviews* **27**, 413–434.

Maciejowski, J. M. (2002), *Predictive Control: with Constraints*, Pearson Education, Prentice Hall.

Mayne, D. Q., Rawlings, J. B., Rao, C. V. & Scokaert, P. O. M. (2000), 'Constrained model predictive control: Stability and optimality', *Automatica* **36**(6), 789–814.

Mc Namara, P., Negenborn, R. R., De Schutter, B. & Lightbody, G. (2013), 'Optimal coordination of a multiple HVDC link system using centralized and distributed control', *IEEE Transactions on Control Systems Technology* **21**(2), 302–314.

Mellor, P. H., Burrow, S. G., Sawata, T. & Holme, M. (2005), 'A wide-speed-range hybrid variable-reluctance/permanent-magnet generator for future embedded aircraft generation systems', *IEEE transactions on industry applications* **41**(2), 551–556.

Molinas, M., Skjervheim, O., Sørby, B., Andreasen, P., Lundberg, S. & Undeland, T. (2007), 'Power smoothing by aggregation of wave energy converters for minimizing electrical energy storage requirements', *Proceedings of the 7th European Wave and Tidal Energy Conference* pp. 3–8.

Murray, D. B., Gallagher, P., Duffy, B. & McCormack, V. (2017), 'Energy storage solutions for offshore wave and tidal energy prototypes', *Ecological Vehicles and Renewable Energies (EVER), 2017 Twelfth International Conference on* pp. 1–8.

Murray, D. B., Hayes, J. G., O'Sullivan, D. L. & Egan, M. G. (2012), 'Supercapacitor testing for power smoothing in a variable speed offshore wave energy converter', *IEEE Journal of Oceanic Engineering* **37**(2), 301–308.

Nambiar, A. J., Forehand, D. I. M., Kramer, M. M., Hansen, R. H. & Ingram, D. M. (2015), 'Effects of hydrodynamic interactions and control within a point absorber array on electrical output', *International Journal of Marine Energy* **9**, 20–40.

Nie, Z., Xiao, X., Kang, Q., Aggarwal, R., Zhang, H. & Yuan, W. (2013), 'SMES-battery energy storage system for conditioning outputs from direct drive linear wave energy converters', *IEEE Transactions on Applied Superconductivity* **23**(3), 5000705.

Oetinger, D., Magaña, M. E. & Sawodny, O. (2014*a*), 'Centralised model predictive controller design for wave energy converter arrays', *IET Renewable Power Generation* **9**(2), 142–153.

Oetinger, D., Magaña, M. E. & Sawodny, O. (2014*b*), 'Decentralized model predictive

control for wave energy converter arrays', *IEEE Transactions on Sustainable Energy* **5**(4), 1099–1107.

O'Sullivan, D., Salcedo, F., Blavette, A., Santos, M. & Lewis, A. W. (2012), 'Case studies on the benefits of energy storage for power quality enhancement: oscillating water column arrays', *Proceedings of the 4th International Conference on Ocean Energy (ICOE2012), Dublin, Ireland* **1719**.

Palha, A., Mendes, L., Fortes, C. J., Brito-Melo, A. & Sarmento, A. (2010), 'The impact of wave energy farms in the shoreline wave climate: Portuguese pilot zone case study using Pelamis energy wave devices', *Renewable Energy* **35**(1), 62–77.

Penalba, M. & Ringwood, J. V. (2016), 'A Review of Wave-to-Wire Models for Wave Energy Converters', *Energies* **9**(7), 506.

Polinder, H., Damen, M. E. C. & Gardner, F. (2004), 'Linear PM Generator System for Wave Energy Conversion in the AWS', *IEEE Transactions on Energy Conversion* **19**(3), 583–589.

Ringwood, J. V., Bacelli, G. & Fusco, F. (2014), 'Control, forecasting and optimisation for wave energy conversion', *IFAC Proceedings Volumes* **47**(3), 7678–7689.

Rourke, F. O., Boyle, F. & Reynolds, A. (2010), 'Tidal energy update 2009', *Applied Energy* **87**(2), 398–409.

Santos-Mugica, M., Haim, D. B., Salcedo, F. & Villate, J. L. (2010), 'Grid Integration of Wave Energy Farms: Basque Country Study', *3rd International Conference on Ocean Energy (ICOE2010)* pp. 1–7.

Savaresi, A. (2016), 'The Paris Agreement: a new beginning?', *Journal of Energy & Natural Resources Law* **34**(1), 16–26.

Schoen, M. P., Hals, J. & Moan, T. (2011), 'Wave prediction and robust control of heaving wave energy devices for irregular waves', *IEEE Transactions on Energy Conversion* **26**(2), 627–638.

Sjolte, J., Tjensvoll, G. & Molinas, M. (2012), 'All-electric wave energy converter connected in array with common dc-link for improved power quality', *Power Electronics for Distributed Generation Systems (PEDG), 2012 3rd IEEE International Symposium on* pp. 431–436.

Stier, D. J. & Kynard, B. (1986), 'Use of radio telemetry to determine the mortality of Atlantic salmon smolts passed through a 17-MW Kaplan turbine at a low-head

hydroelectric dam', *Transactions of the American Fisheries Society* **115**(5), 771–775.

Thorburn, K., Bernhoff, H. & Leijon, M. (2004), 'Wave energy transmission system concepts for linear generator arrays', *Ocean Engineering* **31**(11), 1339–1349.

Tiron, R., Mallon, F., Dias, F. & Reynaud, E. G. (2015), 'The challenging life of wave energy devices at sea: A few points to consider', *Renewable and Sustainable Energy Reviews* **43**, 1263–1272.

Wang, J., Jewell, G. W. & Howe, D. (1999), 'A general framework for the analysis and design of tubular linear permanent magnet machines', *IEEE Transactions on Magnetics* **35**(3), 1986–2000.

Whittaker, T. & Folley, M. (2012), 'Nearshore oscillating wave surge converters and the development of Oyster', *Phil. Trans. R. Soc. A* **370**(1959), 345–364.

Xu, D., Stuhlmeier, R. & Stiassnie, M. (2017), 'Harnessing wave power in open seas II: very large arrays of wave-energy converters for 2D sea states', *Journal of Ocean Engineering and Marine Energy* **3**(2), 151–160.

Chapter 2

Wave-to-Wire Modelling of Grid Connected Point Absorbers

2.1 Introduction

In this chapter, the building blocks are developed for the modelling and time domain simulation of grid connected point absorbers. This chapter first focuses on modelling the motion of a body floating in a fluid. This is described from first principles where the Navier-Stokes equations are introduced. Simplifications are made leading to the potential flow model which is then simplified even further into the linear model which is used throughout this thesis: using a cylindrical point absorber WEC with a uniform cross sectional area, the linear model is justified. This chapter shows how a model can be identified for the radiation forces using Prony's method, that is suitable for time domain analysis and control design. The Hankel method is then introduced as an efficient method for the identification of a dynamic model of the radiation forces for an array of devices.

In this work a linear permanent magnet generator (LPMG) is assumed where the PTO force produced from the LPMG is a function of the generator currents. The control of the generator is then introduced, where a Parks transformation is used to simplify the modelling and control of the three phase synchronous system. The voltage signals that are used to control the LPMG are then described, where the control voltages are dependent on the voltage across the DC link which is kept constant using a grid side voltage controller. The difficulties involved in DC link voltage control are described, however, in the remainder of the thesis it is assumed that a constant DC link voltage is available.

2.2 Point Absorber Modelling

The hydrodynamic model of a point absorber is described in this section, which includes the non-linear Navier-Stokes equations, the hydrodynamic potential flow model and the linear model. Using the linear model throughout the remainder of the thesis, the modelling of the entire point absorber wave energy converter is described, where this involves system identification methods that produce a continuous hydrodynamic model which correlates with the data extracted from hydrodynamic software.

2.2.1 Navier-Stokes Equations

To represent the motion of a body in an incompressible fluid, the following differential Navier-Stokes equations (2.1) can be used to simulate the full non-linear fluid dynamics (Temam 1984). These non-linear equations cannot be analytically solved, therefore numerical solvers such as computational fluid dynamic (CFD) codes are used to simulate the dynamics (Anderson & Wendt 1995). The CFD codes produce high fidelity results, however, with a high computational cost. Potential flow models described in the next subsection are used to produce faster simulation times.

$$\begin{aligned} \frac{\partial \rho}{\partial t} + \nabla.(\rho \mathbf{u}) &= 0 \\ \frac{\partial \mathbf{u}}{\partial t} + (\mathbf{u}.\nabla)\mathbf{u} &= -\frac{1}{\rho}\nabla.p + \mathbf{g} + \frac{\mu}{\rho}\nabla^2\mathbf{u} \end{aligned} \tag{2.1}$$

where,

$$\begin{aligned} \nabla &= \text{gradient operator} \\ \rho &= \text{fluid density} \\ \mathbf{u} &= \text{velocity vector} \\ \mu &= \text{dynamic viscosity} \\ p &= \text{pressure field} \\ \mathbf{g} &= \text{external source.} \end{aligned}$$

2.2.2 Hydrodynamic Potential Flow Models

The potential flow model, which is based on potential theory, is also known as a boundary element method (BEM) (Grilli et al. 1989). It is initially assumed that the fluid is

inviscid, irrotational and has an incompressible incident flow. With these assumptions, Newton's second law can be used to represent the WEC motion (2.2), where the WEC motion in this work is restricted to move in heave,

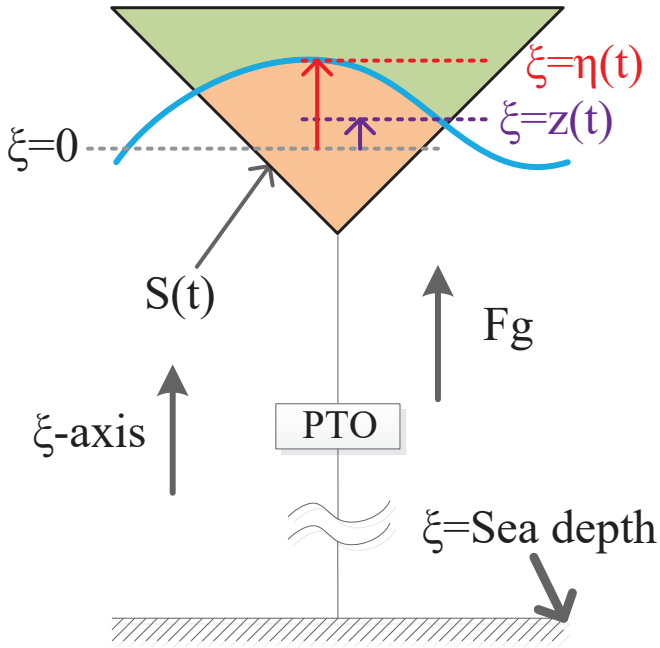

Figure 2.1: A conical WEC with a heave displacement dependent wetted surface area

$$M\ddot{z}(t) = F_g + \int_{S(t)} P_{dp}(t)\mathbf{n}dS + F_{PTO}(t) \tag{2.2}$$

where,

$z(t)$ = WEC vertical displacement
$\eta(t)$ = free surface elevation of wave
g = acceleration due to gravity
M = WEC mass
F_g = gravitational force $= -Mg$
$S(t)$ = instantaneous submerged wetted surface area (as shown in Fig. 2.1)
$F_{PTO}(t)$ = external PTO force
$P_{dp}(t)$ = dynamic pressure
$\mathbf{n}$ = vector normal to the surface
ξ = vertical axis.

The dynamic pressure ($P_{dp}(t)$) can then be formed by using Bernoulli's equations on the incident flow (Penalba Retes et al. 2015),

$$P_{dp}(t) = -\rho g\xi - \rho\frac{\partial\phi(t)}{\partial t} - \frac{\rho\left|\nabla\phi(t)\right|^2}{2} \tag{2.3}$$

where $\phi(t) =$ potential flow. The potential flow can then be broken into three components: the incident flow potential, the diffraction flow potential and the radiation potential,

$$\phi(t) = \phi_I(t) + \phi_D(t) + \phi_R(t) \tag{2.4}$$

Filling (2.4) into (2.3), the following is found,

$$\begin{aligned} P_{dp}(t) = -\rho g\xi - \rho\frac{\partial\phi_I(t)}{\partial t} - \frac{\rho\left|\nabla\phi_I(t)\right|^2}{2} - \rho\frac{\partial\phi_D(t)}{\partial t} - \frac{\rho\left|\nabla\phi_D(t)\right|^2}{2} - \rho\frac{\partial\phi_R(t)}{\partial t} \\ -\frac{\rho\left|\nabla\phi_R(t)\right|^2}{2} - \rho\nabla\phi_I(t)\nabla\phi_R(t) - \rho\nabla\phi_I(t)\nabla\phi_D(t) - \rho\nabla\phi_D(t)\nabla\phi_R(t) \end{aligned} \tag{2.5}$$

where

$$\begin{aligned} P_{st}(t) &= \text{static Froude-Krylov pressure} = (-\rho g\xi) \\ P_{dy}(t) &= \text{dynamic Froud-Krylov pressure} = \left(-\rho\frac{\partial\phi_I(t)}{\partial t} - \frac{\rho\left|\nabla\phi_I(t)\right|^2}{2}\right) \\ P_D(t) &= \text{diffraction pressure} = \left(-\rho\frac{\partial\phi_D(t)}{\partial t} - \frac{\rho\left|\nabla\phi_D(t)\right|^2}{2}\right) \\ P_R(t) &= \text{radiation pressure} = \left(-\rho\frac{\partial\phi_R(t)}{\partial t} - \frac{\rho\left|\nabla\phi_R(t)\right|^2}{2}\right). \end{aligned}$$

The remaining values are second derivatives that are assumed negligible for point absorbers (Penalba Retes et al. 2015). Filling this into (2.2), the non-linear motion equation can be represented as the following, which is restricted to the heave motion,

$$M\ddot{z}(t) = F_h(t) + F_{dy}(t) + F_D(t) + F_R(t) + F_{PTO}(t) \tag{2.6}$$

where,

$$\begin{aligned} F_h(t) &= F_g + \overbrace{\iint_{S(t)} P_{st}(t)\mathbf{n}dS}^{F_{st}(t)} \\ F_{dy}(t) &= + \iint_{S(t)} P_{dy}(t)\mathbf{n}dS \\ F_D(t) &= + \iint_{S(t)} P_D(t)\mathbf{n}dS \\ F_R(t) &= + \iint_{S(t)} P_R(t)\mathbf{n}dS. \end{aligned}$$

2.2.3 Linear Model

The potential equation previously given in (2.6) shows a non-linear equation which is computationally expensive to use during simulation. For a non-linear model, the dynamic Froude-Krylov force has to be continuously recalculated because it does not assume that the wetted surface is constant, e.g. when a conically shaped WEC is used (Fig. 2.1). However it is usually assumed that using a linearised version of the non-linear potential equation is sufficient when a cylindrical point absorber is used, because the cross sectional area is independent of the heave displacement and the motions are small. The linearised model equation is known as Cummins equation (Cummins 1962), where this linear system model (2.7) is in the heave direction only and is the basis of this thesis.

In this work a cylindrical point absorber with a semi-hemispherical base is used, as shown in Fig. 2.2; the design characteristics are shown in Table. 2.1.

Table 2.1: System values

Point absorber values			
Parameter names	Parameters	Units	Value
WEC mass	M	kg	670860
Added mass at infinite frequency	m_μ	kg	156262
Density of salt water	ρ	kg/m^3	1025
Acceleration due to gravity	g	m/s^2	9.81
Hydrostatic coefficient	β	kg/s^2	$\rho g \pi r^2$

It is assumed that the semi-hemispherical base is always submerged hence providing a constant cross-sectional area; therefore the dynamic Froude-Krylov forces are ignored in this case. However, the dynamic Froude-Krylov forces make a significant effect in

the system when a WEC with a non-uniform cross sectional wetted surface is used (Penalba et al. 2017).

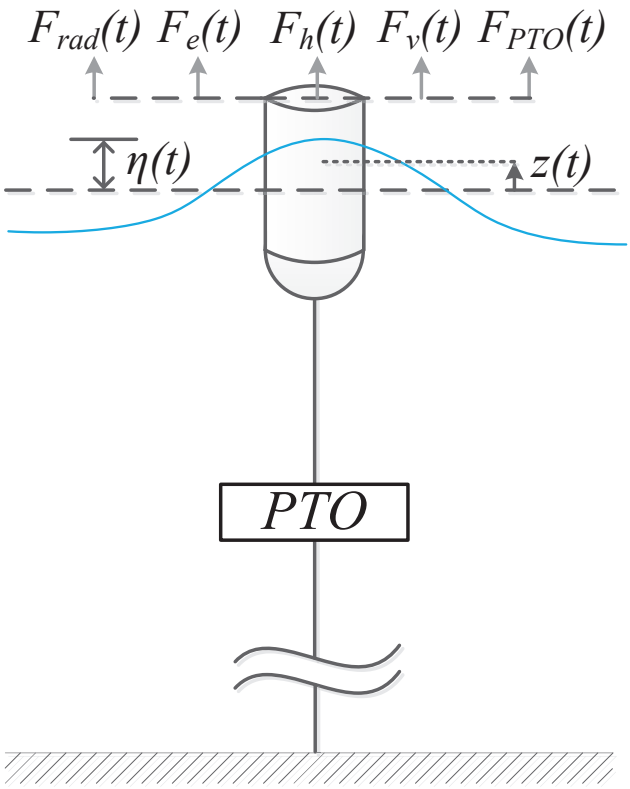

Figure 2.2: A linear modelled cylindrical point absorber WEC with a semi hemispherical bottom (this geometry is used throughout the thesis)

$$M\ddot{z}(t) = F_h(t) + F_{rad}(t) + F_e(t) + F_{PTO}(t) + F_v(t) \tag{2.7}$$

where,

$$\begin{aligned} F_h(t) &= \text{hydrostatic force} \\ F_{rad}(t) &= \text{radiation force} \\ F_e(t) &= \text{excitation force} \\ F_{PTO}(t) &= \text{external PTO force} \\ F_v(t) &= \text{viscous force (optional).} \end{aligned}$$

Using BEM software packages, such as WAMIT (Version 7) (Lee 1995), a linearised integro-differential time-domain model can be found to represent the Froude-Krylov, diffraction and radiation forces in the linear Cummins equation.

By adding the gravitational force F_g to the surface integral of the hydrostatic pressure, the gravitational force is cancelled; yielding the hydrostatic force $F_h(t)$, which is represented as,

$$F_h(t) = -\rho g A z(t), \tag{2.8}$$

where A is the constant cross sectional area, which in this case is πr^2, where r is the radius of the cylindrical WEC.

The viscous force $F_v(t)$ is a force which is usually represented by the semi-empirical Morison's equation (Morison et al. 1950) as shown in (2.9),

$$F_v(t) = -C_{vis}(t)\left(\dot{z}(t) - \dot{\eta}(t)\right) \tag{2.9}$$

where,

$$C_{vis}(t) = \frac{1}{2}\rho C_d A \left|\dot{z}(t) - \dot{\eta}(t)\right|.$$

Here,

$$\begin{aligned} \rho &= \text{density of sea water} \\ C_d &= \text{drag coefficient (Bhinder et al. 2011)} \\ A &= \text{cross sectional area} \\ \dot{\eta}(t) &= \text{vertical velocity of excitation wave surface.} \end{aligned}$$

This viscous term is commonly neglected in the linear model since the relative velocity between the wave and WEC is assumed to be negligible if the WEC acts as a wave follower. For the initial system analysis, the viscous force will be neglected; at a later stage in this work, the viscous force will be incorporated into the system model.

The non-linear radiation force $F_R(t)$ from the potential equation (2.6) can be represented in the Cummins equation (2.7), with two specific terms, as shown in (2.10),

$$F_{rad}(t) = -m_\mu \ddot{z}(t) - \underbrace{\int_{-\infty}^{\infty} h_r(t-\tau)\dot{z}(\tau)d\tau}_{F_r(t)} \tag{2.10}$$

where

$$\begin{aligned} m_\mu &= \text{added mass (at infinity frequency)} \\ h_r(t) &= \text{causal impulse reponse function} \\ F_r(t) &= \text{radiation convolution integral.} \end{aligned}$$

The mass m_μ value is the added mass value at infinite frequency as shown in Fig. 2.3. The radiation impulse response kernel $h_r(t)$ is a causal function which is shown in Fig. 2.4. Two of these components are found using WAMIT. The excitation force $F_e(t)$ in

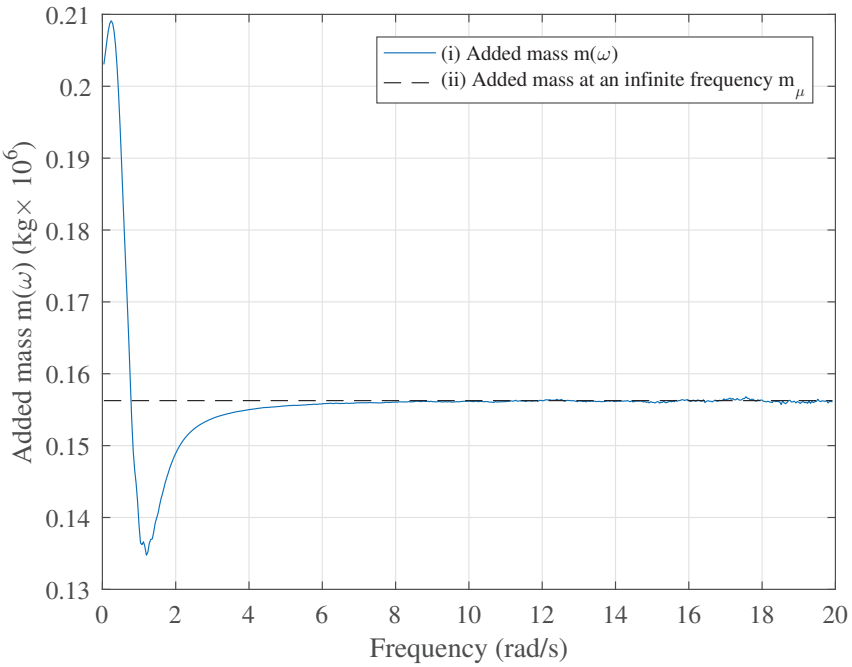

Figure 2.3: (i) Frequency response of the frequency dependent added mass and (ii) added mass at an infinite frequency of a cylindrical point absorber with a semi-hemispherical base with design characteristics shown in Table 2.1.

the Cummins equation represents the combination of the dynamic Froude-Krylov force and the diffraction force from the non-linear potential equation,

$$F_e(t) = F_{dy}(t) + F_D(t)$$

where the excitation force in the Cummins equation is represented as a convolution of the non-causal impulse response $h_e(t)$ and the wave free surface elevation $\eta(t)$,

$$F_e(t) = \int_{-\infty}^{\infty} h_e(t-\tau)\eta(\tau)d\tau.$$

The frequency response $H_e(\omega)$ is shown in Fig. 2.5. For most control techniques in the wave energy industry the excitation wave $F_e(t)$, needs to be known. In this work, a prediction of the wave excitation force is required with multiple steps into the future. Prediction of the excitation wave, is not included in the scope of this work as it represents a substantial research area, which is being covered elsewhere, for example (Fusco & Ringwood 2010). Therefore, in this work it is assumed that present and

future excitation wave forces are known. For a cylindrical point absorber in heave mode, the Cummins equation becomes (2.11),

$$\ddot{z}(t) + \frac{1}{M + m_\mu} \int_{-\infty}^{t} h_r(t)\dot{z}(t-\tau)d\tau + \frac{\beta}{M + m_\mu} z(t) = u_c(t) + v_c(t), \tag{2.11}$$

where $u_c(t)$ is a scaled version of $F_{PTO}(t)$ and $v_c(t)$ is scaled version of $F_e(t)$.

$$u_c(t) = \frac{F_{PTO}(t)}{M + m_\mu} \tag{2.12}$$

$$v_c(t) = \frac{F_e(t)}{M + m_\mu} \tag{2.13}$$

The PTO and excitation forces are scaled to enable simple notation when the control is discussed, as in later chapters. The values of (2.11) are shown in Table 2.2,

Table 2.2: Hydrodynamic system values

Point absorber values			
Parameter names	Parameter	Units	Value
WEC mass	M	kg	670860
Added mass at an infinite frequency	m_μ	kg	156262
Hydrostatic coefficient	β	kg/s^2	789737
Draft	$Draft$	m	10
WEC radius	r	m	5

2.2.4 Excitation Wave Modelling

It is usual to assume regular sinusoidal (Monochromatic waves) for use in simulations to emulate the waves that excite the WEC. With monochromatic waves, the system can be analysed at each individual frequency and the experiments can be repeated with a range of wave amplitudes and approach angles. Monochromatic waves, however, may not be a good emulation of an authentic sea wave as real waves are typically polychromatic. Polychromatic waves are used to emulate realistic sea excitation waves. Using measurement buoys and observers from ships, the height and corresponding frequencies from real waves can be recorded. From these measurements, a wave spectrum could be identified that would give a satisfactory representation of the sea waves at that point. Characteristics such as significant wave height H_s and peak spectral frequency T_p can be used to characterise the wave spectrum. Significant wave height H_s is known as the mean value of the highest one third of the waves and the peak spectral frequency T_p is the period where the highest point in the spectrum exists.

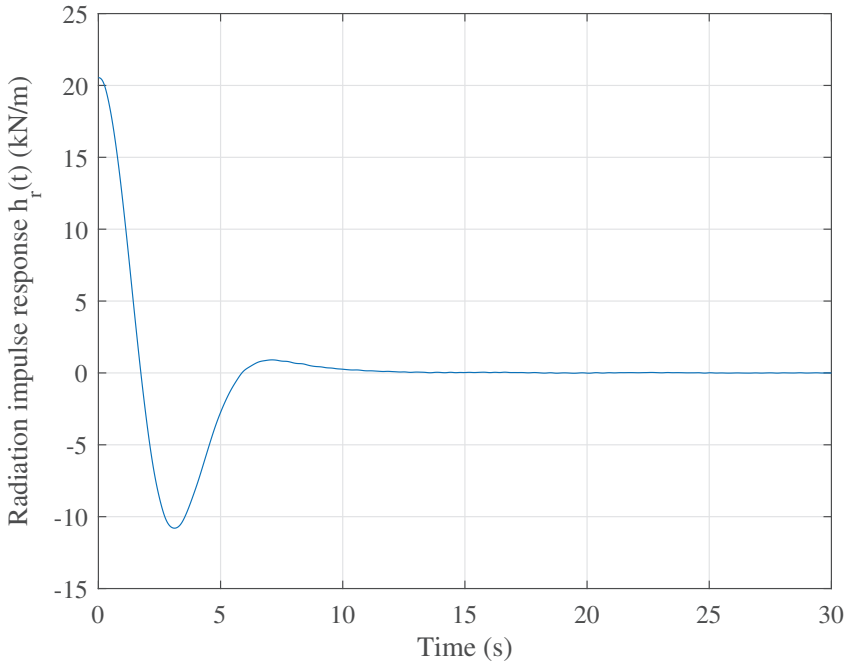

Figure 2.4: Radiation impulse response $h_r(t)$ of a cylindrical point absorber with a semi-hemispherical base with design characteristics shown in Table. 2.1.

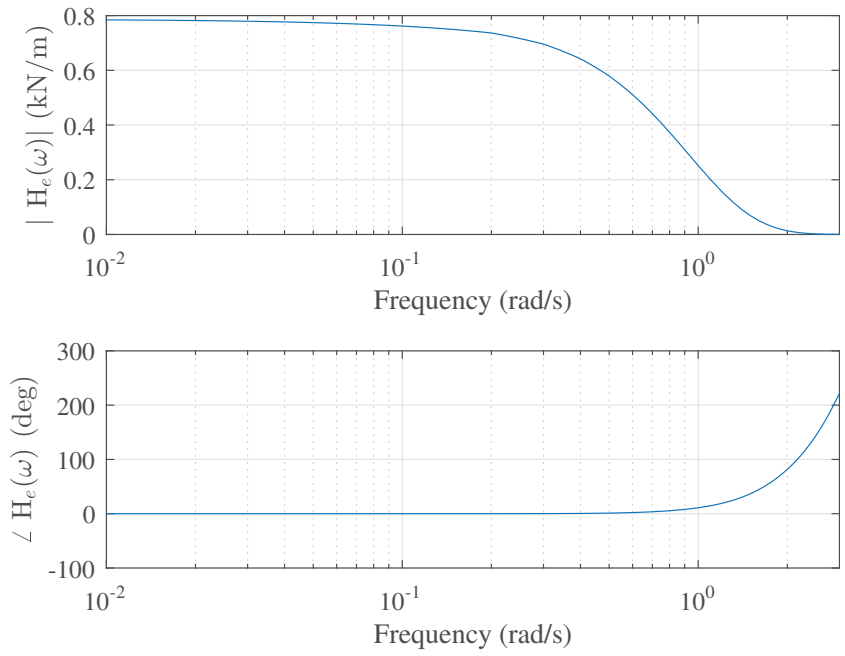

Figure 2.5: Frequency response of the wave surface elevation to the excitation wave force non-causal transfer function ($H_e(\omega)$)

Polychromatic waves can be represented by various spectra such as Ochi Spectrum (Ochi & Hubble 1977), Bretschneider (Tucker & Pitt 2001), Pierson-Maskowitz (Pierson & Moskowitz 1964) and JONSWAP (Hasselmann 1973) spectra. Each of these spectra are used to represent the sea waves from different locations, as each location has its own characteristics that might only be met when using a specific sea spectrum (e.g. the JONSWAP spectrum was developed to represent the North Sea).

In this work the polychromatic sea spectrum used is the Bretschneider spectrum. The Bretschneider spectral densities are shown in Fig. 2.6.

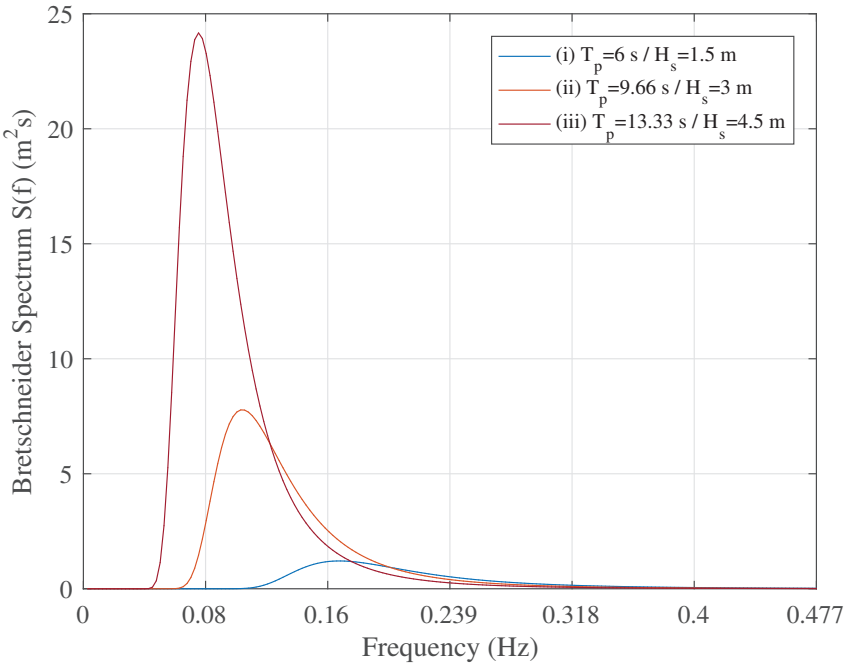

Figure 2.6: A range of different Bretschneider spectral densities $S(f)$ that represent multiple sea states with (i) $T_p = 6$ s with $H_s = 1.5$ m,(ii) $T_p = 9.66$ s with $H_s = 3$ m,(iii) $T_p = 13.33$ s with $H_s = 4.5$ m

The Bretschneider spectrum is represented by a dual-parameter equation (2.14),

$$S(f) = A_s f^{-5} e^{\left(-B_s f^{-4}\right)} \tag{2.14}$$

where,

$$A_s = \frac{5}{16}\frac{H_s^2}{T_p^4} \tag{2.15}$$

$$B_s = \frac{5}{4}\left(\frac{1}{T_p^4}\right) \tag{2.16}$$

The surface elevation $\eta(t)$ can be emulated as shown in (2.17) as the combination of

sinusoidal waves with N_d distinct frequencies , wave amplitudes and randomised phase shifts,

$$\eta(x,t) = \sum_{i=1}^{N_d} a_i \sin\left(2\pi f_i t - k_i x - \delta_i\right). \tag{2.17}$$

Here,

$$k_i = \frac{2\pi}{\lambda_i} \tag{2.18}$$

$$\lambda_i = \frac{g}{2\pi f_i^2} \text{ (in deep water)} \tag{2.19}$$

$$f_i = \sum_{j=1}^{i} \Delta f_j \text{ (Hz)} \tag{2.20}$$

$$\delta_i = \text{randomised phase (rad)} \tag{2.21}$$

$$x = \text{displacement delay (m)} \tag{2.22}$$

Assuming that the amplitude of the surface elevation has a Rayleigh distribution (Pearson 1905), the variance of the wave surface elevation can represented as (2.23),

$$\sigma^2 = \frac{1}{2}a^2 \tag{2.23}$$

where a is the wave amplitude. By using the variance, the sea spectrum can be related to the Bretschneider spectrum using (2.24),

$$S(f) = \lim_{\Delta f \to 0} \frac{\frac{1}{2}a^2}{\Delta f} \tag{2.24}$$

where Δf is the frequency intervals across the spectrum; as $\Delta f \to 0$ the spectrum $S(f)$ tends towards a continuous function.

Assuming a sufficiently small Δf value, the surface elevation amplitude of the i^{th} component can be found,

$$a_i = \sqrt{2S(f_i)\Delta f_i}. \tag{2.25}$$

The irregular sea elevation can be decomposed into its constituent monochromatic components. Using the frequency response $H_e(\omega)$, that was found using WAMIT as shown in Fig. 2.5, each elevation component can then be transformed to produce a monochromatic excitation force. Combining these constituent force components results in the excitation force exerted by the irregular sea (2.26).

$$F_{ex}(x,t) = \sum_{i=1}^{N_d} \left|H_e(2\pi f_i)\right| a_i \sin\left(2\pi f_i t - k_i x - \delta_i + \angle H_e(2\pi f_i)\right). \tag{2.26}$$

Fig. 2.7 shows an example construction of an irregular sea from 4 monochromatic components.

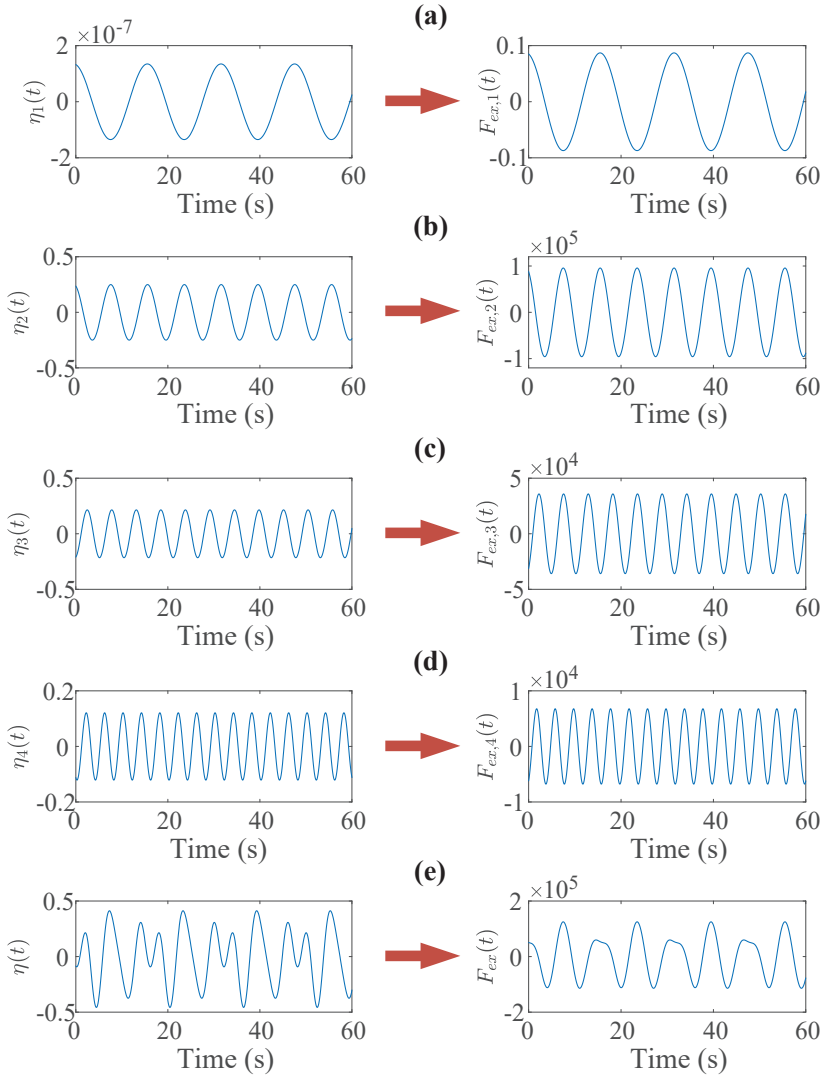

Figure 2.7: An example of an irregular wave surface elevation $\eta(t)$ and their corresponding excitation forces $F_{ex}(t)$ formed from a Bretschneider spectrum with a $H_s = 1$ m, $T_p = 6.981$ s and $\Delta f = 0.0625$ Hz formed from 4 different sine waves with frequencies and magnitudes of (a) $f = 0.0625$ Hz and $a = 1.3484 \times 10^{-7}$ m, (b) $f = 0.125$ Hz and $a = 0.25$ m, (c) $f = 0.1875$ Hz and $a = 0.2153$ m, (d) $f = 0.25$ Hz and $a = 0.1213$ m and (e) the entire irregular excitation surface waveform.

2.2.5 Radiation Kernel Modelling

The radiation component from the linearised potential flow model

$$F_{rad}(t) = -m_\mu \ddot{z}(t) - \underbrace{\int_{-\infty}^{\infty} h_r(t-\tau)\dot{z}(\tau)d\tau}_{F_r(t)},$$

as shown in section 2.2.3, is found using a BEM code (WAMIT). WAMIT produces both the added mass at infinite frequency m_μ and the radiation impulse response kernel $h_r(t)$.

The added mass term can be easily included into the linear model. However, the radiation kernel $h_r(t)$ is difficult to incorporate into the simulation because of the high computational cost of simulating the convolution integral. By using the impulse response data from WAMIT, as shown in Fig. 2.4, a dynamic subsystem Fig. 2.8 can be created which emulates the radiation convolution term and improves computational efficiency, as shown in (2.27).

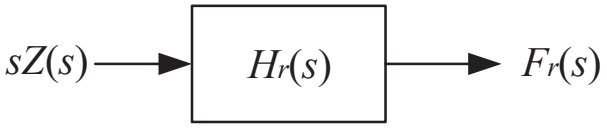

Figure 2.8: Transfer function $H_r(s)$ representing the emulation of the radiation kernel $h_r(t)$

$$\begin{aligned} \dot{\boldsymbol{x}}_{\boldsymbol{r}}(t) &= A_r \boldsymbol{x}_{\boldsymbol{r}}(t) + B_r \dot{z}(t) \\ F_r(t) &= C_r \boldsymbol{x}_{\boldsymbol{r}}(t) + D_r \dot{z}(t) \end{aligned} \tag{2.27}$$

This transfer function $H_r(s)$ (or the state space system) can be obtained using either a frequency or time domain method. Using the radiation time-domain state space system (2.27), the entire continuous system can be formed in state space form (2.28),

$$\frac{d}{dt}\begin{bmatrix} z(t) \\ \dot{z}(t) \\ \boldsymbol{x}_{\boldsymbol{r}}(t) \end{bmatrix} = A_c \begin{bmatrix} z(t) \\ \dot{z}(t) \\ \boldsymbol{x}_{\boldsymbol{r}}(t) \end{bmatrix} + B_c u_c(t) + F_c v_c(t) \tag{2.28}$$

where $A_r \in \mathbb{R}^{n\times n}$, $B_r \in \mathbb{R}^{n\times 1}$,$C_r \in \mathbb{R}^{1\times n}$, $D_r \in \mathbb{R}^{1\times 1}$,

$$A_c = \begin{bmatrix} 0 & 1 & \mathbf{0} \\ -\frac{\beta}{M+m_\mu} & -\frac{D_r}{M+m_\mu} & -\frac{C_r}{M+m_\mu} \\ 0 & B_r & A_r \end{bmatrix}$$

$$Fc = B_c = \begin{bmatrix} 0 \\ 1 \\ \mathbf{0} \end{bmatrix} \quad \boldsymbol{x}(t) = \begin{bmatrix} z(t) \\ \dot{z}(t) \\ \boldsymbol{x_r}(t) \end{bmatrix}. \tag{2.29}$$

The frequency domain method utilises Least-Square (Marquardt 1963), fitting the frequency response information from WAMIT to a rational transfer function. The time domain Least-Square identification of the radiation kernel involves obtaining a parametric model from data of the impulse response found from WAMIT (Yu & Falnes 1995). Explained in this section, are two types of time domain model identifications which include a SISO Least-Squares method (Prony 1795) and a SIMO realisation method (Kung et al. 1983).

2.2.5.1 Prony's Exponential Approximation

Prony's exponential approximation is a sampled data method used to approximate the continuous radiation impulse response $h_r(t)$ (Fig. 2.4). It assumes that the radiation impulse response $h_r(t)$ can be represented in the Laplace domain as the transfer function (2.30),

$$H_r(s) = \frac{F_r(s)}{sZ(s)} = \frac{B_D(s)}{(s-p_1)(s-p_2)\ldots(s-p_{N_{py}})} = \sum_{i=1}^{N} \frac{c_i}{s-p_i}. \tag{2.30}$$

The impulse response is then obtained as a weighted summation of complex exponentials (2.31),

$$h_r\left(t\right) = \sum_{i=1}^{N_{py}} c_i e^{p_i t}. \tag{2.31}$$

The Least-Squares algorithm is used to identify the optimal c_i and p_i parameters from the sampled radiation impulse response. The fidelity of the approximation depends on the order N_{py}, the length of the impulse response data and the sampling time T_{py} that is used to sample the WAMIT impulse response data. The continuous impulse response is shown in Fig. 2.4, when sampled with sample time T_{py} creates the sampled signal, as shown in Fig. 2.9.

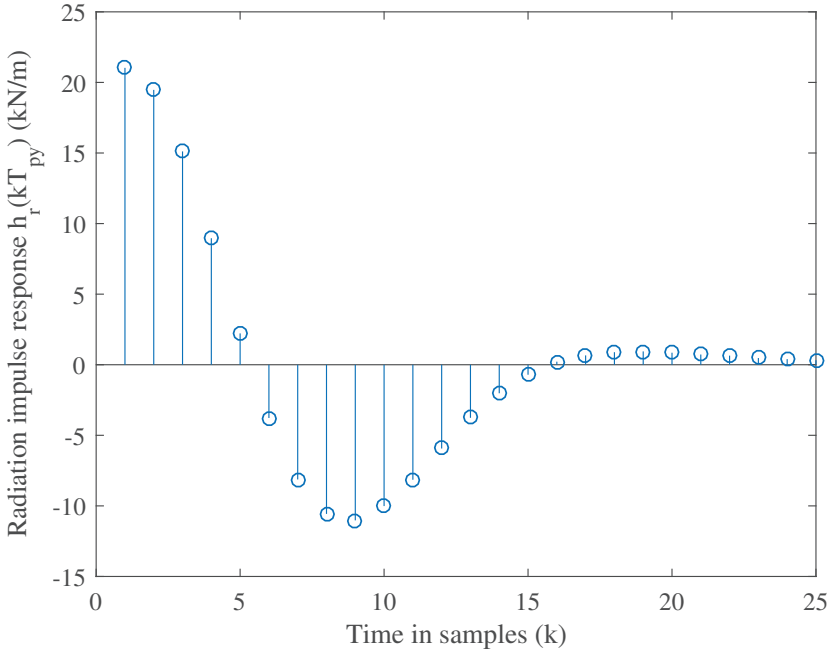

Figure 2.9: Sampled radiation impulse response $h_r(kT_{py})$ of a single device

The sampled impulse response data can be obtained by discretising (2.31) to form (2.32), which shows the k^{th} sample of the radiation impulse response,

$$\begin{aligned} h_r(kT_{py}) &= \sum_{i=1}^{N_{py}} c_i e^{p_i(kT_{py})} \\ \forall k &\in [0, 1, 2, \ldots, m]\,. \end{aligned} \tag{2.32}$$

Developing (2.32) then creates a series of $m+1$ equations, (2.33) each representing one sample of the impulse response,

$$\begin{aligned} h_r(0) &= c_1 + c_2 + \ldots + c_{N_{py}} \\ h_r(T_{py}) &= c_1 e^{p_1 T_{py}} + c_2 e^{p_2 T_{py}} + \ldots + c_{N_{py}} e^{p_{N_{py}} T_{py}} \\ &\vdots \\ h_r(mT_{py}) &= c_1 e^{mp_1 T_{py}} + c_2 e^{mp_2 T_{py}} + \ldots + c_{N_{py}} e^{mp_{N_{py}} T_{py}} \end{aligned} \quad . \tag{2.33}$$

The $m+1$ equations are then aggregated, yielding (2.34),

$$\begin{bmatrix} h_r(0) \\ h_r(1) \\ h_r(2) \\ \vdots \\ h_r(m) \end{bmatrix} = \begin{bmatrix} 1 & 1 & \cdots & 1 \\ e^{p_1 T_{py}} & e^{p_2 T_{py}} & \cdots & e^{p_N T_{py}} \\ e^{2(p_1 T_{py})} & e^{2(p_2 T_{py})} & \cdots & e^{2(p_N T_{py})} \\ \vdots & \vdots & \ddots & \vdots \\ e^{m(p_1 T_{py})} & e^{m(p_2 T_{py})} & \cdots & e^{m(p_N T_{py})} \end{bmatrix} \begin{bmatrix} c_1 \\ c_2 \\ c_3 \\ \vdots \\ c_{N_{py}} \end{bmatrix}. \tag{2.34}$$

Equation (2.34) can then be simplified by substituting $a_i = e^{p_i T_{py}}$ (2.35),

$$\underbrace{\begin{bmatrix} h_r(0) \\ h_r(1) \\ h_r(2) \\ \vdots \\ h_r(m) \end{bmatrix}}_{H} = \underbrace{\begin{bmatrix} 1 & 1 & \cdots & 1 \\ a_1 & a_2 & \cdots & a_{N_{py}} \\ a_1^2 & a_2^2 & \cdots & a_{N_{py}}^2 \\ \vdots & \vdots & \ddots & \vdots \\ a_1^m & a_2^m & \cdots & a_{N_{py}}^m \end{bmatrix}}_{A} \underbrace{\begin{bmatrix} c_1 \\ c_2 \\ c_3 \\ \vdots \\ c_{N_{py}} \end{bmatrix}}_{C}. \tag{2.35}$$

Discretising the continuous radiation transfer function (2.30) using the matched pole zero method yields (2.37) (Franklin et al. 1998),

$$H_r(z) = \frac{F_r(z)}{\dot{Z}(z)} = \frac{B_D(z)}{(z - e^{p_1 T_{py}})(z - e^{p_2 T_{py}}) \ldots (z - e^{p_{N_{py}} T_{py}})} \tag{2.36}$$

$$= \frac{B_D(z)}{(z - a_1)(z - a_2) \ldots (z - a_{N_{py}})}. \tag{2.37}$$

The poles from the discrete transfer function (2.37) are the roots of the N^{th} order characteristic equation (2.38),

$$(z - a_1)(z - a_2) \ldots (z - a_{N_{py}}) = z^{N_{py}} + \lambda_1 z^{N_{py}-1} + \ldots + \lambda_{N_{py}}. \tag{2.38}$$

Combining (2.37) and (2.38) and applying the inverse z transform yields the discrete difference equation (2.39),

$$\begin{aligned} F_r(k) =& b_0 \dot{z}(k) + b_1 \dot{z}(k-1) + \ldots + b_m \dot{z}(k-m) \\ & - \lambda_1 F_r(k-1) - \lambda_2 F_r(k-2) - \ldots - \lambda_{N_{py}} F_r(k - N_{py}), \end{aligned} \tag{2.39}$$

where $N > m$. Defining the impulse input as the following,

$$\text{Impulse response data} \begin{cases} \dot{z}(0) = \delta(0) \\ \dot{z}(k) = 0 \qquad \text{for } k \neq 0, \end{cases}$$

then for measurement sample $k = N_{py}$, (2.39) reduced to (2.40),

$$\begin{aligned} F_r(N_{py}) =& \cancelto{0}{b_0\dot{z}(N_{py})} + \cancelto{0}{b_1\dot{z}(N_{py}-1)} + \ldots + \cancelto{0}{b_m\dot{z}(N_{py}-m)} \\ & - \lambda_1 F_r(N_{py}-1) - \lambda_2 F_r(N_{py}-2) + \ldots + \lambda_{N_{py}} F_r(0). \end{aligned} \tag{2.40}$$

Note that $F_R(t) = h_r(t)$ in this case because an impulse is utilised. Repeating this process for m data points, for measurement samples $k \geq N$, yields the following regression equation (2.41) where the parameter vector λ is unknown.

$$\underbrace{-\begin{bmatrix} F_r(N_{py}) \\ F_r(N_{py}+1) \\ F_r(N_{py}+2) \\ \vdots \\ F_r(N_{py}+m) \end{bmatrix}}_{F} = \underbrace{\begin{bmatrix} F_r(0) & F_r(1) & \cdots & F_r(N_{py}-1) \\ F_r(1) & F_r(2) & \cdots & F_r(N_{py}) \\ F_r(2) & F_r(3) & \cdots & F_r(N_{py}+1) \\ \vdots & \vdots & \ddots & \vdots \\ F_r(m) & F_r(m+1) & \cdots & F_r(m+N_{py}-1) \end{bmatrix}}_{G} \underbrace{\begin{bmatrix} \lambda_{N_{py}} \\ \lambda_{N_{py}-1} \\ \lambda_{N_{py}-2} \\ \vdots \\ \lambda_1 \end{bmatrix}}_{\lambda}. \tag{2.41}$$

Solving for λ in a least squares sense produces $\hat{\lambda}$, (2.42),

$$\hat{\lambda} = -(G^T G)^{-1} G^T F = \begin{bmatrix} \hat{\lambda}_{N_{py}} \\ \hat{\lambda}_{N_{py}-1} \\ \vdots \\ \hat{\lambda}_1 \end{bmatrix}. \tag{2.42}$$

Knowing that $\{a_1, a_2 \ldots a_{N_{py}}\}$ are the N distinct (possibly complex) roots of the characteristic equation (2.43),

$$z^{N_{py}} + \lambda_1 z^{N_{py}-1} + \ldots + \lambda_{N_{py}} = 0; \tag{2.43}$$

the $\{\hat{a}_1, \hat{a}_2, \ldots, \hat{a}_{N_{py}}\}$ can be obtained as the N roots of the newly estimated characteristic equations (2.44),

$$z^{N_{py}} + \hat{\lambda}_1 z^{N_{py}-1} + \ldots + \hat{\lambda}_{N_{py}} = 0. \tag{2.44}$$

This provides the A matrix in (2.35) yielding (2.45),

$$\underbrace{\begin{bmatrix} h_r(0) \\ h_r(1) \\ h_r(2) \\ \vdots \\ h_r(m) \end{bmatrix}}_{H} = \underbrace{\begin{bmatrix} 1 & 1 & \cdots & 1 \\ \hat{a}_1 & \hat{a}_2 & \cdots & \hat{a}_{N_{py}} \\ \hat{a}_1^2 & \hat{a}_2^2 & \cdots & \hat{a}_{N_{py}}^2 \\ \vdots & \vdots & \ddots & \vdots \\ \hat{a}_1^m & \hat{a}_2^m & \cdots & \hat{a}_{N_{py}}^m \end{bmatrix}}_{\hat{A}} \underbrace{\begin{bmatrix} c_1 \\ c_2 \\ c_3 \\ \vdots \\ c_{N_{py}} \end{bmatrix}}_{C}. \tag{2.45}$$

Solving for C from (2.45) yields (2.46),

$$\hat{C} = \begin{bmatrix} \hat{c}_1 \\ \hat{c}_2 \\ \vdots \\ \hat{c}_N \end{bmatrix} = \left(\hat{A}^T \hat{A}\right)^{-1} \hat{A}^T H. \tag{2.46}$$

Furthermore, knowing $\hat{a}_i$ from $\hat{A}$ (2.45) and $\hat{a}_i = e^{\hat{p}_i T_{py}}$, allows $\hat{p}_i$ to be obtained (2.47),

$$\begin{gathered} \hat{p}_i = \frac{1}{T_{py}} \ln \hat{a}_i \\ \forall i \in \{0, 1, 2, \ldots, N_{py}\}. \end{gathered} \tag{2.47}$$

Combining (2.46), (2.47) and (2.30), yields the following transfer function model approximation for the radiation subsystem,

$$H_r(s) = \frac{F_r(s)}{\dot{Z}(s)} \approx \frac{\hat{c}_1}{s - \hat{p}_1} + \frac{\hat{c}_2}{s - \hat{p}_2} + \frac{\hat{c}_3}{s - \hat{p}_3} + \cdots + \frac{\hat{c}_{N_{py}}}{s - \hat{p}_{N_{py}}}. \tag{2.48}$$

An example of the Prony exponential summation method is shown in Fig. 2.10 where 6 exponential terms are combined to approximate the impulse response data found using WAMIT, where the WEC used in this example is a cylindrical point absorber with system characteristics shown in Table 2.1.

By solving for the c_i and p_i coefficients from (2.48), the 6^{th} order radiation kernel shown in Fig. 2.10 can be represented by the sum of real transfer functions (2.49),

$$\frac{F_r(s)}{\dot{Z}(s)} = \frac{2720}{s + 6.73} - \frac{4990}{s + 0.3417} + \frac{22920s + 15890}{s^2 + 0.5768s + 1.066} + \frac{-521.1s + 1511}{s^2 + 3.88s + 6.954}. \tag{2.49}$$

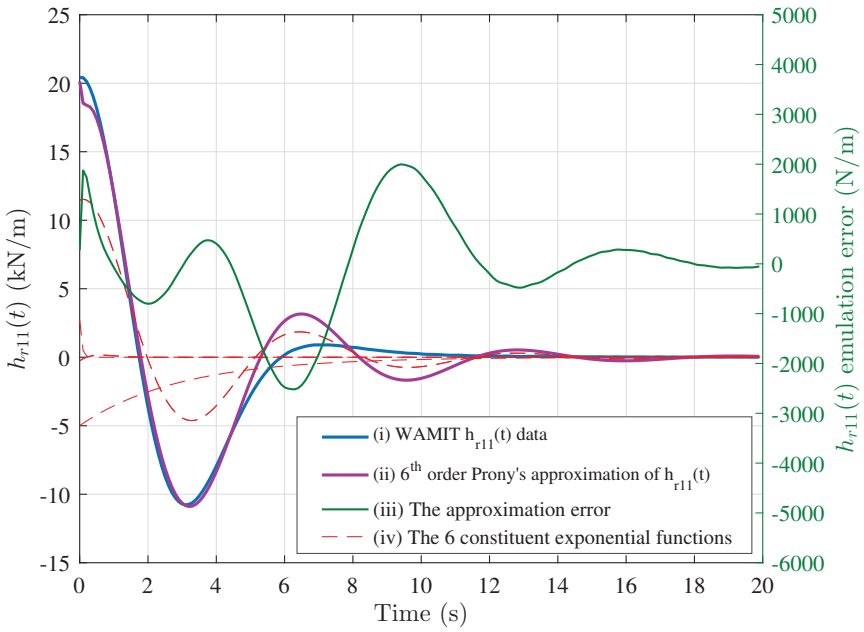

Figure 2.10: Radiation impulse response $h_{r11}(t)$ of a single WEC device: (i) The original WAMIT data with 1000 data points and a sample time of $T_{py} = 0.02$ s. (ii) The impulse response from a 6^{th} order Prony's approximation of $h_{r11}(t)$. (iii) The error between the WAMIT impulse data and the Prony's approximation. (iv) The 6 constituent exponential functions.

2.2.5.2 Balanced Model Reduction using SVD

From Fig. 2.10 it can be shown that there is a noticeable error between the WAMIT data and the impulse response from the 6^{th} order Prony's approximate. To reduce this error, the number of exponential terms N_{py} can be increased which of course yields a higher order transfer function. However, the increase in exponential terms can lead to a large system. Using a singular value decomposition (SVD) balanced model reduction technique, order compression is attainable (Willcox & Peraire 2002). The SVD method reduces the order of the original Prony's approximation whilst maintaining the accuracy of the original high order approximation.

The original continuous model of the radiation kernel can be represented in state space form as the following,

$$\begin{aligned} \dot{\mathbf{x}}_\mathbf{r}(t) &= A_r \mathbf{x}_\mathbf{r}(t) + B_r \dot{z}(t) \\ F_r(t) &= C_r \mathbf{x}_\mathbf{r}(t). \end{aligned} \tag{2.50}$$

Using a transformation matrix T, a set of transformed states can be defined as the

following,

$$\begin{aligned} \mathbf{g}(t) &= T\mathbf{x_r}(t) \\ T^{-1}\mathbf{g}(t) &= \mathbf{x_r}(t) \\ T^{-1}\dot{\mathbf{g}}(t) &= \dot{\mathbf{x}}_\mathbf{r}(t). \end{aligned} \tag{2.51}$$

Combining the transformed states (2.51) and the original system (2.50), the following transformed system is found,

$$\begin{aligned} \dot{\mathbf{g}}(t) &= TA_rT^{-1}\mathbf{g}(t) + TB_ru(t) \\ &= \hat{A}_r\mathbf{g}(t) + \hat{B}_r\dot{z}(t) \\ F_r(t) &= C_rT^{-1}\mathbf{g}(t) + D_r\dot{z}(t) \\ &= \hat{C}_r\mathbf{g}(t) + D_r\dot{z}(t), \end{aligned} \tag{2.52}$$

where,

$$\hat{A}_r = TA_rT^{-1} \tag{2.53}$$

$$\hat{B}_r = TB_r \tag{2.54}$$

$$\hat{C}_r = C_rT^{-1}. \tag{2.55}$$

The Lyapunov equations (2.56) and (2.57),

$$A_rP + PA_r^T + B_rB_r^T = 0 \tag{2.56}$$

$$A_r^TQ + QA_r + C_r^TC_r = 0, \tag{2.57}$$

are a set of equations used to ensure an asymptotically stable system. These Lyapunov equations (Khalil 1996) consist of the systems state space matrices A_r, B_r and C_r along with the controllability gramian P (2.58) and the observability gramian Q (2.59),

$$P = \int_0^\infty e^{A\tau}B_rB_r^Te^{A_r^T\tau}d\tau \tag{2.58}$$

$$Q = \int_0^\infty e^{A_r^T\tau}C_r^TC_re^{A_r\tau}d\tau. \tag{2.59}$$

Here the P and Q matrices are symmetric and positive definite if the system is observable and controllable. To transform the original unbalanced system into a balanced system, both the transformed controllability gramian $\hat{P}$ and observability gramian $\hat{Q}$ must equal each other. When both $\hat{P}$ and $\hat{Q}$ are equal to each other, they are both

diagonal matrices denoted by Σ,

$$\hat{P} = \hat{Q} = \Sigma, \tag{2.60}$$

where this diagonal matrix Σ has eigenvalues σ_i on the diagonal (2.61),

$$\hat{P} = \hat{Q} = \Sigma = \begin{bmatrix} \sigma_1 & 0 & \dots & 0 \\ 0 & \sigma_2 & \dots & 0 \\ \vdots & \vdots & \ddots & \vdots \\ 0 & 0 & \dots & \sigma_{N_{py}} \end{bmatrix}. \tag{2.61}$$

The eigenvalues signify how much energy is produced from each individual state in the system. The values show that some states have the majority of the systems energy whilst others are negligible. With this in mind, the insignificant states in the model can be ignored hence reducing the size of the model. Solving for Σ, the transformed $\hat{P}$ and $\hat{Q}$ matrices must first be found.

Manipulating the original Lyapunov equation (2.62), using the transformation matrix T (2.63), the transformed Lyapunov equation is found (2.64),

$$A_r P + P A_r^T + B_r B_r^T = 0 \tag{2.62}$$

$$T A_r P T^T + T P A_r^T T^T + T B_r B_r^T T^T = 0 \tag{2.63}$$

$$\hat{A}_r \left(T P T^T\right) + \left(T P T^T\right) \hat{A}_r{}^T + \hat{B}_r \hat{B}_r{}^T = 0. \tag{2.64}$$

From this transformed Lyapunov equation, the transformed controllability gramian $\hat{P}$ is found (2.64),

$$\hat{P} = T P T^T. \tag{2.65}$$

To obtain the transformed observability gramian $\hat{Q}$ the identical transformation method is repeated on the second original Lyapunov equation (2.66),

$$A_r^T Q + Q A_r + C_r^T C_r = 0 \tag{2.66}$$

$$T^{T^{-1}} A_r^T Q T^{-1} + T^{T^{-1}} Q A_r T^{-1} + T^{T^{-1}} C_r^T C_r T^{-1} = 0 \tag{2.67}$$

$$\hat{A}_r{}^T (T^{T^{-1}} Q T^{-1}) + (T^{T^{-1}} Q T^{-1}) \hat{A}_r + \hat{C}_r{}^T \hat{C}_r = 0 \tag{2.68}$$

where $\hat{Q}$ is found from the transformed Lyapunov equation (2.68),

$$\hat{Q} = (T Q^{-1} T^T)^{-1}. \tag{2.69}$$

Since a minimised asymptotically stable system is needed, the Hankel singular values Σ must have the following relationship,

$$\hat{P} = \hat{Q} = \Sigma \tag{2.70}$$

therefore,

$$\hat{P}\hat{Q} = \Sigma^2. \tag{2.71}$$

$$\hat{P}\hat{Q} = (TPT^T)(T^{-T}QT^{-1}) = TPQT^{-1} = \Sigma^2 \tag{2.72}$$

Since Q is a symmetric matrix it can be represented as $Q = R^T R$ where R is a square matrix,

$$TPR^T RT^{-1} = \Sigma^2, \tag{2.73}$$

$$(RT^{-1})^{-1} RPR^T (RT^{-1}) = \Sigma^2, \tag{2.74}$$

$$RPR^T = (RT^{-1})\Sigma^2 (RT^{-1})^{-1}, \tag{2.75}$$

$$RPR^T = \underbrace{(RT^{-1})\Sigma^{\frac{1}{2}}}_{U} \Sigma^2 \underbrace{\Sigma^{-\frac{1}{2}}(RT^{-1})^{-1}}_{U^{-1}}, \tag{2.76}$$

$$RPR^T = U\Sigma^2 U^T. \tag{2.77}$$

Solving RPR^T (2.77) using SVD yields the eigenvector matrix U and eigenvalue matrix Σ^2. It was defined in (2.76) that ,

$$U = (RT^{-1})\Sigma^{\frac{1}{2}}. \tag{2.78}$$

Reorientating (2.78), the transformation matrix T is found (2.81),

$$\left(U\Sigma^{-\frac{1}{2}}\right)^{-1} = \left(RT^{-1}\right)^{-1}, \tag{2.79}$$

$$U\Sigma^{-\frac{1}{2}} = RT^{-1}, \tag{2.80}$$

$$T = \Sigma^{\frac{1}{2}} U^{-1} R. \tag{2.81}$$

Neglecting insignificant eigenvalues in the Σ matrix (2.61), the corresponding T matrix (2.81) that results in a system order reduction is found.

For example, an 18^{th} order Pronys radiation kernel is used as the system to be reduced to produce an accurate system whilst compressing the order of the system. By observing the Hankel singular values from the Σ matrix (2.61), as demonstrated when plotted in Fig. 2.11, it can be shown that a small number of the values have the majority of the energy in the system while other eigenvalues are insignificant. To reduce the order of

the system, the insignificant eigenvalues are neglected, forcing a major size reduction in the system. In this example, out of the 18 states that are in the system, the states > 4 are neglected producing a new 4^{th} order system (2.82) which produces an accurate impulse response as shown in Fig. 2.12.

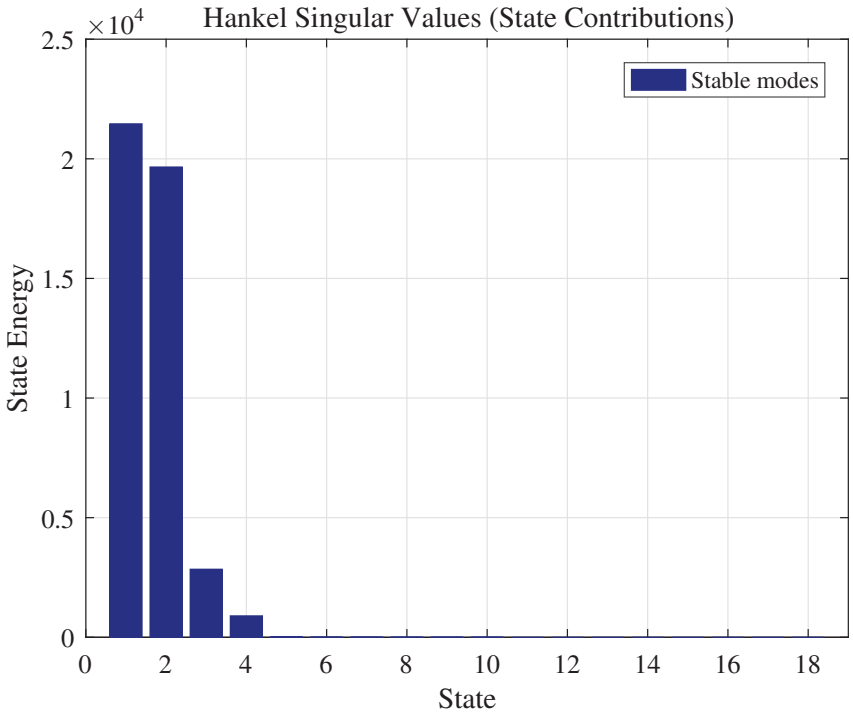

Figure 2.11: Hankel singular eigenvalues for an 18^{th} order Prony's approximated system

$$\dot{\mathbf{x}}_\mathbf{r}(t) = \begin{bmatrix} -1.984 & -1.738 & -1.158 & -0.5432 \\ 2 & 0 & 0 & 0 \\ 0 & 1 & 0 & 0 \\ 0 & 0 & 1 & 0 \end{bmatrix} \mathbf{x}_\mathbf{r}(t) + \begin{bmatrix} 256 \\ 0 \\ 0 \\ 0 \end{bmatrix} \dot{z}(t) \tag{2.82}$$

$$F_r(t) = \begin{bmatrix} 80.39 & 78.18 & 107 & -0.6106 \end{bmatrix} \mathbf{x}_\mathbf{r}(t) + -35.6\dot{z}(t)$$

It is clearly shown from Fig. 2.12 that not only does the 4^{th} order reduced Pronys system maintaining its accuracy from the 18^{th} order system, but it also surpasses the accuracy of the uncompressed 6^{th} order Pronys system that was originally established in section 2.2.5.1.

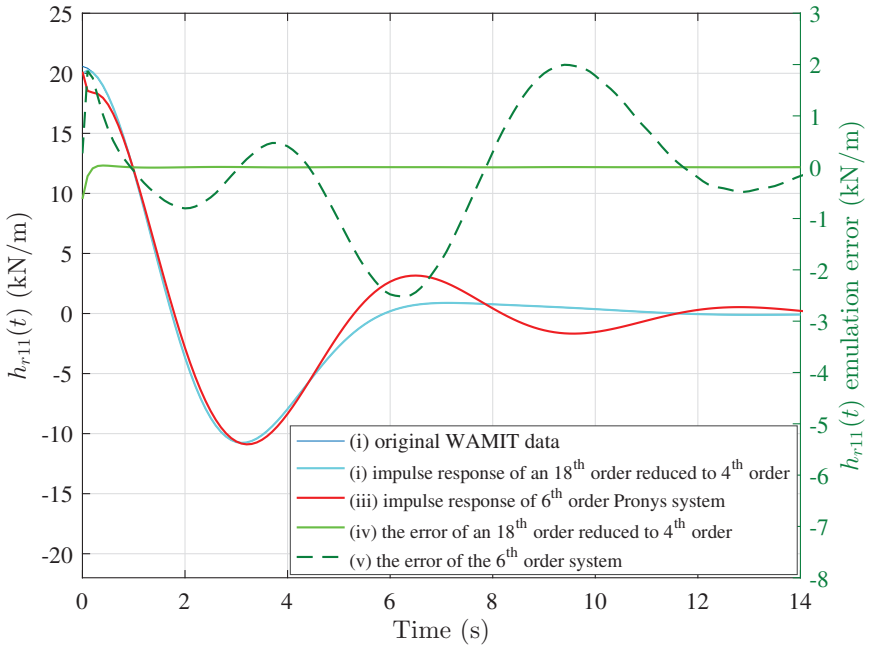

Figure 2.12: $h_{r11}(t)$ radiation impulse responses with (i) the original WAMIT data, (ii) the impulse response from the 4^{th} order Pronys system that was reduced down from an 18^{th} order system, (iii) the impulse response from the 6^{th} order Pronys system that was from Section. 2.2.5.1, (iv) the error between the 4^{th} order Pronys system and the original WAMIT data, (v) the error between the 6^{th} order Pronys system and the WAMIT data

2.2.5.3 Kung's Array Radiation Kernel Realisation

For a single device there is only one radiation force acting on the WEC. With multiple WEC's operating closely together there is interaction between devices. This can be represented by radiation terms that relate the velocity of one device to the radiation force acting on the other WECs, where these extra radiation terms are added to the original Cummins equation (2.7) as shown in (2.83), for the i^{th} device,

$$(M+m_\mu)\ddot{z}_i(t)+\underbrace{\sum_{j=1}^{N_H}\left[\int_{-\infty}^{t}h_{r,ij}(t)\dot{z}_j(t-\tau)d\tau\right]}_{F_{r,i}(t)}+\beta z_i(t)=F_{PTO,i}(t)+F_{ex,i}(t). \tag{2.83}$$

where, N is the number of devices in the WEC array and the viscosity force is neglected. The matrix of continuous time radiation impulse responses can be found using WAMIT. Fig. 2.13 shows the impulse response $h_{r_{11}}(t)$ and $h_{r_{12}}(t)$ obtained using WAMIT for two identical cylindrical point absorber devices at a separation of 40 m.

It is demonstrated that the impulse response from one WEC acting on another device is minor when compared to the impulse response from a device exerting upon itself. Fig. 2.14 shows how the interaction term $h_{r12}(t)$ depends on the separation of devices. It is a fair assumption to say that as the separation distance increases, the radiation interaction become less significant.

In the Laplace domain the entire radiation subsystem can be modelled as a single multi-input multi-output (MIMO) radiation system (2.84),

$$\begin{bmatrix} F_{r,1}(s) \\ F_{r,2}(s) \\ \vdots \\ F_{r,N_H}(s) \end{bmatrix} = \underbrace{\begin{bmatrix} H_{r,11}(s) & H_{r,12}(s) & \dots & H_{r,1N_H}(s) \\ H_{r,21}(s) & H_{r,22}(s) & \dots & H_{r,2N_H}(s) \\ \vdots & \vdots & \ddots & \vdots \\ H_{r,N_H1}(s) & H_{r,N_H2}(s) & \dots & H_{r,N_HN_H}(s) \end{bmatrix}}_{\mathbf{H_r}(s)} \begin{bmatrix} \dot{Z}_1(s) \\ \dot{Z}_2(s) \\ \vdots \\ \dot{Z}_{N_H}(s) \end{bmatrix}. \tag{2.84}$$

This would simplify the modelling complexity when a centralised simulation model is implemented. In this work, the radiation system of (2.83) will, however, be identified as N single-input-multi-output (SIMO) subsystems (2.85). This allows the simulation model to be directly used in both centralised and decentralised control models, as will be shown in chapter 6.

$$\begin{aligned} \underbrace{\begin{bmatrix} F_{r,_1}(s) \\ F_{r,_2}(s) \\ \vdots \\ F_{r,_{N_H}}(s) \end{bmatrix}}_{\tilde{\mathbf{F}}_\mathbf{r}(s)} &= \sum_{j=1}^{N_H} \left(\underbrace{\begin{bmatrix} H_{r,_{1_j}}(s) \\ H_{r,_{2_j}}(s) \\ \vdots \\ H_{r,_{N_Hj}}(s) \end{bmatrix}}_{\tilde{\mathbf{F}}_{\mathbf{r},\mathbf{j}}(s)} \dot{Z}_j(s) \right) \\ \tilde{\mathbf{F}}_\mathbf{r}(s) &= \sum_{j=1}^{N_H} \tilde{\mathbf{F}}_{\mathbf{r,j}}(s) \end{aligned} \tag{2.85}$$

As shown in (2.85), instead of all the N_H radiation forces $F_{r,i}(s)$ being generated by a global system $\mathbf{H_r}(s)$ as in (2.84), the $F_{r,i}(s)$ forces are generated by N_H SIMO subsystems. Even though this does not compress the global radiation system into a single system (2.84), it still reduces the original ${N_H}^2$ subsystems using a SISO system down to N_H subsystems.

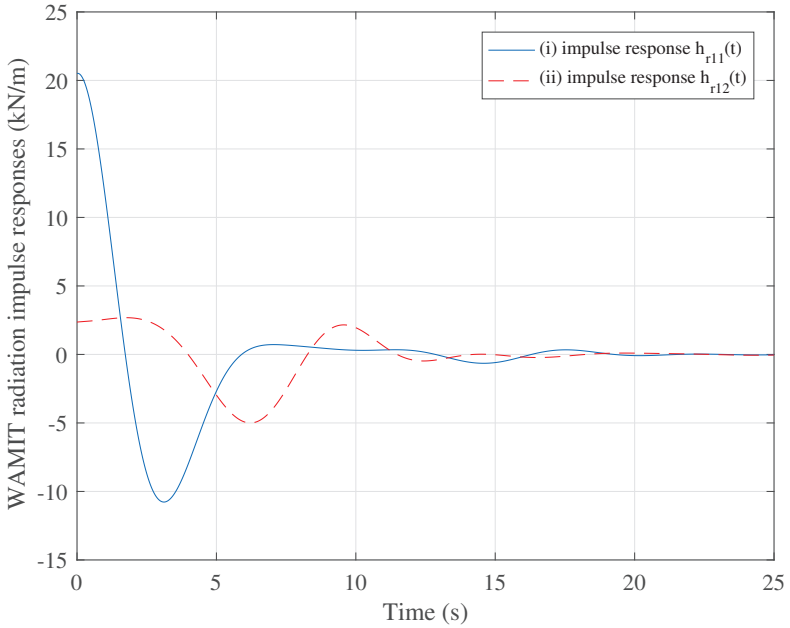

Figure 2.13: WAMIT radiation impulse response data for one devices with a separation distance of 40 m: (i) Impulse response $h_{r11}(t)$ is the self generated radiation force, (ii) Impulse response $h_{r12}(t)$ represented the effect of movement of the second device on device 1

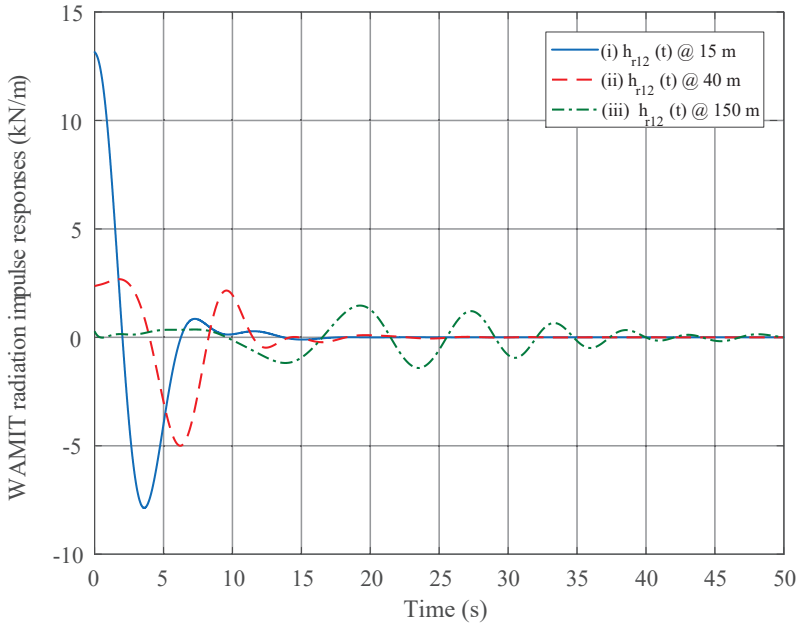

Figure 2.14: WAMIT radiation impulse response $h_{r12}(t)$ for two device with a separation distance (i) 15 m ,(ii) 40 m and (iii) 150 m

To create each SIMO system (2.85) in the continuous state space form (2.86) ,

$$\begin{aligned} \dot{\mathbf{x}}_{\mathbf{r_j}}(t) &= A_{r_j}\mathbf{x}_{\mathbf{r_j}}(t) + B_{r_j}\dot{z}_j(t) \\ \tilde{\mathbf{F}}_{\mathbf{r,j}}(t) &= C_{r,j}\mathbf{x}_{\mathbf{r_j}}(t) + D_{r,j}\dot{z}_j(t) \end{aligned} \tag{2.86}$$

where $\mathbf{x}_{\mathbf{r_j}}(t) \in \mathbb{R}^{n\times 1}$, $\dot{z}_j(t) \in \mathbb{R}^{1\times 1}$, $\tilde{\mathbf{F}}_{\mathbf{r,j}}(t) \in \mathbb{R}^{N_H\times 1}$, $A_{r_j}(t) \in \mathbb{R}^{n\times n}$, $B_{r_j}(t) \in \mathbb{R}^{n\times 1}$, $C_{r_j}(t) \in \mathbb{R}^{N_H\times n}$, $D_{r_j}(t) \in \mathbb{R}^{N_H\times 1}$, a Hankel singular value decomposition (HSVD) method is used (Kung et al. 1983). This was chosen over the Prony's approximation because of its ability to efficiently produce multivariate models from impulse response data.

The HSVD method is based on a singular value decomposition method, where the system model is found in the discrete domain and is then transformed into the continuous domain. To implement an impulse response test in the discrete domain, the initial sampled input $\dot{z}(k)$ has a magnitude of $1/T_H$ to emulate a continuous time impulse, as shown in Fig. 2.15 with a sampling time of $T_H = 0.2$ s.

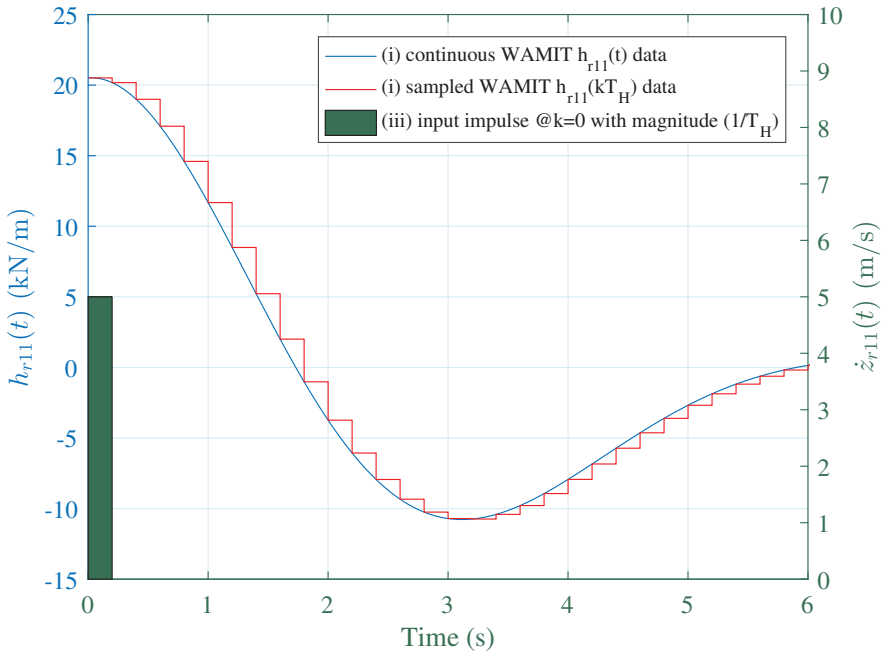

Figure 2.15: WAMIT radiation impulse data with: (i) The continuous $h_{r11}(t)$ impulse. (ii) The continuous WAMIT radiation impulse sampled with $T_H = 0.2$ s (iii) The input discrete impulse signal with a magnitude of $\frac{1}{T_H}$ (in this case $\frac{1}{T_H} = 5$ m.s^{-1})

The multi-output discrete state-space system for the j^{th} velocity can be represented as

the following,

$$\begin{aligned} \mathbf{x_{r,j}}(k+1) &= A_{r,j}\mathbf{x_{r,j}}(k) + B_{r,j}\dot{z}_j(k) \\ \tilde{\mathbf{F}}_{\mathbf{r,j}}(k) &= C_{r,j}\mathbf{x_{r,j}}(k) + D_{r,j}\dot{z}_j(k), \end{aligned} \tag{2.87}$$

where $\mathbf{F_{r,j}}(k) \in \mathbb{R}^{N_H \times 1}$, $\mathbf{x_{r,j}}(k) \in \mathbb{R}^{n\times 1}$ and $\dot{z}_j(k) \in \mathbb{R}^{1\times 1}$, $A_{r_j}(t) \in \mathbb{R}^{n\times n}$, $B_{r_j}(t) \in \mathbb{R}^{n\times 1}$, $C_{r_j}(t) \in \mathbb{R}^{N_H\times n}$, $D_{r_j}(t) \in \mathbb{R}^{N_H\times 1}$,

$$\tilde{\mathbf{F}}_{\mathbf{r,j}}(k) = \begin{bmatrix} F_{r,1j}(k) \\ F_{r,2j}(k) \\ \vdots \\ F_{r,N_Hj}(k) \end{bmatrix} \tag{2.88}$$

$$\dot{z}_j(k) = \frac{1}{T_H}u(k) = \begin{cases} \frac{1}{T_H} & \text{if } k = 0 \\ 0 & \text{otherwise.} \end{cases}$$

This can be rewritten as,

$$\begin{aligned} T_H\mathbf{x_{r,j}}(k+1) &= T_HA_{r,j}\mathbf{x_{r,j}}(k) + B_{r,j}u(k) \\ T_H\tilde{\mathbf{F}}_{\mathbf{r,j}}(k) &= T_HC_{r,j}\mathbf{x_{r,j}}(k) + D_{r,j}u(k); \end{aligned} \tag{2.89}$$

which simplifies to,

$$\begin{aligned} \check{\mathbf{x}}_{\mathbf{r,j}}(k+1) &= A_{r,j}\check{\mathbf{x}}_{\mathbf{r,j}}(k) + B_{r,j}u(k) \\ \check{\mathbf{F}}_{\mathbf{r,j}}(k) &= C_{r,j}\check{\mathbf{x}}_{\mathbf{r,j}}(k) + D_{r,j}u(k), \end{aligned} \tag{2.90}$$

where $\check{\mathbf{x}}_{\mathbf{r,j}}(k) = T_H\mathbf{x_{r,j}}(k)$ and $\check{\mathbf{F}}_{\mathbf{r,j}}(k) = T_H\tilde{\mathbf{F}}_{\mathbf{r,j}}(k)$.

Here, $\check{\mathbf{F}}_{\mathbf{r,j}}(k)$ is the sampled impulse response provided from a post process in WAMIT which transforms a frequency domain WAMIT output to time domain impulse response functions; in this case the impulse responses are also the radiation forces. Stepping the system (2.90) into the future, the known outputs ($\check{\mathbf{F}}_{\mathbf{r,j}}(k)$, $k = 0 \rightarrow (2M-1)$) can be related to the system matrices (2.91). Assuming zero initial conditions, $\check{\mathbf{x}}_{\mathbf{r,j}}(0) = 0$, the following can be developed:

$$
k=0\begin{cases}\check{\mathbf{x}}_{\mathbf{r,j}}(1)=A_{r,j}\cancelto{0}{\check{\mathbf{x}}_{\mathbf{r,j}}(0)}+B_{r,j}\cancelto{1}{u(0)}=B_{r,j}\\ \check{\mathbf{F}}_{\mathbf{r,j}}(0)=C_{r,j}\cancelto{0}{\check{\mathbf{x}}_{\mathbf{r,j}}(0)}+D_{r,j}\cancelto{1}{u(0)}=D_{r,j}\end{cases}
$$

$$
k=1\begin{cases}\check{\mathbf{x}}_{\mathbf{r,j}}(2)=A_{r,j}\check{\mathbf{x}}_{\mathbf{r,j}}(1)+B_{r,j}\cancelto{0}{u(1)}\\ \check{\mathbf{x}}_{\mathbf{r,j}}(2)=A_{r,j}B_{r,j}\\ \check{\mathbf{F}}_{\mathbf{r,j}}(1)=C_{r,j}\check{\mathbf{x}}_{\mathbf{r,j}}(1)+D_{r,j}\cancelto{0}{u(1)}\\ \check{\mathbf{F}}_{\mathbf{r,j}}(1)=C_{r,j}B_{r,j}\end{cases}
$$

$$
k=2\begin{cases}\check{\mathbf{x}}_{\mathbf{r,j}}(3)=A_{r,j}\check{\mathbf{x}}_{\mathbf{r,j}}(2)+B_{r,j}\cancelto{0}{u(2)}\\ \check{\mathbf{x}}_{\mathbf{r,j}}(3)=A_{r,j}^2B_{r,j}\\ \check{\mathbf{F}}_{\mathbf{r,j}}(2)=C_{r,j}\check{\mathbf{x}}_{\mathbf{r,j}}(2)+D_{r,j}\cancelto{0}{u(2)}\\ \check{\mathbf{F}}_{\mathbf{r,j}}(2)=C_{r,j}A_{r,j}B_{r,j}\end{cases} \tag{2.91}
$$

etc.

Extending this $2M-1$ samples, the following can be formed in matrix form,

$$
\begin{bmatrix}\check{\mathbf{F}}_{\mathbf{r,j}}(0)\\ \check{\mathbf{F}}_{\mathbf{r,j}}(1)\\ \check{\mathbf{F}}_{\mathbf{r,j}}(2)\\ \vdots\\ \check{\mathbf{F}}_{\mathbf{r,j}}(2M-1)\end{bmatrix}=\begin{bmatrix}D_{r,j}\\ C_{r,j}B_{r,j}\\ C_{r,j}A_{r,j}B_{r,j}\\ \vdots\\ C_{r,j}A_{r,j}^{2M-2}B_{r,j}\end{bmatrix} \tag{2.92}
$$

From (2.92), it is shown that $\check{\mathbf{F}}_{\mathbf{r,j}}(0)=D_{r,j}$. Orientating the remaining radiation forces $\check{\mathbf{F}}_{\mathbf{r,j}}(k_g)$ (where $k_g\in\{1,2,\ldots,2M-1\}$) in a symmetric square matrix yields (2.93),

$$\begin{aligned}\underbrace{\begin{bmatrix} \check{\mathbf{F}}_{\mathbf{r,j}}(1) & \check{\mathbf{F}}_{\mathbf{r,j}}(2) & \cdots & \check{\mathbf{F}}_{\mathbf{r,j}}(M) \\ \check{\mathbf{F}}_{\mathbf{r,j}}(2) & \check{\mathbf{F}}_{\mathbf{r,j}}(3) & \cdots & \check{\mathbf{F}}_{\mathbf{r,j}}(M+1) \\ \vdots & \vdots & \ddots & \vdots \\ \check{\mathbf{F}}_{\mathbf{r,j}}(M) & \check{\mathbf{F}}_{\mathbf{r,j}}(M+1) & \cdots & \check{\mathbf{F}}_{\mathbf{r,j}}(2M-1) \end{bmatrix}}_{\mathbf{H}\text{ (Hankel matrix)}} \\ = \underbrace{\begin{bmatrix} C_{r,j}B_{r,j} & C_{r,j}A_{r,j}B_{r,j} & \cdots & C_{r,j}A_{r,j}^{M-1}B_{r,j} \\ C_{r,j}A_{r,j}B_{r,j} & C_{r,j}A_{r,j}^{2}B_{r,j} & \cdots & C_{r,j}A_{r,j}^{M}B_{r,j} \\ \vdots & \vdots & \ddots & \vdots \\ C_{r,j}A_{r,j}^{M-1}B_{r,j} & C_{r,j}A_{r,j}^{M}B_{r,j} & \cdots & C_{r,j}A_{r,j}^{2M-2}B_{r,j} \end{bmatrix}}_{\mathbf{G}}\end{aligned} \tag{2.93}$$

where $\mathbf{G}$ can be written in terms of the observability and controllability matrices,

$$\mathbf{G} = \begin{bmatrix} C_{r,j} \\ C_{r,j}A_{r,j} \\ C_{r,j}A_{r,j}^{2} \\ \vdots \\ C_{r,j}A_{r,j}^{M-1} \end{bmatrix} \begin{bmatrix} B_{r,j} & A_{r,j}B_{r,j} & A_{r,j}^{2}B_{r,j} & \cdots & A_{r,j}^{M-1}B_{r,j} \end{bmatrix}. \tag{2.94}$$

Singular value decomposition of the Hankel matrix $\mathbf{H}$ (2.93), yields,

$$\mathbf{H} = \mathbf{USV^T} \tag{2.95}$$

where $\mathbf{S}$ (2.96) contains the eigenvalues that correspond to the dominance of each state,

$$\mathbf{S} = \begin{bmatrix} \sigma_1 & 0 & \cdots & 0 \\ 0 & \sigma_2 & \cdots & 0 \\ \vdots & \vdots & \ddots & \vdots \\ 0 & 0 & \cdots & \sigma_M \end{bmatrix}. \tag{2.96}$$

The SVD (2.95) can be broken down further, producing matrices $\mathbf{\Omega}$ and $\mathbf{\Lambda}$,

$$\begin{aligned}\mathbf{\Omega} &= \mathbf{US}^{\frac{1}{2}} \\ \mathbf{\Lambda} &= \mathbf{S}^{\frac{1}{2}}\mathbf{V}^{T}.\end{aligned} \tag{2.97}$$

These two matrices can then be related directly to the observability and controllability matrices (2.94), since $\mathbf{G} = \mathbf{H} = \mathbf{USV^T} = \mathbf{US}^{\frac{1}{2}}\mathbf{S}^{\frac{1}{2}}\mathbf{V^T}$

$$\mathbf{\Omega} = \mathbf{U}\mathbf{S}^{\frac{1}{2}} = \begin{bmatrix} C_{r,j} \\ C_{r,j}A_{r,j} \\ C_{r,j}A_{r,j}^2 \\ \vdots \\ C_{r,j}A_{r,j}^{M-1} \end{bmatrix} \in \mathbb{R}^{NM \times M} \tag{2.98}$$

$$\mathbf{\Lambda} = \mathbf{S}^{\frac{1}{2}}\mathbf{V}^T = \begin{bmatrix} B_{r,j} & A_{r,j}B_{r,j} & A_{r,j}^2B_{r,j} & \cdots & A_{r,j}^{M-1}B_{r,j} \end{bmatrix} \in \mathbb{R}^{M \times M} \tag{2.99}$$

The $A_{r,j}$ matrix can then be found, based on Ω, which is constructed from the eigenvalues and eigenvectors of the Hankel matrix $\mathbf{H}$, where $\underline{\Omega}$ is constructed from the first $(M-1)$ rows of Ω and $\bar{\Omega}$ is constructed from the last $(M-1)$ rows of Ω.

$$A_{r,j} = \begin{bmatrix} C_{r,j} \\ C_{r,j}A_{r,j} \\ C_{r,j}A_{r,j}^2 \\ \vdots \\ C_{r,j}A_{r,j}^{M-2} \end{bmatrix}^{\dagger} \begin{bmatrix} C_{r,j}A_{r,j} \\ C_{r,j}A_{r,j}^2 \\ C_{r,j}A_{r,j}^3 \\ \vdots \\ C_{r,j}A_{r,j}^{M-1} \end{bmatrix} = \underline{\Omega}^{\dagger}\bar{\Omega}. \tag{2.100}$$

The $B_{r,j}$ and $C_{r,j}$ matrices can easily be found by taking the first N columns of the $\mathbf{\Lambda}$ matrix and the first N rows of the $\mathbf{\Omega}$ matrix. From (2.92) it was shown that $\check{\mathbf{F}}_{\mathbf{r,j}}(0) = D_{r,j}$. Taking these $A_{r,j}$, $B_{r,j}$, $C_{r,j}$ and $D_{r,j}$ matrices, a continuous system can be formed by transforming the discrete system into the continuous domain.

To reduce the systems order, some of the insignificant eigenvalues in $\mathbf{S}$ need to be ignored. For example consider the SIMO system with a 40 m separation distance between the two devices, $N_H = 2$ (Fig. 2.13), with $M = 500$. When plotting the eigenvalues of $\mathbf{S}$, it is clearly shown that the majority of the eigenvalues are negligible when compared to the dominant eigenvalues, Fig. 2.16.

By neglecting these insignificant eigenvalues in the $\mathbf{S}$ matrix, the order of the system can be drastically reduced without any disadvantage. Fig. 2.17 shows a 7^{th} order approximation showing that the system order can be dramatically reduced.

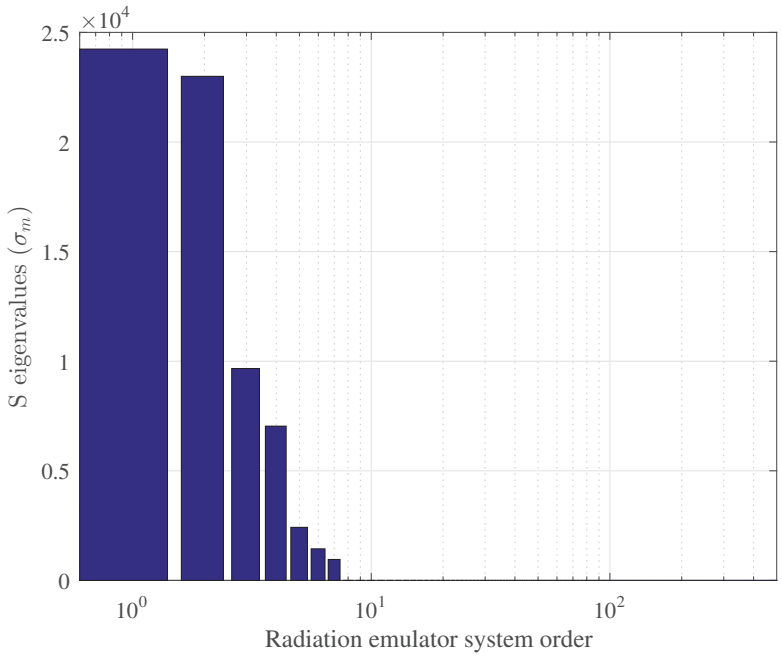

Figure 2.16: Eigenvalues σ_m from $\mathbf{S}$ matrix when using two device 40 m apart, showing that the states 8 to 500 can be ignored

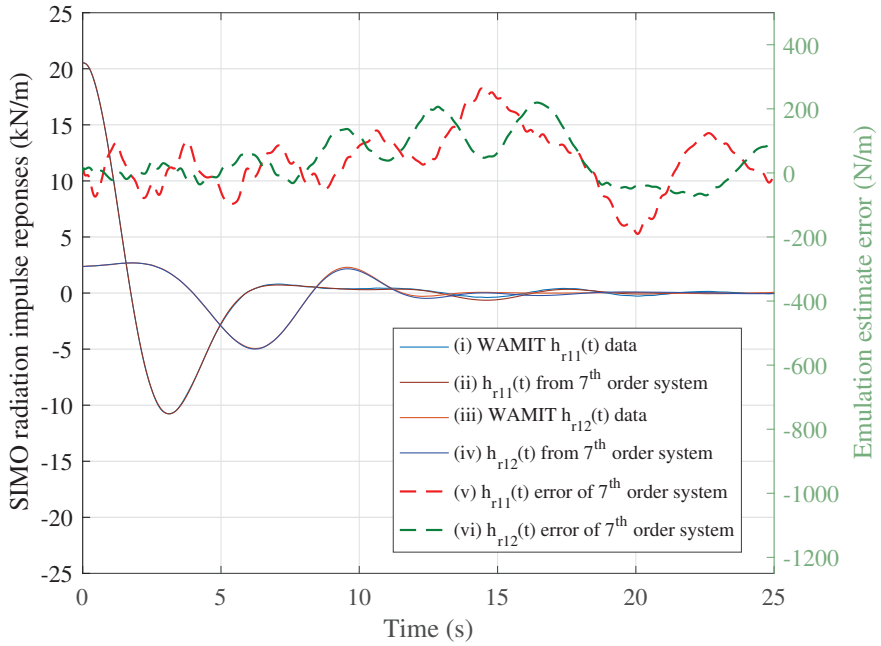

Figure 2.17: With two devices at a separation distance apart of 40 m. (i) Original WAMIT $h_{r11}(t)$ data. (ii) Impulse data $h_{r11}(t)$ from the 7^{th} order model. (iii) Original WAMIT $h_{r12}(t)$ data. (iv) Impulse data $h_{r12}(t)$ from the 7^{th} order model. (v) The error between the WAMIT $h_{r11}(t)$ data and the 7^{th} order approximation. (v) The error between the WAMIT $h_{r12}(t)$ data and the 7^{th} approximation

2.3 Modelling the Electrical System

The wave to grid electrical system is made up of multiple components, as shown in Fig. 2.18. The WEC is connected to a generator, which in this case is a linear permanent magnet generator (LPMG) (Leijon et al. 2005). The LPMG three phase terminals are connected to a voltage source power converter (VSC) (Rodrguez et al. 2007), which is made up of a bank of IGBTs. The power converter is connected to a DC voltage source which is ideally kept at a constant voltage across a DC link capacitor. The currents flowing in the LPMG are controlled by creating voltages from the power converter using certain IGBT switching patterns. Transforming the three phase balanced system into a two phase system using DQ transformation, the system becomes simplified, hence allowing easier system control. Using a phase lock loop (PLL) (Chung 2000) on the grid side enables the DQ transformation to synchronise with the three phase system. The grid side control method consists of DC link voltage control and reactive power control. Controlling the switching of the IGBTs within the power converter, the DC-link voltage is maintained at a constant value, which is crucial for decoupling and to ensure correct operation of the machine side converter.

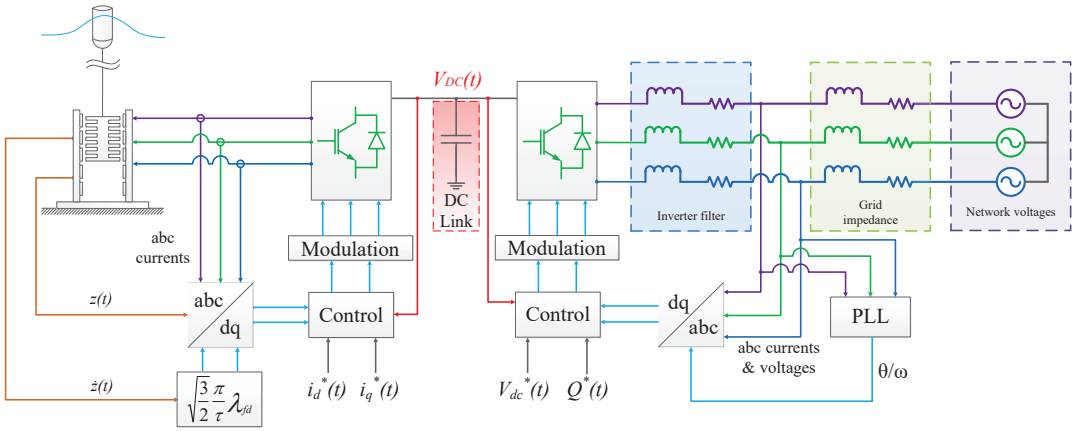

Figure 2.18: Schematic of the Wave to Grid electrical system which includes: a point absorber WEC connected to a LPMG, the machine side converter, the machine side controller using dq transformations, the DC-link capacitor, a grid side converter, grid side converter filters, grid impedance network, network voltages, the grid side controller utilising a dq transformation with a PLL.

2.3.1 Linear Permanent Magnet Generator (LPMG)

To extract the energy from the WEC system a power take off (PTO) is utilised. With so many device design variations in the wave industry, different PTO systems are utilised to suit the various WECs operations (Antonio 2010). Some of the WEC operations would include the oscillating water column (OWC) which uses the water level within a chamber to compress air through an air turbine (Amundarain et al. 2011). An overtopping device allows water to gather in a floating reservoir where gravity pushes the water down through a fluid turbine (Igic et al. 2011). In (Henderson 2006) a Pelamis WEC is utilised where hydraulic PTOs are used to extract energy from multiple hinges that are flexing while being excited by incoming waves. In (Tedeschi et al. 2011) a direct drive rotary generator connected to a point absorber is utilised in extracting power from the incoming waves. In (Wu et al. 2008) an Archimedes waves swing (AWS) is utilised with a linear permanent magnet generator, where the LPMG has higher power density and efficiency due to the transverse flux permanent magnet design.

In this thesis, the chosen PTO is a LPMG (Polinder et al. 2004). The LPMG, when compared to a generic rotary generator, has a much higher force density and has fewer mechanical components such as gearboxes and stator brushes. These characteristics make the LPMG well suited for the WEC application. Choosing the power rating of the LPMG is an important matter, where a small PTO force range can occur if the LPMG is underrated. Without a generous PTO force range, the control operation of the system may become restricted leading to possible system damages. By correctly choosing the PTO power rating, the chances of potential system damages will decrease. Choosing the appropriate PTO power rating depends on multiple factors (Aubry et al. 2012), which are not necessarily electrically related, such as the geographical location of the WEC which is characterised by a sea spectrum (Lenee-Bluhm et al. 2011), the design of the WEC (Garcia-Rosa & Ringwood 2016), the electrical constraints on the grid side, the power ratings of the power electronics and cabling (Lovelace et al. 2000, Molinas et al. 2007).

In this thesis, a 2 MW peak power rated LPMG was used (Polinder et al. 2004), where the LPMGs characteristics are shown in Table 2.3

With the combination of the PTO force and velocity constraints, the power is inherently restricted. The heave $z(t)$ constraint is included as there is a limitation on how far the translator can travel before the common surface area between the translator and the stator starts to become a function of the translator heave position, as shown in Fig. 2.19, reducing the flux linkage and hence reducing the LPMG force density. Like a

Table 2.3: LPMG design characteristics

LPMG values			
Parameter names	Parameters	Units	Value
Leakage inductance	L	H	0.028
Stator resistance	R	Ω	0.27
Pole pitch	τ	m	0.1
Flux linkage	λ_{fd}	Wb	46
Translator velocity	$z(t)_{max}$	m	± 3.5
Translator velocity limit	$\dot{z}(t)_{max}$	m/s	± 2.2
PTO force limit	$F_{PTO}(t)_{max}$	N	± 933000
Current controller sample time	T_{gen}	s	0.001
Switching time of IGBTs	T_{switch}	s	0.0001

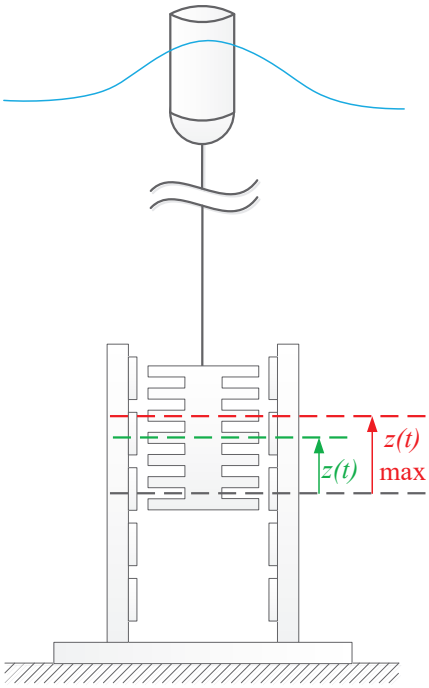

Figure 2.19: Schematic of a point absorber WEC connected to an LPMG with the translators/WEC heave displacement $z(t)$. The heave displacement restriction of $-z(t)_{MAX} \leq z(t) \leq +z(t)_{MAX}$. When the heave displacement of the LPMG exceeds the heave displacement constraint, the common surface between the stator and translator is reduced, hence reducing the force density of the generator

generic rotary generator, the LPMG is a three phase machine where each phase can be represented by a set of symmetrical equations (2.101), as shown in the circuit diagram Fig. 2.20,

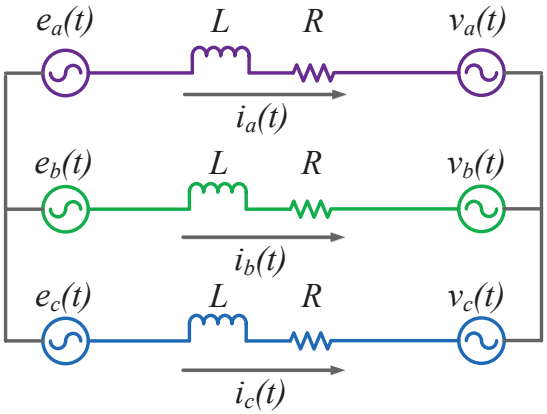

Figure 2.20: A circuit diagram of a balanced three phase generator

$$\begin{bmatrix} e_a(t) \\ e_b(t) \\ e_c(t) \end{bmatrix} - R \begin{bmatrix} i_a(t) \\ i_b(t) \\ i_c(t) \end{bmatrix} - L\frac{d}{dt} \begin{bmatrix} i_a(t) \\ i_b(t) \\ i_c(t) \end{bmatrix} = \begin{bmatrix} v_a(t) \\ v_b(t) \\ v_c(t) \end{bmatrix}, \tag{2.101}$$

where $e_a(t)$, $e_b(t)$ and $e_c(t)$ are the induced voltages generated by the movement of the translator. With a sinusoidally wound stator, the induced voltages $e_{abc}(t)$ are a function of the heave displacement and velocity as shown in (2.102), where each induced voltage is 120^o out of phase with each other,

$$\begin{bmatrix} e_a(t) \\ e_b(t) \\ e_c(t) \end{bmatrix} = \begin{bmatrix} \dot{z}(t)\frac{\pi}{\tau}\lambda_{fd}\sin\left(\frac{\pi}{\tau}z(t)\right) \\ \dot{z}(t)\frac{\pi}{\tau}\lambda_{fd}\sin\left(\frac{\pi}{\tau}z(t) - \frac{2\pi}{3}\right) \\ \dot{z}(t)\frac{\pi}{\tau}\lambda_{fd}\sin\left(\frac{\pi}{\tau}z(t) - \frac{4\pi}{3}\right) \end{bmatrix}. \tag{2.102}$$

As a comparison, consider the 'a' phase of a standard rotary machine as shown in (2.103),

$$\begin{aligned} e_a(t) &= +\omega(t)\lambda_{fd}\sin\left(\theta(t)\right) \\ \theta(t) &= \int_0^t \omega(\tau)d\tau, \end{aligned} \tag{2.103}$$

when operating in steady state with a constant rotating speed, the induced voltage for rotary machine looks sinusoidal, as shown in Fig. 2.21.

On the other hand, for an LPMG being used in a wave energy application the translator reciprocates. If, for simplicity, a monochromatic wave is assumed, then both the velocity $\dot{z}(t)$ and the heave displacement $z(t)$ vary sinusoidally, creating an amplitude modulated waveform as shown in Fig. 2.22,

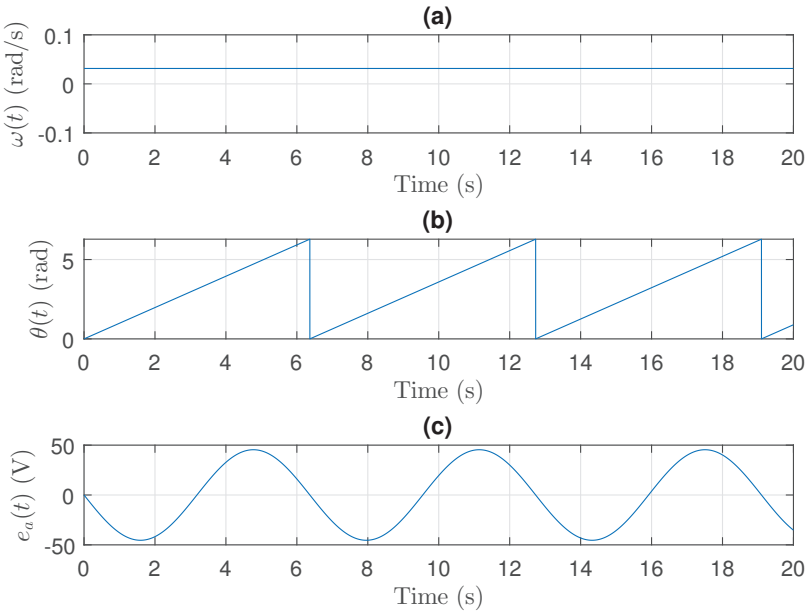

Figure 2.21: The waveforms corresponding to a single phase induced voltage from a generic rotary generator with (a) the angular velocity $\omega(t)$ of the machine, (b) the angular displacement $\theta(t)$ of the machine and (c) the resulting single phase induced voltage $e_a(t)$ of the machine

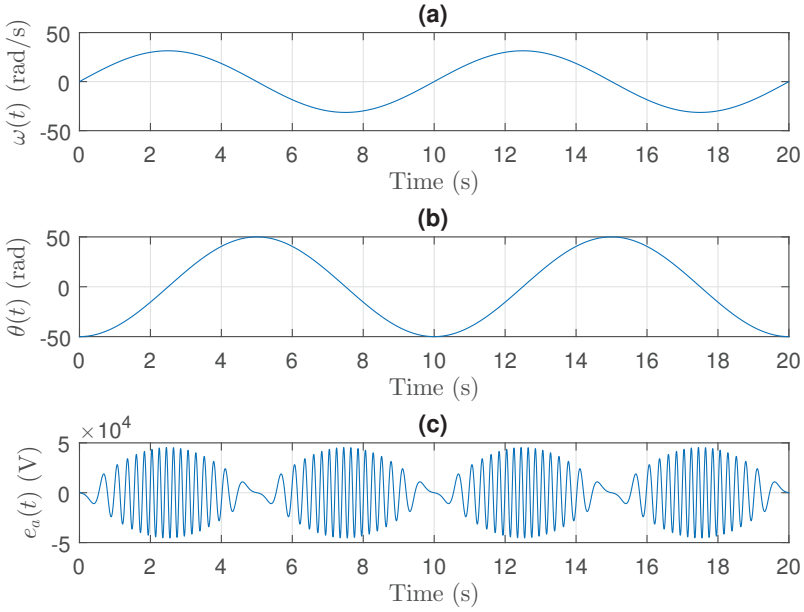

Figure 2.22: The waveforms corresponding to a single phase induced voltage from an LPMG with (a) the angular velocity $\omega(t)$ of the LPMG, (b) the angular displacement $\theta(t)$ of the LPMG and (c) the resulting single phase induced voltage $e_a(t)$ of the LPMG

2.3.2 Parks Transformation

Utilising Parks transformation a two phase system can represent the balanced three phase system (Mohan 2014), where this transformation matrix is a function of the electrical angular position $\theta(t)$ (2.105). In the case of the LPMG the angular position depends on the heave displacement of the translator (2.104),

$$\theta(t) = \frac{\pi}{\tau} z(t) \tag{2.104}$$

Using the transformation matrix (2.105), the three phase signals can be transformed onto the dq0 axis,

$$\begin{bmatrix} x_d(t) \\ x_q(t) \\ x_0(t) \end{bmatrix} = \sqrt{\frac{2}{3}} \begin{bmatrix} \cos(\theta(t)) & \cos(\theta(t) - \frac{2\pi}{3}) & \cos(\theta(t) - \frac{4\pi}{3}) \\ -\sin(\theta(t)) & -\sin(\theta(t) - \frac{2\pi}{3}) & -\sin(\theta(t) - \frac{4\pi}{3}) \\ \frac{1}{\sqrt{2}} & \frac{1}{\sqrt{2}} & \frac{1}{\sqrt{2}} \end{bmatrix} \begin{bmatrix} x_a(t) \\ x_b(t) \\ x_c(t) \end{bmatrix}. \tag{2.105}$$

With this transformation, the dq0 model of the LPMG is produced (2.106),

$$L\frac{d}{dt}\begin{bmatrix} i_d(t) \\ i_q(t) \end{bmatrix} = \begin{bmatrix} e_d(t) \\ e_q(t) \end{bmatrix} - \begin{bmatrix} v_d(t) \\ v_q(t) \end{bmatrix} - L\frac{\pi}{\tau}\dot{z}(t)\begin{bmatrix} -i_q(t) \\ i_d(t) \end{bmatrix} - R\begin{bmatrix} i_d(t) \\ i_q(t) \end{bmatrix} \tag{2.106}$$

where,

$$\begin{bmatrix} e_d(t) \\ e_q(t) \end{bmatrix} = \begin{bmatrix} 0 \\ \sqrt{\frac{3}{2}}\lambda_{fd}\frac{\pi}{\tau}\dot{z}(t) \end{bmatrix}. \tag{2.107}$$

The real and imaginary power values in the dq0 domain are (2.108),

$$\begin{aligned} P(t) &= v_q(t)i_q(t) + v_d(t)i_d(t) \\ Q(t) &= v_d(t)i_q(t) - v_q(t)i_d(t) \end{aligned} \tag{2.108}$$

The PTO force produced by the LPMG, depends on the stator currents, the flux linkage and the pole pitch, as shown in (2.109),

$$F_{PTO}(t) = \frac{\pi}{\tau}\sqrt{\frac{3}{2}}\left(\lambda_d i_q(t) - \lambda_q i_d(t)\right). \tag{2.109}$$

The LPMG used in this thesis is a non-salient machine, hence the PTO force can then be simplified to $\lambda_q = 0$ and $\lambda_d = \lambda_{fd}$. The force for the LPMG used in this thesis is

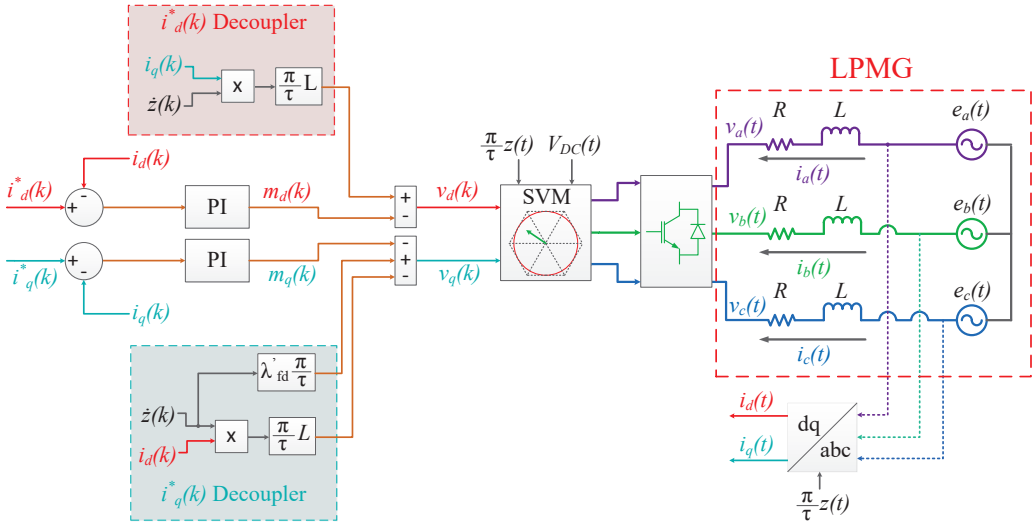

Figure 2.23: A block diagram of the interface between the digital current control and the 3 phase LPMG, which includes the SVM and the parks transformation block that transforms the $i_{abc}(t)$ currents into the dq domain $i_{dq}(t)$.

given by (2.110),

$$F_{PTO}(t) = \frac{\pi}{\tau}\sqrt{\frac{3}{2}}\lambda_{fd} i_q(t) = \frac{\pi}{\tau}\lambda'_{fd} i_q(t) \tag{2.110}$$

$$u_c(t) = \frac{\pi}{(M+m_\mu)\tau}\sqrt{\frac{3}{2}}\lambda_{fd} i_q(t) = \frac{\pi}{(M+m_\mu)\tau}\lambda'_{fd} i_q(t) \tag{2.111}$$

where $\lambda'_{fd} = \sqrt{\frac{3}{2}}\lambda_{fd}$.

2.3.3 LPMG Control

Fig. 2.23 shows a block diagram for an LPMG, with inner digital current controllers. Since the PTO force does not depend on $i_d(t)$ (2.110), the D axis current is typically regulated to $i^*_d(k) = 0$ A. A current set point $i^*_q(k)$ is sent to the $i_q(t)$ control loop to produce the desired force $F^*_{PTO}(k)$. In this work a digital proportional-integral gain controller is used for both current control loops. Utilising the following decoupling configurations in the control scheme (2.112),

$$\begin{aligned} v_d(k) &= \underbrace{L\frac{\pi}{\tau} i_q(k)\dot{z}(k)}_{i^*_d(k)\text{ Decoupler}} - \underbrace{m_d(k)}_{\text{control signal}} \\ v_q(k) &= \underbrace{-L\frac{\pi}{\tau} i_d(k)\dot{z}(k) + \lambda'_{fd}\frac{\pi}{\tau}\dot{z}(k)}_{i^*_q(k)\text{ Decoupler}} - \underbrace{m_q(k)}_{\text{control signal}}, \end{aligned} \tag{2.112}$$

then the disturbances such as coupling $i_{dq}(k)$ currents and the LPMG velocity become diminished, hence improving the current control of the system and simplifying the current controller design. Passing the dq discrete voltages $v_{dq}(k)$ through a space vector modulator (SVM) (Habetler et al. 1992) after the decoupling process the switching patterns of the power converters for each phase are set, as shown in Appendix A. Taking the mean of the pulse width modulated (PWM) (Holmes & Lipo 2003) voltages over the current controller sampling time T_{gen}, the continuous three phase voltages $v_{abc}(t)$ are formed, where a time delay of T_{gen} represents the response of the IGBT switching.

Fig. 2.24 shows an equivalent layout to Fig. 2.23, substituting the SVM and power converters with a time delay T_{gen} and the 3 phase LPMG and parks transformation with a corresponding DQ model. The simplified control scheme as shown in Fig. 2.24 is also the simulation model used throughout the remainder of the thesis.

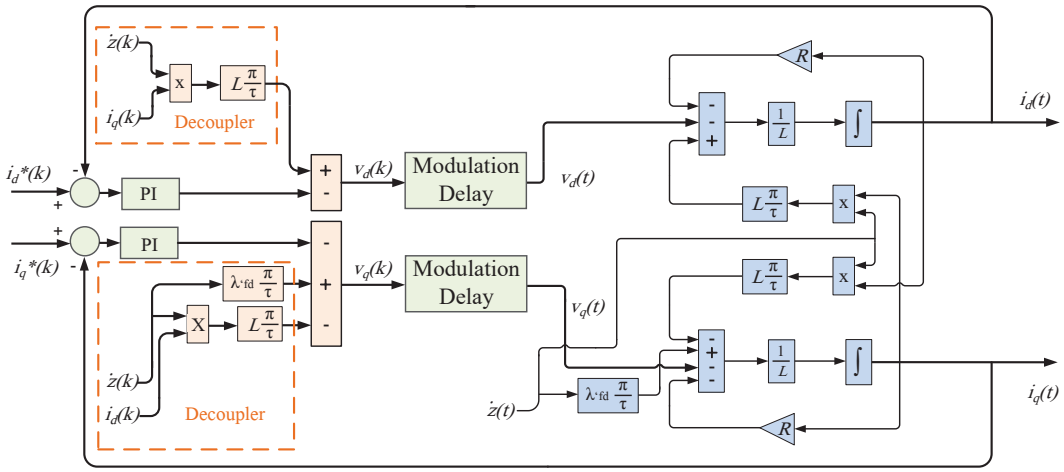

Figure 2.24: A block diagram of the digital current control for the LPMG in the DQ domain.

Assuming the decouplers produce disturbance rejection and the switching process is representable by a time delay, neglecting terms in (2.106) yields (2.113),

$$L\frac{d}{dt}\begin{bmatrix} i_d(t) \\ i_q(t) \end{bmatrix} = \begin{bmatrix} m_d(t-T_{gen}) \\ m_q(t-T_{gen}) \end{bmatrix} - R\begin{bmatrix} i_d(t) \\ i_q(t) \end{bmatrix}. \tag{2.113}$$

Using the Laplace transform, the continuous time equations (2.113) are represented in

the s domain (2.114),

$$\begin{aligned}\frac{I_d(s)}{M_d(s)} &= \frac{\frac{1}{L}}{s+\frac{R}{L}}e^{-sT_{gen}} \\ \frac{I_q(s)}{M_q(s)} &= \frac{\frac{1}{L}}{s+\frac{R}{L}}e^{-sT_{gen}}.\end{aligned} \tag{2.114}$$

Assuming a zero order hold (ZOH) with a sampling time T_{gen}, the continuous transfer function (2.114) is discretised using a modified z-transform (Kanasewich 1981), this yields (2.116),

$$\frac{I_d(z)}{M_d(z)} \quad = \boldsymbol{Z}\left\{\left(\frac{1-e^{-sT_{gen}}}{s}\right)\left(\frac{\frac{1}{L}}{s+\frac{R}{L}}\right)e^{-sT_{gen}}\right\} \tag{2.115}$$

$$\frac{I_d(z)}{M_d(z)} = \frac{z^{-2}\left(1-e^{-\frac{R}{L}T_{gen}}\right)}{R\left(1-z^{-1}e^{-\frac{R}{L}T_{gen}}\right)}. \tag{2.116}$$

Substituting the system parameters from Table 2.3 into (2.116), yields (2.117),

$$\frac{I_d(z)}{M_d(z)} = G_d(z) = \frac{0.0355}{z\,(z-0.9904)}. \tag{2.117}$$

Since $i_q(t)$ has the same structure as $i_d(t)$ (2.113), the modified z transform produces the same discrete transfer function, as shown in (2.118),

$$\frac{I_q(z)}{M_q(z)} = G_q(z) = \frac{0.0355}{z\,(z-0.9904)}. \tag{2.118}$$

With the power converter delay incorporated in the discrete model, a corresponding discrete PI controller is then designed. A PI controller is chosen, as a zero tracking error is attainable. With the IGBT switching included in the system as a time delay, the controlled system can become harder to control. However, using a piecewise-linear outer controller input signal, the overshoot effect of the inner loop control system can become insignificant. In this case a fully discrete PI controller is designed. First, the discrete PI transfer function is presented as (2.119),

$$\frac{M_q(z)}{E_q(z)} = C_q(z) = K_1\left(\frac{z-K_2}{z-1}\right). \tag{2.119}$$

The standard layout of the closed loop control schematic is shown in Fig 2.25, where $H_d(z) = H_q(z) = 1$ in this case.

Since the two discrete systems (2.117) and (2.118) are identical, it is only necessary to

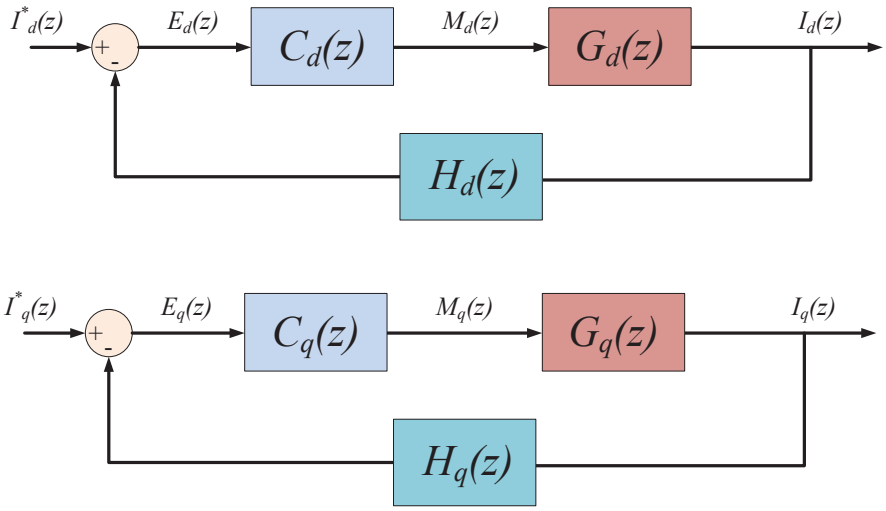

Figure 2.25: A block diagram of the digital current control for the LPMG in the DQ domain.

design a single current controller and then use the same controller design for the other current loop. In this case, the PI controller is designed using a discrete root locus. Inner controller design parameters were chosen to allow a fast inner loop response time while maintaining an acceptable step response overshoot. Hence, allowing a proper reference tracking of the outer control, which utilises an outer sampling time of $T_L = 0.1$ s,

$$\begin{aligned} \text{Peak overshoot} &= 100e^{\frac{-\zeta\pi}{\sqrt{1-\zeta^2}}}\% = 14\% \\ \text{Settling time} &= \frac{4}{\zeta\omega_n} = 0.015 \text{ s}, \end{aligned}$$

which corresponds to

$$\begin{aligned} \zeta &= 0.5339 \\ \omega_n &= 499.388 \text{ rad/s}. \end{aligned}$$

With these design parameters, the continuous design pole becomes (2.120),

$$\begin{aligned} s &= -\zeta\omega_n \pm j\omega_n\sqrt{1-\zeta^2} \\ &= -266.666 \pm j422.229, \end{aligned} \tag{2.120}$$

which in the discrete domain becomes (2.121),

$$\begin{aligned} z &= e^{sT_{gen}} \\ &= e^{\left(-\zeta\omega_n \pm \omega_n\sqrt{1-\zeta^2}\right)T_{gen}} \\ &= 0.76592e^{\pm j0.422} = 0.6987 \pm j0.3137. \end{aligned} \tag{2.121}$$

The controller is designed to place the 2 closed loop poles at $z = 0.6987 \pm j0.3137$. This yields the discrete PI controller (2.122),

$$\frac{M_q(z)}{E_q(z)} = C_q(z) = 11.968 \left(\frac{z - 0.8187}{z - 1} \right). \tag{2.122}$$

The resulting closed loop step response and the frequency response are shown in Fig. 2.26 and Fig. 2.27. The closed loop bandwidth of the controlled LPMG system is 986 rad/s, which is sufficient for controlling the $i_{dq}(t)$ currents when the outer control system has a much lower bandwidth, as will be shown in the next chapter.

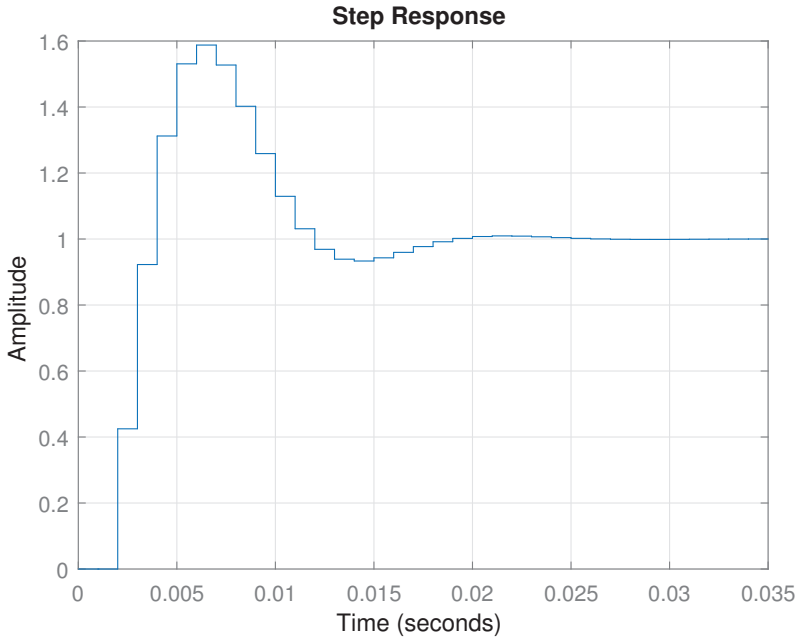

Figure 2.26: Step response of closed loop controlled LPMG with a settling time of 0.025 s and a peak overshoot percentage of 58%.

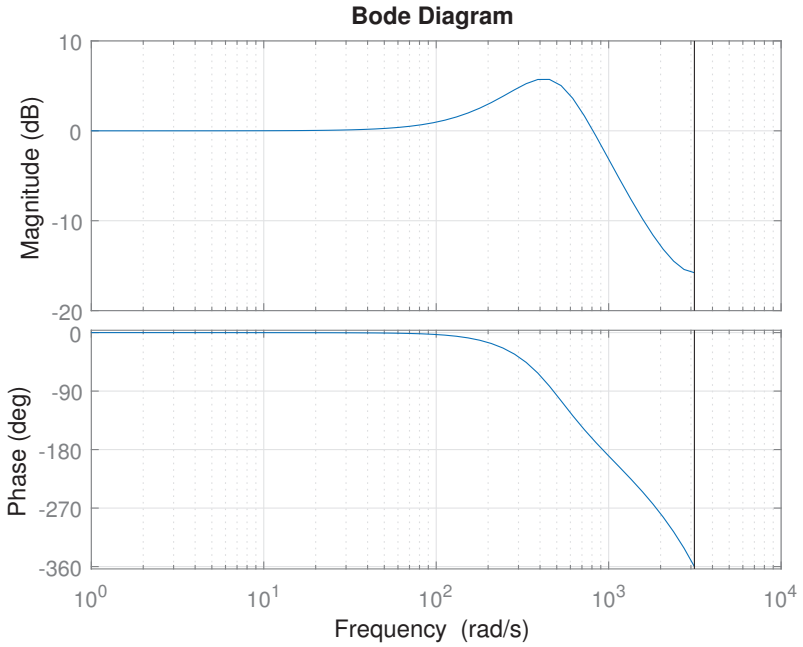

Figure 2.27: Frequency response of closed loop controlled LPMG with a bandwidth of 986 rad/s.

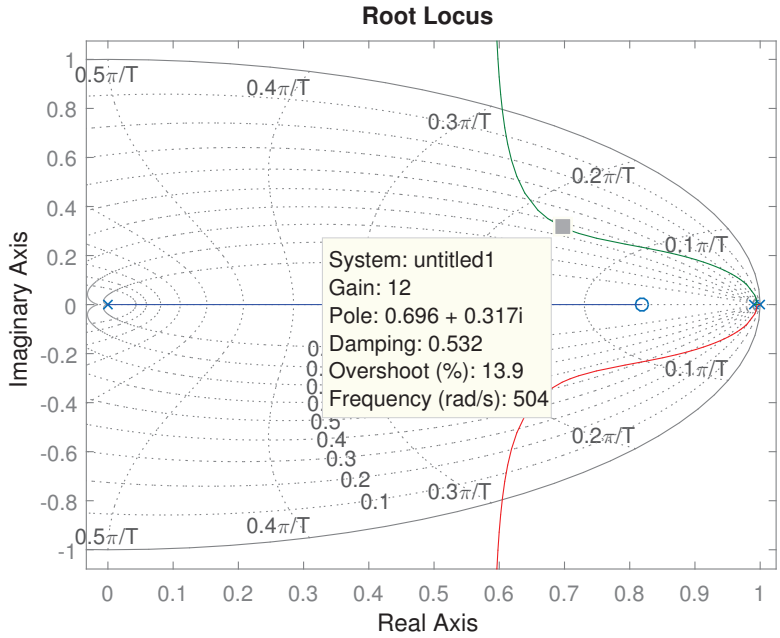

Figure 2.28: Root locus plot of LPMG system with closed loop poles matching the second order design poles.

2.3.4 Grid Integration

As was shown in section 2.3.3, the DQ currents are controlled by manipulating the DQ controlling voltages $v_d(k)$ and $v_q(k)$. In a real life system, the DQ controlling voltages are created using pulsed signals that are produced using SVM, where the DQ voltages are limited to $\sqrt{v_d^2(k) + v_q^2(k)} \leq \frac{\sqrt{3}}{2} V_{DC}(t)$. The SVM produces three phase controlling voltages $v_{abc}(t)$ that are directly dependent on $V_{DC}(t)$. Without a reliable constant $V_{DC}(t)$, the control of the LPMG can become difficult.

Controlling the $V_{DC}(t)$ voltage to be constant using the grid side converter, decouples the generation from the grid side (Lakshmi & Hemamalini 2016). As shown in Fig. 2.29, the grid and DC-link are represented by the following DQ domain continuous

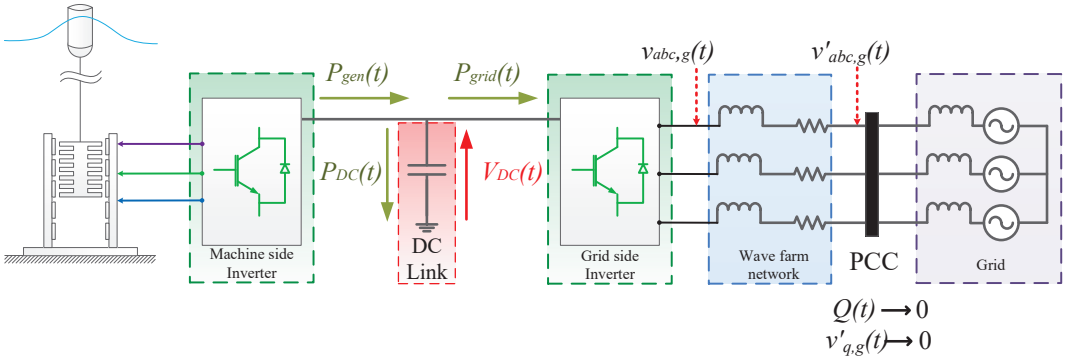

Figure 2.29: A schematic of the overall system from wave to wire; starting from the WEC connected to the LPMG, which is controlled by the voltages generated from the machine side inverter that is limited by the voltage across the DC-link. The DC-link is controlled by the grid side inverter that interacts with (in this case) an ideal grid.

equation,

$$P_{grid}(t) = P_{gen}(t) - P_{DC}(t) \tag{2.123}$$

where

$$P_{grid}(t) = v_{d_g}(t) i_{d_g}(t) + v_{q_g}(t) i_{q_g}(t)$$

$P_{gen}(t)$ is the power generated from the WEC,

$$P_{DC}(t) = C_{dc} V_{DC}(t) \frac{dV_{DC}}{dt},$$

yielding (2.124),

$$C_{dc} V_{DC}(t) \frac{dV_{DC}}{dt} = P_{gen}(t) - \left(v_{d_g}(t) i_{d_g}(t) + v_{q_g}(t) i_{q_g}(t) \right). \tag{2.124}$$

The active and reactive power flows at the point of common coupling (PCC) on the grid side are represented as (2.125) and (2.126),

$$P(t) = v^{'}_{d_g} i_{d_g}(t) + v^{'}_{q_g} i_{q_g}(t) \tag{2.125}$$

$$Q(t) = v^{'}_{d_g} i_{q_g}(t) - v^{'}_{q_g} i_{d_g}(t), \tag{2.126}$$

where $v^{'}_{d_g}$ and $v^{'}_{q_g}$ are the DQ voltage at the PCC which are assumed constant. With the PLL connected to the PCC, as shown in Fig. 2.29, it becomes possible to align $v^{'}_{q_g} = 0$ (Vittal & Ayyanar 2012). With $v^{'}_{q_g} = 0$, the active and reactive powers are independently controlled by the D and Q grid side converter currents respectively, as shown in (2.127) and (2.128),

$$P(t) = v^{'}_{d_g} i_{d_g}(t) \tag{2.127}$$

$$Q(t) = v^{'}_{d_g} i_{q_g}(t). \tag{2.128}$$

The current dynamics of the grid-side converter are modelled by (2.129) and (2.130),

$$L_w \frac{di_{d_g}}{dt} = -R_w i_{d_g}(t) + L_w \omega(t) i_{q_g}(t) + v_{d_g}(t) - v^{'}_{d_g} \tag{2.129}$$

$$L_w \frac{di_{q_g}}{dt} = -R_w i_{q_g}(t) - L_w \omega(t) i_{d_g}(t) + v_{q_g}(t) - v^{'}_{q_g} \tag{2.130}$$

where ω is the electrical speed (in this case $\omega = 314.159$ rad/s because the grid frequency is 50 Hz); $v^{'}_{d_g}(t)$ and $v^{'}_{q_g}(t)$ are the voltages at the PCC and R_w and L_w are the values that respectively represent the impedance between the grid side converter and the PCC (Perera et al. 2013). Controlling $i_{q_g}(t) = 0$ so that $Q(t) = 0$ and assuming $v^{'}_{q_g} = 0$, (2.124), (2.129) and (2.130) are combined, yielding (2.131), which is a non-linear system,

$$\frac{dV_{DC}}{dt} = \frac{1}{C_{dc} V_{DC}(t)} \left[P_{gen}(t) - L_w i_{d_g}(t) \frac{di_{d_g}}{dt} + R_w i^2_{d_g}(t) + v^{'}_{d} i_{d_g}(t) \right]. \tag{2.131}$$

Linearising (2.131) yields (2.132),

$$\tilde{V_{DC}}(s) = \frac{K_{gen}}{s} \tilde{P_{gen}}(s) + \frac{K_{i_d}(1 + sT_{i_d})}{s} \tilde{I_{d_g}}(s). \tag{2.132}$$

The DC-link voltage $V_{DC}(t)$ is controlled using a cascade controller as shown in Fig. 2.30. The outer $V_{DC}(t)$ controller sends $i^*_{d_g}(t)$ reference signals to the inner loop of the cascade controller which controls the $i_{d_g}(t)$ current at a much higher bandwidth than the outer control loop. In respect to the outer control loop, the inner $i_{d_g}(t)$ controller

loop is estimated as a first order transfer function (2.133) and the outer control loop utilises a PI controller (2.134).

$$\frac{\tilde{I_{d_g}}(s)}{\tilde{I^*_{d_g}}(s)} = \frac{1}{1+s\tau} \tag{2.133}$$

$$\frac{\tilde{I^*_{d_g}}(s)}{\tilde{E}(s)} = \frac{K_p\left(s+K_T\right)}{s}. \tag{2.134}$$

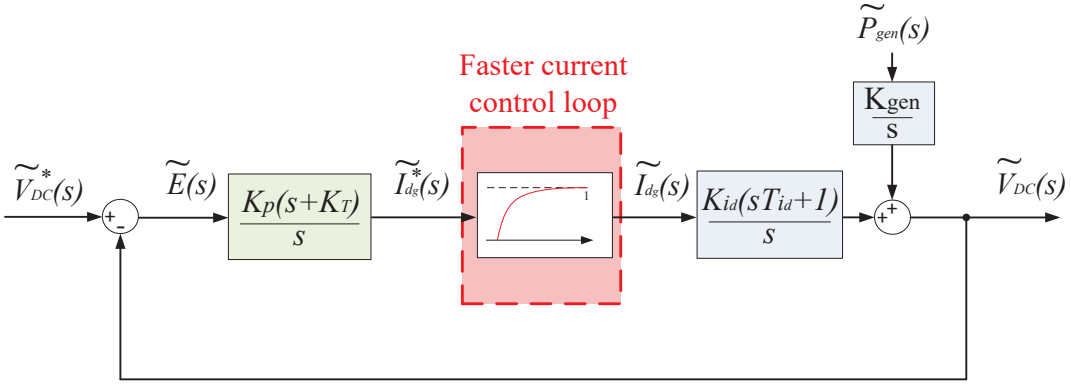

Figure 2.30: The cascade control scheme which shows the slower outer $V_{DC}(t)$ controller and a faster inner $i_{d_g}(t)$ controller which in this case is estimated as a first order system.

Ignoring the disturbances from (2.132), the open loop transfer function $\tilde{V_{DC}}(s)/\tilde{E}(s)$ is found (2.135),

$$\frac{\tilde{V_{DC}}(s)}{\tilde{E}(s)} = \frac{K_p K_{i_d}\left(s+K_T\right)\left(sT_{i_d}+1\right)}{s^2\left(s\tau+1\right)}, \tag{2.135}$$

where

$$K_{i_d} = -\frac{v'^{\star}_d + 2R_w i^{\star}_{d_g}}{C_{dc}V^{\star}_{DC}} \tag{2.136}$$

and

$$T_{i_d} = \frac{L_w i^{\star}_{d_g}}{v'^{\star}_d + 2R_w i^{\star}_{d_g}}, \tag{2.137}$$

where the systems operating point are denoted using $\star$.

The sensitivity of the closed loop system depends on the $P_{gen}(t)$ level, where the corresponding $i^{\star}_d$ operating point can become negative which consequently makes the systems zero $1/T_{i_d}$ negative (2.135) where,

$$T_{i_d} < 0 : \text{if } \{-\frac{v'^{\star}_d}{2R_w} < i^{\star}_d < 0\} \qquad \text{non-minimum phase system.} \tag{2.138}$$

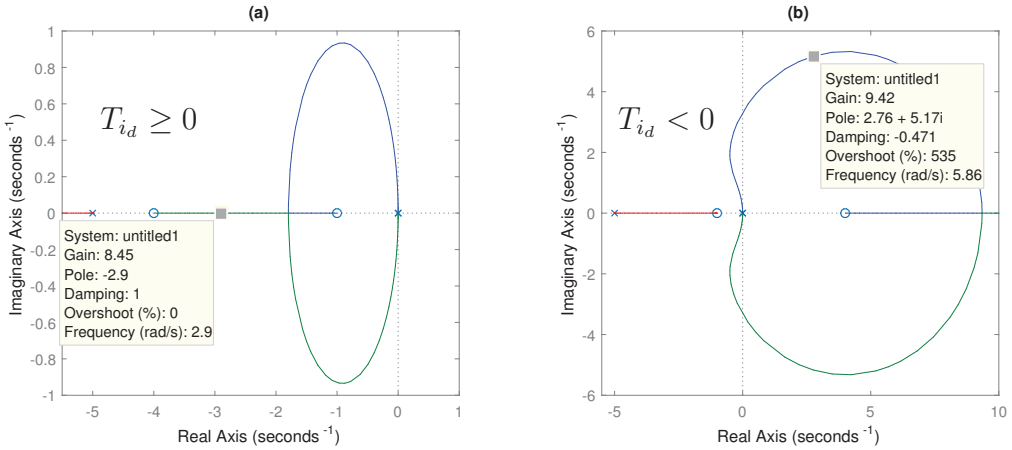

Figure 2.31: The cascade control scheme which shows the slower outer $V_{DC}(t)$ controller and a faster inner $i_{d_g}(t)$ controller which in this case is estimated as a first order system.

If $T_{i_d} \geq 0$, the closed loop system is an easily controlled minimum phase system, as shown in Fig. 2.31(a).If $T_{i_d} < 0$ (2.138), the closed loop system becomes a non-minimum phase system, which can lead to an unstable system if over-tuned (Dirscherl et al. 2017). An example of a non-minimum phase system occurring due to a negative T_{i_d} is shown in Fig. 2.31(b). It is demonstrated in Fig. 2.31 that during a minimum phase system, a stable system is feasible at a gain of $K_p \geq 0$. However, the controller during a non-minimum phase has to be carefully detuned to maintain system stability. Furthermore, by detuning the $V_{DC}(t)$ controller, the controller consequently increases the DC-link voltage $V_{DC}(t)$ variability which is undesirable as problems may arise on the generation side.

How easily controllable the $V_{DC}(t)$ link is depends on the power exported from the generation side $P_{gen}(t)$ onto the grid side and the weakness of the grid. The most convenient method is to treat the grid network, as shown in Fig. 2.29, as an ideal network where the voltages from the grid $v_q^{'}(t)$ and $v_d^{'}(t)$ are assumed constant. This method would be sufficient when importing close to constant power and when the grid is strong. However, for weaker grids and fluctuating power levels, stability problems may transpire (Kundur et al. 1994). With wave energy resources located in remote areas, there is a high probability that long transmission lines will be used, hence causing a weak grid (Huang et al. 2012).

Grid networks, as was estimated in Fig. 2.29, are modelled using a series impedance $Z_s = R_s + jX_s$, as shown in Fig. 2.32, where $V_{abc}(t)$ is the three phase source voltage which is constant. The series impedance Z_s is found using a grid impedance angle Ψ_g

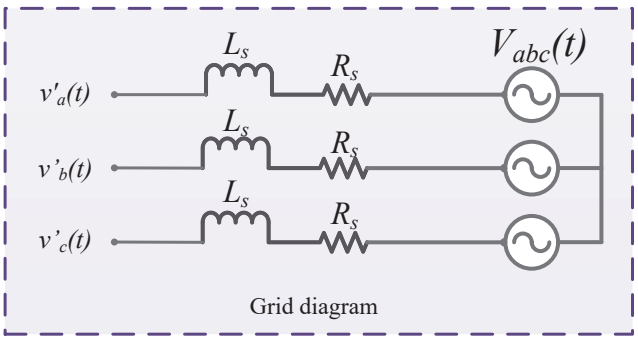

Figure 2.32: A circuit diagram showing an equivalent grid impedance, selecting these values will define the grid strength.

and the short circuit ratio (SCR) (Drbal et al. 1996). The SCR is defined as (2.139),

$$SCR = \frac{S_{sc}}{S_n} \tag{2.139}$$

where S_{sc} is the short circuit level of a certain point on the grid and S_n is the nominal power level produced from the generation side. The grid is considered weak if $SCR < 3$ (Krishayya et al. 1997), although there have been cases where wind farms were able to operate during $SCR = 2$ (Diedrichs et al. 2012). By knowing the grid impedance angle Ψ_g and the SCR values of the grid the grid impedance can be found, as in (2.140) and (2.141),

$$\tan(\Psi_g) = \frac{X_s}{R_s} \tag{2.140}$$

$$S_{sc} = \frac{V^2}{\sqrt{R_s^2 + X_s^2}}, \tag{2.141}$$

where V is the line-to-line voltage of $v'_{abc_g}(t)$. With these parameter found, the grid network can be modelled and simulated. However, in this thesis the main objective is maximising electrical power extraction from the energy source and only dealing with the wave to DC-link system, therefore assuming an ideal constant DC-link at all times.

2.4 Summary

In this chapter, the entire system from wave to grid was analysed. The point absorber modelling was introduced where it was shown how the nonlinear Navier-Stokes equations could be simplified down into a simplistic linear Cummins equation. The modelling of polychromatic waves was then covered where sea spectrum and excitation wave surface elevation modelling was analysed. The modelling of the radiation convo-

lution integral was then introduced. Prony's exponential method was analysed, where an acceptable approximation for a SISO radiation subsystem could be found if a high order system was utilised. Using SVD to accomplish a balanced model reduction, the high order Prony's approximation was simplified. Using multiple impulse responses, HSVD was utilised to create a SIMO radiation subsystem, where a balanced model reduction is unnecessary.

An LPMG model was then introduced, where the differences in operation between a linear PMG and a rotary PMG were highlighted. Assuming a balanced three phase LPMG model, the Parks transformation transformed the three phase system into a convenient two phase DQ system. The LPMG currents were then controlled to produce forces, where the current control was accomplished using a digital PI controller with a high bandwidth. The dependency on a constant DC link voltage was then emphasised, where matters such as voltage instabilities due to weak grids and fluctuating power levels could cause problems in controlling a constant DC link voltage which in turn could cause LPMG force control problems.

References

Amundarain, M., Alberdi, M., Garrido, A. J. & Garrido, I. (2011), 'Modeling and simulation of wave energy generation plants: Output power control', *IEEE Transactions on Industrial Electronics* **58**(1), 105–117.

Anderson, J. D. & Wendt, J. (1995), *Computational fluid dynamics*, Vol. 206, Springer.

Antonio, F. d. O. (2010), 'Wave energy utilization: A review of the technologies', *Renewable and sustainable energy reviews* **14**(3), 899–918.

Aubry, J., Ahmed, H. B. & Multon, B. (2012), 'Sizing optimization methodology of a surface permanent magnet machine-converter system over a torque-speed operating profile: Application to a wave energy converter', *IEEE Transactions on Industrial Electronics* **59**(5), 2116–2125.

Bhinder, M. A., Babarit, A., Gentaz, L. & Ferrant, P. (2011), Assessment of Viscous Damping via 3D-CFD Modelling of a Floating Wave Energy Device, *in* 'In Proceedings of the 9th European Wave and Tidal Energy Conference (EWTEC)', pp. 1–6.

Chung, S.-K. (2000), 'Phase-locked loop for grid-connected three-phase power conversion systems', *IEE Proceedings-Electric Power Applications* **147**(3), 213–219.

Cummins, W. E. (1962), 'The impulse response function and ship motions'.

Diedrichs, V., Beekmann, A., Busker, K., Nikolai, S. & Adloff, S. (2012), Control of wind power plants utilizing voltage source converter in high impedance grids, *in* 'Power and Energy Society General Meeting, 2012 IEEE', IEEE, pp. 1–9.

Dirscherl, C., Hackl, C. M. & Schechner, K. (2017), 'Modeling and control of modern wind turbine systems: An introduction', *CoRR* **abs/1703.08661**.

Drbal, L. F., Boston, P., Westra, K. & Veatch, B. &. (1996), *Power Plant Engineering*, IFAC proceedings series, Springer.

Franklin, G. F., Powell, J. D. & Workman, M. L. (1998), *Digital control of dynamic systems*, Vol. 3, Addison-Wesley Menlo Park, CA.

Fusco, F. & Ringwood, J. V. (2010), 'Short-term wave forecasting for real-time control of wave energy converters', *IEEE Transactions on Sustainable Energy* **1**(2), 99–106.

Garcia-Rosa, P. B. & Ringwood, J. V. (2016), 'On the sensitivity of optimal wave energy device geometry to the energy maximizing control system', *IEEE Transactions on Sustainable Energy* **7**(1), 419–426.

Grilli, S. T., Skourup, J. & Svendsen, I. A. (1989), 'An efficient boundary element method for nonlinear water waves', *Engineering Analysis with Boundary Elements* **6**(2), 97–107.

Habetler, T. G., Profumo, F., Pastorelli, M. & Tolbert, L. M. (1992), 'Direct torque control of induction machines using space vector modulation', *IEEE Transactions on Industry Applications* **28**(5), 1045–1053.

Hasselmann, K. (1973), 'Measurements of wind wave growth and swell decay during the Joint North Sea Wave Project (JONSWAP)', *Dtsch. Hydrogr. Z.* **8**, 95.

Henderson, R. (2006), 'Design, simulation, and testing of a novel hydraulic power take-off system for the Pelamis wave energy converter', *Renewable Energy* **31**(2), 271–283.

Holmes, D. G. & Lipo, T. A. (2003), *Pulse width modulation for power converters: principles and practice*, Vol. 18, John Wiley & Sons.

Huang, S.-H., Schmall, J., Conto, J., Adams, J., Zhang, Y. & Carter, C. (2012), Voltage control challenges on weak grids with high penetration of wind generation: ERCOT experience, *in* 'Power and Energy Society General Meeting, 2012 IEEE', IEEE, pp. 1–7.

Igic, P., Zhou, Z., Knapp, W., MacEnri, J., Sørensen, H. C. & Friis-Madsen, E. (2011), 'Multi-megawatt offshore wave energy converters–electrical system configuration and generator control strategy', *IET renewable power generation* **5**(1), 10–17.

Kanasewich, E. R. (1981), *Time sequence analysis in geophysics*, University of Alberta.

Khalil, H. K. (1996), 'Noninear Systems', *Prentice-Hall, New Jersey* **2**(5), 1–5.

Krishayya, P. C. S., Adapa, R., Holm, M. & Others (1997), 'IEEE guide for planning DC links terminating at AC locations having low short-circuit capacities, part I: AC/DC system interaction phenomena', *IEEE Std. France: CIGRE* .

Kundur, P., Balu, N. J. & Lauby, M. G. (1994), *Power system stability and control*, Vol. 7, McGraw-Hill New York.

Kung, S.-Y., Arun, K. S. & Rao, D. V. B. (1983), 'State-space and singular-value decomposition-based approximation methods for the harmonic retrieval problem', *JOSA* **73**(12), 1799–1811.

Lakshmi, M. & Hemamalini, S. (2016), 'Decoupled control of grid connected photovoltaic system using fractional order controller', *Ain Shams Engineering Journal.*

Lee, C.-H. (1995), *WAMIT Theory Manual*.

Leijon, M., Bernhoff, H., Agren, O., Isberg, J., Sundberg, J., Berg, M., Karlsson, K. E. & Wolfbrandt, A. (2005), 'Multiphysics simulation of wave energy to electric energy conversion by permanent magnet linear generator', *IEEE Transactions on energy conversion* **20**(1), 219–224.

Lenee-Bluhm, P., Paasch, R. & Özkan-Haller, H. T. (2011), 'Characterizing the wave energy resource of the US Pacific Northwest', *Renewable Energy* **36**(8), 2106–2119.

Lovelace, E. C., Jahns, T. M. & Lang, J. H. (2000), 'Impact of saturation and inverter cost on interior PM synchronous machine drive optimization', *IEEE Transactions on Industry Applications* **36**(3), 723–729.

Marquardt, D. W. (1963), 'An algorithm for least-squares estimation of nonlinear parameters', *Journal of the society for Industrial and Applied Mathematics* **11**(2), 431–441.

Mohan, N. (2014), *Advanced electric drives: analysis, control, and modeling using MATLAB/Simulink*, John Wiley & Sons.

Molinas, M., Skjervheim, O., Andreasen, P., Undeland, T., Hals, J., Moan, T. & Sorby, B. (2007), Power electronics as grid interface for actively controlled wave energy converters, *in* '2007 International Conference on Clean Electrical Power', IEEE, pp. 188–195.

Morison, J. R., Johnson, J. W., Schaaf, S. A. & Others (1950), 'The force exerted by surface waves on piles', *Journal of Petroleum Technology* **2**(05), 149–154.

Ochi, M. K. & Hubble, E. N. (1977), Six-parameter wave spectra, *in* 'Coastal Engineering 1976', pp. 301–328.

Pearson, K. (1905), 'The problem of the random walk', *Nature* **72**(1905), 294.

Penalba, M., Mérigaud, A., Gilloteaux, J.-C. & Ringwood, J. V. (2017), 'Influence

of nonlinear Froude–Krylov forces on the performance of two wave energy points absorbers', *Journal of Ocean Engineering and Marine Energy* pp. 1–12.

Penalba Retes, M., Mérigaud, A., Gilloteaux, J.-C. & Ringwood, J. (2015), Nonlinear Froude-Krylov force modelling for two heaving wave energy point absorbers, *in* 'Proceedings of the 11th European Wave and Tidal Energy Conference', European Wave and Tidal Energy Conference 2015.

Perera, B. K., Ciufo, P. & Perera, S. (2013), Point of common coupling (PCC) voltage control of a grid-connected solar photovoltaic (PV) system, *in* 'Industrial Electronics Society, IECON 2013-39th Annual Conference of the IEEE', IEEE, pp. 7475–7480.

Pierson, W. J. & Moskowitz, L. (1964), 'A proposed spectral form for fully developed wind seas based on the similarity theory of SA Kitaigorodskii', *Journal of geophysical research* **69**(24), 5181–5190.

Polinder, H., Damen, M. E. C. & Gardner, F. (2004), 'Linear PM Generator System for Wave Energy Conversion in the AWS', *IEEE Transactions on Energy Conversion* **19**(3), 583–589.

Prony, R. (1795), 'Essai exprimental et analytique: Sur les lois de la dilatabilit des fluides lastiques et sur celles de la force expensiver de la vapeur del'eau et de la vapeur de l'alkool', *l'Ecola Polytechnique* **1**, 24–76.

Rodrguez, J., Bernet, S., Wu, B., Pontt, J. O. & Kouro, S. (2007), 'Multilevel voltage-source-converter topologies for industrial medium-voltage drives', *IEEE Transactions on industrial electronics* **54**(6), 2930–2945.

Tedeschi, E., Carraro, M., Molinas, M. & Mattavelli, P. (2011), 'Effect of control strategies and power take-off efficiency on the power capture from sea waves', *IEEE Transactions on Energy Conversion* **26**(4), 1088–1098.

Temam, R. (1984), *Navier-stokes equations*, Vol. 2, North-Holland Amsterdam.

Tucker, M. J. & Pitt, E. G. (2001), *Waves in ocean engineering*, number Volume 5.

Vittal, V. & Ayyanar, R. (2012), *Grid Integration and Dynamic Impact of Wind Energy*, Power Electronics and Power Systems, Springer New York.

Willcox, K. & Peraire, J. (2002), 'Balanced model reduction via the proper orthogonal decomposition', *AIAA journal* **40**(11), 2323–2330.

Wu, F., Zhang, X.-P., Ju, P. & Sterling, M. J. H. (2008), 'Modeling and control of AWS-

based wave energy conversion system integrated into power grid', *IEEE Transactions on Power Systems* **23**(3), 1196–1204.

Yu, Z. & Falnes, J. (1995), 'State-space modelling of a vertical cylinder in heave', *Applied Ocean Research* **17**(5), 265–275.

Chapter 3

Control of Wave Energy Converters

3.1 Introduction

In the wave energy industry, there are many different WEC mechanical designs, each of which could benefit from active control to ensure that the best power extraction occurs and that the system is not driven beyond its physical and electrical design limitations. In this chapter, WEC control techniques are investigated, where both classical control and more modern control techniques are discussed.

Classical control methods, such as reactive control and latching (Budal & Falnes 1977, 1980) can be used to optimise the mechanical power extracted. These methods are popularly used because of their causality which enables the system to produce sub-optimal or optimal results without the need for a prediction of the future oncoming excitation wave. However, with the classical methods aggressive mechanical forces occur, causing a forced system oscillation which can lead to system damages. With classical control methods it is possible for system constraints to be included in the control. However, with modern techniques such as predictive control, maximum average mechanical power can be extracted while easily considering the systems linear and non-linear restrictions.

In this chapter, model predictive control (MPC) (Maciejowski 2002) is discussed, where most of the work in this thesis focuses on an economic MPC (O'Sullivan & Lightbody 2017). First, economic MPC is shown to produce close to optimal average mechanical power. Furthermore, the omission of losses within the optimisation process yields a significant reduction in power yield (even negative) at lower frequencies; this is important since the sea spectrum is dominated by lower frequencies for

energetic seas. By including the generator (LPMG) losses (Polinder et al. 2004) in the optimisation, the maximum average electrical power is captured. By implementing a first order hold (FOH) instead of a zero order hold (ZOH), the quality of the instantaneous electrical power can be improved for grid integration (O'Sullivan & Lightbody 2015).

3.2 Classical Control

The simplest method for extracting power from the incoming excitation waves is to use passive damping. With a passive damper, the PTO force produced is the product of the WEC velocity $\dot{z}(t)$ and a constant damping value ζ, which can be pre-set. Depending on the ζ value, the power extraction across the frequency domain can be altered. A damped system will decrease oscillations around the natural frequency of the WEC, as shown in Fig. 3.1. Passive damping control is easy to implement, once the appropriate damping coefficient has been chosen (i.e. the damping coefficient would have to be tuned differently for each frequency to obtain the most power). Even though the control is simplistic, it is not the most efficient method in extracting power since the only frequency where maximum average power extraction can occur is at the natural frequency of the WEC, which is shown in Fig. 3.1.

To combat this inefficiency, classical control methods were introduced (Falnes 2007). Classical control methods were incorporated into the WEC system initially to maximise the average mechanical power absorption from the excitation waves. For this to occur there needs to be an active PTO force which will cause the system to oscillate, hence causing higher instantaneous speeds and greater instantaneous power.

3.2.1 Latching Control

Latching control is a control method that was introduced by (Falnes & Budal 1978) to produce close to maximum average mechanical power from the WEC system. The latching control operation, as shown in Fig. 3.2, uses a mechanical latching brake to force the WEC's velocity to be in phase with the excitation wave force; this phase lock enables optimum average power absorption. As shown in Fig. 3.2, the latching break is applied when the WEC's velocity reaches zero. The latching break is enabled for a duration of T_{LH}. The latching duration T_{LH} is tuned so that the WEC velocity will be in phase with the excitation wave, causing optimum conditions for maximising average

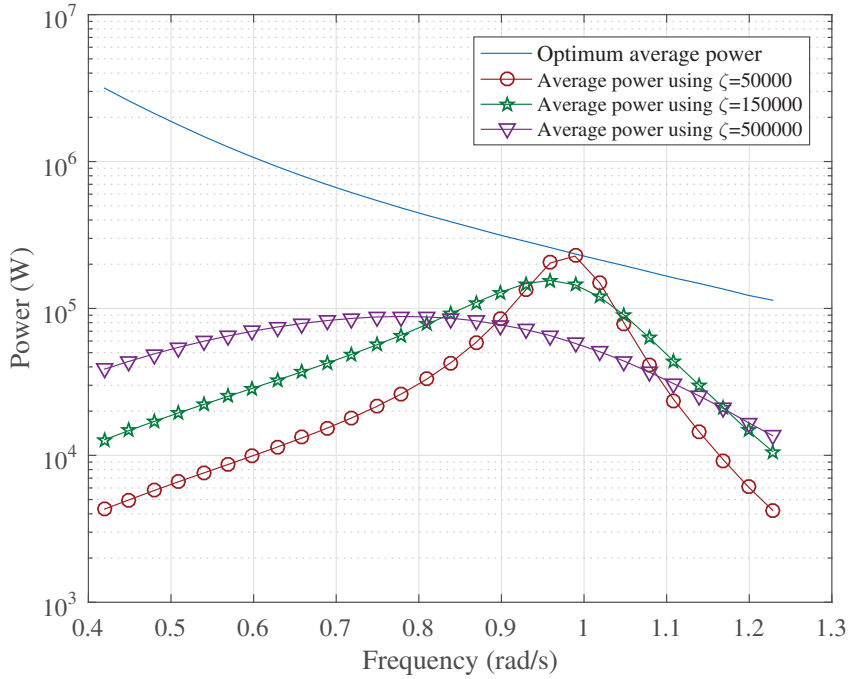

Figure 3.1: Average power curves corresponding to a range of ζ damping coefficients, superimposed on the maximum average power curve for monochromatic wave excitation with 1 m wave height.

power absorption. As shown from Fig. 3.2, the velocity is zero for the T_{LH} duration, disabling power absorption. However, forcing the WEC velocity to be in phase with the wave excitation force causes an increased power absorption on average.

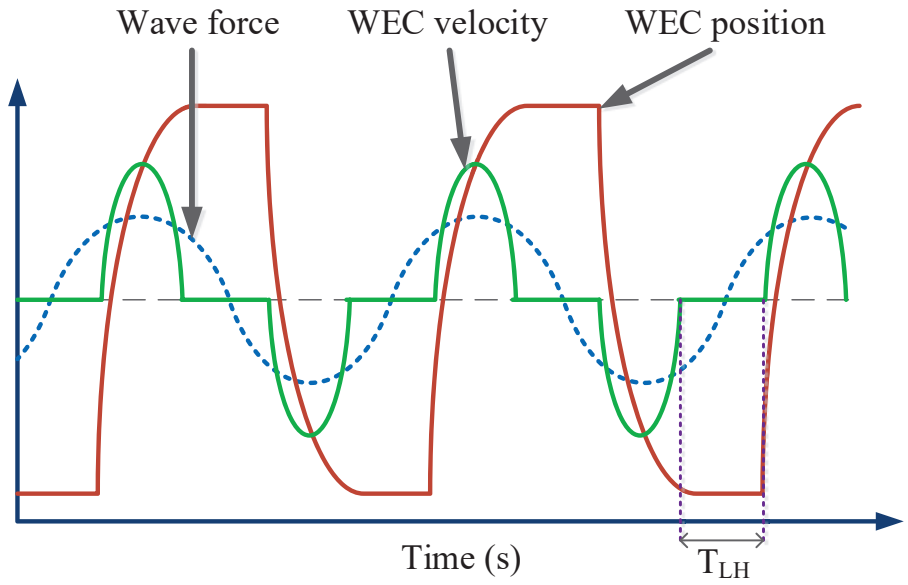

Figure 3.2: Example WEC motion waveforms created from latching control when exerting a sinusoidal excitation wave

Latching has been applied to maximise the mechanical power extracted from oscillating water columns (OWC) (de O Falcão 2002). The OWC, as shown in Fig. 3.3, when moving in heave motion, compresses air from the air chamber which is between the water surface and the latching mechanism. When the OWC is unlatched, air is allowed to flow through a bi-directional turbine. Previous devices using this method have been

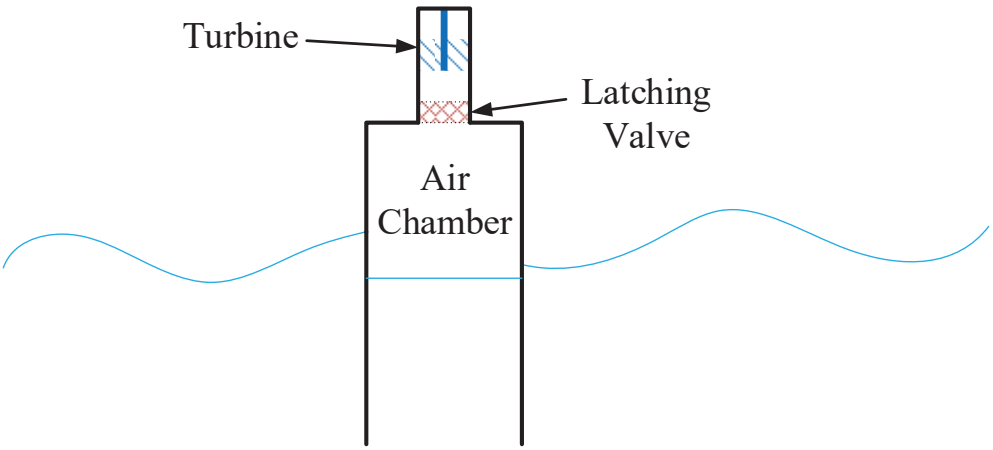

Figure 3.3: Example of the oscillating water column WEC device

inefficient due to the design of the latching mechanism and turbine (Antonio 2010). However, in recent times, with much better latching valves and turbine design, the effectiveness of the system seems promising (Henriques et al. 2017).

Other derivatives of the latching method have also been investigated, such as declutching (Babarit et al. 2009). Declutching control involves disengaging the PTO from the WEC, allowing the WEC to free-wheel. By disengaging the PTO from the WEC, the WEC's velocity is allowed to naturally synchronise with the excitation wave force. Latching and declutching methods are very similar in their concepts. However, given a certain frequency range, one method can be preferable over the other (Feng & Kerrigan 2013). For standard latching, the control system is optimal when the resonance period of the WEC is shorter than the period of the excitation wave. Furthermore, for declutching control, the opposite applies, where the performance is optimal when the resonance period is longer than the period of the excitation wave. Both of these methods can produce close to maximum energy extraction from the system if the timing sequences are optimally tuned, hence these methods are sufficient replacements for passive damping control. Considering that these methods are designed for monochromatic seas, the operation becomes problematic when the WEC is introduced to polychromatic excitation waves, where the optimum control actions are non-unique (Babarit et al. 2004).

3.2.2 Reactive Control (Optimal Control)

Reactive control (otherwise known as impedance matching control) was one of the first control methods developed to maximise the average mechanical power from the WEC system (Budal & Falnes 1977). The method involves controlling the magnitude and phase of the WEC velocity in relation to the excitation wave; in this case a phase-lock occurs between the WEC velocity and the excitation wave.

For regular excitation waves, the reactive control algorithm creates optimum control forces that force the WEC's velocity to be in phase with the excitation wave, hence cancelling the systems reactive components and extracting the maximum amount of average power. For a regular wave with excitation frequency ω, the system (2.11, page 29) can be represented in the frequency domain as (3.1),

$$\dot{Z}(\omega)\Omega_i(\omega) = F_{ex}(\omega) + F_{PTO}(\omega), \tag{3.1}$$

where $\dot{Z}(\omega)$, $F_{ex}(\omega)$ and $F_{PTO}(\omega)$ are the WEC velocity, the excitation wave force and the external PTO force, all defined in the frequency domain. Furthermore, $\Omega_i(\omega)$ is the system impedance in the frequency domain (3.2),

$$\Omega_i(\omega) = \left[j\omega \left(M + m_\mu\right) + H_r(\omega) + \frac{\beta}{j\omega} \right]. \tag{3.2}$$

Theoretically, the following PTO force choice will maximise the mechanical energy extracted,

$$F^*_{PTO}(\omega) = \dot{Z}(\omega)\bar{\Omega}_i(\omega), \tag{3.3}$$

where $\bar{\Omega}_i(\omega)$ here indicates a complex conjugate. With this choice, the resultant optimal velocity is (3.4),

$$\begin{aligned} \dot{Z}^*(\omega) &= \frac{1}{\Omega_i(\omega) + \bar{\Omega}_i(\omega)} F_{ex}(\omega) \\ &= \frac{1}{2\Re\{H_r(\omega)\}} F_{ex}(\omega) \end{aligned} \tag{3.4}$$

3.2.3 Implementing Reactive Control

In practice, reactive control is usually expressed as a speed control problem, in which the F_{PTO} is manipulated to force the WEC to travel at this desired optimal velocity (as shown in Fig. 3.4). For irregular seas with a narrow-banded spectrum, if the in-

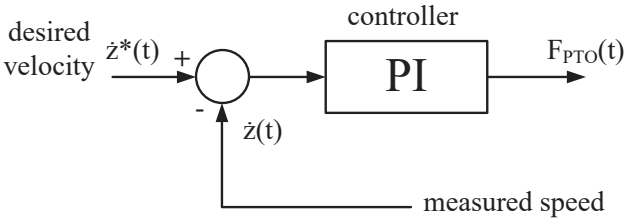

Figure 3.4: Basic reactive control system

stantaneous frequency, $\hat{\omega}(t)$, of the wave is estimated (Fusco & Ringwood 2013) and the excitation wave is assumed to have a narrow frequency bandwidth, then the desired velocity can be approximated as $\dot{z}^*(t) = \frac{1}{2\Re\{H_r(\hat{\omega})\}} f_{ex}(t)$ which uses the estimate $\hat{\omega}$ to provide a realisable controller. Using $\frac{1}{2\Re\{H_r(\omega)\}}$ as a look up table, the reactive control scheme is shown in Fig. 3.5, including the LPMG PTO, with current control.

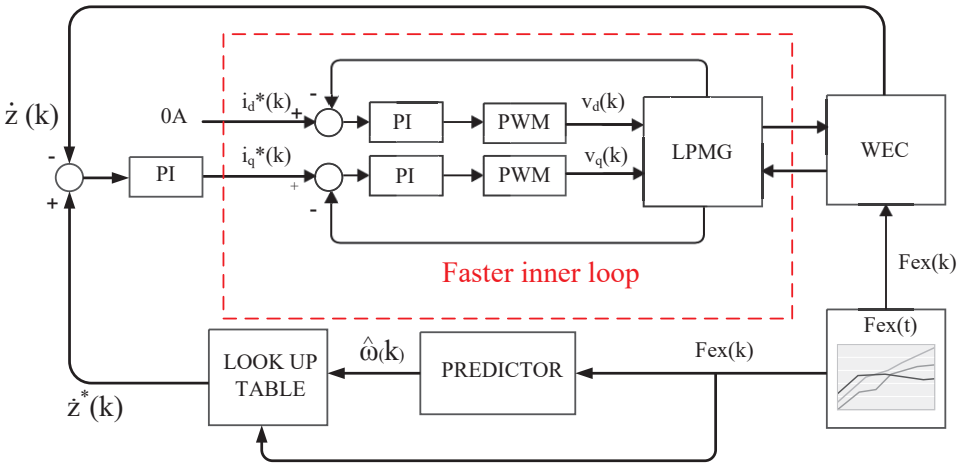

Figure 3.5: Reactive control schematic

This is a cascade controller, in which the inner current control is of a high bandwidth and the outer control designed to control the reference optimum speed is of a lower bandwidth. Fig. 3.6 shows the average power absorbed from the system using reactive control, where the excitation waves are regular monochromatic waves with an amplitude of 1 m. The ideal PTO shows the average power extracted from the wave, which is 50% of the available power in the wave. This average power produced is the maximum that can be extracted from the unconstrained system. However, the disadvantages to this method are:

- For optimum velocity references to be found, the excitation wave height and frequency must be predictable.
- The PTO forces to create these maximum average powers may be unrealistically large, causing major instantaneous power swings that would be unacceptable for exporting onto the grid .

A causal approximation of the impedance matching method was created (Fusco & Ringwood 2011) which produces sub-optimal results. Using a constant velocity reference gain to estimate the frequency dependent velocity reference gain across a certain bandwidth, the control system becomes causal and produces promising results once the excitation wave stays within the designated narrow-bandwidth. Other methods, such as the Galerkin method (Barcelli & Ringwood 2013), decomposes the irregular excitation wave into a series of frequency components; this allows the impedance matching theory to be implemented on a system that is being excited by polychromatic waves, however this assumes a discrete spectrum. Even with these improvements, there is still the problem that the PTO forces created maybe unacceptably high.

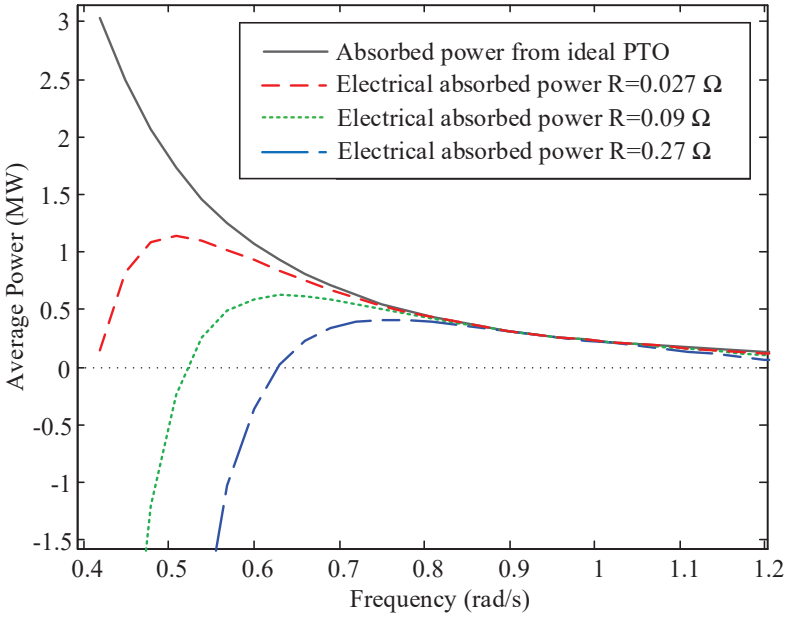

Figure 3.6: Average power extracted from monochromatic waves with amplitude of 1 m using reactive control with an (i)Ideal PTO (ii)LPMG with resistance of 0.027 Ω (iii)LPMG with resistance of 0.09 Ω (iv)LPMG with realistic resistance of 0.27 Ω

When a realistic PTO is included (Polinder et al. 2004), with a resistance of $R = 0.27\ \Omega$, the actual electrical power extracted is substantially reduced. Even using a PTO with an unrealistically low resistance value of $R = 0.027\ \Omega$, the absorbed average power has deteriorated at frequencies other than the natural frequency of the WEC; this however could still be viable, depending on the spectrum of the excitation wave.

If the flux linkage λ_{fd} (2.107) is not large enough, the LPMG will be under-excited in the low velocity regions. This may require the converter voltages $v_q(t)$ and $v_d(t)$ to change sign, resulting in a draw of power from the grid, in order to control the speed of the machine. From these results, it is clearly shown that the classical reactive control technique is not suitable when a non-ideal PTO is used.

3.3 Model Predictive Control (MPC)

3.3.1 Reference Point Tracking MPC

Classical control methods are acceptable for monochromatic waves when the mechanical and electrical constraints of the system are unimportant. However, with modern control techniques, better average power can be found for irregular seas whilst easily incorporating the systems restrictions into the control. Model predictive control (MPC) (Maciejowski 2002) is an ideal candidate for maximising the energy harvest from WECs; it is based on finding optimal control variables that minimises a discretised cost function that is dependent on the future states of the system.

Standard reference point tracking MPC is the most popular form of MPC (Camacho & Alba 2013), where the concept is shown in Fig. 3.7. This method involves having future set points $s(k+i)$, which in this case is a constant value across the prediction horizon N_p (Fig. 3.7). The predicted outputs $\hat{y}(k+i|k)$ of the system (3.5) are required to reach the controller set point $s(k+i)$ after a stated time period; in this case it is T_{set}.

$$\begin{aligned} \hat{x}(k+i+1|k) &= A\hat{x}(k+i|k) + B\hat{u}(k+i|k) \\ \hat{y}(k+i|k) &= C\hat{x}(k+i|k) + D\hat{u}(k+i|k), \end{aligned} \tag{3.5}$$

where

$$\hat{u}(k+i|k) = \begin{cases} \hat{u}(k+i|k), & \text{if } i < N_c + 1 \\ \hat{u}(k+N_c|k), & \text{if } i > N_c, \end{cases}$$

where $i \in \{0, 1, \ldots, N_p\}$, N_p is the prediction horizon and N_c is the control horizon, where $N_c <= N_p$.

To reach this set point value at time T_{set}, reference trajectory points $r(k+i)$ are incorporated which are user specified. Utilising the reference trajectory points across the prediction horizon N_p, the future control variables $\hat{u}(k+i|k)$ can be found by solving a least squares minimisation problem (3.6); essentially minimising the error between

the reference trajectory points $r(k+i|k)$ and the N_p $\hat{u}(k+i|k)$ dependent predicted outputs $\hat{y}(k+i|k)$ across the prediction horizon (Fig. 3.7).

$$\min_{\hat{u}(k|k),\ldots,\hat{u}(k+N_c-1|k)} \left\{ \sum_{i=1}^{N_p} \|\hat{y}(k+i|k) - r(k+i|k)\|^2 \right\} \tag{3.6}$$

where N_p is the prediction horizon, N_c is the control horizon and $1 \leq N_c \leq N_p$.

After solving for the control variables $\hat{u}(k+i|k)$ by minimising (3.6), it is only the first value $\hat{u}(k|k)$ that is implemented on the system. The process is then repeated at the next time step. The prediction horizon N_p and control horizon N_c stay the same length at each optimisation time step, hence given the name *receding horizon*. It is common to choose a control horizon N_c that is much shorter than the prediction horizon; this reduces aggressive control action and increases system stability.

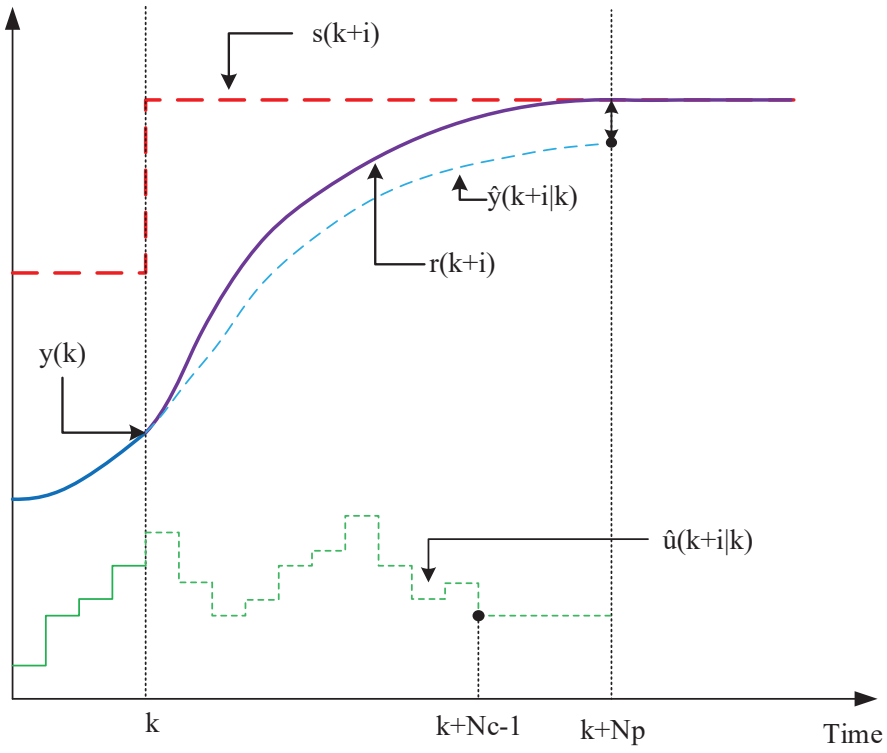

Figure 3.7: Fundamental concept of a reference point tracking MPC with $i \in \{0, 1, \ldots, N_p\}$, N_p is the prediction horizon, N_c is the control horizon

3.3.2 Economic MPC

Similar to the reference point tracking MPC, the economic MPC (O'Sullivan & Lightbody 2017) produces future optimal control variables $\hat{u}(k+i|k)$ by minimising a specific discretised cost function. However, there are differences between the objectives of the two MPC methods. For the reference point tracking MPC, the objective is to minimise the error between the output of the system and its corresponding reference trajectory. The economic MPC cost function is based on an actual economic cost function, where the objective is to minimise the cost function to produce the minimum outcome and not follow a certain output reference point. Therefore the economic MPC does not have a predeclared reference trajectory to track.

In this chapter, an economic MPC is used to maximise the average power absorption from a WEC over the prediction horizon, where the optimal control variables found by minimising the cost function are the PTO forces $\hat{F}_{PTO}(k+i|k)$ to be produced by the LPMG. Using a reference tracking point MPC, subsection 3.3.1, the control horizon N_c would have to be much less than the prediction horizon N_p to allow a stable system. However, with an economic MPC being used in an ocean wave energy application, the cost function is used to approximate the power over the prediction horizon. At each discrete step across the prediction horizon, there is a corresponding $\hat{F}_{PTO}(k+i|k)$ value that collectively causes a power maximisation. Therefore, choosing a shorter control horizon N_c will cause ill-defined average power approximation. The control horizon N_c is the same length as the prediction horizon N_p throughout this chapter.

3.4 Mechanical Power Maximisation - MPC

The control scheme for the MPC used in this work is shown in Fig. 3.8. The MPC requires measurements of the hydrodynamic system states and the predicted excitation force over the finite prediction horizon. In this work it is assumed that these are available (O'Sullivan & Lightbody 2015). The MPC finds the minimum of a cost function which corresponds to finding the optimum PTO forces that produce maximum mechanical power. The MPC then sends the optimal PTO force in the form of a q-axis current set point to the faster inner current control loop of the cascade control, which controls the force produced from the LPMG. Initially it is assumed that there is no field weakening (Rahman et al. 1997), and hence the d-axis current, $i_d(t)$, is regulated at 0 A. As previously stated, with conventional MPC, the optimum inputs are found when the system cost function is minimised; this cost function is usually the sum of

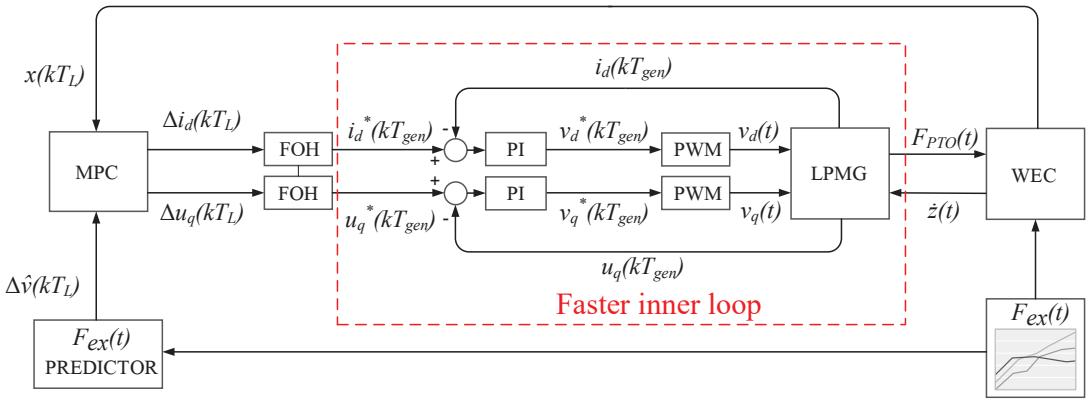

Figure 3.8: Cascade control scheme: Faster loop controlling the LPMG dynamics and the slower outer loop controlling the mechanical dynamics of the system via MPC

the squared error between the desired set point trajectory and the output of the system. For this system however, a reference trajectory is not available and the objective is to maximise the average power function as shown in (3.7).

$$P_{avg} = -\frac{1}{T}\int_{t=0}^{T} F_{PTO}(t)\dot{z}(t)dt \tag{3.7}$$

Ideally, the discrete cost function used in the MPC would be an accurate approximation of the average power (3.7). The accuracy of this approximation will depend on the type of hold assumed for the PTO force. If a ZOH is assumed, then the PTO force is piecewise constant over the sample time T_L, as shown in Fig. 3.9. A suitable approximation here is a Eulers/trapezoidal hybrid, which incorporates the piecewise constant PTO force and a piecewise linear approximation for the velocity over the sample time T_L.

To increase the accuracy of the power extraction, a FOH MPC was employed (Cretel et al. 2011). The FOH allows the PTO force to be represented as a piecewise linear motion instead of a piecewise constant, as shown in Fig. 3.9. Since the FOH PTO force is piecewise linear, it allows a traditional trapezoidal rule to be implemented.

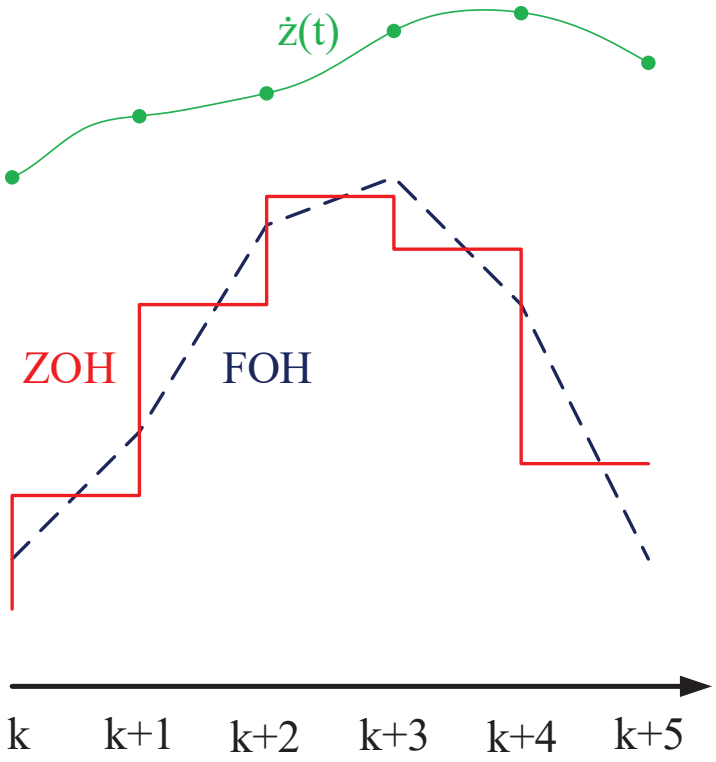

Figure 3.9: Waveforms of (i) continuous WEC $\dot{z}(t)$ with sample points (ii) Piecewise constant PTO force from a ZOH controller (iii) Piecewise linear PTO force from a FOH controller

3.4.1 Zero Order Hold MPC

The average power shown in (3.7) can approximated by the discrete formulation (3.8), where the PTO force is a piecewise constant signal,

$$\begin{aligned} P_{avg}(t) &= -\frac{1}{N_p T_L} \int_{t=0}^{N_p T_L} F_{PTO}(t)\dot{z}(t)dt \\ &= -\frac{1}{N_p T_L} \int_{t=0}^{N_p T_L} (M + m_\mu)\, u_d(t)\dot{z}(t)dt \\ \approx P_z(k) &= -\frac{(M + m_\mu)}{N_p} \sum_{i=1}^{N_p} u_d(k+i-1) \left[\frac{\dot{z}(k+i) + \dot{z}(k+i-1)}{2} \right]. \end{aligned} \tag{3.8}$$

Simplifying the estimation (3.8), the following discrete-time cost function (3.9) is formed, which is then minimised over the prediction horizon N_p to obtain the opti-

mal $u_d(k)$ value that produces the maximum amount of absorbed mechanical power,

$$J_z(k) = \sum_{i=1}^{N_p} u_d(k+i-1)\left[\dot{z}(k+i) - \frac{\Delta\dot{z}(k+i)}{2}\right]. \tag{3.9}$$

The system model (2.11) was converted from the continuous to the discrete domain, producing (3.10),

$$\begin{aligned} \boldsymbol{x}(k+1) &= A_d\boldsymbol{x}(k) + B_d u_d(k) + F_d v_d(k) \\ \boldsymbol{y_d}(k) &= C_d\boldsymbol{x}(k) \end{aligned} \tag{3.10}$$

$$\begin{aligned} A_d &= e^{\boldsymbol{A_c}T_L} \in \mathbb{R}^{(n+2)\times(n+2)} \\ B_d &= \int_{\eta=0}^{T_L} e^{\boldsymbol{A_c}\eta} B_c d\eta \in \mathbb{R}^{(n+2)\times 1} \\ F_d &= \int_{\eta=0}^{T_L} e^{\boldsymbol{A_c}\eta} F_c d\eta \in \mathbb{R}^{(n+2)\times 1} \\ C_d &= \begin{bmatrix} 1 & 0 & 0\cdots 0 \\ 0 & 1 & 0\cdots 0 \end{bmatrix} \in \mathbb{R}^{2\times(n+2)} \end{aligned}$$

where A_c, B_c and C_c are the matrices of the continuous system (2.28) and T_L is the outer mechanical sampling time. Integral action can then be incorporated by augmenting the model to form the augmented version as shown in equation (3.12).

$$\Delta u_z(k) = u_d(k) - u_d(k-1) \tag{3.11}$$

$$\begin{aligned} \boldsymbol{x_z}(k+1) &= A_z\boldsymbol{x_z}(k) + B_z\Delta u_z(k) + F_z\Delta v_z(k) \\ \boldsymbol{y_z}(k) &= C_z\boldsymbol{x_z}(k) \end{aligned} \tag{3.12}$$

$$A_z = \left[\begin{array}{c|ccc} A_d & B_d & F_d & \mathbf{0} \\ \hline \mathbf{0} & 1 & 0 & 0 \\ \mathbf{0} & 0 & 1 & 0 \\ \Upsilon\left(A_d - I\right) & 0 & 0 & 0 \end{array}\right] \in \mathbb{R}^{(n+5)\times(n+5)}$$

$$B_z = \left[\begin{array}{c} B_d \\ \hline 1 \\ 0 \\ \Upsilon B_d \end{array}\right] \quad F_z = \left[\begin{array}{c} F_d \\ \hline 0 \\ 1 \\ \Upsilon F_d \end{array}\right] \in \mathbb{R}^{(n+5)\times 1}$$

$$C_z = \left[\begin{array}{c|ccc} C_d & \mathbf{0} & \mathbf{0} & \mathbf{0} \\ \hline \mathbf{0} & 1 & 0 & 0 \\ \mathbf{0} & 0 & 0 & 1 \end{array}\right] \in \mathbb{R}^{4\times(n+5)}$$

$$\boldsymbol{x_z}(k) = \left[\begin{array}{c} \boldsymbol{x}(k) \\ \hline u_d(k-1) \\ v_d(k-1) \\ \Delta\dot{z}(k) \end{array}\right] \boldsymbol{y_z}(k) = \left[\begin{array}{c} z(k) \\ \dot{z}(k) \\ \hline u_d(k-1) \\ \Delta\dot{z}(k) \end{array}\right]$$

where

$$\Upsilon = \left[\begin{array}{ccccc} 0 & 1 & 0 & \cdots & 0 \end{array}\right] \in \mathbb{R}^{1\times(n+5)}$$

3.4.2 First Order Hold MPC

Using a FOH, the continuous average power (3.7) can be estimated using a standard trapezoidal rule (3.13), since the PTO force is piecewise linear,

$$\begin{aligned} P_{avg}(t) &= -\frac{1}{N_p T_L} \int_{t=0}^{N_p T_L} F_{PTO}(t)\dot{z}(t)dt \\ &= -\frac{1}{N_p T_L} \int_{t=0}^{N_p T_L} \left(M + m_\mu\right) u_q(t)\dot{z}(t)dt \\ &\approx P_f(k) = -\frac{\left(M + m_\mu\right)}{N_p}\left(\frac{1}{2}\left(u_q(k)\dot{z}(k) + u_q(k+N_p)\dot{z}(k+N_p)\right)\right) \\ &\qquad + \frac{\left(M + m_\mu\right)}{N_p} \sum_{i=1}^{N_p-1} u_q(k+i)\dot{z}(k+i). \end{aligned} \tag{3.13}$$

Due to the nature of the FOH, $u_q(k)$ has already been assigned from the previous control sample. The trapezoidal estimation can then be reduced to produce the cost function (3.14), which is minimised over the prediction horizon N_p to produce the

optimum PTO force that will cause maximum average power absorption.

$$J_f(k) = \frac{1}{2}u_q(k+N_p)\dot{z}(k+N_p) + \sum_{i=1}^{N_p-1} u_q(k+i)\dot{z}(k+i) \tag{3.14}$$

The structure of the system with the FOH is similar to the ZOH method except that the inputs of the system are shifted into the future by one sample (Cretel et al. 2011).

$$\begin{aligned} \boldsymbol{x_f}(k+1) &= A_f\boldsymbol{x_f}(k) + B_f\Delta u_q(k+1) + F_f\Delta v_f(k+1) \\ \boldsymbol{y_f}(k) &= C_f\boldsymbol{x_f}(k) \end{aligned} \tag{3.15}$$

$$\boldsymbol{x_f}(k) = \begin{bmatrix} \boldsymbol{x}(k) \\ u_d(k) \\ v_d(k) \end{bmatrix} \boldsymbol{y_f}(k) = \begin{bmatrix} z(k) \\ \dot{z}(k) \\ u_d(k) \end{bmatrix}$$

$$A_f = \begin{bmatrix} e^{A_cT_L} & \Lambda & \Lambda \\ \mathbf{0} & 1 & 0 \\ \mathbf{0} & 0 & 1 \end{bmatrix} \in \mathbb{R}^{(n+4)\times(n+4)}$$

$$B_f = \begin{bmatrix} \Gamma \\ 0 \\ 1 \end{bmatrix} B_f = \begin{bmatrix} \Gamma \\ 1 \\ 0 \end{bmatrix} \in \mathbb{R}^{(n+4)\times 1}$$

where $\Lambda = A_c^{-1}\left(e^{A_cT_L} - I\right)B_c \in \mathbb{R}^{(n+2)\times 1}$ and $\Gamma = \frac{1}{T_L}A_c^{-1}\left(\Lambda - T_LB_c\right) \in \mathbb{R}^{(n+2)\times 1}$

3.4.3 System Prediction

For the minimisation of the cost functions (3.9) and (3.14) to occur, the velocity predictions, $\dot{z}(k+i)$ where $i \in \{1 \dots N_p\}$, must be found in terms of the predicted scaled PTO force increments $\boldsymbol{\Delta\hat{u}}(k)$ over the horizon. The output vector of the system $\boldsymbol{\hat{y}}(k)$, can be predicted over the N_p step prediction horizon using (3.16). It is assumed that the future scaled excitation wave force increments $\boldsymbol{\Delta\hat{v}}(k)$ are known over the prediction horizon,

$$\boldsymbol{\hat{y}}(k) = P\boldsymbol{x}(k) + Ha\boldsymbol{\Delta\hat{u}}(k) + Hw\boldsymbol{\Delta\hat{v}}(k), \tag{3.16}$$

where,

$$P = \begin{bmatrix} CA \\ CA^2 \\ : \\ CA^N \end{bmatrix} Ha = \begin{bmatrix} CB & 0 & .. & 0 \\ CAB & CB & .. & 0 \\ : & : & \ddots & : \\ CA^{N-1}B & CA^{N-2}B & .. & CB \end{bmatrix} \tag{3.17}$$

$$Hw = \begin{bmatrix} CF & 0 & .. & 0 \\ CAF & CF & .. & 0 \\ : & : & \ddots & : \\ CA^{N-1}F & CA^{N-2}F & .. & CF \end{bmatrix} \tag{3.18}$$

$$\hat{\boldsymbol{u}}_{\boldsymbol{z}}(k) = \begin{bmatrix} u_z(k|k-1) \\ : \\ : \\ u_z(k+N_p-1|k-1) \end{bmatrix} \hat{\boldsymbol{v}}_{\boldsymbol{z}}(k) = \begin{bmatrix} v_z(k|k-1) \\ : \\ : \\ v_z(k+N_p-1|k-1) \end{bmatrix} \in \mathbb{R}^{N_p \times 1}$$

$$\hat{\boldsymbol{y}}_{\boldsymbol{z}}(k) = \begin{bmatrix} y_z(k+1|k-1) \\ : \\ : \\ y_z(k+N_p|k-1) \end{bmatrix}$$

when a ZOH is used $P \in \mathbb{R}^{4N_p \times (n+4)}$, $H_a \in \mathbb{R}^{4N_p \times N_p}$, $H_w \in \mathbb{R}^{4N_p \times N_p}$,$\hat{\boldsymbol{y}}_{\boldsymbol{z}}(k) \in \mathbb{R}^{4N_p \times 1}$. When a FOH is used $P \in \mathbb{R}^{3N_p \times (n+4)}$, $H_a \in \mathbb{R}^{3N_p \times N_p}$, $H_w \in \mathbb{R}^{3N_p \times N_p}$,$\hat{\boldsymbol{y}}_{\boldsymbol{f}}(k) \in \mathbb{R}^{3N_p \times 1}$,

$$\hat{\boldsymbol{u}}_{\boldsymbol{q}}(k) = \begin{bmatrix} u_q(k+1|k) \\ : \\ : \\ u_q(k+N_p|k) \end{bmatrix} \hat{\boldsymbol{v}}_{\boldsymbol{f}}(k) = \begin{bmatrix} v_f(k+1|k) \\ : \\ : \\ v_f(k+N_p|k) \end{bmatrix} \in \mathbb{R}^{N_p \times 1}$$

$$\hat{\boldsymbol{y}}_{\boldsymbol{f}}(k) = \begin{bmatrix} y_f(k+1|k) \\ : \\ : \\ y_f(k+N_p|k) \end{bmatrix}.$$

By using the predicted outputs (3.16), the cost function of (3.14) can then be represented in matrix form as (3.19),

$$J(k) = \frac{1}{2}\hat{\boldsymbol{y}}(k)^T Q \hat{\boldsymbol{y}}(k), \tag{3.19}$$

where $Q_z \in \mathbb{R}^{4N_p \times 4N_p}$ (3.20) when using a ZOH and $Q_f \in \mathbb{R}^{3N_p \times 3N_p}$ (3.21) when using a FOH.

$$Q_z = \begin{bmatrix} M_z & 0 & .. & 0 \\ 0 & M_z & .. & 0 \\ : & : & \ddots & : \\ 0 & 0 & 0 & M_z \end{bmatrix} M_z = \begin{bmatrix} 0 & 0 & 0 & 0 \\ 0 & 0 & 1 & 0 \\ 0 & 1 & 0 & \frac{-1}{2} \\ 0 & 0 & \frac{-1}{2} & 0 \end{bmatrix} \tag{3.20}$$

$$Q_f = \begin{bmatrix} M_f & 0 & .. & 0 \\ 0 & M_f & .. & 0 \\ : & : & \ddots & : \\ 0 & 0 & 0 & \frac{M_f}{2} \end{bmatrix} M_f = \begin{bmatrix} 0 & 0 & 0 \\ 0 & 0 & 1 \\ 0 & 1 & 0 \end{bmatrix}. \tag{3.21}$$

Expansion of (3.19) yields,

$$\begin{aligned} J = \frac{1}{2}\boldsymbol{\Delta\hat{u}}^T H_a^T Q H_a \boldsymbol{\Delta\hat{u}} + \boldsymbol{\Delta\hat{u}}^T H_a^T Q \left(P\boldsymbol{x} + H_w \boldsymbol{\Delta\hat{v}}\right) \\ + \frac{1}{2}\left(P\boldsymbol{x} + H_w \boldsymbol{\Delta\hat{v}}\right)^T Q \left(P\boldsymbol{x} + H_w \boldsymbol{\Delta\hat{v}}\right). \end{aligned} \tag{3.22}$$

It can be shown from (3.22) that the constant term can be neglected since it is independent of the control increments $\boldsymbol{\Delta\hat{u}}(k)$, as shown in (3.23).

$$J_1 = \frac{1}{2}\boldsymbol{\Delta\hat{u}}^T H_a^T Q H_a \boldsymbol{\Delta\hat{u}} + \boldsymbol{\Delta\hat{u}}^T H_a^T Q \left(P\boldsymbol{x} + H_w \boldsymbol{\Delta\hat{v}}\right) \tag{3.23}$$

The Hessian matrices of both ZOH and FOH costs have different dimensions to each other due to the size of the state matrices of both systems. The FOH cost function is similar to (3.19) except that the computation order is smaller than that of the ZOH system due to having one less state in its state matrix. Quadratic programming (QP) methods available in software such as MATLAB (R2016a) (Matlab 2010) or AMPL (Version 1) (Hürlimann 1993) can be used to minimise such cost functions within a receding horizon scheme, subject to constraints. From this minimisation, the optimal $\boldsymbol{\Delta\hat{u}}(k)$ is obtained, the first variable of $\boldsymbol{\Delta\hat{u}}(k)$ is then implemented on the system and the process is repeated at the next outer sample T_L.

3.4.4 Mechanical Power Maximisation Results

Initially the mechanical power cost function (3.23) was utilised. As the prediction horizon N_p increases the mechanical power absorbed approaches the ideal maximum, as shown in Fig. 3.10. However it is also shown in Fig. 3.10 that for a shorter prediction horizon N_p, the electrical extracted power is actually better than the electrical power obtained via a longer horizon. As the mechanical power absorbed converges towards the ideal maximum, excessive PTO forces are required and hence the current $i_q(t)$ must be large (assuming that $i_d(t) = 0$), and electrical losses increase.

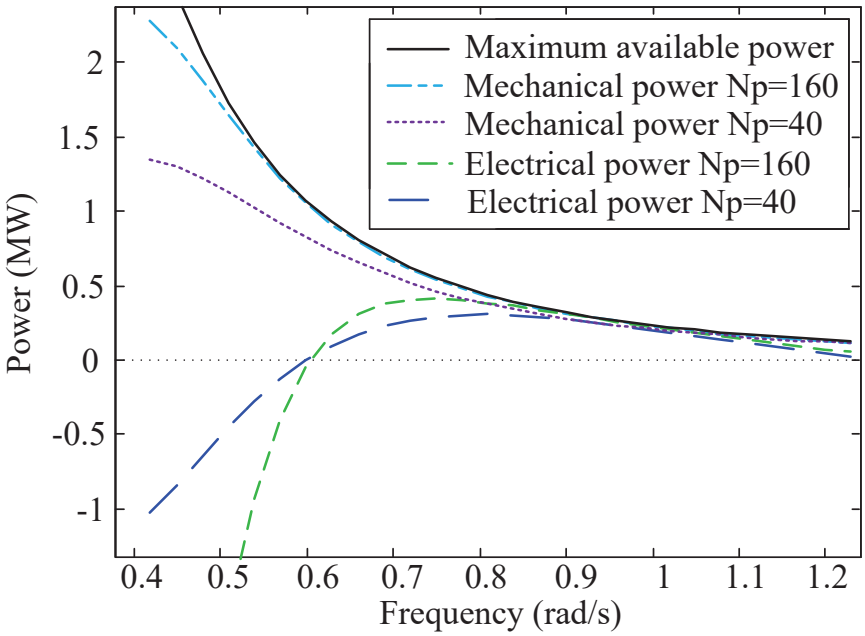

Figure 3.10: Average power extracted from monochromatic waves (i)Ideal reactive control (maximum available power) (ii)Mechanical (lossless) power absorbed using MPC with a ZOH and N_p=160(16 s) (iii)Mechanical (lossless) power absorbed using MPC with a ZOH and N_p=40(4 s) (iv)Electrical power absorbed (with losses $R = 0.27\ \Omega$) using MPC with a ZOH and N_p=160(16 s) (v)Electrical power absorbed (with losses $R = 0.27\ \Omega$) using MPC with a ZOH and N_p=40(4 s)

As shown from Fig. 3.10, the average electrical power at lower frequencies improves as the horizon is reduced. Even though this is an improvement to reactive control results, it is still unacceptable as a solution because it runs the risk of an unstable system if the prediction horizon is over reduced. Therefore, it is imperative that the losses from the LPMG are included within the optimisation.

3.5 Electrical Power Maximisation - MPC

The control scheme for this MPC is the same as the scheme used for the mechanical average power optimisation, Fig. 3.8, where it is assumed that a perfect excitation wave prediction is available and there is no field weakening used. For the average electrical power to be maximised, the losses of the LPMG must be included in the original mechanical average power equation (3.7) (O'Sullivan & Lightbody 2015).

3.5.1 The Cost Function

The purpose of the MPC presented here is to maximise the average electrical power absorbed from the combined WEC and LPMG system. For the system to be optimised for this objective, the average electrical power absorbed in the continuous domain can be expressed as (3.24),

$$P_e = -\frac{1}{T}\int_{t=0}^{T}\left(F_{PTO}(t)\dot{z}(t) + Ri_q^2(t)\right)dt \tag{3.24}$$

Here $-F_{PTO}(t)\dot{z}(t)$ is the instantaneous mechanical power and $-Ri_q^2(t)$ is the resistive losses of the LPMG. Substituting (2.110) and (2.111) into (3.24) yields,

$$\begin{aligned} -P_e(t) &= \frac{1}{T}\int_{t=0}^{T}\left(\left(M+m_\mu\right)u_q(t)\dot{z}(t) + \frac{R}{\psi^2}u_q^2(t)\right)dt \\ &= \frac{1}{N_pT_L}\int_{t=0}^{N_pT_L}\left(\left(M+m_\mu\right)u_q(t)\dot{z}(t) + \frac{R}{\psi^2}u_q^2(t)\right)dt \end{aligned} \tag{3.25}$$

$$\begin{aligned} -P_e(k) = \frac{\left(M+m_\mu\right)}{N_p}&\left(\frac{1}{2}\left(u_q(k)\dot{z}(k) + u_q(k+N_p)\dot{z}(k+N_p)\right)\right) \\ &+ \frac{\left(M+m_\mu\right)}{N_p}\sum_{i=1}^{N_p-1}u_q(k+i)\dot{z}(k+i) \\ &+ \frac{R}{\psi^2N_p}\left(\frac{1}{2}\left(u_q^2(k) + u_q^2(k+N_p)\right) + \sum_{i=1}^{N_p-1}u_q^2(k+i)\right) \end{aligned} \tag{3.26}$$

As described in section 3.4, a cascade control system was utilised here, in which the inner current controllers are designed as a high bandwidth system, with a small sample time $T_{gen} = 1$ ms. The outer power maximisation loop is slower, with a longer sample

time $T_L = 0.1$ s that allows a first order hold to be utilised, which effectively then provides a ramp trajectory for the current references $i_d^*(T_L + (k+j)T_{gen})$ and $i_q^*(T_L + (k+j)T_{gen})$, when sampled at the faster inner-loop sampling period T_{gen}. Similar to (3.13), with $u_q(k)$ and $\dot{z}(k)$ both piecewise linear between the outer samples, a trapezoidal approximation can be used to estimate the average electrical power integral (3.25), as shown in (3.27),

$$\begin{aligned} -P_e(k) = \frac{(M+m_\mu)}{N_p}\left(\frac{1}{2}\left(u_q(k)\dot{z}(k) + u_q(k+N_p)\dot{z}(k+N_p)\right)\right) \\ + \frac{(M+m_\mu)}{N_p}\sum_{i=1}^{N_p-1} u_q(k+i)\dot{z}(k+i) \\ + \frac{R}{\psi^2 N_p}\left(\frac{1}{2}\left(u_q^2(k) + u_q^2(k+N_p)\right) + \sum_{i=1}^{N_p-1} u_q^2(k+i)\right). \end{aligned} \tag{3.27}$$

Using (3.27) the discrete cost $J(k)$, (3.28), is formed,

$$\begin{aligned} J(k) = \frac{1}{2}u_q(k+N_p)\dot{z}(k+N_p) + \sum_{i=1}^{N_p} u_q(k+i)\dot{z}(k+i) \\ + \frac{R(M+m_\mu)}{(\lambda'_{fd}\frac{\pi}{\tau})^2}\left(\frac{1}{2}u_q^2(k+N_p) + \sum_{i=1}^{N_p} u_q^2(k+i)\right). \end{aligned} \tag{3.28}$$

Since there are no changes to the mechanical system, the same output array (3.16) can be used. With this output array, the cost function (3.28) can then be represented in matrix form (3.19). When using a ZOH, $Q_z \in \mathbb{R}^{4N_p \times 4N_p}$ and $M_z \in \mathbb{R}^{4\times 4}$

$$Q_z = \begin{bmatrix} M_z & 0 & .. & 0 \\ 0 & M_z & .. & 0 \\ : & : & \ddots & : \\ 0 & 0 & 0 & M_z \end{bmatrix} \quad M_z = \begin{bmatrix} 0 & 0 & 0 & 0 \\ 0 & 0 & 1 & 0 \\ 0 & 1 & 2G & \frac{1}{2} \\ 0 & 0 & -\frac{1}{2} & 0 \end{bmatrix}.$$

When using a FOH, $Q_f \in \mathbb{R}^{3N_p \times 3N_p}$ and $M_f \in \mathbb{R}^{3\times 3}$,

$$Q_f = \begin{bmatrix} M_f & 0 & .. & 0 \\ 0 & M_f & .. & 0 \\ : & : & \ddots & : \\ 0 & 0 & 0 & \frac{1}{2}M_f \end{bmatrix} M_f = \begin{bmatrix} 0 & 0 & 0 \\ 0 & 0 & 1 \\ 0 & 1 & 2G \end{bmatrix}$$

and

$$G = \frac{R(M + m_\mu)}{(\lambda'_{fd\frac{\pi}{\tau}})^2}.$$

3.5.2 Electrical Average Power Results

A prediction horizon of $N_p = 160$ with an outer sample time $T_L = 0.1$ s produced a horizon of 16 s, which was sufficient for the selected bandwidth; this was compared with a shorter prediction horizon of $N_p = 40$. Regular monochromatic waves with an amplitude of 1 m and irregular waves with a range of significant heights and peak spectrum periods were used to analyse the performance of the control system, where a Bretschneider spectrum was assumed for the irregular waves. The results for the average electrical power optimisation are shown in Fig. 3.11 and Fig. 3.12. From these results, it is shown that by including the resistive losses within the cost function, the overall electrical power is much improved when compared to the results using reactive control (Fig. 3.6, page 83). For irregular waves, the ratio of the average powers produced from both horizons ($P_{avg,N_p=160}/P_{avg,N_p=40}$) is shown in Fig. 3.12. It is shown that across the multiple sea states, there is little difference between the outcomes of the two horizons. For monochromatic waves, the $N_p = 40$ prediction horizon produces the equivalent average electrical power, with less computational power needed; therefore, a prediction horizon of $N_p = 40$ is suitable for the electrical power optimisation.

3.5.3 Power Quality

Up to this point in the chapter section, all the MPC results shown have been from an MPC system based on the ZOH method (section 3.5.2). The inner electrical controllers of the LPMG utilise a much faster sampling time than the outer mechanical loop of the system (Fig. 3.8). This allows for the programming of the current setpoints with faster sampling to be piecewise linear over the long outer sampling time. The difference between the average power absorbed from a MPC using a ZOH and a FOH is actually

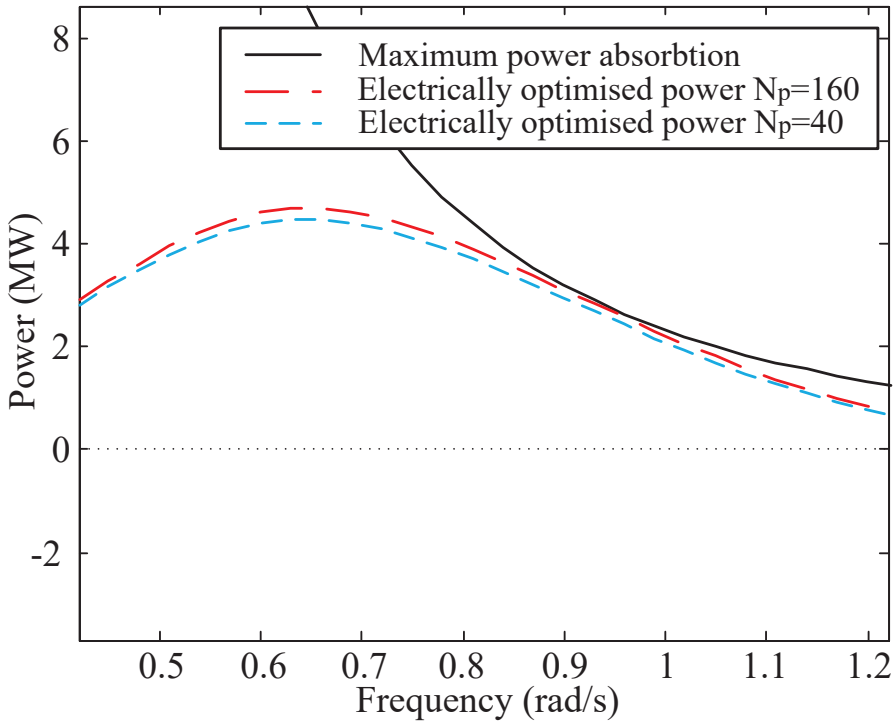

Figure 3.11: Average power extracted from monochromatic waves with R=0.27 Ω (i)Ideal power using reactive control (ii) Electrical power optimisation MPC with N_p=160 (iii) Electrical power optimisation MPC with N_p=40

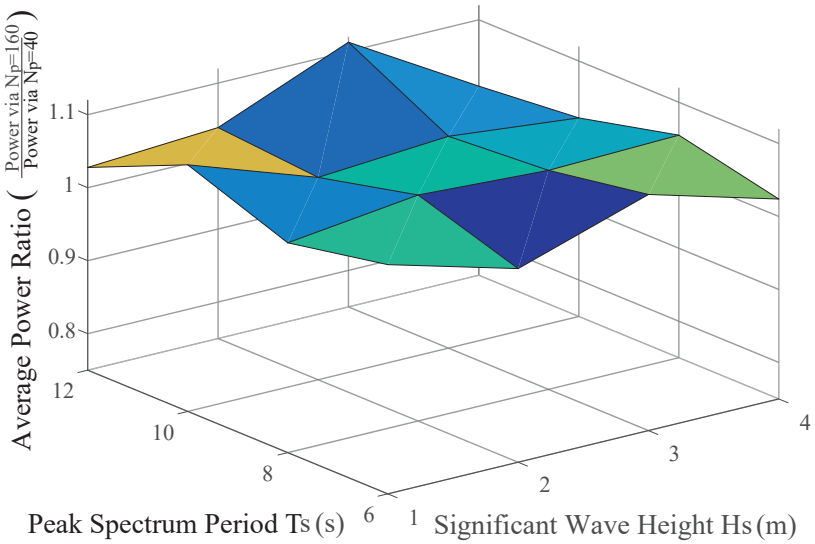

Figure 3.12: Ratio of the average powers extracted using N_p= 160 to the average power extracted with N_p= 40 across a range of irregular waves with different significant heights and peak spectrum periods using a Bretschneider spectrum

negligible, since the ZOH method is an adequate estimation. However when the instantaneous power produced by both the ZOH and FOH MPC systems are compared, the difference is clear. Using both FOH and ZOH outer controller reference points, Fig. 3.13, the currents produced from the faster inner current controlled LPMG are

compared. It is shown that when using a ZOH outer control signal Fig. 3.13.(a), the inner current control loop over shoots the reference point. Furthermore, when using a FOH outer control signal, the inner current controller has negligible current overshoot and there is near perfect current tracking.

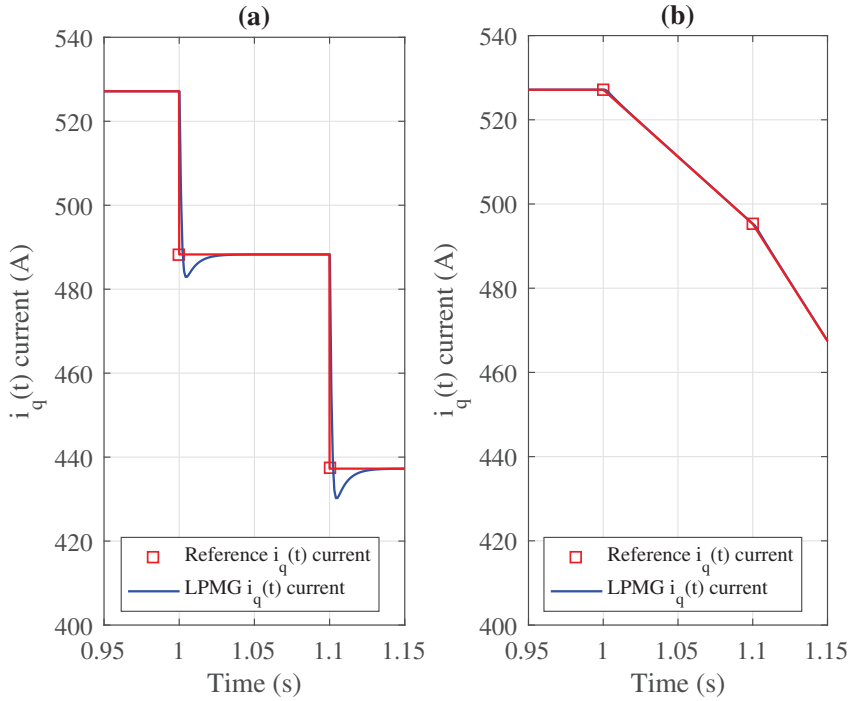

Figure 3.13: Examples of q-axis current reference signals and q-axis current produced from the LPMG when utilising a (i)ZOH MPC (ii)FOH MPC

However, with the ZOH, the converter voltages that are used to control the $i_q(t)$ current are corrupted with high frequency transients when the machine is moving with a high velocity. The converter voltages for the FOH based system look like a filtered version of the ZOH converter voltages, as can be seen in Fig. 3.14. Over an average time period this would not be a problem, however this would lead to poor instantaneous power quality, unnecessary high harmonics on the grid and unavoidable instantaneous overvoltages which could lead to permanent damage to the LPMG, the machine side converter and the grid side converter.

The simulated waveform shown in Fig. 3.15 displays the instantaneous powers from the ZOH and the FOH systems extracted from an irregular excitation wave with Bretsc-hneider Spectrum with a significant height $H_s = 3$ m and a peak wave period $T_p = 6.98$ s (Bretschneider 1959). The combination of the voltage spikes in the ZOH converter voltage and the overshoots in the current transients produce high frequency transients in the instantaneous power.

The current setpoints for the LPMG for a FOH system are effectively linearly inter-

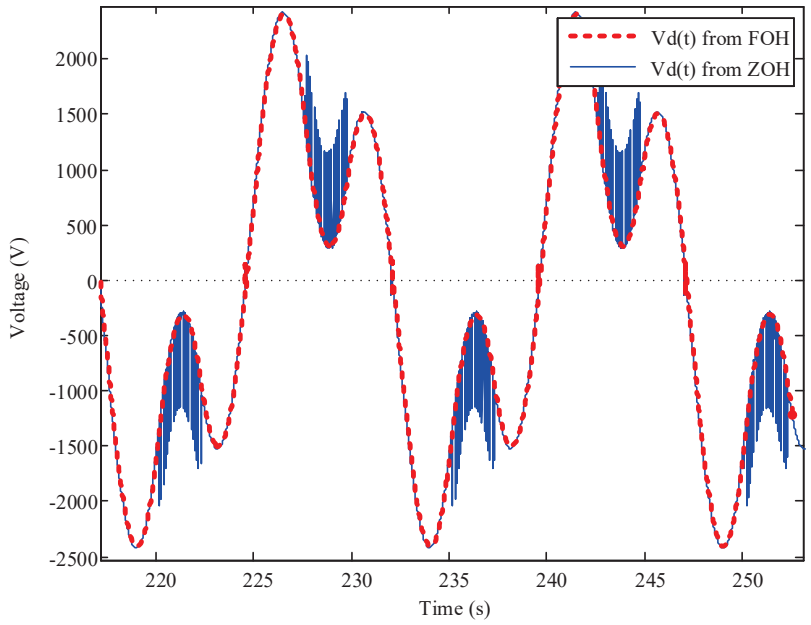

Figure 3.14: q-axis voltage produced from the voltage source converter produced from monochromatic waves at 0.418 rad.s^{-1} (i)FOH MPC (ii)ZOH MPC

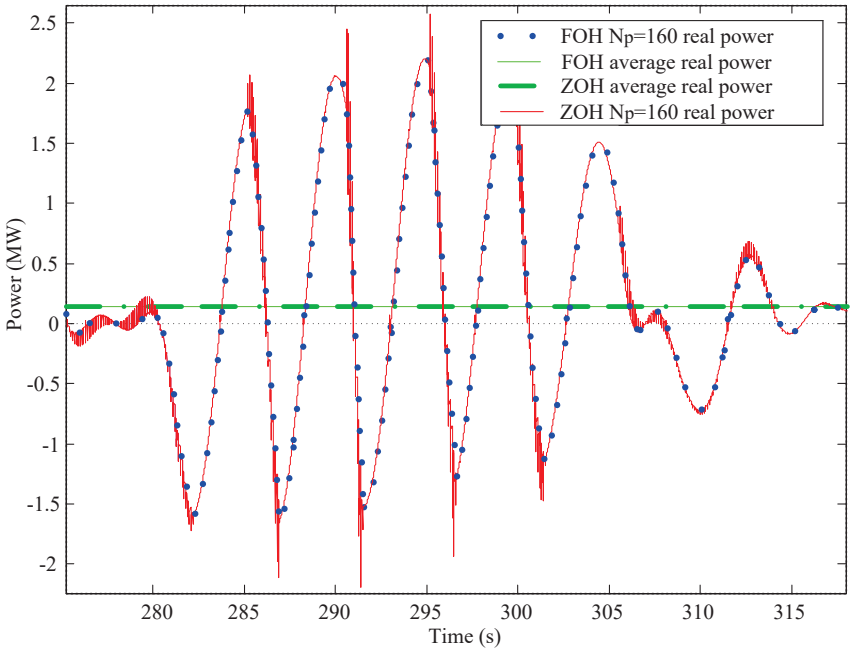

Figure 3.15: Instantaneous electrical power with R=0.27 Ω from a Bretscheinder spectrum for constrained current and heave motion, using (i) FOH MPC N_p=160 (16 s) (ii) FOH average power (iii) ZOH average power (iv) ZOH MPC N_p=160(16 s)

polated over the outer sampling time, unlike the piecewise constant setpoints used by the ZOH outer loop as seen in Fig. 3.9. The sampling time of the LPMG ($T_{gen} = 1 \times 10^{-3}$ s) is much smaller then the outer loop sampling time. This means that the inner control of the LPMG has a reference current which is changing linearly and gradually over the outer sample time. With the ZOH there is a sudden change in the

reference current sent to the inner LPMG loop which is kept constant for the outer sampling time duration. The sharp steps in the current reference cause these overshoots. With the combination of the current waveforms and the voltages that do not contain spikes, the clean instantaneous power waveforms show that a cascade controller with a FOH in the outer slower loop is essential for better power quality.

The quality of the instantaneous power can be examined using a spectrum analyser (Fig. 3.16). With the spectrum analysis it is shown that the power from the FOH system at frequencies higher than the Bretschneider spectrum bandwidth are superior when compared to the powers from the ZOH system. This reduction of noise at higher frequencies could reduce the design complexity of components connected to the grid.

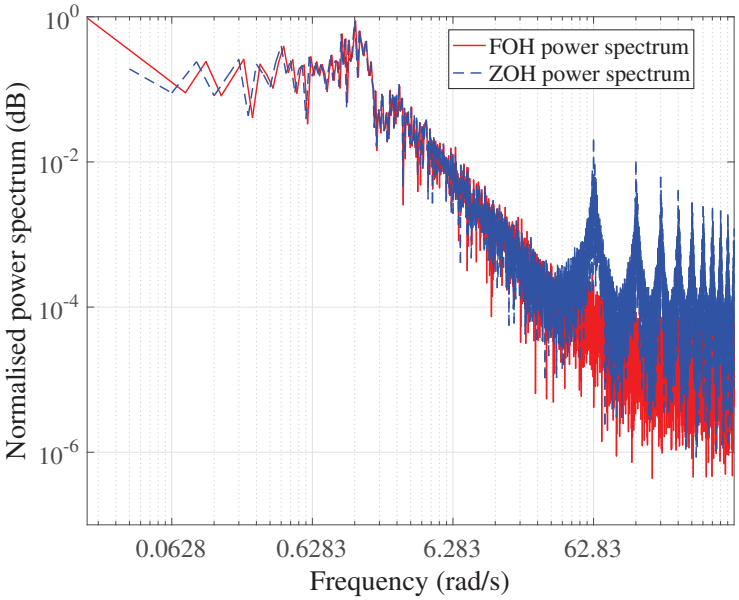

Figure 3.16: Normalised power spectrum of the instantaneous electrical power from a (i) FOH MPC (ii) ZOH MPC which was excited by a Bretschneider spectrum with a significant height $H_s = 3$ m and a peak wave period $T_p = 6.98$ s

3.6 Conclusion

This chapter investigated the optimisation of average electrical power from the LPMG coupled to a point absorber WEC. Optimal mechanical control was implemented in section 3.2.3 using a classical control method called reactive control. Reactive control was shown to produce substantial amounts of extracted mechanical power, but when a realistic PTO was included in the model, the electrical power extracted from the system was dramatically reduced, especially at lower frequencies.

Model Predictive Control (MPC) was introduced in section 3.3 and section 3.4, where the MPC was designed to maximise mechanical average power using either a ZOH or a FOH. It was shown that as the prediction horizon N_p was reduced, the average electrical power increased for lower frequencies but slightly dipped at higher frequencies. It was then concluded that the need to include the resistive losses of the PTO within the optimisation itself was imperative.

In section 3.5, average electrical power optimisation was implemented using MPC by including the resistive losses from the LPMG within the cost function. The system was tested under regular monochromatic and irregular excitation waveforms. The results showed that this average electrical power based MPC produced greater results when compared to the results found using control methods that were optimised for mechanical power.

The usual objective of the wave energy industry has been to maximise the average mechanical PTO power. Whilst in this chapter, one of the objectives was to show the importance of optimising the electrical power from the system, the other objective was to show the importance of the power quality which will be transmitted onto the grid. The results from section 3.5.3 showed that by using a FOH instead of a ZOH in the outer control loop, yields a significant increase in power quality.

References

Antonio, F. de O. (2010), 'Wave energy utilization: A review of the technologies', *Renewable and sustainable energy reviews* **14**(3), 899–918.

Babarit, A., Duclos, G. & A.H. Clément (2004), 'Comparison of latching control strategies for a heaving wave energy device in random sea', *Applied Ocean Research* **26**(5), 227–238.

Babarit, A., Guglielmi, M. & Clément, A. H. (2009), 'Declutching control of a wave energy converter', *Ocean Engineering* **36**(12), 1015–1024.

Barcelli, G. & Ringwood, J. (2013), 'Constrained control of arrays of wave energy devices', *International Journal of Marine Energy* **3**, 53–69.

United States. Beach Erosion Board and Bretschneider, C.L., (1959), *Wave Variability and Wave Spectra for Wind-Generated Gravity Waves*, *in* 'Technical memorandum', The Board.

Budal, K. & Falnes, J. (1977), 'Optimum operation of improved wave-power converter', *Marine Science Communications* **3**, 133–150.

Budal, K. & Falnes, J. (1980), Interacting point absorbers with controlled motion, *in* B. Count, ed., 'Power from Sea Waves', Academic Press, London, pp. 381–399.

Camacho, E. F. & Alba, C. B. (2013), *Model predictive control*, Springer Science & Business Media.

Cretel, J., Lightbody, G., Thomas, G. P. & Lewis, A. W. (2011), 'Maximisation of energy capture by a wave-energy point absorber using model predictive control', *IFAC Proceedings Volumes (IFAC-PapersOnline)* **18**(PART 1), 3714–3721.

Falcão, A.F. de O (2002), 'Control of an oscillating-water-column wave power plant for maximum energy production', *Applied Ocean Research* **24**(2), 73–82.

Falnes, J. (2007), 'A review of wave-energy extraction', *Marine Structures* **20**(4), 185–201.

Falnes, J. & Budal, K. (1978), 'Wave - power conversion by point absorbers', *Norwegian Maritime research* **6**(4), 1–11.

Feng, Z. & Kerrigan, E. C. (2013), Latching control of wave energy converters using derivative-free optimization, *in* 'Decision and Control (CDC), 2013 IEEE 52nd Annual Conference on', IEEE, pp. 7474–7479.

Fusco, F. & Ringwood, J. (2011), 'Suboptimal Causal Reactive Control of Wave Energy Converters Using a Second Order System Model WEC', *Proceedings of the 21st International Offshore and Polar Engineering Conference* pp. 1–8.

Fusco, F. & Ringwood, J. V. (2013), 'A Simple and Effective Real-Time Controller for Wave Energy Converters', *IEEE Transactions on Sustainable Energy* **4**(1), 21–30.

Henriques, J., Lemos, J., Eça, L., Valério, J., Gato, L. & Falcão, A. (2017), 'A Discontinuous Galerkin Method for optimal and sub-optimal control applied to an oscillating water column wave energy converter', *IFAC-PapersOnLine* **50**, 15670—-15677.

Hürlimann, T. (1993), 'AMPL: A mathematical programming language', *OR Spektrum* **15**(1), 43–56.

Maciejowski, J. M. (2002), *Predictive Control: with Constraints*, Pearson Education, Prentice Hall.

Matlab (2010), *Version 7.10.0*, The MathWorks Inc., Natick, Massachusetts.

O'Sullivan, A. C. & Lightbody, G. (2015), 'Wave to Wire Power Maximisation from a Wave Energy Converter', *In Proceedings of the 11th European Wave and Tidal Energy Conference (EWTEC)* pp. 1–9.

O'Sullivan, A. C. & Lightbody, G. (2017), 'Co-design of a wave energy converter using constrained predictive control', *Renewable Energy* **102**, 142–156.

Polinder, H., Damen, M. E. C. & Gardner, F. (2004), 'Linear PM Generator System for Wave Energy Conversion in the AWS', *IEEE Transactions on Energy Conversion* **19**(3), 583–589.

Rahman, M. F., Zhong, L. & Lim, K. W. (1997), A direct torque controlled interior permanent magnet synchronous motor drive incorporating field weakening, *in* 'Industry Applications Conference, 1997. thirty-second IAS Annual Meeting, IAS'97., Conference Record of the 1997 IEEE', Vol. 1, IEEE, pp. 67–74.

Chapter 4

The Effect of Constraints on the Optimisation of Electrical Power from a WEC

4.1 Introduction

In order to absorb maximum average power, be it mechanical or electrical, the WEC must oscillate (O'Sullivan & Lightbody 2015). However, with these substantial oscillations there may be consequences when real life constraints are included. These include both mechanical and electrical constraints which limit the operation region of the WEC system.

The linear sets of constraints in this work include the mechanical limitations of the LPMG (Polinder et al. 2004) and the WEC combined such as the heave displacement, WEC velocity and PTO force. If the system exceeds these mechanical limitations, damages may occur which would lead to operation shutdown. There are also electrical constraints which are non-linear (O'Sullivan & Lightbody 2017). The electrical constraints take into consideration the current limitations of the LPMG when field weakening is included, the voltage limitation of the machine side converter and the power flow restriction of the power flowing onto the grid. When reached, excessive currents can cause insulation breakdown in the LPMGs windings (Elmore 2003). The optimisation must also include the maximum controller voltage level, which restricts the feasible current region particularly for high speed operation (Camm et al. 2009). High power level fluctuations can cause grid instabilities for the grid side converter (Yazdani & Iravani 2010) when connected to a weak grid. By restricting the WEC

system to produce only uni-directional power flow, the chances of grid instabilities are reduced.

In this chapter, the mechanical and electrical constraints that are incorporated within the MPC are described (O'Sullivan & Lightbody 2015, 2016, 2017). For the mechanical restrictions, the linear set of constraints are easily implemented in the MPC optimisation. However, when the electrical restrictions are incorporated, this leads to non-linear constraints in the optimisation which increases the complexity.

4.2 Mechanical Constraints

In chapter 3, the maximum amount of average electrical power was extracted using an unconstrained system. However, it should be considered that most systems contain operation restrictions, which becomes apparent when a constrained MPC approach is required. Here quadratic programming optimisation is used. Without the incorporation of these constraints in the optimisation, mechanical and electrical damage may occur, leading to system shut down. In this section the mechanical restrictions are introduced and are included in the optimisation.

The mechanical constraints of the system would include heave displacement, velocity and the maximum force output. These can be easily included in the optimisation since they are only linear constraints. Optimisers such as QP (`quadprog`) in MATLAB (R2016a) (Matlab 2010) are suitable for such optimisation tasks. However, if non-linear constraints are used, then a more sophisticated optimisation package, such as the interior point algorithm IPOPT (Wächter & Biegler 2006) available in AMPL (Version 1) (Hürlimann 1993), is required.

The constraints for the PTO force, velocity and heave displacement, for each discrete step across the prediction horizon N_p, can be expressed as the linear constraint set,

$$\begin{aligned} F_{min} \leq F_{PTO}(k+i) \leq F_{max} \\ z_{min} \leq z(k+i) \leq z_{max} \qquad \forall i = \{1, \ldots, N_p\}. \\ \dot{z}_{min} \leq \dot{z}(k+i) \leq \dot{z}_{max} \end{aligned} \tag{4.1}$$

Since an incremented prediction model is used in this work, (3.16), this constraint set is expressed in terms of the incremented control $\boldsymbol{\Delta \hat{u}_q}(k)$.

$$\begin{aligned}(u_{min} - u_q(k))\,\boldsymbol{\Theta} &\leq \boldsymbol{\Phi}\boldsymbol{\Delta}\hat{\boldsymbol{u}}_{\boldsymbol{q}}(k)\\ -(u_{max} - u_q(k))\,\boldsymbol{\Theta} &\leq -\boldsymbol{\Phi}\boldsymbol{\Delta}\hat{\boldsymbol{u}}_{\boldsymbol{q}}(k)\end{aligned} \tag{4.2}$$

$$\begin{aligned}WHa\boldsymbol{\Delta}\hat{\boldsymbol{u}}_{\boldsymbol{q}}(k) &\leq -WP\boldsymbol{x}_{\boldsymbol{f}}(k) - WHw\boldsymbol{\Delta}\hat{\boldsymbol{v}}(k) + \boldsymbol{\Theta}z_{max}\\ -WHa\boldsymbol{\Delta}\hat{\boldsymbol{u}}_{\boldsymbol{q}}(k) &\leq +WP\boldsymbol{x}_{\boldsymbol{f}}(k) + WHw\boldsymbol{\Delta}\hat{\boldsymbol{v}}(k) + \boldsymbol{\Theta}z_{min}\end{aligned} \tag{4.3}$$

$$\begin{aligned}FHa\boldsymbol{\Delta}\hat{\boldsymbol{u}}_{\boldsymbol{q}}(k) &\leq -FP\boldsymbol{x}_{\boldsymbol{f}}(k) - FHw\boldsymbol{\Delta}\hat{\boldsymbol{v}}(k) + \boldsymbol{\Theta}\dot{z}_{max}\\ -FHa\boldsymbol{\Delta}\hat{\boldsymbol{u}}_{\boldsymbol{q}}(k) &\leq +FP\boldsymbol{x}_{\boldsymbol{f}}(k) + FHw\boldsymbol{\Delta}\hat{\boldsymbol{v}}(k) + \boldsymbol{\Theta}\dot{z}_{min}\end{aligned} \tag{4.4}$$

where $\boldsymbol{\Theta} = \begin{bmatrix} 1 & 1 & ... & 1 \end{bmatrix}^T \in \mathbb{R}^{N_p \times 1}$

$$\boldsymbol{\Phi} = \begin{bmatrix} 1 & 0 & 0 & ... & 0 \\ 1 & 1 & 0 & ... & 0 \\ : & : & : & \ddots & : \\ 1 & 1 & 1 & ... & 1 \end{bmatrix} \in \mathbb{R}^{N_p \times N_p}, \tag{4.5}$$

where $K = \begin{bmatrix} 1 & 0 & 0 \end{bmatrix}$,

$$W = \begin{bmatrix} K & .... & .... & \mathbf{0} \\ .... & K & .... & \mathbf{0} \\ : & : & \ddots & : \\ ... & .... & .... & K \end{bmatrix} \in \mathbb{R}^{N_p \times 3N_p},$$

where $K_F = \begin{bmatrix} 0 & 1 & 0 \end{bmatrix}$

$$F = \begin{bmatrix} K_F & .... & .... & \mathbf{0} \\ .... & K_F & .... & \mathbf{0} \\ : & : & \ddots & : \\ ... & .... & .... & K_F \end{bmatrix} \in \mathbb{R}^{N_p \times 3N_p}.$$

Fig. 4.1 and Fig. 4.2 show the average electrical power absorbed under monochromatic excitation, for both a 1 m and a 3 m wave amplitude, with heave displacement, velocity and PTO force constraints included. It can be shown that the constraints have a significant effect on the power absorbed. It is shown in this example that the power absorbed is mostly restricted by the velocity and PTO force constraints. At low frequencies the PTO force constraint is the most dominant, whilst at higher frequencies the velocity constraint is the most dominant.

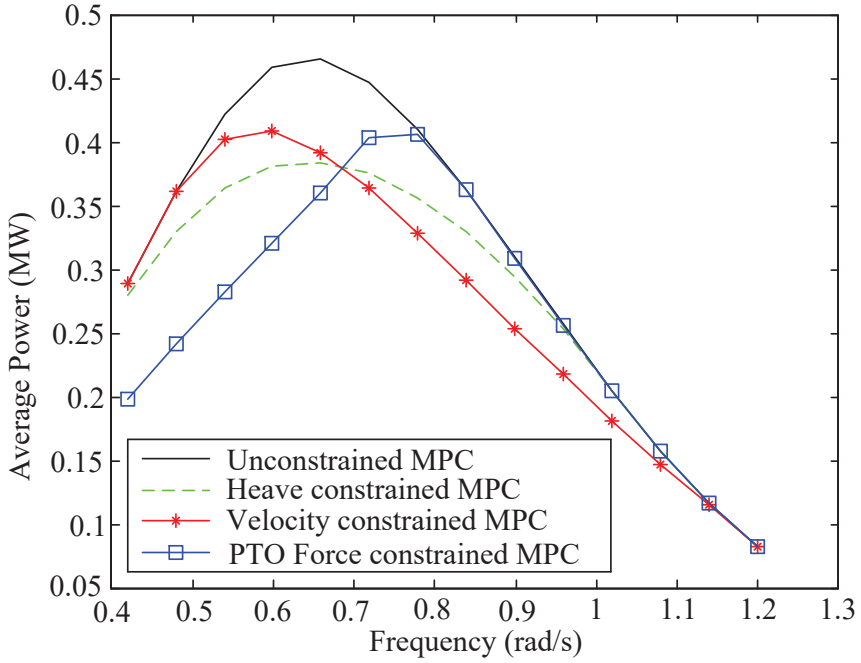

Figure 4.1: Average electrical power extracted from 1 m amplitude monochromatic waves with a prediction horizon N_p=100 and machine resistance R=0.27 Ω and (i) No constraints (ii) Heave constraint (iii) Velocity constraint (iv) PTO force constraint

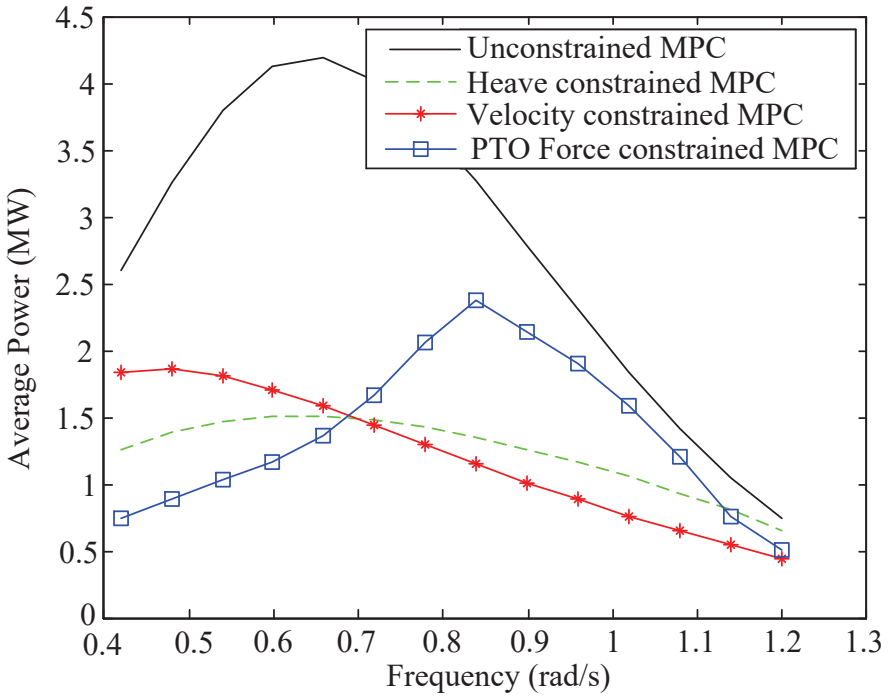

Figure 4.2: Average electrical power extracted from 3 m amplitude monochromatic waves with a prediction horizon N_p=100 and machine resistance R=0.27 Ω and (i) no constraints (ii) heave constraint (iii) velocity constraint (iv) PTO force constraint

4.3 Electrical Constraints

The configuration of a single WEC-to-Grid system is shown in Fig. 4.3. The LPMG in real life is controlled by a space vector modulated (SVM) (Habetler et al. 1992) voltage supplied by the machine side converter. SVM is a modulated signal that is formed from the DC voltage, provided usually by the DC-link capacitor. The SVM signal, as explained in appendix A, is then seen at the LPMG (Polinder et al. 2004) as an averaged voltage over a longer period of time. The SVM voltage operation region, as shown in Fig. 4.4, depends on the LPMG's rotational displacement θ, where the largest available average SVM voltage can be between $V_{dc}(t)$ and $\frac{\sqrt{3}}{2}V_{dc}(t)$. With this converter voltage limitation, some desired PTO forces may become unreachable, restricting the feasible region. Therefore, a voltage constraint needs to be included in the optimisation to guarantee system feasibility.

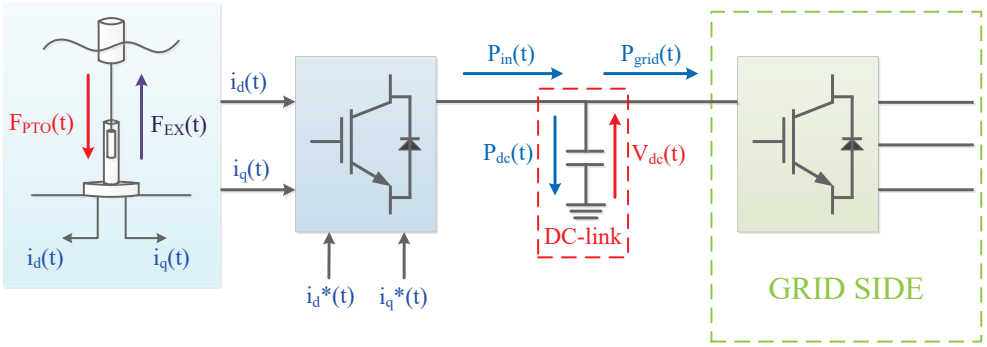

Figure 4.3: System model with WEC and PTO

With linear constraints, the simpler QP algorithm can be utilised without difficulties. However with non-linear constraints, interior point techniques are required. Interior point quadratic programming was employed in this work using IPOPT in AMPL, controlled via MATLAB. In this problem, the non-linear constraints include the converter voltages and current constraints (when field weakening is used).

The LPMG is easily controlled in the $dq0$ domain because it causes an independence from the translator position $z(t)$. This is due to the fact that the $dq0$-axis synchronously rotates, locked to the translator position, as shown in Fig. 4.4. Fig. 4.4 also shows that the converter voltage limit is hexagonal in the stationary $\alpha\beta$-axis, due to the nature of SVM. If, however, a more conservative circular limit is assumed (as shown in Fig. 4.4), then the voltage constraints in the dq0 domain are independent of the translator position and the optimisation problem is simplified. The converter voltage constraint

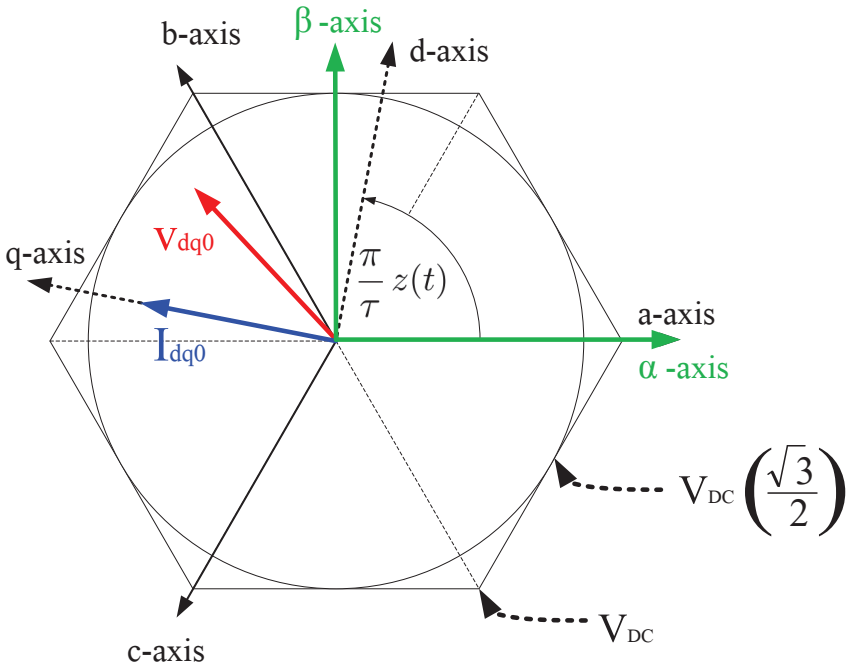

Figure 4.4: Switching pattern of voltage source converter with a common circular constraint for all switching patterns

can be now expressed as,

$$\left(\sqrt{\frac{3}{2}}v_d(k)\right)^2 + \left(\sqrt{\frac{3}{2}}v_q(k)\right)^2 \leq \left(v_{dc}(t)\frac{\sqrt{3}}{2}\right)^2 \tag{4.6}$$

which can then be simplified to (4.7),

$$v_d(k)^2 + v_q(k)^2 \leq \left(\frac{v_{dc}(t)}{\sqrt{2}}\right)^2. \tag{4.7}$$

If it is assumed that for simplicity, $i_d(t) = 0$, then in quasi-steady state, the D and Q axis voltages can be expressed as functions of the WEC velocity $\dot{z}(t)$ and the PTO scaled force $u_q(t)$, based on equations (2.106) and (2.111),

$$v_q(k) = u_q(k)\frac{R}{\psi} + \frac{\pi}{\tau}\dot{z}(k)\lambda'_{fd} \tag{4.8}$$

$$v_d(k) = -\frac{L}{\psi}\frac{\pi}{\tau}\dot{z}(k)u_q(k). \tag{4.9}$$

Substituting (4.8) and (4.9) into (4.7), the converter voltage constraints can be represented as (4.10). The voltage constraint can now be applied to each step over the

prediction horizon, utilising the velocity prediction values provided by (3.16, page 91),

$$\left(-\frac{L}{\psi}\frac{\pi}{\tau}\dot{z}(k+i|k)(u_q(k+i))\right)^2+\left(u_q(k+i)\frac{R}{\psi}+\frac{\pi}{\tau}\dot{z}(k+i|k)\lambda'_{fd}\right)^2\leq\left(\frac{v_{dc}(t)}{\sqrt{2}}\right)^2 \tag{4.10}$$

The voltage constraint circles are plotted in Fig. 4.5 for a variety of constant positive velocities and DC-link voltages. The current limit circle is superimposed. It can be seen from Fig. 4.5 that if $i_d(t)=0$ there is no feasible selection for $i_q(t)$ that satisfies both the current and voltage constraints at a low DC-link voltage of 1050 V and a velocity of 2.2 m/s. With a lower DC-link voltage, the system would be forced to operate at lower speeds to maintain feasibility. When $i_d(t)=0$, the feasible range of i_q is dramatically reduced as the velocity increases.

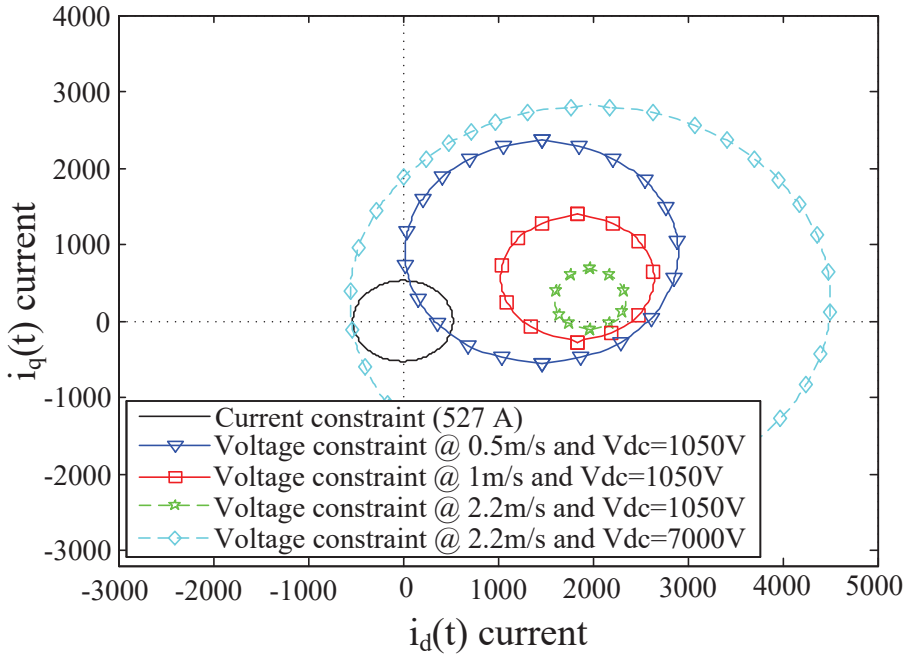

Figure 4.5: Voltage constraints in terms of $i_q(t)$ and $i_d(t)$ with a DC-link of 1050 V and a constant velocity of i) 0.5 m/s ii) 1 m/s iii) 2.2 m/s iv) DC-link values of 7000 V with a velocity of 2.2 m/s

For the $i_q(t)$ current range to be expanded for maximum PTO force production for a velocity of 2.2 m/s, a large enough DC-link voltage must be chosen. Fig. 4.6 shows the average electrical power absorbed from 1 m high monochromatic excitation waves across a range of frequencies, subject to velocity and voltage constraints for a variety of DC-link voltages. It is shown that at low DC-link voltages, the absorbed power is significantly reduced when compared to higher DC-link levels. As the DC-link voltage is increased, the average power generally increases until the average power can go no further, due to the velocity constraint which consequently limits the voltage produced

from the VSC.

Choosing an overrated DC-link voltage marginally increases the system capabilities; however, it increases the cost of the power electronics (Lovelace et al. 2000) and the insulation of the generator windings (Siddique et al. 2005). In this work, the LPMG design optimisation was not taken into consideration due to the complexity of the design (Polinder et al. 2004), where multiple parameters such as the slot size and the machine size determine the LPMG characteristics. Therefore, choosing an appropriate DC-link voltage in terms of maximizing system capabilities and minimising the cost is an important matter.

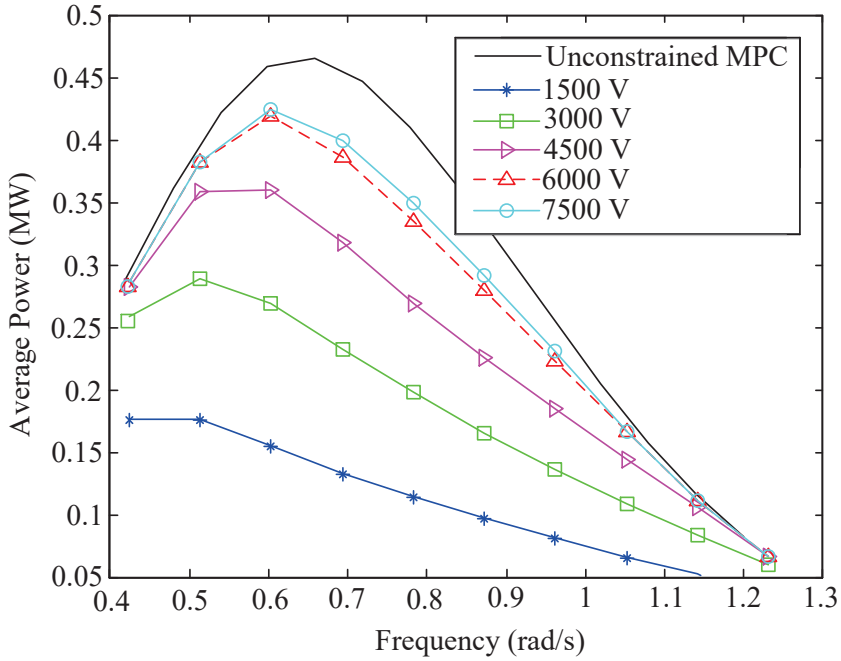

Figure 4.6: Average power absorbed with a velocity constraint of 2.2 m/s, a prediction horizon of $N_p = 100$ and a voltage constraint with a DC-link value of (i)1500 V, (ii)3000 V, (iii)4500 V, (iv)6000 V and (v) 7500 V

4.3.1 Introduction of Field Weakening

If the DC-link voltage is too low, the feasible region for the optimal force will contract as the velocity of the device increases. There may come a point where there is no feasible choice for force ($i_q(t)$ current). When field weakening is utilised (O'Sullivan & Lightbody 2016), the introduction of D axis current $i_d(t)$ increases the feasible region, allowing for higher velocities and decreases the time that the crowbar protection system is enabled (Appendix B) (O'Sullivan & Lightbody 2016, Morren & de Haan 2007). The constraints for the current and the converter voltage are similar to (4.10).

The only difference is that the $i_d(t)$ current is non-zero. This is shown in equation (4.11),

$$\left(u_q(k+i)\frac{R}{\psi}+\frac{\pi}{\tau}\dot{z}(k+i|k)\lambda'_{fd}-L\frac{\pi}{\tau}\dot{z}(k+i|k)i_d(k+i)\right)^2 + \left(-i_d(k+i)R-\frac{L}{\psi}\frac{\pi}{\tau}\dot{z}(k+i|k)(u_q(k+i))\right)^2 \leq \left(\frac{v_{dc}}{\sqrt{2}}\right)^2 \quad \forall i=\{1,\ldots,N_p\} \tag{4.11}$$

Since the $i_d(t)$ current is non-zero, the current constraint can be expressed as (4.12),

$$(i_d(k+i))^2+\left(-\frac{u_q(k+i)}{\psi}\right)^2 \leqq i^2_{dq0MAX} \quad \forall i=\{1,\ldots,N_p\}. \tag{4.12}$$

Fig. 4.5 shows the voltage and current constraints for a range of speeds at a DC-link of 1050 V. It is shown that the feasible region contracts as the velocity increases. Including the $i_d(t)$ current in the optimisation allows the system to operate at higher speeds, hence, extracting more power.

Fig. 4.5 also shows the voltage constraint for a DC-link of 7000 V at the rated speed of 2.2 m/s. It is shown that the constraint circle of 7000 V contains the current constraint circle. Therefore, the $i_q(t)$ current range is the same, whether or not field weakening is incorporated. Effectively, in this case the converter voltage constraint is never active up to the rated velocity. Hence, it would be unnecessary to include field weakening in the optimisation for such a large DC-link voltage.

4.3.1.1 MPC with Field Weakening

With field weakening introduced, the following discrete-time state space model is obtained (4.13), where $i_d(k)$ is now included as a state,

$$\begin{aligned}\boldsymbol{x_w}(k+1) &= A_w\boldsymbol{x_w}(k)+B_w\Delta U(k+1)+F_w\Delta v(k+1)\\ \boldsymbol{y_w}(k) &= C_w\boldsymbol{x_w}(k)\end{aligned} \tag{4.13}$$

where

$$A_w = \begin{bmatrix} A_f & \mathbf{0} \\ \mathbf{0} & 1 \end{bmatrix} \quad B_w = \begin{bmatrix} B_f & \mathbf{0} \\ 0 & 1 \end{bmatrix} \tag{4.14}$$

$$F_w = \begin{bmatrix} F_f \\ 0 \end{bmatrix} \quad \boldsymbol{x_w}(k) = \begin{bmatrix} \boldsymbol{x_f}(k) \\ i_d(k) \end{bmatrix}$$

$$\boldsymbol{y_w}(k) = \begin{bmatrix} \boldsymbol{y_f}(k) \\ i_d(k) \end{bmatrix} \quad \Delta U(k) = \begin{bmatrix} \Delta u_q(k) \\ \Delta i_d(k) \end{bmatrix}$$

With the inclusion of field weakening, the function (4.15) for the average electrical power must include the resistive losses from the $i_d(t)$ current,

$$P_w = P_e - \frac{1}{T}\int_{t=0}^{T} R i_d^2(t) dt, \tag{4.15}$$

where

$$P_e = -\frac{1}{T}\int_{t=0}^{T} \left(F_{PTO}(t)\dot{z}(t) + R i_q^2(t)\right) dt, \tag{4.16}$$

expanding (4.15) yields (4.17),

$$P_w = (M + m_\mu)\left(\frac{P_e}{M + m_\mu} - \frac{1}{T}\int_{t=0}^{T} \frac{R i_d^2(t)}{M + m_\mu} dt\right). \tag{4.17}$$

With the $i_d(k)$ current included as a state (4.14), then (4.17) can be represented as a discrete-time cost (4.18),

$$J_w(k) = J(k) + \epsilon\left(\frac{1}{2} i_d^2(k+N) + \sum_{i=1}^{N} i_d^2(k+i)\right), \tag{4.18}$$

where

$$\begin{aligned} J(k) = {} & \frac{1}{2} u_q(k+N_p)\dot{z}(k+N_p) + \sum_{i=1}^{N_p} u_q(k+i)\dot{z}(k+i) \\ & + \frac{R(M+m_\mu)}{(\lambda'_{fd}\frac{\pi}{\tau})^2}\left(\frac{1}{2} u_q^2(k+N_p) + \sum_{i=1}^{N_p} u_q^2(k+i)\right). \end{aligned} \tag{4.19}$$

The cost of (4.18) could be written as,

$$J_w(k) = \frac{1}{2}\hat{\boldsymbol{y}}_{\boldsymbol{\omega}}(k)^T Q_w \hat{\boldsymbol{y}}_{\boldsymbol{\omega}}(k), \tag{4.20}$$

where,

$$Q_w = \begin{bmatrix} M_w & 0 & .. & 0 \\ 0 & M_w & .. & 0 \\ : & : & \ddots & : \\ 0 & 0 & 0 & \frac{1}{2}M_w \end{bmatrix} M_w = \begin{bmatrix} 0 & 0 & 0 & 0 \\ 0 & 0 & 1 & 0 \\ 0 & 1 & 2G & 0 \\ 0 & 0 & 0 & 2\epsilon \end{bmatrix} \quad \epsilon = \frac{R}{M + m_\mu} \tag{4.21}$$

The dimensions of M_ω (4.21) increase, as $i_d(k)$ is included as another output. The size of the input prediction array $\boldsymbol{\Delta}\hat{\boldsymbol{U}}(k)$ doubles in size since each step needs $\Delta u_q(k)$ and $\Delta i_d(k)$ to be optimised. Therefore this MPC method is more computationally expensive than the one presented earlier (3.28).

4.3.1.2 Implementation of Field Weakening

The two MPC approaches, with costs (3.28, page 96) and (4.18), were tested with a selection of DC-link voltages (1050 V, 3500 V and 7000 V) under irregular wave excitations. Here, irregular waves were generated from a Bretschneider spectrum, with a peak wave period of $T_p = 8$ s, and a significant height ranging from $H_s = 1$ m to 6 m. Both MPC approaches, used a prediction horizon of $N_p = 40$ and an outer sampling time of $T_L = 0.1$ s and a faster inner sampling time of $T_{gen} = 1$ ms.

Fig. 4.7 shows the electrical power extracted using these MPC techniques with and without field weakening for the DC-link values of 1050 V, 3500 V and 7000 V. It can be observed from Fig. 4.7, that as the DC-link voltage increases, the absorbed average electrical power increases until it reaches a point where the system is constrained more by the velocity constraint than by the DC-link voltage. The results for 1050 V show that the difference between the power extracted between the MPC with and without field weakening diverges as the significant height increases. It can be seen in Fig. 4.5 that for a DC-link of 1050 V, a higher velocity can be reached using field weakening, as it allows a higher $i_q(t)$ current to be reached even when the voltage constraint circle does not intersect the $i_q(t)$ axis; this is highlighted in Table 4.1. With the potential for greater velocity comes an increase in higher power extraction. However, as the DC-link voltage is increased, the contribution that field weakening introduces becomes less significant. This is because the common $i_q(t)$ current range of the two methods converges as the DC-link voltage increases.

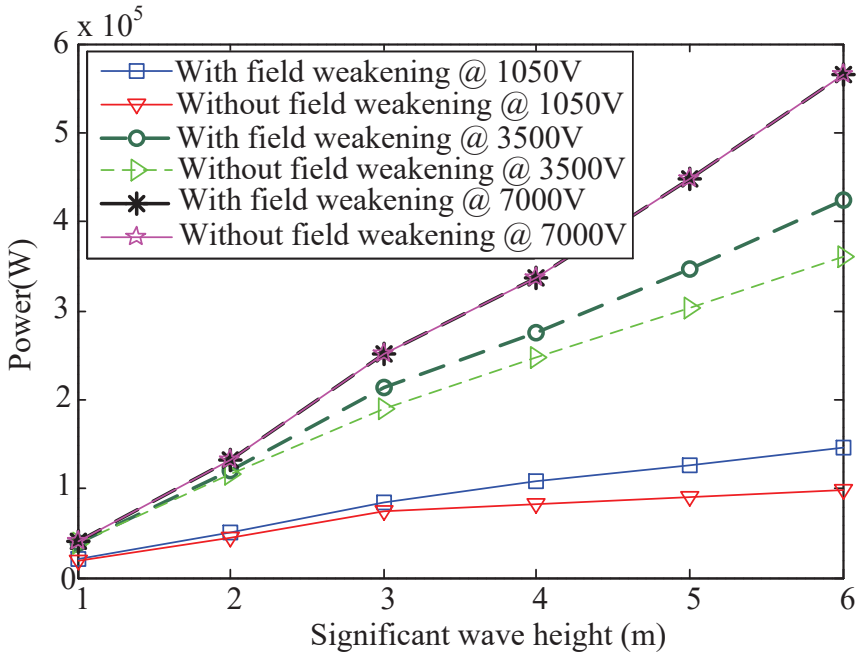

Figure 4.7: Average electrical power extracted from irregular waves modelled using a Bretschneider spectrum, with a peak wave period of $T_p = 8$ s, and a significant height ranging from $H_s = 1$ m to 6 m, using MPC with a prediction horizon of $N_p = 40$, with and without field weakening at a DC-link voltage of 1050V, 3500V and 7000V

If the DC-link voltage is large enough, both MPC approaches (with and without field weakening) will share a common $i_q(t)$ range (at $\dot{z}(t) \leqslant 2.2$ m/s); hence field weakening becomes obsolete. This is the case for a DC-link voltage of 7000 V, as shown in Fig. 4.7. The average power from the two methods, at a DC-link of 7000 V, are the same, hence $i_d(t) = 0$ for both cases.

Table 4.1: Measured peak velocities during an irregular wave, modelled using a Bretschneider spectrum, with a peak wave period of $T_p = 8$ s and a significant height Hs=5 m. Showing the increase in peak velocity when field weakening is incorporated into a voltage constrained MPC

	Peak Velocities from System	
DC-link Voltage	With Field Weakening	Without Field Weakening
1050 V	0.4700 m/s	0.3905 m/s
3500 V	1.3746 m/s	1.3156 m/s
7000 V	1.9026 m/s	1.9026 m/s

4.3.2 Power Constraint

The majority of research in the wave energy industry makes use of control systems which obey the general rule that the PTO force should ideally cause the velocity to be in phase with the excitation wave force acting on the WEC (Falnes & Budal 1978).

However, for this to occur the PTO force must oscillate, which causes large power swings on the grid. Ideally, electrical power should not be taken from the grid as it may lead to grid side DC-link voltage control instabilities, poor power quality and voltage flickering. Negative power flow will complicate the design of the grid side DC-link voltage controller, as it introduces a non-minimum phase zero, which significantly affects the achievable closed-loop bandwidth of the DC-link voltage control system (Huang et al. 2015). Therefore, there is a need for a constraint to be included within the optimisation, which restricts the instantaneous power flow to be uni-directional. The formulation of the power constraint is shown in (4.22). This power constraint must be applied at every step over the prediction horizon.

$$P(k+i) = \lambda'_{fd}\frac{\pi}{\tau}i_q(k+i)\dot{z}(k+i) - Ri_q^2(k+i) - Ri_d^2(k+i) \geq 0 \quad \forall i = \{1, \ldots, N_p\} \tag{4.22}$$

The power constraint for positive velocity is plotted in Fig. 4.8; these circular constraints shrink in diameter as the speed decreases. The corresponding constraints for negative velocity are these circles reflected about the D-axis.

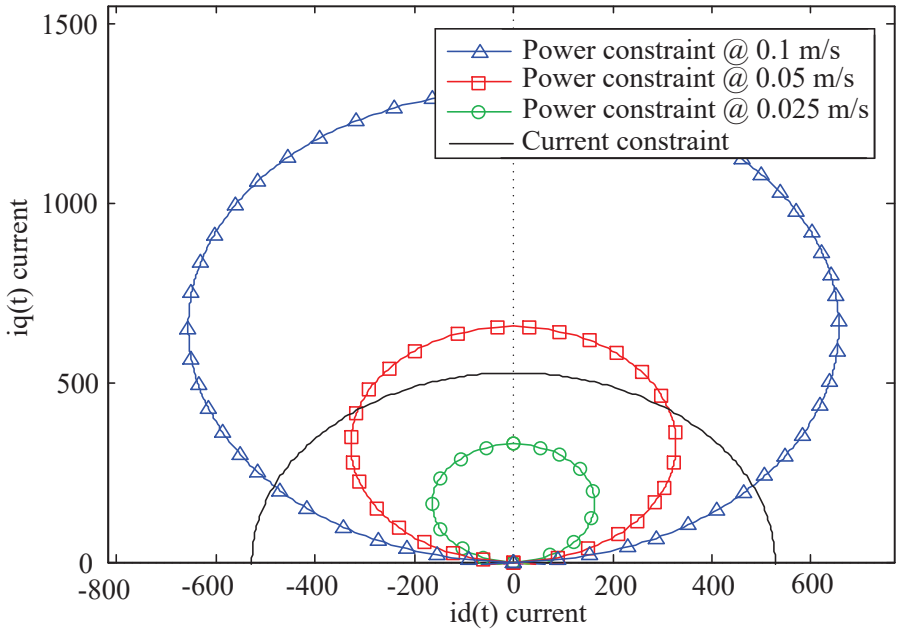

Figure 4.8: Positive power constraints for a range of slow positive velocities, superimposed on the current constraint

The MPC with the power flow constraint (4.22) was simulated with and without field weakening. The two MPC types were tested using an excitation wave based on a Bretschneider spectrum with a range of significant heights and a peak period of $T_p = 8$ s. The average absorbed electrical power resulting from uni-directional MPC is shown in Fig. 4.9.

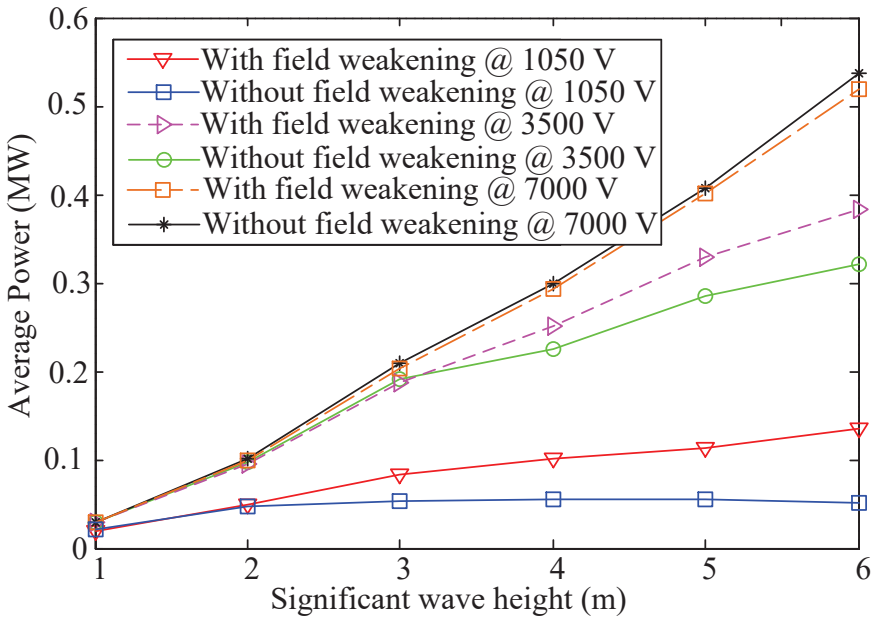

Figure 4.9: Average electrical power extracted from irregular waves, modelled using a Bretschneider spectrum with a peak wave period of $T_p = 8$ s and a significant height ranging from $H_s = 1$ m to 6 m; utilising a uni-directional power flow MPC with a prediction horizon of $N_p = 40$, with and without field weakening at a DC-link voltage of 1050 V, 3500 V and 7000 V

Fig. 4.10 shows the typical time responses when an MPC with a uni-directional power flow is utilised with a DC-link of 1050 V and excited by an irregular wave (Bretschneider spectrum $H_s = 4$ m, $T_p = 8$ s). It can be seen that the MPC with no field weakening struggles to find the necessary PTO forces to maintain feasibility under a low DC-link voltage, even though the velocity is low and is only a medium sized significant excitation wave height.

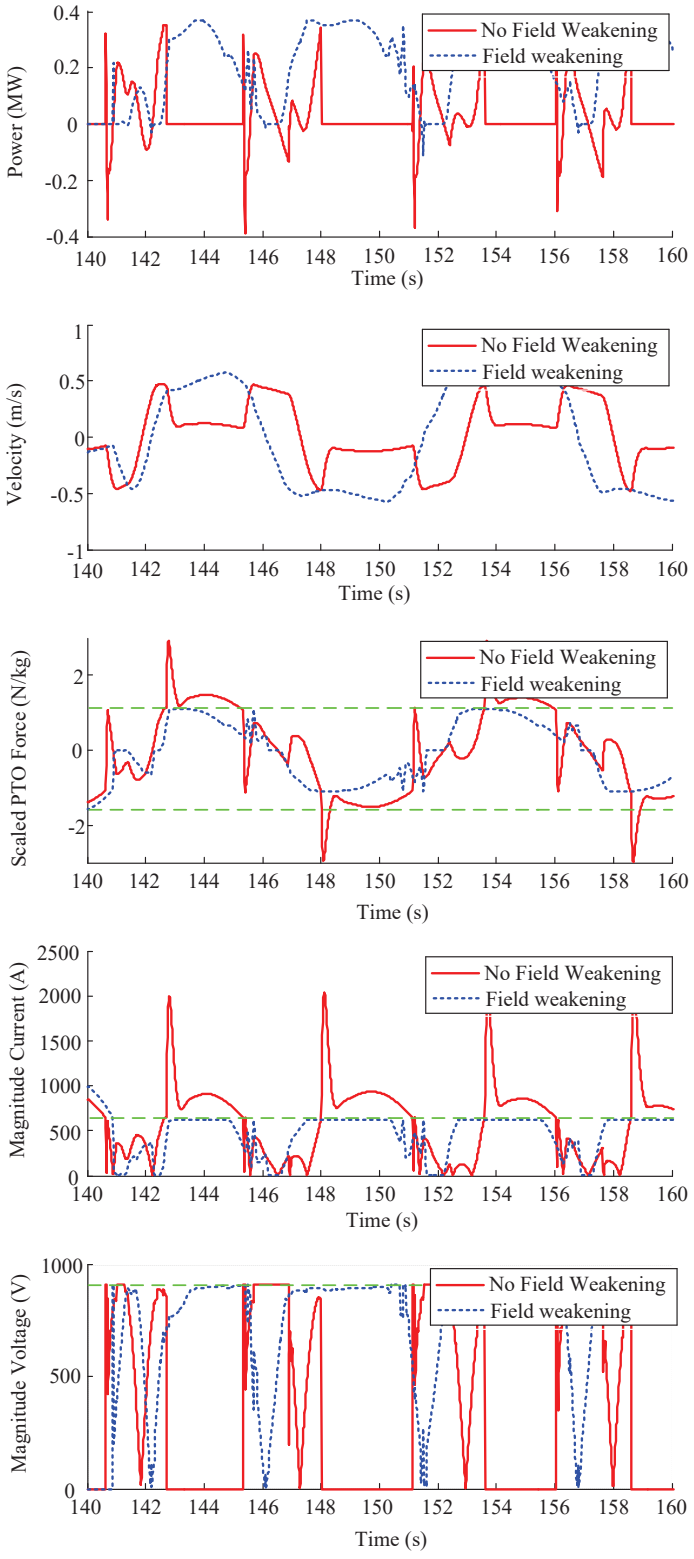

Figure 4.10: Results of Uni-directional power flow MPC with a prediction horizon of $N_p = 40$, with and without field weakening using a 1050 V DC-link during a Bretschneider irregular wave with $H_s = 4$ m and $T_p = 8$ s, i)The instantaneous electrical power, ii)Velocity, iii)Scaled PTO Force, iv)Magnitude of $i_d(t)$,$i_q(t)$ currents, v)Magnitude of $v_d(t)$,$v_q(t)$ voltages

With the combination of the power constraint at low velocities and the voltage constraint at high velocities, there is a very narrow feasible region for all velocities. This narrow feasible region reduces the PTO force range, hence, reducing power extraction and PTO capabilities. When the system struggles to remain below the current limit, the crowbar is enabled (O'Sullivan & Lightbody 2016, Morren & de Haan 2007), therefore causing a short circuit across the LPMG terminals and an open circuit between the LPMG and the VSC. This protection method is repeatedly enabled in Fig. 4.10 when no field weakening is used. This process is further described in appendix B.

Introducing field weakening creates a larger feasibility region. From Fig. 4.11 it is shown that the crowbar was not enabled, hence no damage occurred, and the velocity was higher than the system without field weakening, therefore creating more power.

Fig. 4.11 shows the performance of the MPC with field weakening and uni-directional power flow with a DC-link voltage of 7000 V during the same irregular wave that was used in Fig. 4.10. Fig. 4.11 shows that the instantaneous electrical power is unidirectional, the velocity reaches its limits at ± 2.2 m/s, the scaled PTO force is nearly reaching its limits at ± 1.128 N/kg and the current magnitude is under the limit of 527 A. From these results it is shown that the system is pushed to the limits in absorbing the maximum possible amount of power from the system, whilst maintaining feasibility.

However, what is interesting is that the magnitude of the $v_d(t)$ and $v_q(t)$ voltages is well below the constraint of 6062 V (the radius of the circular voltage limit shown in Fig. 4.4). Fig. 4.6 shows that if the DC-link level is increased past a certain point, it does not necessarily mean that the overall power absorption will increase due to the velocity restriction; hence, it is essential that an appropriate DC-link voltage is chosen to balance the controlled power electronics with potential power extraction benefits.

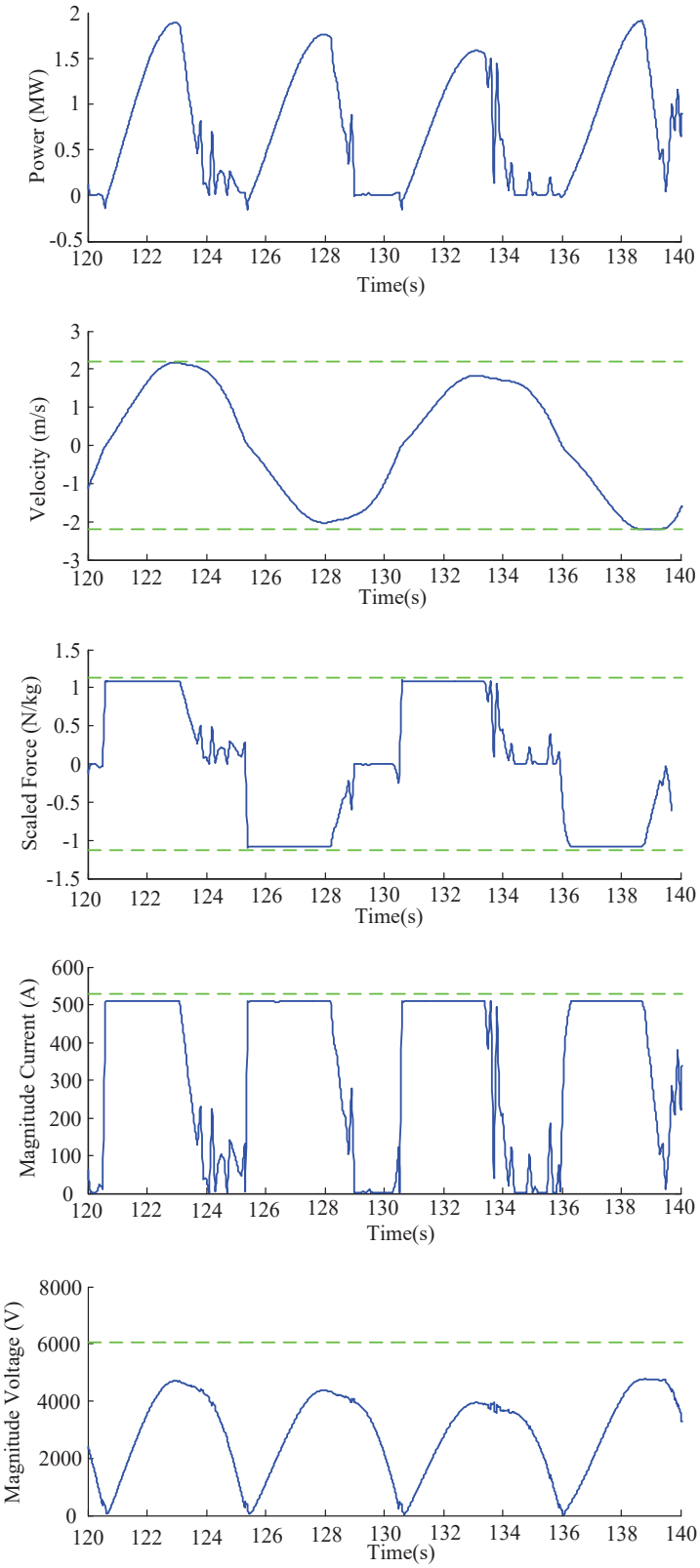

Figure 4.11: Results of uni-directional power flow MPC with a prediction horizon of $N_p = 40$, with field weakening using a 7000 V DC-link during a Bretschneider irregular wave with $H_s = 4$ m and $T_p = 8$ s, i)The instantaneous electrical power, ii)Velocity, iii)Scaled PTO Force, iv)Magnitude of $i_d(t)$,$i_q(t)$ currents, v)Magnitude of $v_d(t)$,$v_q(t)$ voltages

4.4 Discussion

Fig. 4.12 and Fig. 4.13 show the instantaneous power from the MPC with and without the uni-directional power flow constraint, where both methods used field weakening. It can be seen in Fig. 4.14 that the system with bi-directional power flow during large significant wave heights produces only slightly more average power than the system with the uni-directional power flow. This is due to the multiple physical and electrical constraints that are introduced into the system. The constraints restrict the system oscillations at large significant heights, hence the instantaneous power of both uni-directional and bi-directional powers are similar, as can be seen in Fig. 4.12. Effectively, the need to reduce losses has forced the power extracted from the bidirectional MPC to be almost unidirectional, without the need for a power constraint.

For waves with a low significant height, the instantaneous power is oscillatory with significant negative power flows when the bi-directional power is used, (Fig. 4.13). With the uni-directional power constraint implemented, there is a better mean to peak power ratio. Furthermore, as shown in Fig. 4.14, the mean power difference between the two MPC methods is inconsequential.

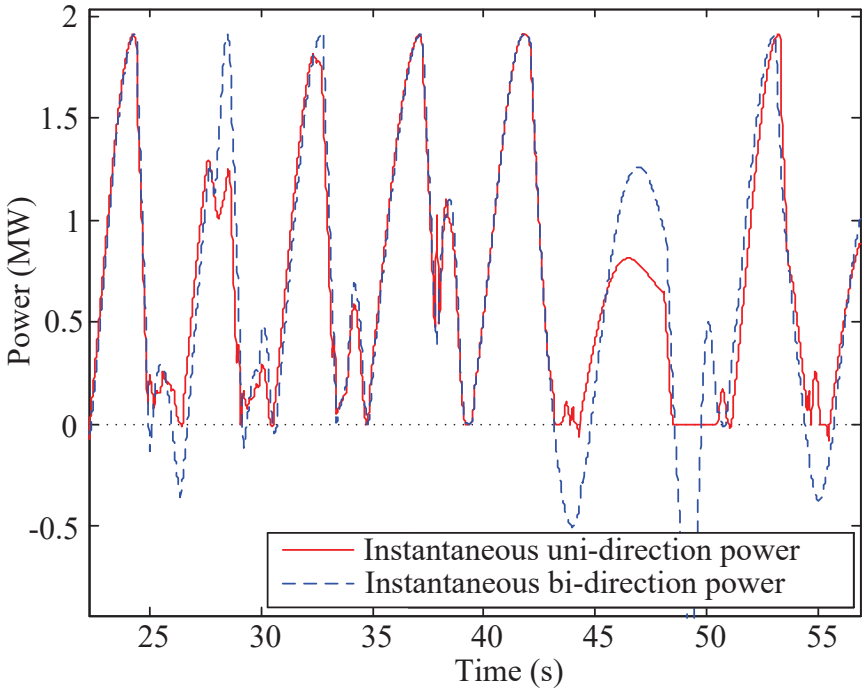

Figure 4.12: Instantaneous power from a bi-directional and uni-directional power constrained MPC with a prediction horizon of $N_p = 40$ and a DC-link voltage of 7000 V. The irregular excitation wave was modelled using a Bretschneider spectrum with a peak wave period of $T_p = 8$ s and a significant height of $H_s = 6$ m

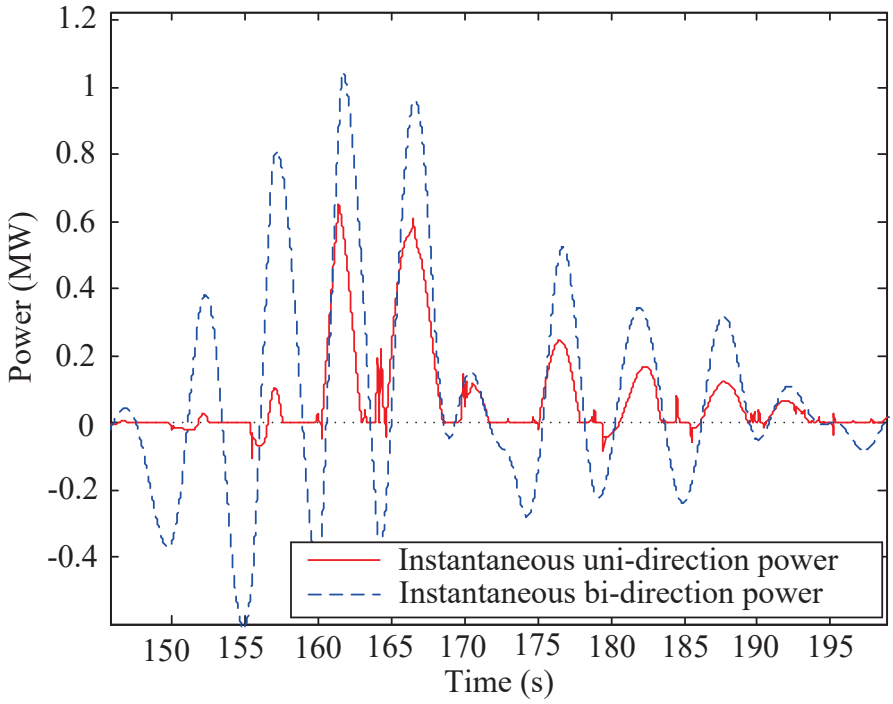

Figure 4.13: Instantaneous power from a bi-directional and uni-directional power constrained MPC with a prediction horizon of $N_p = 40$. The irregular excitation wave was modelled using a Bretschneider spectrum with a peak wave period of $T_p = 8$ s, at a significant height of $H_s = 1$ m and a DC-link voltage of 7000 V.

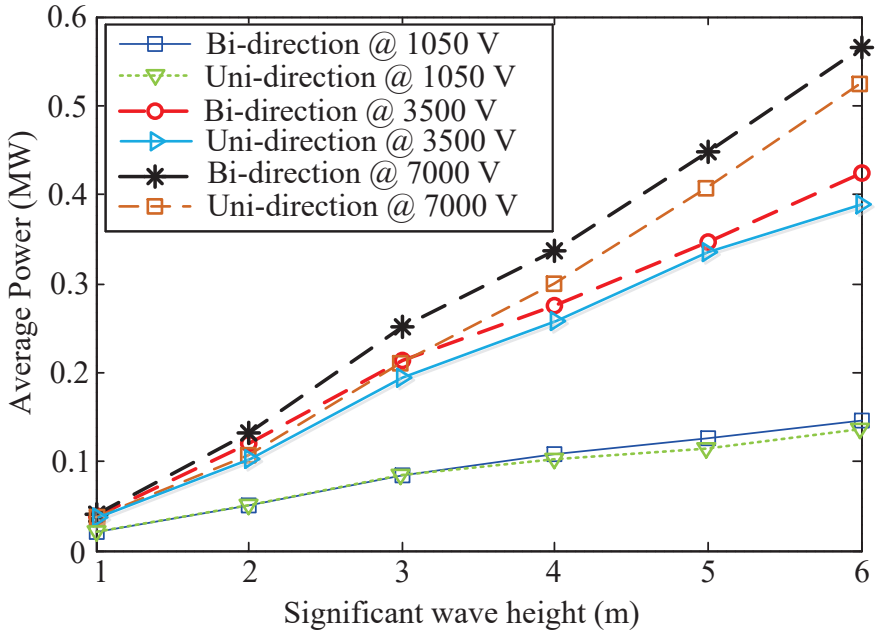

Figure 4.14: Average power from a bi-directional and a uni-directional power flow MPC with a prediction horizon of $N_p = 40$ with field weakening at a DC-link voltage of 1050 V, 3500 V and 7000 V

Fig. 4.13 shows the uni-directional power having a minimum of -0.5×10^5 W and a maximum of 6×10^5 W, while the bi-directional power flow has a minimum of -6×10^5 W and a maximum of 10×10^5 W. This means that the uni-directional constraint produces an instantaneous power which has reduced the power fluctuations by as much as 59.37%. By implementing the uni-directional power flow constraint and the field weakening, the instantaneous power consistently remains positive and the peak to average ratio is reduced. This will have a significant impact on the design and, of course, the rating and cost of the power electronics and the machine to meet the peak power for a desired mean power. Any reduction in the variation of power delivered onto the DC-link will lead to improved DC-link voltage regulation by the grid side converter. Further improvements can be achieved by the aggregation of the powers from multiple devices onto a single DC-link (Molinas et al. 2007).

The grid side converter is typically utilised to regulate the DC-link voltage at a constant level. In control terms, the power from the generation side acts as a disturbance. Therefore, for the DC-link voltage to remain constant, the power exported to the grid through the grid side converter must ideally match the power from the generation side; hence, the power on the grid side would be very oscillatory from a typical WEC. It should be noted that the control of the DC-link voltage is a non-linear control problem; the dynamics depend on the power operating point. As the power delivered to the DC link from the WEC fluctuates widely over the period of a wave, the dynamics are constantly changing - this would imply that a conservative controller is required for the DC-link voltage control problem that will ensure satisfactory (robust) performance over the wave period. Such a conservative design employs a low bandwidth controller for the DC-link - and hence the DC-link voltage will not be tightly controlled. Alternatively a more sophisticated gain scheduled controller could be used in which the controller tuning depends on the power operating point (Apkarian & Adams 1998), or a non-linear technique such as feedback linearisation can be used (Mullane et al. 2005). This problem is exacerbated if the power-flow switches direction; when the power flows from the grid, the DC-link voltage problem becomes non-minimum phase - this will further limit the performance of the closed loop DC-link voltage control system.

To combat these grid power fluctuations, it may be beneficial to have a low bandwidth DC-link voltage regulator, in which the DC-link voltage is allowed to vary. By incorporating a short-term energy storage system (O'Sullivan et al. 2011) on the DC-link, such as a flywheel, battery or a super-capacitor, the control of the DC-link can be made more flexible. With field weakening included in the design, the grid side converter can regulate the grid power by allowing the DC-link voltage to change, whilst

the field weakening enables the generation side to optimise for maximum power absorption while simultaneously maintaining good control over the WEC, despite a possible reduction in the DC-link voltage. However, there are drawbacks on how much the DC-link can be varied as the DC-link voltage directly effects the converter voltage constraints, hence, affecting the average power and feasibility.

4.5 Conclusion

The maximisation of power absorbed from a point absorber needs to factor in the physical, electrical and economical restrictions that would be found in a real life application; this could be the design optimisation of the WEC (De Backer 2009), the PTO (Drew et al. 2009), the power electronics (Lovelace et al. 2000) or the DC-link energy storage size. Even with an improvement in electrical power optimisation as shown in section 3.5.2, it is still necessary to include the physical constraints of the system. Section 4.2 showed that the introduction of linear constraints in the MPC maximised the average electrical power whilst maintaining the physical constraints within the systems restrictions. Section 4.3 then introduced the non-linear voltage constraint that the DC-link would restrict the voltage capabilities of the machine side converter.

The importance of choosing the correct DC-link was discussed in section 4.3. If the DC-link voltage is too low the system becomes uncontrollable; too large and the controllability is maximised but the power electronics may be overrated, leading to unnecessary costs. With a low DC-link voltage the system may become ineffective due to a limited feasible range. To increase the feasibility of the system, field weakening was introduced.

Section 4.3.2 introduced field weakening and showed how the feasibility can be extended, allowing higher velocities to be obtained. Field weakening was shown to be of particular benefit when the DC-link voltage was 1050 V.

One of the main problems besides the electrical power maximisation and system feasibility is the power quality on the grid side. Section 4.4 showed that by implementing a uni-directional power flow constraint, the peak to average power ratio was significantly decreased whilst producing slightly less power when compared to the bi-directional power flow.

The control system methodology provided here ensured that the resulting system provided optimal electrical power was feasible for whatever physical parameter design choice and system constraints encountered. The control design problem is hence now

invisible to the designer. It is now therefore possible to compare and contrast various design choices, such as the flux density, the choices of DC-link voltage, the mass, heave limits etc., knowing that in each case, the control system is providing optimal, feasible results - i.e. a level playing field.

References

Apkarian, P. & Adams, R. J. (1998), 'Advanced gain-scheduling techniques for uncertain systems', *IEEE Transactions on control systems technology* **6**(1), 21–32.

Camm, E. H., Behnke, M. R., Bolado, O., Bollen, M., Bradt, M., Brooks, C., Dilling, W., Edds, M., Hejdak, W. J., Houseman, D. & Others (2009), Wind power plant grounding, overvoltage protection, and insulation coordination: IEEE PES wind plant collector system design working group, *in* 'Power & Energy Society General Meeting, 2009. PES'09. IEEE', IEEE, pp. 1–8.

De Backer, G., Hydrodynamic design optimization of wave energy converters consisting of heaving point absorbers, PhD thesis, University of Ghent.

Drew, B., Plummer, A. R. & Sahinkaya, M. N. (2009), 'A review of wave energy converter technology', *Proceedings of the Institution of Mechanical Engineers, Part A: Journal of Power and Energy* **223**(8), 887–902.

Elmore, W. A. (2003), *Protective relaying: theory and applications*, Vol. 1, CRC press.

Falnes, J. & Budal, K. (1978), 'Wave - power conversion by point absorbers', *Norwegian Maritime research* **6**(4), 1–11.

Habetler, T. G., Profumo, F., Pastorelli, M. & Tolbert, L. M. (1992), 'Direct torque control of induction machines using space vector modulation', *IEEE Transactions on Industry Applications* **28**(5), 1045–1053.

Huang, Y., Yuan, X., Hu, J. & Zhou, P. (2015), 'Modeling of VSC Connected to Weak Grid for Stability Analysis of DC-Link Voltage Control', *IEEE Journal of Emerging and Selected Topics in Power Electronics* **3**(4), 1193–1204.

Hürlimann, T. (1993), 'AMPL: A mathematical programming language', *OR Spektrum* **15**(1), 43–56.

Lovelace, E. C., Jahns, T. M. & Lang, J. H. (2000), 'Impact of saturation and inverter

cost on interior PM synchronous machine drive optimization', *IEEE Transactions on Industry Applications* **36**(3), 723–729.

Matlab (2010), *Version 7.10.0*, The MathWorks Inc., Natick, Massachusetts.

Molinas, M., Skjervheim, O., Sørby, B., Andreasen, P., Lundberg, S. & Undeland, T. (2007), Power smoothing by aggregation of wave energy converters for minimizing electrical energy storage requirements, *in* 'Proceedings of the 7th European Wave and Tidal Energy Conference', pp. 3–8.

Morren, J. & de Haan, S. W. H. (2007), 'Short-Circuit Current of Wind Turbines With Doubly Fed Induction Generator', *IEEE Transactions on Energy Conversion* **22**(1), 174–180.

Mullane, A., Lightbody, G. & Yacamini, R. (2005), 'Wind-Turbine Fault Ride-Through Enhancement', *IEEE Transactions on Power Systems* **20**(4), 1929–1937.

O'Sullivan, A. C. & Lightbody, G. (2015), 'Wave to Wire Power Maximisation from a Wave Energy Converter', *In Proceedings of the 11th European Wave and Tidal Energy Conference (EWTEC)* pp. 1–9.

O'Sullivan, A. C. & Lightbody, G. (2017), 'Co-design of a wave energy converter using constrained predictive control', *Renewable Energy* **102**, 142–156.

O'Sullivan, A. C. M. & Lightbody, G. (2016), 'Predictive control of a wave to wire energy conversion system - the importance of field weakening', *2016 UKACC 11th International Conference on Control (CONTROL)* (August), 1–6.

O'Sullivan, D., Lewis, A. W., Murray, D., Hayes, J. & Egan, M. G. (2011), *The benefits of device level short term energy storage in ocean wave energy converters*, INTECH Open Access Publisher.

Polinder, H., Damen, M. E. C. & Gardner, F. (2004), 'Linear PM Generator System for Wave Energy Conversion in the AWS', *IEEE Transactions on Energy Conversion* **19**(3), 583–589.

Siddique, A., Yadava, G. S. & Singh, B. (2005), 'A review of stator fault monitoring techniques of induction motors', *IEEE transactions on energy conversion* **20**(1), 106–114.

Wächter, A. & Biegler, L. T. (2006), 'On the implementation of an interior-point filter line-search algorithm for large-scale nonlinear programming', *Mathematical programming* **106**(1), 25–57.

Yazdani, A. & Iravani, R. (2010), *Voltage-sourced converters in power systems: modeling, control, and applications*, John Wiley & Sons.

Chapter 5

The Effect of Model Uncertainty, Viscosity and MPC Simplification on Electrical Power Production

5.1 Introduction

In chapter 3 (O'Sullivan & Lightbody 2017*a*) an electrical power maximisation economic MPC was introduced, where a long prediction horizon and a perfect (matched) model was assumed, hence allowing the control system to produce the ideal optimal control for the system. In this chapter the effects of model mismatch and optimisation simplification are examined. Since WEC dynamics can be uncertain and may indeed vary over their lifetime, due for example to biofouling (Wright et al. 2016), the performance of the control system may therefore in reality become sub-optimal, leading to mechanical and electrical degradation if the system constraints are exceeded.

In this chapter, the non-linear effects of viscosity on the average power absorption are investigated. First, the effect that unmodelled viscosity in the WEC has on the electrical power absorption when a linear economic MPC is investigated. A non-linear MPC approach based on the linear parameter-varying (LPV) method is then utilised, in which the non-linear viscosity effect is approximated within the predictive model at each prediction step. When utilising a linear viscous damping within the predictive model, which is optimally tuned for each sea state, the optimisation becomes simplified and reduces the computational complexity. The MPC is further optimised by utilising a reduced control horizon, where the simplified MPC is then analysed when a model mismatch occurs between the control and system. With the appropriate control

horizon reduction, the performance of the MPC will be maintained with a much less computational expense.

5.2 Model Mismatch

In previous chapters there have been positive results in absorbing maximum electrical power from a cylindrical WEC. However, the hydrodynamics model used in the MPC control system was the same as the systems simulation model itself. For normal tracking MPC, the control system can track the system reference points with some robustness (Garcia et al. 1989). However, with economic MPC the objective is to maximise the electrical power which is dependent on the system model and cost function (Ellis et al. 2014). In a real life situation, the system may change over time due to external factors. This can cause a mismatch between the model in the controller and the real life system which is shown in Fig. 5.1.

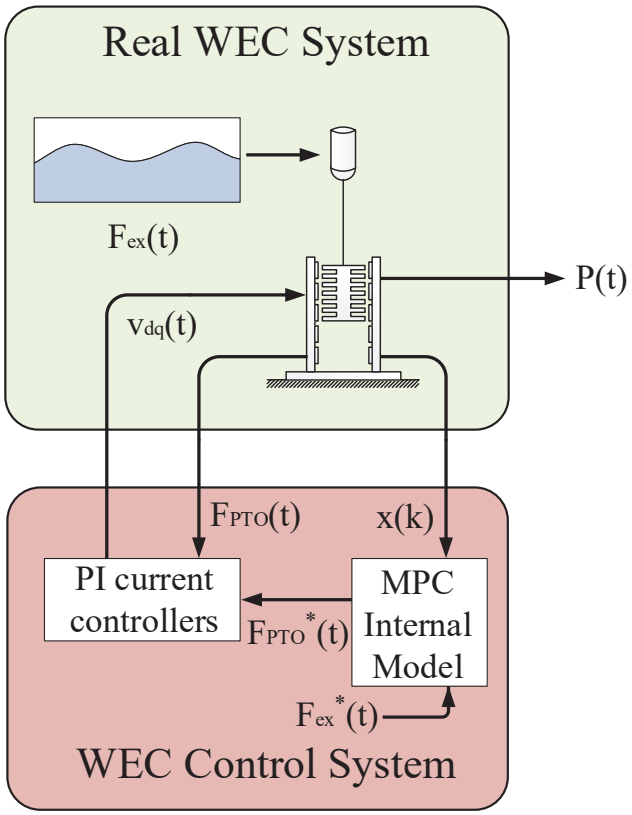

Figure 5.1: Outer loop control system. Situation: 1) the controller model and the system are the same. 2) the system changes over time introducing a mismatch between the controller model and the system

With the MPC so finely tuned to maximise the average electrical power from the ideal system, a mismatch could lead to a reduction in the average electrical power absorption. In this section the model mismatch effects between the control model and the system are investigated.

The main factors of model mismatch include: the mass of the WEC (which could increase due to bio-fouling) (O'Sullivan & Lightbody 2017*b*), the hydrostatic stiffness coefficient (which would change if there is dynamic change in cross sectional area), the radiation kernel and the non-linear viscosity effect (which could fluctuate with bio-fouling growth). For each of these factors, the average electrical power absorbed from a matched and unmatched MPC system are compared.

5.2.1 Mass Variation

Here the mismatch between the WEC mass in the control model and the system model is analysed. In reality the modelling mismatch of the WEC mass should be very small. However to test the control system during this mass mismatch, the control model was kept constant at the nominal plant model and the WEC model mass was varied by $\pm 10\%$ and $\pm 20\%$ from the nominal model. For this analysis the system was excited by 1 m high monochromatic waves and was controlled by a linearly constrained economic MPC, where the linear mechanical constraints include the heave displacement, the WEC velocity and the PTO force, as stated in (4.1). The effects on the average electrical absorbed power from the WEC mass mismatch are shown in Fig. 5.2. To have a fair analysis of the mismatch, the same systems were then tested with matching control models where the controller model has been retuned to be the same as the perturbed plant. Fig. 5.3 shows the ratio of the average power extracted from the mismatched system to that obtained if the controller model is retuned to match the perturbed plant.

From Fig. 5.2 it is clearly shown that when the mass of the WEC changes, there is a shift in average electrical power across the monochromatic spectrum. This figure shows the effect that the change in WEC mass has on the average power. However, Fig. 5.3 shows that the results obtained from the mismatched systems are not necessarily poor. Here it is shown that the mismatched system performs well (with a power ratio between 1 and 0.9) until the mismatched system starts to operate in frequencies higher than 1.1 rad.s^{-1}, where the average electrical power absorbed between the mismatched and matched systems start to diverge.

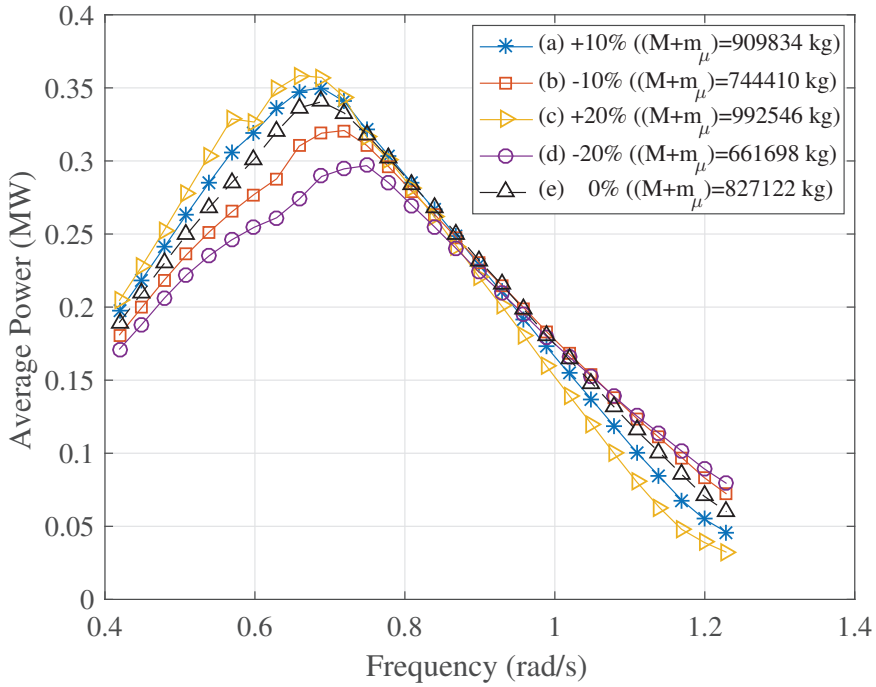

Figure 5.2: Average electrical powers absorbed from 1 m amplitude monochromatic waves, during a WEC mass mismatch of (a) $+10\%$, (b) -10%, (c) $+20\%$, (d) -20% and (e) a fully matched system

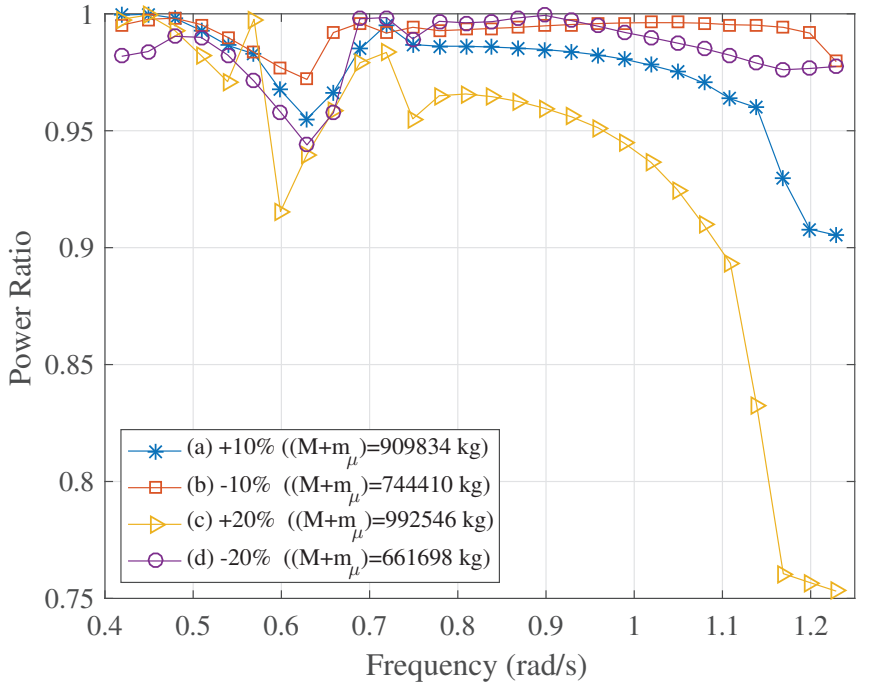

Figure 5.3: Power ratio from 1 m amplitude monochromatic waves (average power from mismatched system/average power from matched system) during a WEC mass mismatch of (a) $+10\%$, (b) -10%, (c) $+20\%$, (d) -20%

5.2.2 Hydrostatic Stiffness Coefficient Variation

The mismatch between the control model and the system model was then tested with changes in the hydrostatic stiffness. It is known from other research that non-linear effects produced from hydrodynamic Froude Krylov forces can affect the performance of the system, especially if the system is being actively controlled (Giorgi et al. 2016), or if the WEC has non-linear wetted surface area (Ringwood et al. 2014); which in this case, it does not. With the employment of active control in this work, it is essential that the mismatch in the hydrostatic stiffness coefficient is tested. As before, the average electrical power absorbed from the mismatched system was compared against the average power absorbed from the fully matched model when excited by 1 m high monochromatic waves.

The average electrical power absorbed from the mismatched models are shown in Fig. 5.4, while the ratio of the average power absorbed from the mismatch to the matched systems (with controller model returned to match the perturbed system) are shown in Fig. 5.5.

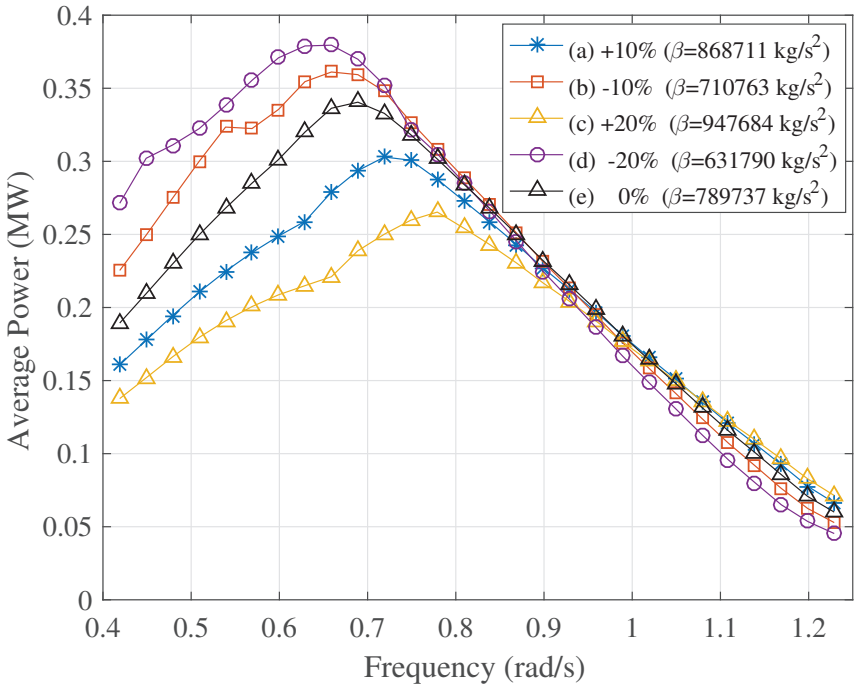

Figure 5.4: Average electrical powers absorbed from 1 m amplitude monochromatic waves, during hydrostatic stiffness coefficient mismatch of (a) $+10\%$, (b) -10%, (c) $+20\%$, (d) -20% and (e) a fully matched system

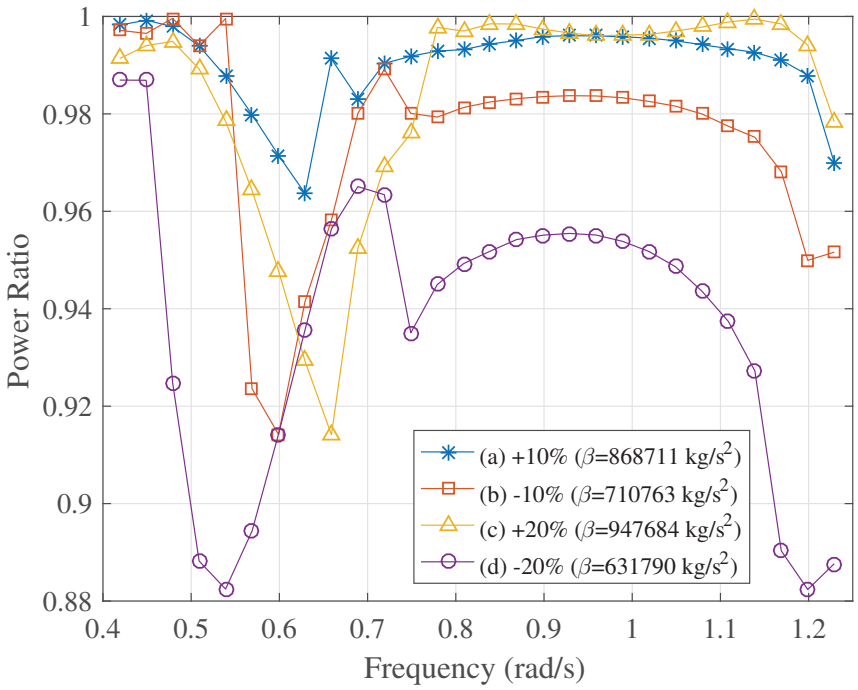

Figure 5.5: Power ratio absorbed from 1 m high monochromatic waves, (average power from mismatched system/average power from matched system) during a hydrostatic stiffness coefficient mismatch of (a) $+10\%$, (b) -10%, (c) $+20\%$, (d) -20%

As seen in Fig. 5.4, when there are mismatches between the system model and the control model, there are minor average power differences for frequencies greater than 0.9 rad.s^{-1}. However, there are substantial average power differences for lower frequencies (i.e. 0.1 MW between systems with a 0% and $+20\%$ mismatch at 0.7 rad.s^{-1}). Therefore, the extracted average electrical power from the system is highly dependent on the change in the hydrostatic stiffness coefficient. Even though the average power significantly fluctuates depending on the hydrostatic stiffness, the mismatch between the control model and the system model seems to have hardly any effect on the amount of average electrical power absorbed from the mismatched system, as can be seen in Fig. 5.5. The worst case was during the -20% model mismatch where the the power ratio dropped to 0.88. Furthermore, the use of an MPC with a hydrostatic stiffness mismatch in the control model can still produce an acceptable amount of average electrical power.

5.2.3 Radiation Kernel Variation

This subsection focusses on the mismatch between the control model and the system model in terms of uncertainty in the radiation kernel. The mismatched system was tested as before, excited with 1 m high monochromatic waves. The system mismatch

was achieved by varying the gain, poles and zeros of the radiation kernel within the mismatch bounds of $\pm 10\%$ and $\pm 20\%$. To test this mismatch in an unbiased manner, multiple variations of the mismatched radiation kernels had to be analysed since the radiation kernel is dependent on a number of parameters. The amount of tested randomised radiation kernel systems was increased until the mean average electrical power values across the ensemble was within $\pm 1\%$ of the average power absorbed from an ideal matched system (Metropolis & Ulam 1949); in this case, 70 randomised radiation kernel systems were tested for each monochromatic frequency, where a $\pm 1\%$ average electrical power tolerance was met for each frequency.

Fig. 5.6 shows the Monte-Carlo (Metropolis & Ulam 1949) results for the average electrical power absorbed from the system with a radiation kernel mismatch bounds of $\pm 10\%$ and $\pm 20\%$. For example at 0.7 rad.s^{-1}, the range of power extracted is anywhere between 0.28 and 0.36 MW, for combinations of the kernel parameters (gains, zeros and poles) perturbed in the range $\pm 20\%$ about their nominal values.

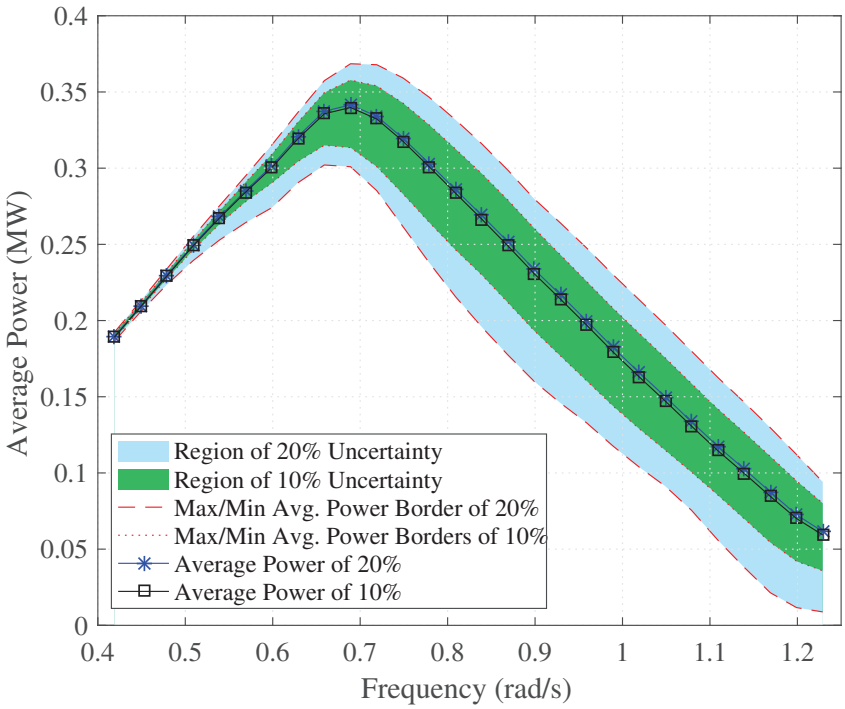

Figure 5.6: Average electrical power absorbed from 1m amplitude monochromatic waves, for a) matched, b) $\pm 10\%$ and c) $\pm 20\%$ mismatch. The $\pm 10\%$ and $\pm 20\%$ boundaries are also shown.

The change in radiation kernel has a great effect on the absorbable average electrical power, as shown in Fig. 5.6. To have a fair comparison, the power extracted for the mismatched radiation kernel systems that caused the maximum and minimum average power points for both $\pm 10\%$ and $\pm 20\%$ are now compared to the performance of

the matched control systems. Fig. 5.7 shows the power ratio, comparing the average power extracted when the system radiation kernel is mismatched to the controller, to the average electrical power extracted when the controller model is retuned to match the system. It is shown that over low frequencies of $(0.4 - 1.05)$ rad.s^{-1} that the mismatched control model produces acceptable results, since the power ratio is higher than 0.9 for both $\pm 10\%$ and $\pm 20\%$ cases. However, for frequencies > 1 rad.s^{-1}, the power ratios for the mismatched system begin to degrade. The worst case is for a 20% mismatch in the radiation kernel for high frequencies, leading to a minimum power ratio of 0.25. This may seem unacceptable, however, depending on the spectrum of the excitation waves, the power content at those frequencies may actually be inconsequential.

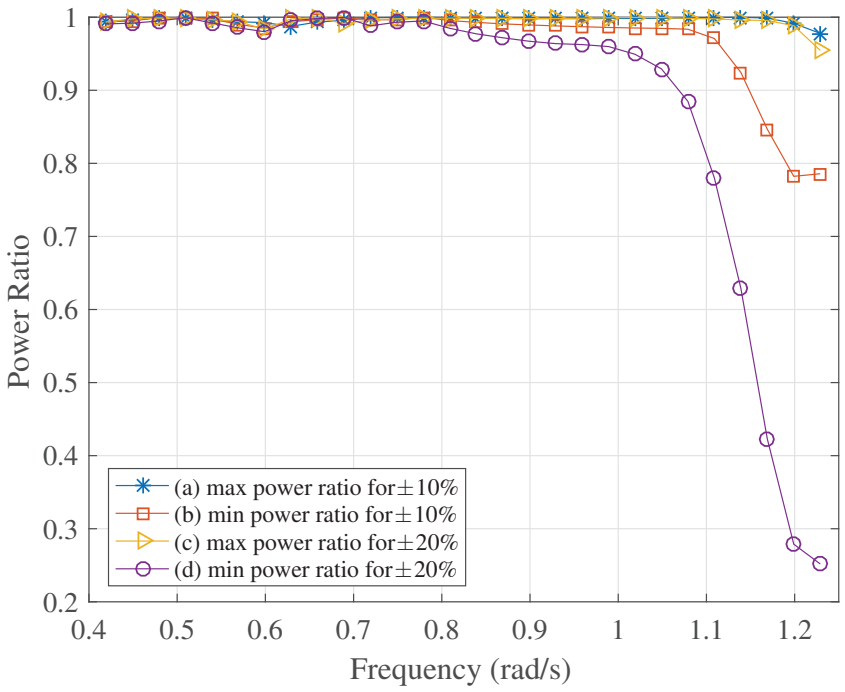

Figure 5.7: Power ratio absorbed from 1 m high monochromatic waves, (average power from mismatched system/average power from matched system) during a radiation kernel mismatch (a) Max power ratio over the ensemble for $\pm 10\%$ bounds on the parameters. (b) Min power ratio for $\pm 10\%$. (c) Max power ratio for $\pm 20\%$. (d) Min power ratio for $\pm 20\%$ bounds.

5.3 Effects of Viscosity on Power Absorption

One category that has been somewhat assumed as insignificant in previous wave energy research is the importance of including and modelling the non-linear components of the WEC system. The main non-linearity in the hydrodynamic system are the Froude-Krylov forces and the viscosity forces. In both (Guérinel et al. 2011, Penalba Retes et al. 2015), the effects of including non-linear Froude-Krylov forces in the hydrodynamics model were demonstrated. Whilst in (Bhinder et al. 2011, Giorgi et al. 2016), it was shown that without the implementation of active control, the effects on the power extraction are insignificant. However, when active control is used, the performance from the non-linear model considerably deviates from the linear model (Giorgi et al. 2016). In previous chapters (O'Sullivan & Lightbody 2017*a*), viscosity effects were not considered. In this section, it is initially assumed that the MPC prediction model is linear as in (O'Sullivan & Lightbody 2015) with no viscous modelling included. However, a non-linear WEC simulation model is now used, which includes viscosity as described in equation (5.1), which is in a convenient state space form from the original viscous Cummins equation (2.11, page 29).

$$\frac{d}{dt}\begin{bmatrix} z(t) \\ \dot{z}(t) \\ \boldsymbol{x_r}(t) \end{bmatrix} = A_c(t)\begin{bmatrix} z(t) \\ \dot{z}(t) \\ \boldsymbol{x_r}(t) \end{bmatrix} + B_c u_q(t) + F_c v(t) + E_c(t)\dot{\eta}(t) \tag{5.1}$$

where,

$$A_c(t) = \begin{bmatrix} 0 & 1 & \mathbf{0} \\ -\frac{\beta}{M+m_\mu} & -\frac{(D_r+C_{vis}(t))}{M+m_\mu} & -\frac{C_r}{M+m_\mu} \\ 0 & B_r & A_r \end{bmatrix}$$

$$F_c = B_c = \begin{bmatrix} 0 \\ 1 \\ \mathbf{0} \end{bmatrix} \quad E_c(t) = \begin{bmatrix} 0 \\ \frac{C_{vis}(t)}{M+m_\mu} \\ \mathbf{0} \end{bmatrix} \quad \boldsymbol{x}(t) = \begin{bmatrix} z(t) \\ \dot{z}(t) \\ \boldsymbol{x_r}(t) \end{bmatrix}. \tag{5.2}$$

As shown in chapter 3 (O'Sullivan & Lightbody 2016), the MPC involves maximising the average electrical power (5.3) within the mechanical linear constraints (WEC heave, WEC velocity and PTO force); this includes the resistive losses from the LPMG. For this section, no field weakening or non-linear electrical constraints are included in the MPC algorithm.

$$P_e = -\frac{1}{T}\int_{t=0}^{T}\left((M+m_\mu)\,u_q(t)\dot{z}(t) + \frac{R}{\psi^2}u_q^2(t)\right)dt \tag{5.3}$$

where,

$$\psi = \frac{\lambda'_{fd}\frac{\pi}{\tau}}{M+m_\mu}$$

λ'_{fd}, τ and R are the flux linkage, the pole pitch and the resistance of the LPMG. The system was tested using monochromatic waves of amplitude 1 m, ranging between 0.219 rad/s and 1.23 rad/s. The linear MPC (O'Sullivan & Lightbody 2017*a*) was tested on the system with and without constraints. This work examines the effect of including the viscous forces in the WEC system model. It is clear from Fig. 5.8 that the viscous force in the system model which is not accounted for in the linear MPC prediction model has a dramatic effect on the electrical power production. In fact, in this example, negative electrical power is produced over a wide frequency range. This points to the fact that the relative velocity between the device and the sea surface must be significant, hence causing a serious model mismatch. Some improvement in performance of the viscous system is obtained by the presence of the mechanical constraints, since it decreases the model mismatch by restricting the relative velocity. However, the power absorption across the frequency range is still unsatisfactory.

5.3.1 Non-linear Model Predictive Control

The inclusion of viscosity within the MPC model yields a non-linear MPC problem. In this work, a NMPC, which is comparable to (Huzmezan & Maciejowski 1998), is implemented. To simplify the optimisation problem, the prediction model is linearised at each step across the prediction horizon, using the predicted velocities obtained from the solution to the optimal control problem at the last control sample. By using predicted velocities, the non-linear viscous coefficient can then be linearised at each control sample (5.4) across the prediction horizon,

$$\tilde{\boldsymbol{C}}_{\boldsymbol{vis}}(k+i) = \rho C_d A\left|\dot{\boldsymbol{z}}^*(k+i|k-1) - \dot{\boldsymbol{\eta}}(k+i)\right|, \tag{5.4}$$

where $\dot{\boldsymbol{z}}^*(k+i|k-1)$ is the predicted velocity at the i^{th} step into the future, from the optimal state trajectory predicted as part of the solution for the controls at the $(k-1)^{th}$ sample. It is assumed here that the sea surface velocity $\dot{\boldsymbol{\eta}}(k+i)$ is known over the prediction horizon.

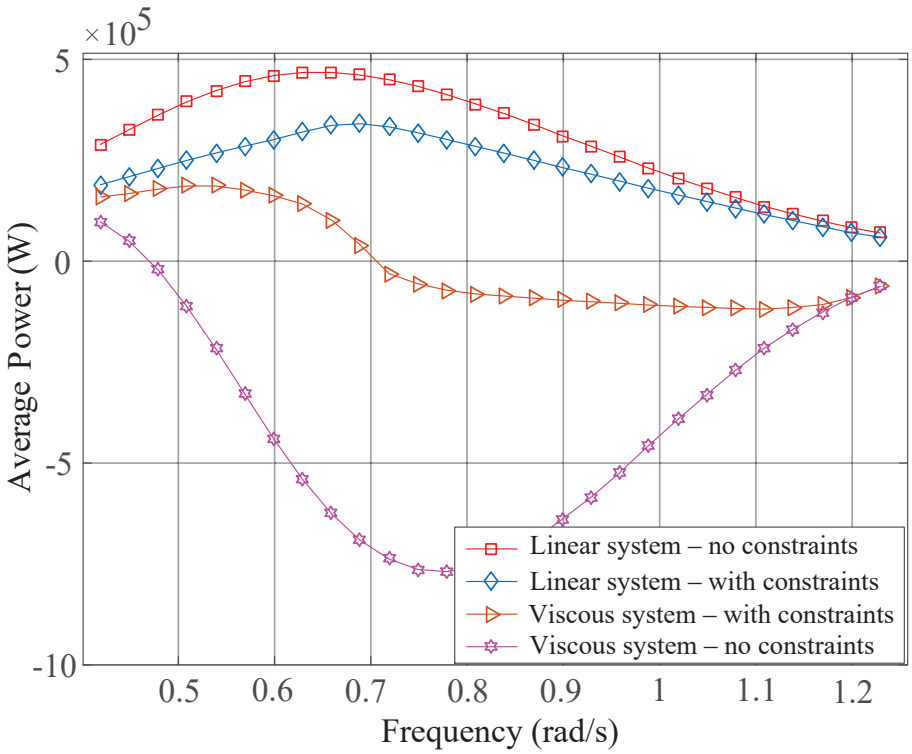

Figure 5.8: Average electrical power produced from monochromatic waves with amplitude 1 m. A linear inviscid control model is used within the MPC in each case. i) Linear inviscid system, without constraints ii) Linear inviscid system with constraints, iii) Non-linear viscous system with constraints, iv) Non-linear viscous system without constraints

Using these predicted velocities, $\dot{\boldsymbol{z}}^*(k+i|k-1)$ and $\dot{\boldsymbol{\eta}}(k+i)$, the non-linear $A_c(t)$ and $E_c(t)$ matrices from (5.1) can then be linearised at each control step over the horizon, as shown in (5.5),

$$\tilde{A}_c(k+i) = \begin{bmatrix} 0 & 1 & \mathbf{0} \\ -\frac{\beta}{M+m_\mu} & -\frac{(D_r+\tilde{C}_{vis}(k+i))}{M+m_\mu} & -\frac{C_r}{M+m_\mu} \\ 0 & B_r & A_r \end{bmatrix}$$
$$\tilde{E}_c(k+i) = \begin{bmatrix} 0 \\ \frac{\tilde{C}_{vis}(k+i)}{M+m_\mu} \\ \mathbf{0} \end{bmatrix}. \tag{5.5}$$

The digitisation of the continuous model (5.1) was accomplished assuming a first order hold (FOH) (Cretel et al. 2011). Integral action was also included. This results in the

following discrete time, LPV prediction model (Tóth 2010),

$$\begin{aligned}\boldsymbol{x_b}(k+i+1) &= A_b(k+i)\boldsymbol{x_b}(k+i) + B_b(k+i)\Delta u(k+i+1)\\ &+F_b(k+i)\Delta v(k+i+1) + E_b(k+i)\Delta\dot{\eta}(k+i+1)\\ \boldsymbol{y_b}(k+i+1) &= C_b\boldsymbol{x_b}(k+i+1),\end{aligned} \tag{5.6}$$

where $i \in \{0, 1, .., (N_p - 1)\}$ and

$$\boldsymbol{x_b}(k) = \begin{bmatrix} z(k)\\ \dot{z}(k)\\ \boldsymbol{x_r}(k)\\ u(k)\\ v(k)\\ \dot{\eta}(k)\end{bmatrix} \boldsymbol{y_b}(k) = \begin{bmatrix} z(k)\\ \dot{z}(k)\\ u(k)\\ \dot{\eta}(k)\end{bmatrix}$$

$$A_b(k+i) = \left[\begin{array}{c|ccc} e^{\tilde{A}_c(k+i)T_L} & \Lambda_B(k+i) & \Lambda_B(k+i) & \Lambda_V(k+i)\\ \hline \mathbf{0} & 1 & 0 & 0\\ \mathbf{0} & 0 & 1 & 0\\ \mathbf{0} & 0 & 0 & 1\end{array}\right].$$

Here $A_b(k+i) \in \mathbb{R}^{(n+5)\times(n+5)}$, $\Lambda_B(k+i) = \tilde{A}_c(k+i)^{-1}\left(e^{\tilde{A}_c(k+i)T_L} - I\right)B_c$, $\Gamma_B(k+i) = \frac{1}{T_L}\tilde{A}_c(k+i)^{-1}\left(\Lambda_B(k+i) - T_L B_c\right)$. Then using the linear approximation $\tilde{E}_c(k+i)$ from (5.5), the following can be constructed,

$$B_b(k+i) = \left[\begin{array}{c} \Gamma_B(k+i)\\ \hline 1\\ 0\\ 0\end{array}\right] \in \mathbb{R}^{(n+5)\times 1}$$

$$F_b(k+i) = \left[\begin{array}{c} \Gamma_B(k+i)\\ \hline 0\\ 1\\ 0\end{array}\right] \in \mathbb{R}^{(n+5)\times 1}$$

$$E_b(k+i) = \left[\begin{array}{c} \Gamma_V(k+i)\\ \hline 0\\ 0\\ 1\end{array}\right] \in \mathbb{R}^{(n+5)\times 1}$$

where, $\Lambda_V(k+i) = \tilde{A}_c(k+i)^{-1}\left(e^{\tilde{A}_c(k+i)T_L} - I\right)\tilde{E}_c(k+i)$, $\Gamma_V(k+i) = \frac{1}{T_L}\tilde{A}_c(k+i)^{-1}\left(\Lambda_V(k+i) - T_L\tilde{E}_c(k+i)\right)$

The following prediction equation can be formed to predict the output vector at the k^{th} sample over the N_p steps of the prediction horizon,

$$\hat{\boldsymbol{Y}}(k) = P\boldsymbol{x}_b(k) + G\boldsymbol{\Delta U}(k) + H\boldsymbol{\Delta V}(k) + M_o\boldsymbol{\Delta\dot{\eta}}(k), \tag{5.7}$$

where $\hat{\boldsymbol{Y}}(k) \triangleq \left[\boldsymbol{y_b}(k+1|k)^T .....\boldsymbol{y_b}(k+N_p|k)^T\right]^T$ and $\boldsymbol{\Delta U}(k)$, $\boldsymbol{\Delta V}(k)$ and $\boldsymbol{\Delta\dot{\eta}}(k)$ have the same structure. $P \in \mathbb{R}^{4N_p\times(n+5)}$, $G \in \mathbb{R}^{4N_p\times N_p}$, $H \in \mathbb{R}^{4N_p\times N_p}$ and $M_o \in \mathbb{R}^{4N_p\times N_p}$,

$$P = \begin{bmatrix} C_bA_b(k) \\ C_b\boldsymbol{\Phi}_1A_b(k) \\ : \\ C_b\boldsymbol{\Phi}_{N-1}A_b(k) \end{bmatrix},$$

$$H = \begin{bmatrix} C_bB_b(k) & 0 & .. & 0 \\ C_b\boldsymbol{\Phi}_1B_b(k) & C_bB_b(k+1) & .. & 0 \\ : & : & \ddots & : \\ C_b\boldsymbol{\Phi}_{N-1}B_b(k) & C_b\boldsymbol{\Phi}_{N-2}B_b(k+1) & .. & C_bB_b(k+N_p-1) \end{bmatrix} \tag{5.8}$$

Here G, H and M_o have a similar structure to H (5.8) and $\boldsymbol{\Phi}_n = \prod_{j=1}^{n} A_b(k+j)$.

As shown in chapter 3 (O'Sullivan & Lightbody 2017*a*), by using (5.7), a cost function (5.9) can be formed. By minimising this cost function with the incorporation of the linear constraints, using linear QP via MATLAB (R2016a) (Matlab 2010) `quadprog` the optimal $\boldsymbol{\Delta u}(k+i|k)$ values can be found; these optimal values allow maximum power absorption.

$$\begin{aligned} J = &\frac{1}{2}\boldsymbol{\Delta U}^TG^TQG\boldsymbol{\Delta U} + \boldsymbol{\Delta U}^TG^TQ\left(P\boldsymbol{x_b} + H\boldsymbol{\Delta V} + M_o\boldsymbol{\Delta\dot{\eta}}\right) \\ &+\frac{1}{2}\left(P\boldsymbol{x_b} + H\boldsymbol{\Delta V} + M_o\boldsymbol{\Delta\dot{\eta}}\right)^TQ\left(P\boldsymbol{x_b} + H\boldsymbol{\Delta V} + M_o\boldsymbol{\Delta\dot{\eta}}\right) \end{aligned} \tag{5.9}$$

This non-linear viscid hydrodynamic system was then tested with the NMPC algorithm with and without linear mechanical constraints. To provide reference results showing the optimal electrical power extraction that is available, the models in the simulation and controller are matched. The system was tested under multiple sea states, with the significant height and mean wave period selected for each sea state. Each sea state was implemented using a Bretschneider spectrum (Tucker & Pitt 2001), which produced

irregular waveforms, where the sea state characteristics are shown in table 5.1. It was assumed that the future excitation waveforms were known for the finite horizon, with $N_p = 100$ and an outer sampling period of $T_L = 0.1$ s,

Table 5.1: Sea states

Sea state no.	Significant height H_s (m)	Peak Wave Period T_p (s)
1	1.5	6
2	1.5	9.66
3	1.5	13.326
4	3	9.66
5	3	13.326
6	4.5	9.66
7	4.5	13.326
8	6	13.326
9	6	17

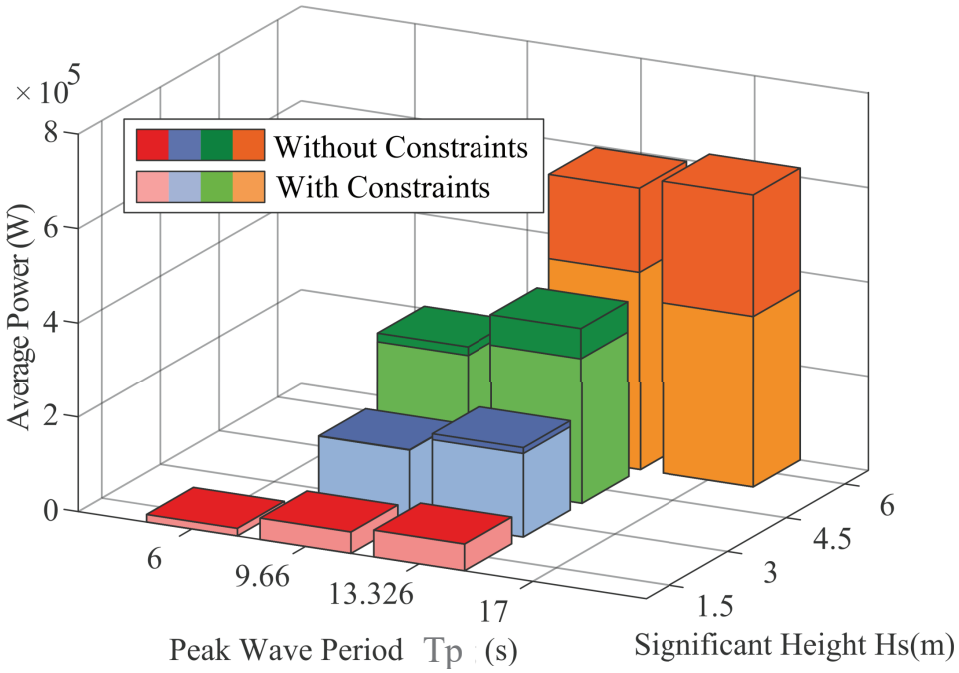

Figure 5.9: NMPC Monte Carlo test results of the average electrical power absorbed from irregular waves using a Bretschneider spectrum with a range of different peak wave periods and significant heights

It is shown in Fig. 5.9 that the NMPC succeeds in producing positive average electrical power, unlike the previous case in which there was no viscosity term in the MPC model (Fig. 5.8). When the NMPC with and without constraints are compared, it is shown that the impact of the linear constraints on the absorbed average electrical power is insignificant until the seventh sea state ($T_p = 13.326$ s $H_s = 4.5$ m) . From the seventh sea state, the PTO force is then used from time to time to prevent the system from

operating outside the feasible region in the near future, hence, reducing the average electrical power from the unconstrained maximum.

5.4 MPC Algorithm Simplification

5.4.1 Linear Viscid Model Predictive Control

The NMPC shown in section 5.3.1 produces promising results, but at the cost of increased computational effort for this application. The NPMC uses approximately 2.5 times the computational time of the linear MPC for the unconstrained case and 5 times the computational time when constraints are included. A more efficient method for dealing with the viscous forces in the MPC model would be a linear MPC which includes a linear estimate of the non-linear viscosity force, that is fine tuned for each sea state.

The linear viscid Model Predictive Controller is used to approximate the NMPC, where the linear viscous coefficient estimate ($\tilde{C}_{vis}$) is chosen to produce similar average electrical power at each sea-state when compared to the full NMPC, but without the computational complexity. Here a constant $\tilde{C}_{vis}$ is selected for each sea-state, to provide constant matrices $\tilde{A}_c$ and $\tilde{E}_c$ as defined in (5.5) and (5.10). Hence, for a given sea-state this represents a linear MPC problem.

$$\tilde{F}_v(t) = -\tilde{C}_{vis}\left(\dot{z}(t) - \dot{\eta}(t)\right) \tag{5.10}$$

The results in Fig. 5.10 show how the electrical power extracted depends on the choice of $\tilde{C}_{vis}$. Here the MPC system was tested for sea state 3 ($T_p = 13.326$ s $H_s = 1.5$ m) and sea state 8 ($T_p = 13.326$ s $H_s = 6$ m), with and without constraints. There is a unique $\tilde{C}_{vis}$ value that corresponds to the maximum extractable average electrical power; the optimum $\tilde{C}_{vis}$ value for sea state 3 is 1×10^5 kg/s and the optimum $\tilde{C}_{vis}$ value for sea state 8 is 2.1×10^5 kg/s.

When the linear constraints are included in the MPC, the relative velocity between the wave and WEC is restricted, especially at higher sea states where the WEC velocity constraints are frequently active. This relative velocity restriction causes the average electrical power to be insensitive to choices of $\tilde{C}_{vis}$ at higher sea states, as shown in Fig. 5.10(b).

The linear MPC, with and without constraints, was tested across the entire sea state

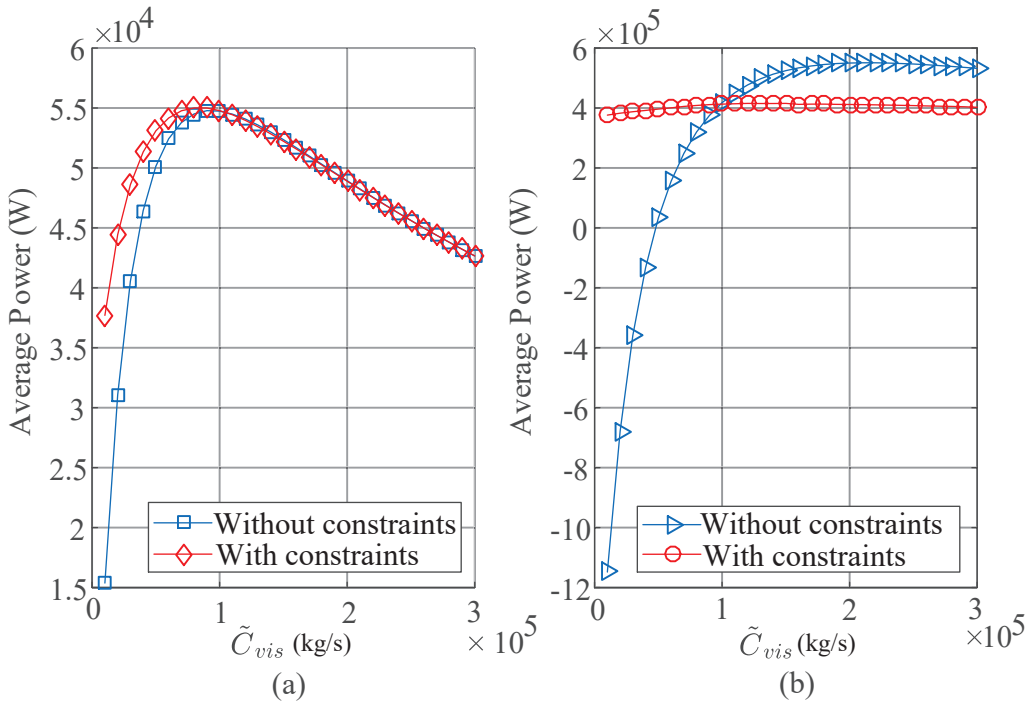

Figure 5.10: Linear MPC performance (assuming a linear viscosity model in the controller) with and without constraints. Average electrical power absorbed from (a) sea state 3 ($T_p = 13.326$ s $H_s = 1.5$ m), (b) sea state 8 ($T_p = 13.326$ s $H_s = 6$ m) using a Bretschneider spectrum

range, where the optimum $\tilde{C}_{vis}$ values corresponding to the maximum average power points are shown in Fig. 5.11. This also shows the $\tilde{C}_{vis}$ regions where the average power is above 98% of the maximum average power available ($\tilde{\boldsymbol{C}}_{\boldsymbol{vis98\%}}$).

From Fig. 5.11, the optimal $\tilde{C}_{vis}$ value with constraints increases somewhat proportionally with the corresponding sea state, but at a much reduced rate than when constraints are not included. It is also shown that when the constraints are included, the $\tilde{\boldsymbol{C}}_{\boldsymbol{vis98\%}}$ regions broaden, which then causes a larger common $\tilde{\boldsymbol{C}}_{\boldsymbol{vis98\%}}$ overlap across the sea states. Therefore, a sea state invariant $\tilde{C}_{vis}$ estimate value can be found, which allows the average electrical power for all sea states to operate between 96% to 100% of the maximum power available, hence allowing a simple and efficient way of sub-optimally extracting acceptable electrical power. In this example, when the constraints are included, a constant $\tilde{C}_{vis} = 1 \times 10^5$ kg/s would provide between $96 - 100\%$ of the average electrical power extracted by optimally tuning $\tilde{C}_{vis}$ for each sea-state.

Variations in the viscosity force could be caused by increasing growth of biofouling on the WEC itself (Wright et al. 2016), which could change the hydrodynamic properties of the WEC. Furthermore, it is important to analyse the effects that a mismatched control model has on the average power absorbed from the viscous system, since the viscous drag coefficient could vary around a certain value in practice (Nepf 1999).

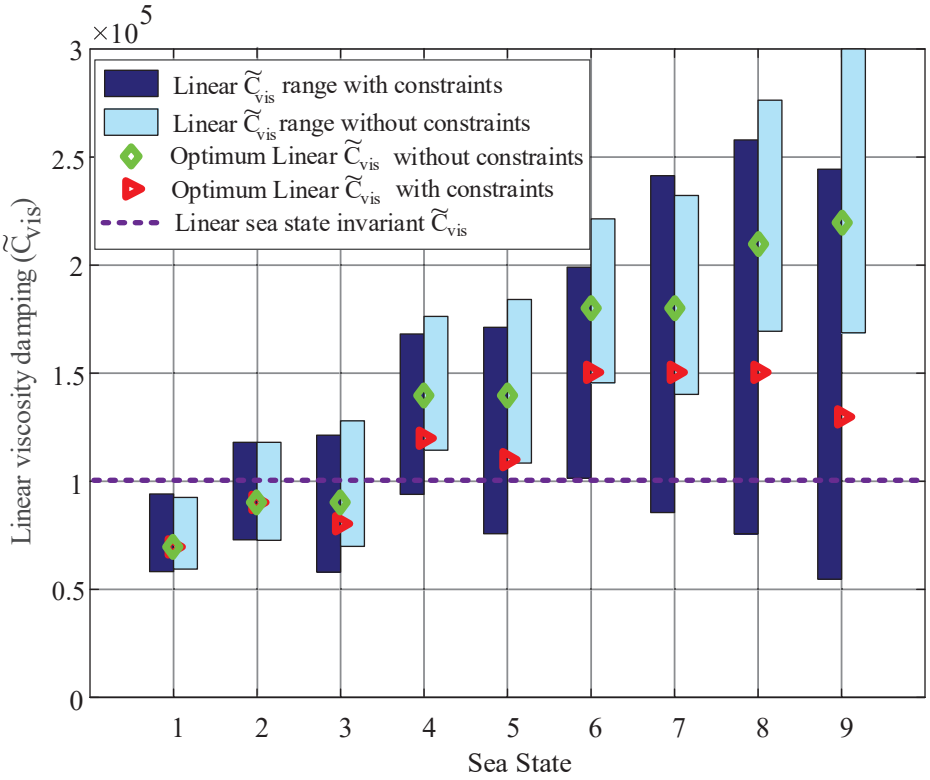

Figure 5.11: The linear viscous term $\tilde{C}_{vis}$ versus the range of sea states. Showing the $\tilde{C}_{vis}$ values which correspond to an MPC with an efficiency greater than 98%, $\tilde{\boldsymbol{C}}_{\boldsymbol{vis98\%}}$ (results found using an NMPC were taken as 100% efficiency). This figure shows that as linear mechanical constraints are included into the MPC algorithm, the $\tilde{\boldsymbol{C}}_{\boldsymbol{vis98\%}}$ regions decrease to a point where a single $\tilde{C}_{vis}$ value of $\tilde{C}_{vis} = 1 \times 10^5$ can be utilised to allow efficiency greater than 96% across all sea states.

The robustness of the MPC due to a viscous mismatch is tested by changing the non-linear viscosity drag coefficient C_d in the hydrodynamic system by $\pm 10\%$ and $\pm 20\%$, where $C_d = 1.8$ when a mismatch of 0% occurs; the robustness analysis utilises 1 m high monochromatic excitation waves. The economic MPC with a constant linear viscous approximation $\tilde{C}_{vis} = 1 \times 10^5$ kg/s, (O'Sullivan & Lightbody 2017*c*), is used in this section to analyse the robustness of the linear MPC when changes in the non-linear hydrodynamic model occur. Fig. 5.12 shows the resulting absorbed average electrical power found from a hydrodynamic system with a $\pm 10\%$ and $\pm 20\%$ mismatched viscous drag coefficient C_d. As shown in Fig. 5.12, as the C_d viscous drag coefficient increases $(+10\%,\ +20\%)$ and the MPC's linear viscous coefficient $\tilde{C}_{vis}$ stays constant, the average electrical power decreases. Furthermore, as the viscous drag coefficient C_d is reduced $(-10\%,\ -20\%)$, the average electrical power increases. Fig. 5.13 shows the power ratio (5.11) that each mismatched system has against its corresponding matched system; the corresponding matched system involves changing the non-linear drag coefficient C_d in the NMPC's internal model to obtain maximum average electrical power levels from each hydrodynamic model variation,

$$\text{Power Ratio} = \frac{P_{e,mismatch}}{P_{e,match}}, \tag{5.11}$$

where $P_{e,mismatch}$ is the average electrical power from a WEC system with a varying C_d coefficient, controlled with an MPC with a constant $\tilde{C}_{vis} = 1 \times 10^5$ kg/s. $P_{e,match}$ is the average electrical power from a WEC system with a varying C_d, controlled with an NMPC with the same C_d value as the WEC system.

It is shown in Fig. 5.13 that the power ratios for both the $\pm 10\%$ and $\pm 20\%$ cases are all above 0.91; therefore the linear viscous approximated MPC is acceptable for use when the viscosity is uncertain.

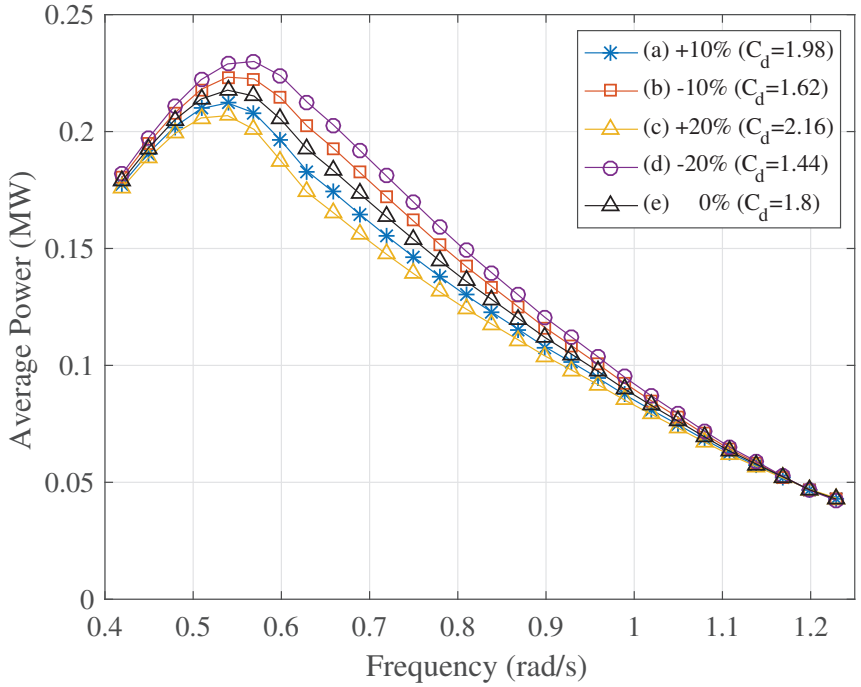

Figure 5.12: Average electrical power absorbed from 1 m high monochromatic excitation waves when an MPC with a constant viscous coefficient $\tilde{C}_{vis} = 1 \times 10^5$ is tested on a hydrodynamic system with a non-linear drag coefficient mismatch of (a) $+10\%$ ($C_d = 1.98$), (b) -10% ($C_d = 1.62$), (c) $+20\%$ ($C_d = 2.16$), (d) -20% ($C_d = 1.44$) and (e) 0% ($C_d = 1.8$)

5.4.1.1 Performance of Linear MPC

The performance of the system under NMPC, linear MPC (with optimal $\tilde{C}_{vis}$ selected for each sea-state) and a linear MPC with constant linear viscous damping ($\tilde{C}_{vis} = 1 \times 10^5$ kg/s) was compared over the 9 sea states as defined in Table 5.1. In Fig. 5.14, it is shown that in the unconstrained case, the average electrical power produced by the

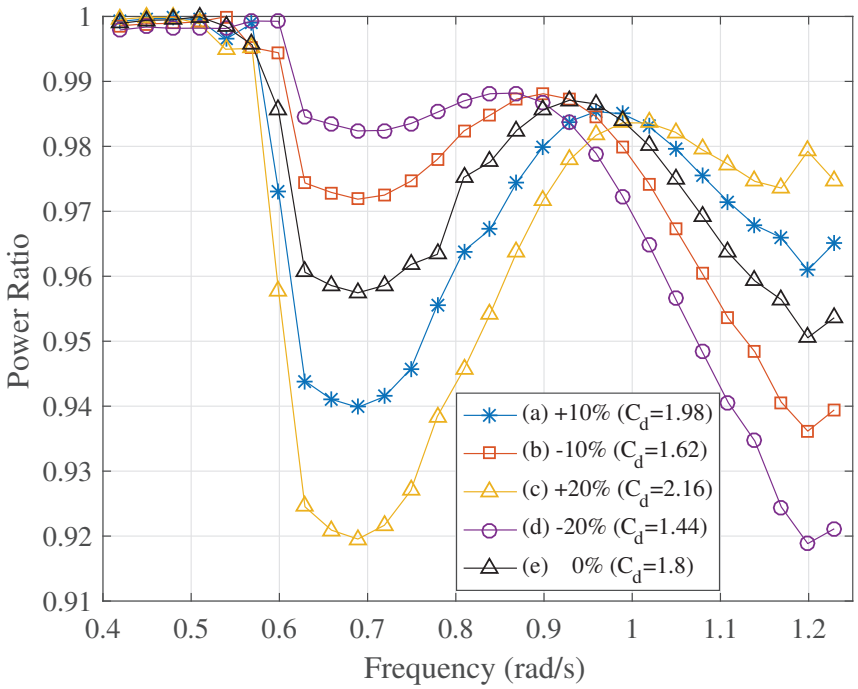

Figure 5.13: Power ratio from 1 m high monochromatic excitation waves when an MPC with a constant viscous coefficient $\tilde{C}_{vis} = 1 \times 10^5$ is tested on a hydrodynamic system with a non-linear drag coefficient of (a) $+10\%$ ($C_d = 1.98$), (b) -10% ($C_d = 1.62$), (c) $+20\%$ ($C_d = 2.16$), (d) -20% ($C_d = 1.44$) and (e) 0% ($C_d = 1.8$)

NMPC and the linear MPC (with optimal $\tilde{C}_{vis}$ selected for each sea-state) are similar up to sea-state 7. Furthermore, the average electrical powers produced when using the linear MPC with a constant linear viscous damping ($\tilde{C}_{vis} = 1 \times 10^5$ kg/s) diverged from the NMPC average electrical powers as the sea-state increased.

When examining the constrained case, where these MPC methods all included linear mechanical constraints within their algorithms (4.1), as shown in Fig. 5.15, it is important to note that all three controllers provided similar average electrical power extraction, except at the energetic sea-state 9. This implies that mechanical constraints in this example, limit the relative velocity and allow for excellent performance of the linear MPC, with a fixed linear viscous damping model.

5.4.2 Reduction of the Computational Load using Move-blocking

Constrained optimisation forms the basis of most MPC control laws, which makes it advantageous over other control methods. However, the computational load that comes with it is undesirable (Genest & Ringwood 2016), especially when the computationally expensive NMPC is implemented. In this section, an assessment of different control horizon curtailments is carried out to simplify the online complexity of the MPC opti-

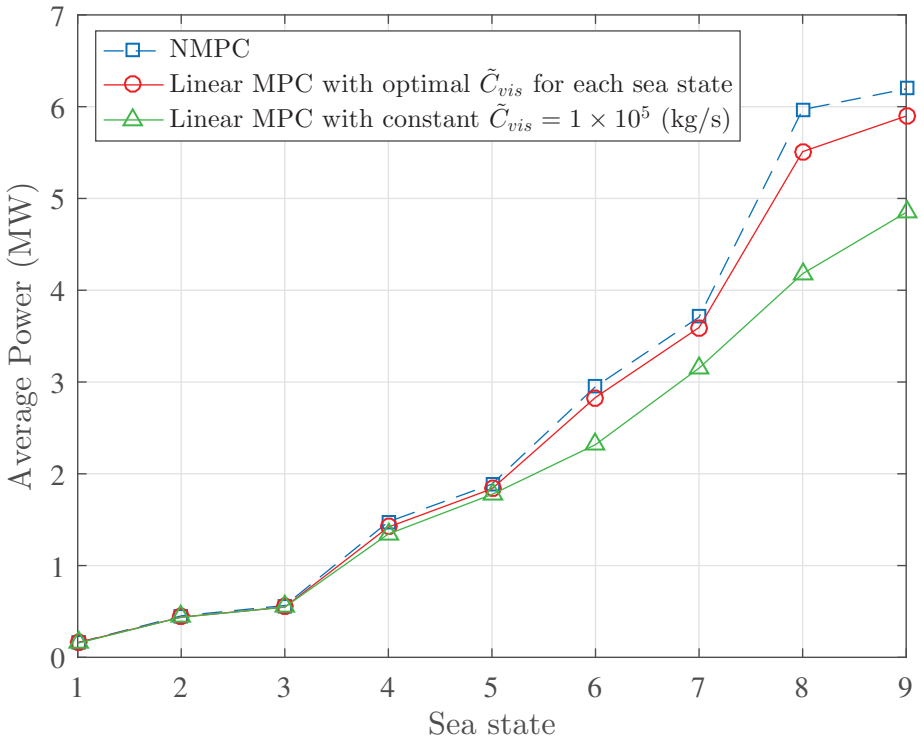

Figure 5.14: Unconstrained case: A comparison of the average electrical powers obtained using i) NMPC, ii) Linear MPC, where $\tilde{C}_{vis}$ optimally tuned for each sea state and iii) Linear MPC, with $\tilde{C}_{vis} = 1 \times 10^5$ (kg/s) which is constant for all sea states.

misation, whilst not sacrificing the performance of the system. Using a move-blocking technique (Cagienard et al. 2007), the number of free variables in the control horizon can be significantly reduced while maintaining a similar performance when compared with a standard economic MPC with a longer control horizon. This curtailment reduces the amount of unnecessary computational power that would have previously been used to calculate the variables in the control horizon that would have had an insignificant effect on the performance of the controller.

An economic MPC controller typically uses a control horizon of $N_c \leq N_p$ free control choices over the prediction horizon. The computational burden can be lowered by decreasing N_c, but at the cost of reducing performance.

Two types of control horizons are used in this section. First a standard control horizon reduction is applied where the control variables $\Delta u_q(k+i)$ are set to zero after the first N_c steps of the prediction horizon,

$$\boldsymbol{\Delta u_{qh}}(k) = \left[\begin{array}{c|c} \boldsymbol{I}_{N_c} & \boldsymbol{0}_{N_c \times N_r} \\ \hline \boldsymbol{0}_{N_r \times N_c} & \boldsymbol{0}_{N_r \times N_r} \end{array}\right] \boldsymbol{\Delta u_q}(k),$$

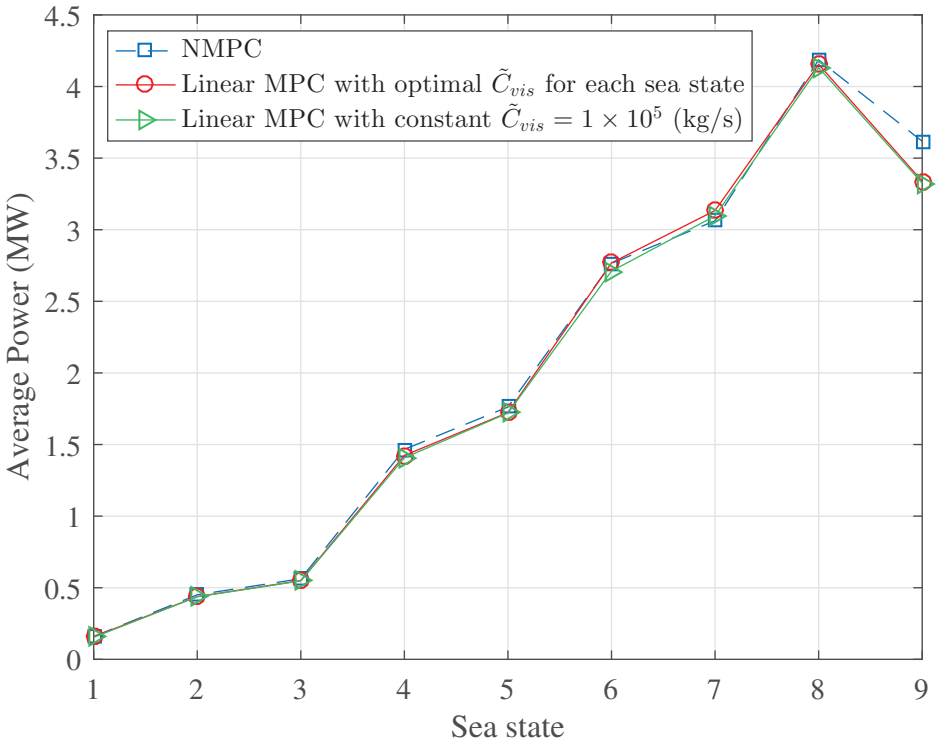

Figure 5.15: Constrained case: A comparison of the average electrical powers using i) NMPC, ii) Linear MPC, where the optimally tuned $\tilde{C}_{vis}$ estimations are used and iii) Linear MPC, with a sea state invariant $\tilde{C}_{vis} = 1 \times 10^5$ (kg/s) which is constant for all sea states. The constraints used in these tests were linear mechanical constraints, including heave displacement, WEC velocity and PTO force.

where $\boldsymbol{\Delta u_{qh}}(k) \in \mathbb{R}^{N_c \times 1}$, $N_r = (N_p - N_c)$. For example, if $N_p = 4$ and $N_c = 2$ then,

$$\mathbf{\Delta u_{qh}}(k) = \left[\begin{array}{cc:cc} 1 & 0 & 0 & 0 \\ 0 & 1 & 0 & 0 \\ \hdashline 0 & 0 & 0 & 0 \\ 0 & 0 & 0 & 0 \end{array}\right] \left[\begin{array}{c} \Delta u_q(k+1) \\ \Delta u_q(k+2) \\ \Delta u_q(k+3) \\ \Delta u_q(k+4) \end{array}\right] = \left[\begin{array}{c} \Delta u_q(k+1) \\ \Delta u_q(k+2) \end{array}\right]. \tag{5.12}$$

In the second method, a move-blocking is used where the N_c control variables are appropriately spread out across the prediction horizon N_p (Cagienard et al. 2007), with the control variables concentrated over the early stages of the prediction horizon,

$$\boldsymbol{\Delta u_{q_m}}(k) = \left[\begin{array}{cccc} \mathbf{\Phi}_1 & \mathbf{0} & \dots & \mathbf{0} \\ \mathbf{0} & \mathbf{\Phi}_2 & \dots & \mathbf{0} \\ \vdots & \vdots & \ddots & \vdots \\ \mathbf{0} & \mathbf{0} & \dots & \mathbf{\Phi}_{N_c} \end{array}\right] \boldsymbol{\Delta u_q}(k) \tag{5.13}$$

where $\boldsymbol{\Delta u_{q_m}}(k) \in \mathbb{R}^{N_c \times 1}$,

$$\boldsymbol{\Phi}_j = \left[\begin{array}{c:c} \mathbf{1}_{\boldsymbol{n}_j \times 1} & \mathbf{0}_{\boldsymbol{n}_j \times (\boldsymbol{n}_j - 1)} \end{array} \right] \in \mathbb{R}^{n_j \times n_j}, \tag{5.14}$$

where matrix $\boldsymbol{n} \in \mathbb{R}^{N_c \times 1}$ is a user defined array and $\sum_{j=1}^{N_c} \boldsymbol{n}_j = N_p$. For example, if $N_p = 10$, $N_c = 4$, hence

$$\boldsymbol{n} = \begin{bmatrix} 1 \\ 2 \\ 3 \\ 4 \end{bmatrix} \in \mathbb{R}^{4 \times 1}, \ \sum_{j=1}^{4} \boldsymbol{n}_j = 10. \tag{5.15}$$

This yields,

$$\boldsymbol{\Delta u_{q_m}}(k) = \left[\begin{array}{c:cc:ccc:ccc} 1 & 0 & 0 & 0 & 0 & 0 & 0 & 0 & 0 & 0 \\ \hdashline 0 & 1 & 0 & 0 & 0 & 0 & 0 & 0 & 0 & 0 \\ 0 & 1 & 0 & 0 & 0 & 0 & 0 & 0 & 0 & 0 \\ \hdashline 0 & 0 & 0 & 1 & 0 & 0 & 0 & 0 & 0 & 0 \\ 0 & 0 & 0 & 1 & 0 & 0 & 0 & 0 & 0 & 0 \\ 0 & 0 & 0 & 1 & 0 & 0 & 0 & 0 & 0 & 0 \\ \hdashline 0 & 0 & 0 & 0 & 0 & 0 & 1 & 0 & 0 & 0 \\ 0 & 0 & 0 & 0 & 0 & 0 & 1 & 0 & 0 & 0 \\ 0 & 0 & 0 & 0 & 0 & 0 & 1 & 0 & 0 & 0 \\ 0 & 0 & 0 & 0 & 0 & 0 & 1 & 0 & 0 & 0 \end{array} \right] \left[\begin{array}{c} \Delta u_q(k+1) \\ \hdashline \Delta u_q(k+2) \\ \Delta u_q(k+3) \\ \hdashline \Delta u_q(k+4) \\ \Delta u_q(k+5) \\ \Delta u_q(k+6) \\ \hdashline \Delta u_q(k+7) \\ \Delta u_q(k+8) \\ \Delta u_q(k+9) \\ \Delta u_q(k+10) \end{array} \right], \tag{5.16}$$

where

$$\boldsymbol{\Delta u_{q_m}} = \left[\begin{array}{c} \Delta u_q(k+1) \\ \hdashline \Delta u_q(k+2) \\ \Delta u_q(k+2) \\ \hdashline \Delta u_q(k+4) \\ \Delta u_q(k+4) \\ \Delta u_q(k+4) \\ \hdashline \Delta u_q(k+7) \\ \Delta u_q(k+7) \\ \Delta u_q(k+7) \\ \Delta u_q(k+7) \end{array} \right] \in \mathbb{R}^{10 \times 1}. \tag{5.17}$$

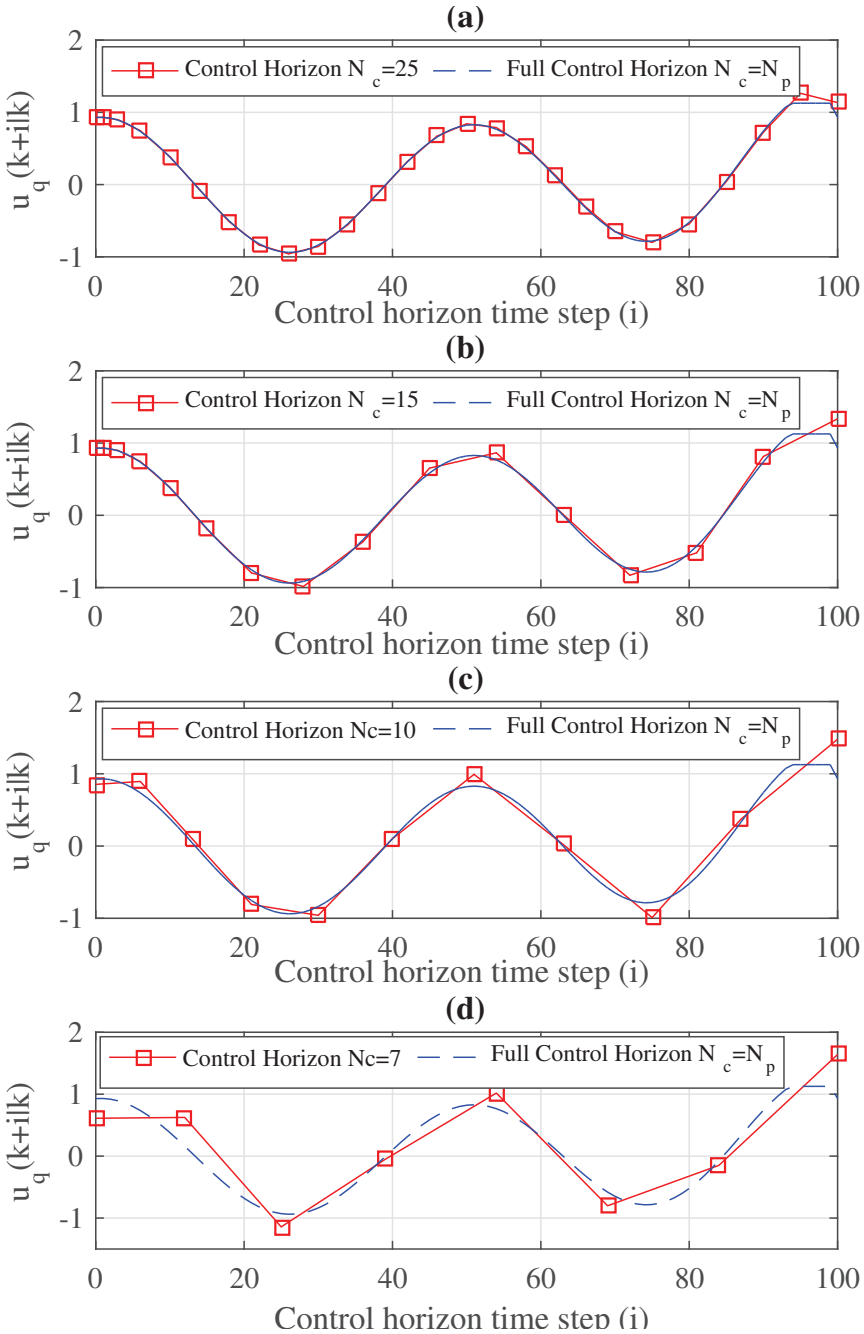

Figure 5.16: A comparison between the control variables $u_q(k+i)$ created when using a full control horizon ($N_c = 100$) and when a move-blocking control horizon of (a) $N_c = 25$,(b) $N_c = 15$, (c) $N_c = 10$ and (d) $N_c = 7$ is used

It is shown from the waveforms in Fig. 5.16 that as the control horizon N_c decreases, the control action across the prediction horizon becomes more disjointed and deviates from the control waveform when $N_c = N_p$; this results in the deterioration of average power. However, by incorporating a move-blocking fewer control variables need to be calculated over the prediction horizon. Therefore, there needs to be a balance between minimising the amount of control variables and maintaining an acceptable amount of absorbed average power.

5.4.2.1 Performance of Move-blocking Method

First, the performance of the MPC with a perfect (matched) hydrodynamic model was investigated using a full control horizon $N_c = N_p$, a reduced control horizon $\boldsymbol{\Delta u_{qh}(k)}$ and a move-blocking control horizon $\boldsymbol{\Delta u_{q_m}(k)}$. For all tests, a 1 m monochromatic excitation wave was used; linear constraints incorporated were WEC heave, velocity and the PTO force. Fig. 5.17 shows the average electrical powers absorbed from the system when the different control horizons were used. When a standard reduced horizon is used with $N_c = 30$, the average power has significantly reduced when compared to the average power obtained when using a full control horizon with $N_c = N_p$. However, when a move-blocking control horizon of $N_c = 10$ was used, the average power extracted was observed to be very close to that obtained with a full control horizon of $N_c = N_p = 100$. However, any decrease from $N_c = 10$ with the move-block technique resulted in a degradation of the average power. Nevertheless, the average power results from the move-blocking technique for $N_c < 10$ show much improved power levels when compared with the standard control horizon reduction with a much greater control horizon N_c.

To show the serious advantages of using a move-blocking control horizon, the average optimisation solution times for the unconstrained and linearly constrained problems were recorded. As shown in Fig. 5.18, the difference between the solution times for constrained and unconstrained MPC is very clear. For both unconstrained and constrained cases the solve time decreases as the control horizon N_c decreases, with the constrained optimisation solution time decreasing at a much higher rate than the unconstrained optimisation. Furthermore, this figure also shows the corresponding power ratio obtained for the various control horizons. The power ratio here is the ratio of the average power extracted using a reduced move-blocking horizon against the average power extracted when a full control horizon is used. It is clearly shown that as the control horizon N_c reduces, the power ratio stays at unity until the control horizon $N_c < 15$, when the power ratio begins to decrease. From this figure, it is shown that

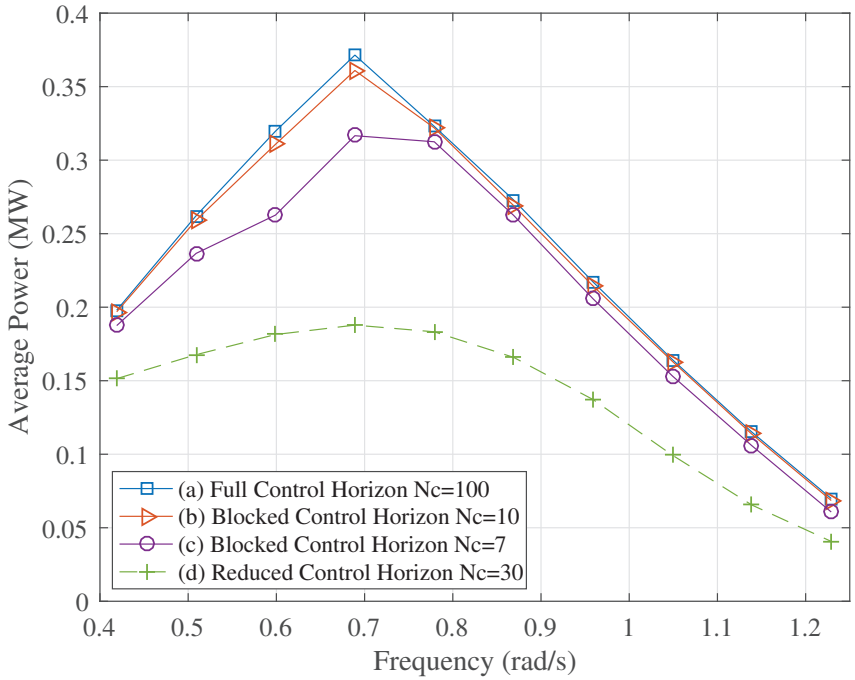

Figure 5.17: Average electrical power absorbed from 1 m monochromatic waves using an MPC with linear mechanical constraints (4.1) when (a) a full control horizon is used, (b) a move-blocked control horizon of $N_c = 10$ is used, (c) a move-blocked control horizon of $N_c = 7$ is used and (d) a reduced control horizon of $N_c = 30$ is used

the optimisation of the problem can be simplified without diminishing the performance of the average power extraction from the system.

The move-blocked MPC was then tested with non-linear voltage and uni-directional power constraints, as shown in Fig. 5.19. It is clearly shown that as the move blocking control horizon order N_c is reduced, the computational solve time is significantly reduced while maintaining a similar optimisation performance to the MPC with a full control horizon of $N_c = N_p$. Therefore there are serious advantages of using move blocking in MPC when linear and non-linear constraints are incorporated.

5.4.2.2 System Robustness during System Mismatch

As shown in section 5.2, all the system mismatches between the control model and system model can affect the amount of absorbable average electrical power. In this section, the effects of a reduced control horizon N_c on the mismatched systems performance is investigated.

Here the move-blocking technique is used on a mismatched system where the robustness of the system will be analysed. From section 5.2 it was shown that some mis-

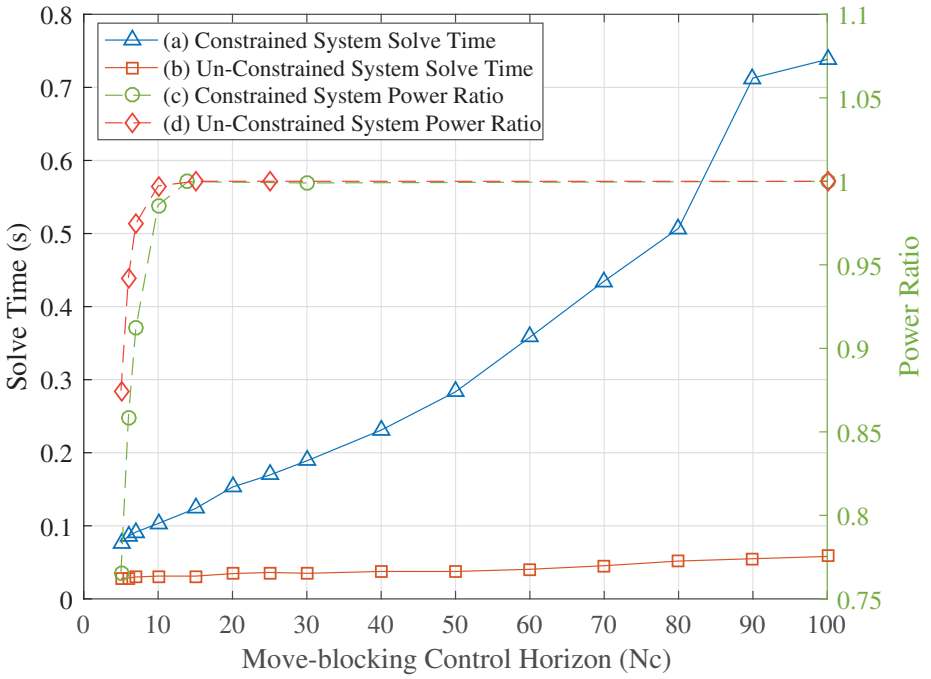

Figure 5.18: (Left axis) The optimisation solve time vs the control horizon N_c (a) with constraints, (b) without constraints; (Right axis) The power ratio (average power from an MPC with control horizon N_c divided by the average power from an MPC with a full control horizon) vs the control horizon N_c (c) with constraints (d) without constraints

matches within the system can affect the average power extracted from the system, with some characteristics having more of an effect on the outcome than others. Here the hydrostatic mismatch (section 5.2.2) in the system is used in the robustness analysis since it affects the average power extraction the most at lower frequencies, where the system will spend the majority of its operating time.

To test the robustness of the system, the move-blocking technique was used on the mismatched system where a -20% hydrostatic stiffness coefficient mismatch was used; 1 m high monochromatic waves are used in this analysis. The resulting extracted average electrical power from the mismatched system are shown in Fig. 5.20. From Fig. 5.20 it is shown that to some degree, the inclusion of the move-blocking technique does not cause any significant difference in performance. It is only when the control horizon has been decreased to the point (e.g. $N_c = 10$) where $\Delta u_q(k+2) = \Delta u_q(k+1)$ that the average power starts to significantly deviate.

When move-blocking results in a $\Delta u_q(k+2)$ and $\Delta u_q(k+1)$ which are equal to each other, the calculated PTO force $\Delta u_q(k)$ becomes damped; this is shown in Fig. 5.21. This damped PTO force control action can lead to problems in satisfying the hard constraints.

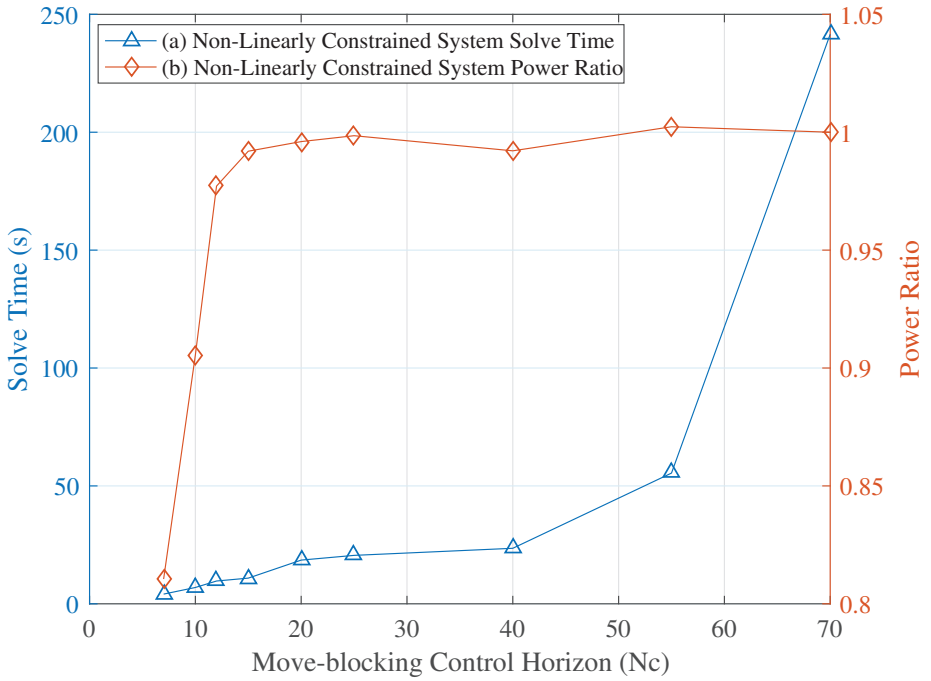

Figure 5.19: (Left axis) The optimisation solve time vs the control horizon N_c (a) with non-linear power and voltage constraints ; (Right axis) The power ratio (average power from an MPC with control horizon N_c divided by the average power from an MPC with a full control horizon) vs the control horizon N_c (b) with non-linear power and voltage constraints

In Fig. 5.22 it is shown for a 1 m high monochromatic wave with a frequency of 0.419 rad.s^{-1} that the heave of the WEC and LPMG stay within the heave limitation of ± 3.5 m when a control horizon of $N_c = 100$ is used. However, when a control horizon of $N_c = 10$ is implemented, the PTO force (Fig. 5.21) becomes damped and the heave of the system exceeds the heave limitation, which could cause damage. If the control horizon N_c is too low, then there is a higher chance of $\Delta u_q(k+2) = \Delta u_q(k+1)$ which would degrade the systems performance. However, as stated in section 5.4.2.1, if the control horizon N_c is selected too high, then the optimisation solve time will increase. Therefore, there needs to be a compromise where the move-blocking control horizon is wisely chosen to have the lowest possible control horizon whilst having acceptable system performance which obeys the systems constraints.

5.5 Conclusion

In section 5.2, each characteristic in the hydrodynamic model was analysed with a degree of model mismatch introduced between the control system and the actual system. System model uncertainty included the WEC mass, hydrostatic coefficient and the ra-

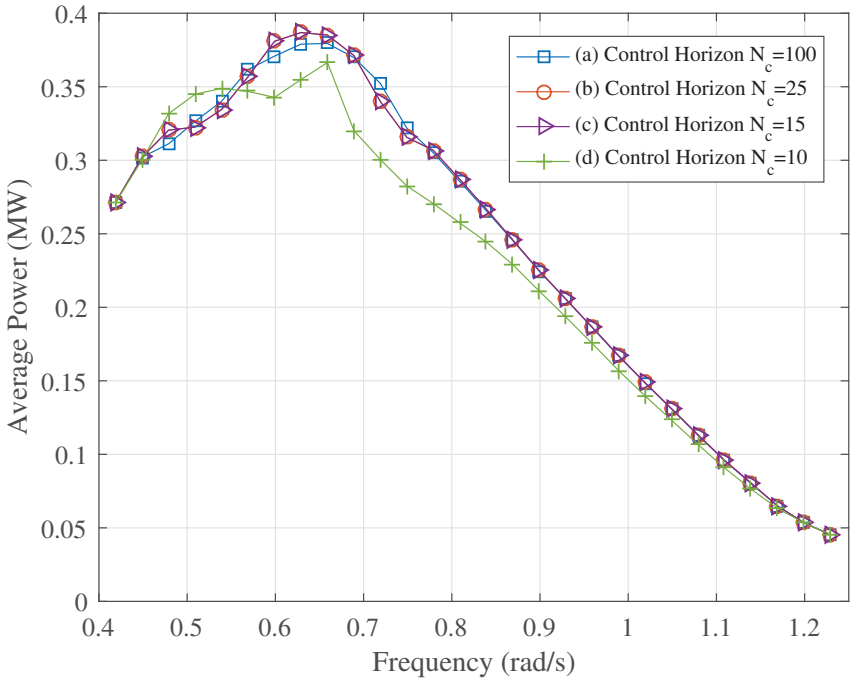

Figure 5.20: Average electrical powers from 1 m monochromatic waves using MPC with linear mechanical constraints (4.1) for hydrostatic stiffness coefficient mismatch of -20% when a control horizon of (a) $N_c = 100$ (full control horizon), (b) $N_c = 25$, (c) $N_c = 15$ and (d) $N_c = 10$

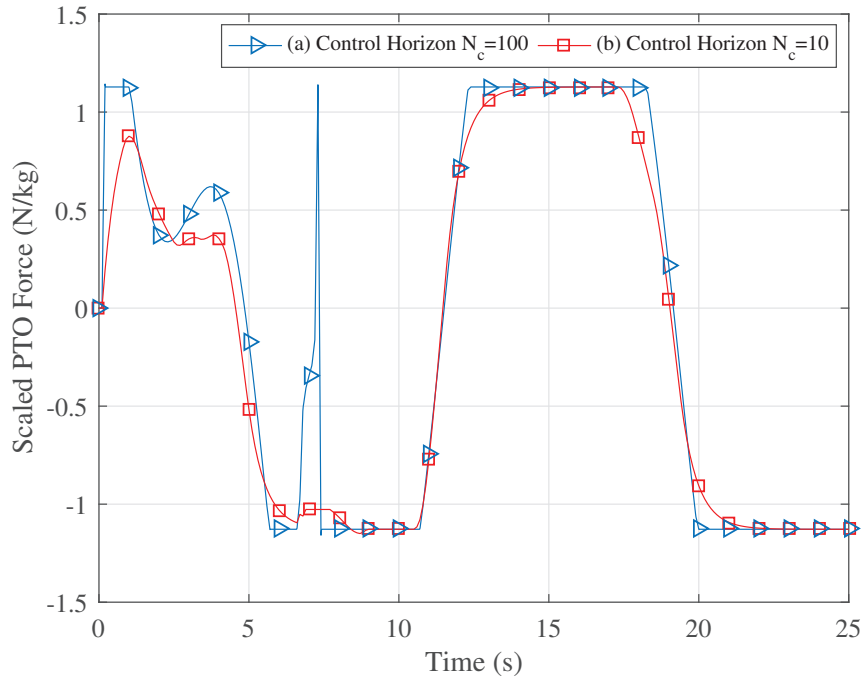

Figure 5.21: The scaled PTO force $u_q(t)$ during a 1 m, 0.4487 rad.s^{-1} monochromatic excitation wave when an MPC with a control horizon of (a) $N_c = 100$ (full control horizon) and (b) $N_c = 10$ are used

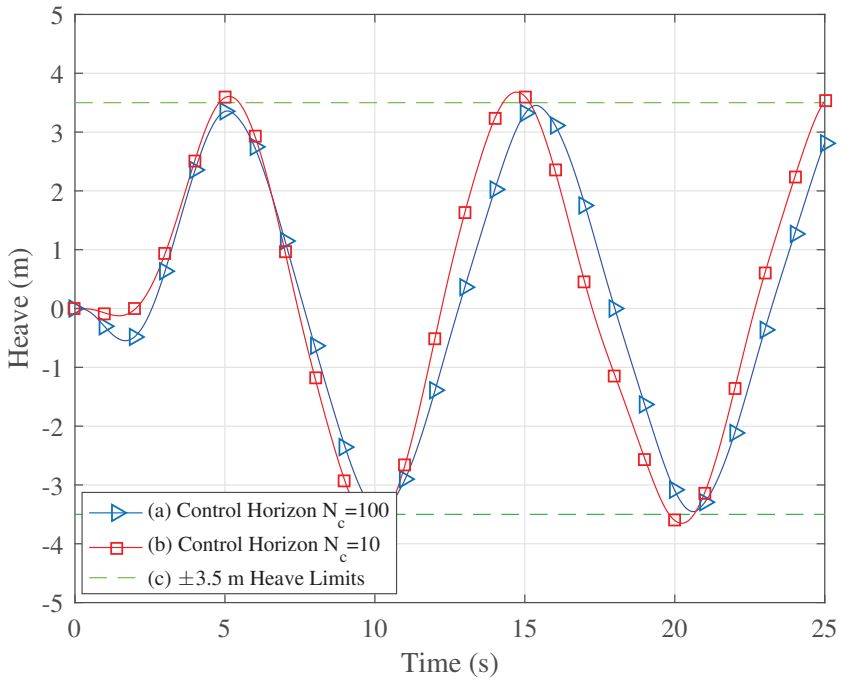

Figure 5.22: The WEC heave $z(t)$ for a 1 m, 0.6613 rad.s^{-1} monochromatic excitation wave when an MPC with a control horizon of (a) $N_c = 100$ (full control horizon) and (b) $N_c = 10$ are used

diation kernel. The results showed that each mismatch introduced a certain degree of average electrical power loss when it was compared to the average electrical power absorbed from a fully matched system. Sections 5.2.1 and 5.2.3 showed the effects that the mismatches had on the average electrical power. These two sections showed similar results where the difference in average power between the mismatched and fully matched systems was acceptable up to 1 rad.s^{-1}. For frequencies $\omega > 1$ rad.s^{-1} the average power between the matched and mismatched systems deviated. From a mathematical point of view, this seems unacceptable. However, from a practical point of view the fundamental frequency of a realistic excitation wave spectrum would be much lower, therefore the effects from the higher frequencies would seem negligible. Section 5.2.2 showed that at lower frequencies (frequencies that would actually be active during a realistic sea spectrum), there were large changes in average electrical power when the hydrostatic coefficient varied over the $\pm 20\%$ range (e.g. at 0.65 rad.s^{-1} there was 0.155 MW of a difference in average power between the systems with a $\pm 20\%$ hydrostatic coefficient mismatch). Even though the smallest power ratio produced from the hydrostatic coefficient mismatch was 0.88, this power ratio drop occurred for the lower frequencies where there would be a much greater effect due to the system's inherent sensitivity to hydrostatic coefficient changes.

In section 5.3, the negative effects of the non-linear viscosity force on the average

electrical power absorption when using an inviscid MPC model was shown. With the inclusion of linear constraints in the optimisation, the effects of the viscosity that was neglected in the control model marginally decreased. A LPV NPMC was then implemented in simulation which included the viscosity terms; this provided the reference performance where maximum electrical power is produced. However, the NMPC performance came at the cost of a significantly increased computational burden. To decrease the computational complexity, a linear damping viscosity model was incorporated into the linear MPC. It was found that when the $\tilde{C}_{vis}$ value was tuned for each individual sea state, the average power collected was comparable to the results produced using the NMPC. By introducing linear mechanical constraints into the MPC optimisation, the average power became less sensitive to the choice of $\tilde{C}_{vis}$ when compared to the unconstrained case. Furthermore, a constant sea-state invariant $\tilde{C}_{vis}$ was used to create a controller which could extract between 96% and 100% of the electrical power obtained using the optimal $\tilde{C}_{vis}$ for each sea-state. Comparing the results from the NMPC and the linear MPC approximations, it is shown that the system is robust to model mismatches in viscous drag coefficient values producing a power ratio of > 0.93 for a -20% mismatch. It is also shown that the inclusion of the linear constraints within the optimisation cause a convergence of the performance across all three controllers. From this, it can be said that with the help of linear constraints, satisfactory power maximisation can be accomplished, with the inclusion of a single simple linear drag coefficient $\tilde{C}_{vis}$, without the complexity associated with NPMC.

In section 5.4.2, a move-blocking technique was incorporated into the control horizon. The move-blocking method allowed for a reduction of the number of free control variables needed to be calculated. Unlike other control horizon minimisation techniques where a reference trajectory is used, the move-blocking technique is better suited to this economic MPC application due to its ability to represent the pseudo-periodic nature of the control action across the prediction horizon with a small number of free control variables.

In section 5.4.2.1, the MPC with the standard reduced control horizon is compared against the MPC with the move-blocking horizon and an MPC with a full horizon. It was shown that an MPC with a move-blocking control horizon of $N_c = 10$ can produce average electrical power results which are closer to the results found using an MPC with a full control horizon. It was when the MPC with a move-blocking control horizon of $N_c < 10$, the fidelity of the MPC became dissimilar. However, when compared to the results found when using the MPC with a standard reduced horizon, the advantages of implementing the move-blocking technique became apparent. An MPC with a standard reduced control horizon of $N_c = 30$ is incomparable to the re-

sults found from an MPC with a full control horizon. It was then shown how by using the move-blocking technique, the fidelity of the MPC can be maintained, while the QP's computational time is drastically reduced (e.g. for a linearly constrained MPC, when $N_c = 15$, the power ratio is unity while reducing the solve time by 83%). Furthermore, including linear mechanical constraints and non-linear (voltage and unidirectional power flow) constraints into the MPC algorithm, the implementation of the move-blocking technique nearly became essential (e.g. with $N_c = 25$, the power ratio is unity while reducing the solve time by 90%).

In section 5.4.2.2, the move-blocking technique was then tested on a mismatched system, with a -20% mismatched hydrostatic coefficient. It was shown that the inclusion of move-blocking in the control horizon had a minor affect on the absorption of average electrical power when compared to a full control horizon. However, it was clear that if the control horizon was set low enough, yielding $\Delta u_q(k+1) = \Delta u_q(k+2)$, then the control bandwidth would be reduced, which then causes the system to exceed the systems constraints leading to possible damages. Therefore, using a move-block technique for the control horizon whilst operating in a mismatched system is highly advantageous once the allocation of the control variables within the control horizon are arranged in a manner that allows a sufficient resolution at the beginning of the prediction horizon.

References

Bhinder, M., Babarit, A., Gentaz, L. & Ferrant, P. (2011), '*9th European Wave and Tidal Energy Conference (EWTEC), Southampton*', *9th European Wave and Tidal Energy Conference* .

Cagienard, R., Grieder, P., Kerrigan, E. C. & Morari, M. (2007), 'Move blocking strategies in receding horizon control', *Journal of Process Control* **17**(6), 563–570.

Cretel, J., Lightbody, G., Thomas, G. P. & Lewis, A. W. (2011), 'Maximisation of energy capture by a wave-energy point absorber using model predictive control', *IFAC Proceedings Volumes (IFAC-PapersOnline)* **18**(PART 1), 3714–3721.

Ellis, M., Durand, H. & Christofides, P. D. (2014), 'A tutorial review of economic model predictive control methods', *Journal of Process Control* **24**(8), 1156–1178.

Garcia, C. E., Prett, D. M. & Morari, M. (1989), 'Model predictive control: theory and practice—a survey', *Automatica* **25**(3), 335–348.

Genest, R. & Ringwood, J. V. (2016), 'A critical comparison of model-predictive and pseudospectral control for wave energy devices', *Journal of Ocean Engineering and Marine Energy* **2**(4), 1–15.

Giorgi, G., Penalba, M. & Ringwood, J. V. (2016), 'Nonlinear Hydrodynamic Models for Heaving Buoy Wave Energy Converters', *Proceedings of the Asian Wave and Tidal Energy Conference AWTEC* (October), 1–10.

Guérinel, M., Alves, M. & Sarmento, A. (2011), 'Nonlinear modelling of the dynamics of a free floating body', *EWTEC, Southampton* pp. 1–5.

Huzmezan, M. & Maciejowski, J. (1998), Reconfiguration and scheduling in flight using quasi-LPV high-fidelity models and MBPC control, *in* 'Proceedings of the 1998 American Control Conference. ACC ', Vol. 6, pp. 3649–3653 vol.6.

Matlab (2010), *Version 7.10.0*, The MathWorks Inc., Natick, Massachusetts.

Metropolis, N. & Ulam, S. (1949), 'The monte carlo method', *Journal of the American statistical association* **44**(247), 335–341.

Nepf, H. M. (1999), 'Drag, turbulence, and diffusion in flow through emergent vegetation', *Water resources research* **35**(2), 479–489.

O'Sullivan, A. C. & Lightbody, G. (2015), 'Wave to Wire Power Maximisation from a Wave Energy Converter', *In Proceedings of the 11th European Wave and Tidal Energy Conference (EWTEC)* pp. 1–9.

O'Sullivan, A. C. & Lightbody, G. (2017*a*), 'Co-design of a wave energy converter using constrained predictive control', *Renewable Energy* **102**, 142–156.

O'Sullivan, A. C. & Lightbody, G. (2017*b*), 'The Effect of Model Inaccuracy and Move-blocking on the Performance of a Wave-to-wire Wave Energy Converter, under Economic Predictive Control', *In Proceedings of the 12th European Wave and Tidal Energy Conference (EWTEC)* pp. 1–10.

O'Sullivan, A. C. M. & Lightbody, G. (2016), 'Predictive control of a wave to wire energy conversion system - the importance of field weakening', *2016 UKACC 11th International Conference on Control (CONTROL)* (August), 1–6.

O'Sullivan, A. C. M. & Lightbody, G. (2017*c*), 'The Effect of Viscosity on the Maximisation of Electrical Power from a Wave Energy Converter under Predictive Control', *IFAC-PapersOnLine* **50**(1), 14698–14704.

Penalba Retes, M., Mérigaud, A., Gilloteaux, J.-C. & Ringwood, J. (2015), 'Nonlinear Froude-Krylov force modelling for two heaving wave energy point absorbers', *Proceedings of the 11th European Wave and Tidal Energy Conference* pp. 1–10.

Ringwood, J. V., Bacelli, G. & Fusco, F. (2014), 'Energy-maximizing control of wave-energy converters: The development of control system technology to optimize their operation', *IEEE Control Systems* **34**(5), 30–55.

Tóth, R. (2010), *Modeling and identification of linear parameter-varying systems*, Vol. 403, Springer.

Tucker, M. J. & Pitt, E. G. (2001), *Waves in ocean engineering*, Vol. 5, Elsevier B.V.

Wright, C., Murphy, J., Pakrashi, V. & Murphy, J. (2016), 'The Dynamic Effects of Marine Growth on a Point Absorbing Wave Energy', *In Proceedings of the Offshore Energy & Storage Symposium and Industry Connector* (July), 1–5.

Chapter 6

Benefits of Centralised Predictive Control for Optimal Electrical Power Generation from WEC Arrays

6.1 Introduction

FORCING an array of WECs to operate in a region of constructive interference can generate more electrical power per device, when compared to a single WEC of the same power rating (Barcelli & Ringwood 2013). Optimising a group of wave energy converters in an array formation, including the layout of the array and the global control of the array can improve constructive interference (Garcia-Rosa et al. 2015). It is also important to note that due to the natural phase differences in instantaneous electrical power produced from each individual device, there is the potential for power smoothing when WECs are grouped together; this is advantageous when exporting the power onto the grid (Göteman et al. 2015).

WEC arrays can be categorised into multi-body WECs and a separate body WEC array (Babarit et al. 2012). A multi-body WEC consists of multiple small WECs which are attached to a main body which is larger in size, as shown in Fig. 6.1(a). This type of array has electrical and mechanical infrastructure advantages, where the PTOs and power electronics are above water. The underwater cabling going to the large multi-body WEC is simplistic and the individual WECs are bound to the larger body causing a low probability of a collision. However, with the devices so close to each other, there is a greater chance of hydrodynamic shadowing which can cause power extraction inefficiencies. Furthermore, with smaller devices, friction can be an important factor.

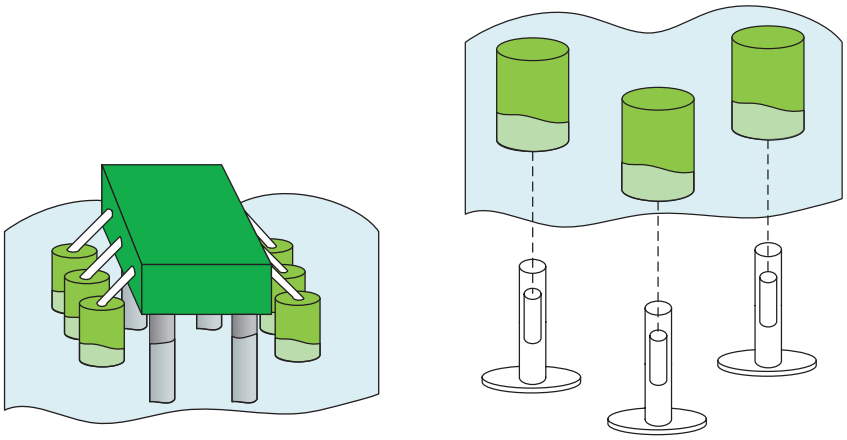

(a) Multi-body array (b) Separate body array

Figure 6.1: The two structural types of WEC arrays.

For the system to overcome this friction, the individual WEC must be scaled appropriately. This can become an economic problem as the main body holding the WECs in position has to scale also, which can become significant in size and uneconomical.

The WECs in a conventional WEC array are not structurally bound to a larger structure, they are dealt with as individual WECs operating in a relatively close space, as shown in Fig. 6.1(b). With larger WEC separation distances, larger WECs can be utilised, hydrodynamic shadowing effects decrease, destructive interference is weakened and the probability of a WEC collision is reduced. However, a larger separation distance consequentially leads to a greater electrical infrastructure cost (Thorburn et al. 2004). The electrical costs are affected by the cabling, the network topology, the type of power converters, where to locate the power converters, should each WEC have its own AC/DC/AC converter, should they all have a AC/DC converter feeding a common DC-link bus; what type of DC-link should it have, should there be multiple DC-link buses instead of one large DC-link bus?

The electrical infrastructure is based on two fundamental cabling layouts (López et al. 2013) - the string layout and the star layout, as shown in Fig. 6.2. The string layout (Fig. 6.2.(a)) uses shorter cabling hence saving costs on the electrical infrastructure. However, the WECs are limited to how much power can be generated since there is a power limitation on the coupled wire which carries all the power onto the common bus. Since each device on the branch is directly connected to each other in series, the system is less reliable since the branch of WECs can all be effected if a shut down fault occurs from a single WEC device. The star layout is utilised in WEC farms where the WECs are closely spaced together. If the distance between the devices is over a

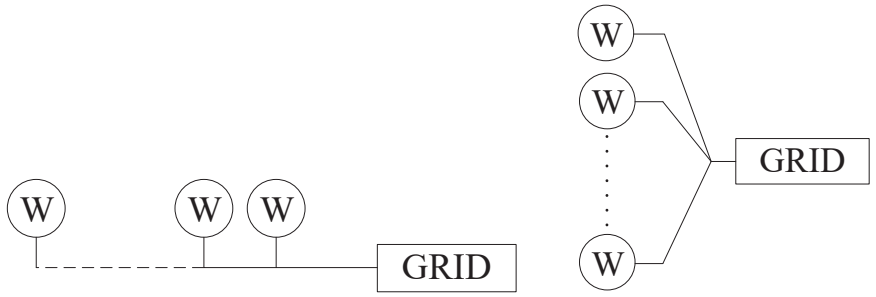

(a) String electrical cabling infrastructure layout (b) Star electrical cabling infrastructure layout

Figure 6.2: The two fundamental electrical cabling infrastructure layouts.

certain threshold, the cost increases to a certain point where it becomes uneconomical. However, the star layout is much more reliable than the string layout since each WEC is electrically decoupled from each other; allowing the remaining WECs to continue operating during a shut down fault on one of the machines.

Furthermore, with the string electrical layout from Fig. 6.2.(b), the power converter layout also needs to be considered to design an economically viable system. For example, one orientation is the individual variable speed layout (Fig. 6.3.(a)), where each WEC with its own dedicated back-to-back VSC converter feeds an offshore AC bus. This layout uses multiple transformers and converters which increases the cost of the electrical infrastructure. In Fig. 6.3.(b), a string electrical layout is shown which does not incorporate the individual back-to-back converter systems. Each WEC has its own AC/DC VSC which feed a common offshore DC bus where a single DC/AC VSC converts the aggregated powers into AC power; decreasing the amount of converters needed.

All of the electrical layouts shown in Fig. 6.3 use a HVAC transmission method to transport the electrical power to shore. However, there is also the HVDC method which transmits DC voltage to a land based DC/AC power station. HVDC power transmission only becomes the most economical and efficient transmission method when wave farms are more than 50 km away from the on land power station. However, for these distances the practical issues involved with the installation of such wave farms so far away from land are substantial (Van Eeckhout et al. 2010).

When implementing a WEC farm of multiple hydrodynamically coupled WECs (Fig. 6.1(b)), greater power levels can be found with the potential of instantaneous power balancing of the power exported onto the grid (Sjolte et al. 2012). However, for greater power levels, larger devices will be needed which would require larger spacing dis-

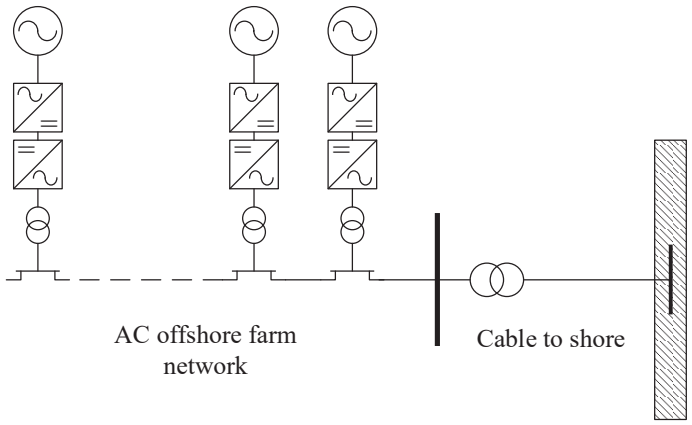

(a) The individual variable speed layout

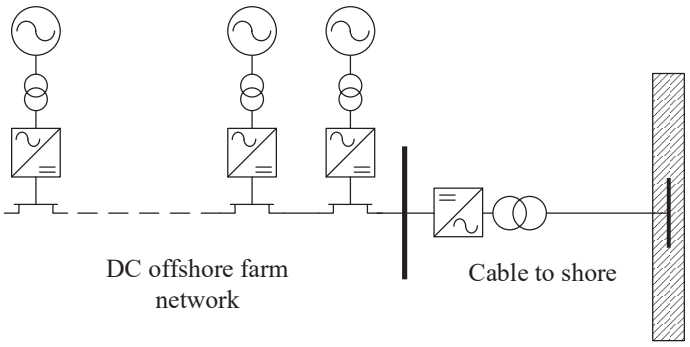

(b) The HVAC transmission topology

Figure 6.3: The two fundamental power converter layouts, including generator sources, AC/DC power converters, DC/AC power converters, transformers, a common bus and the grid.

tance between the devices. With a large spacing distance, it was shown above that an electrical string formation can become more economical. However, it was also shown that with this electrical layout, the system as a whole is more vulnerable to WEC farm branch shut down; if one WEC faults on the branch, all devices become disconnected. This shows the need for a control system which enables maximum power extraction while taking the mechanical and electrical constraints into account.

WEC array control methods used can be categorised into three categories: decentralised, centralised and distributed control. Decentralised control of a WEC array (Oetinger et al. 2014*b*), as shown in Fig. 6.4, is a simplistic method where each device in the array is independently controlled; the control assumes no external disturbances caused by surrounding WECs. This method is convenient as the computational expense is low and the logistics are simplified since there is no data shared between the WECs in the array. However, the decentralised method can be prone to inaccuracies if

the interactions between the WECs increases, causing power extraction inefficiencies and the potential for constraints to be breached.

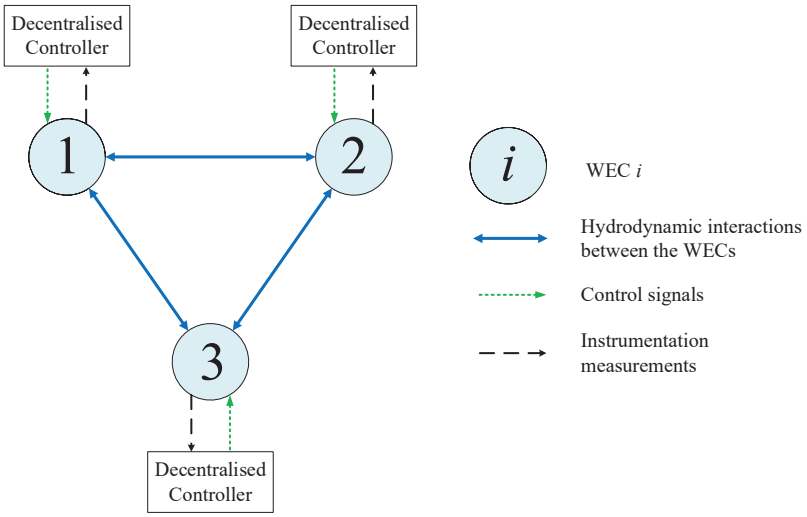

Figure 6.4: The three decentralised control algorithm layout of a three WEC equilateral triangle wave energy array, including the local measurements from the PTO and WEC, and the control signals sent to the PTOs.

Using centralised control (Oetinger et al. 2014*a*), as shown in Fig. 6.5, a global optimum solution can be found since the information of all the WECs within the array is aggregated into a single control algorithm. This enables the possibility of constructive interference since the hydrodynamic interactions between the devices are incorporated into the centralised control algorithm. It will also improve safety, since the probability of electrical and mechanical system constraint breaching is relatively low when compared to an array controlled using decentralised control. In this work, there is a maximum of three devices investigated. However, for commercial applications many WECs may be considered, which would require an unrealistic amount of computational power. Therefore, with centralised control there is a practical limitation.

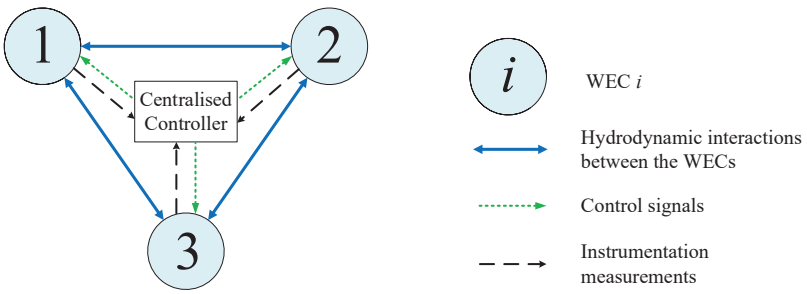

Figure 6.5: The single centralised control algorithm layout optimally controlling all three WEC that are in an equilateral triangle orientation, including the global measurements from the PTOs and WECs, and the control signals sent to the PTOs.

Distributed control (Mc Namara et al. 2013), as shown in Fig. 6.6, is a hybrid of a

decentralised and centralised control systems. Distributed control utilises controllers for each WEC that solve their local optimisation problems, and after each iteration of the optimum problem solver, each controller sends their solutions to their neighbouring WECs. After a certain number of iterations, all the WECs will converge to an agreed optimal solution. This distributed control method is advantageous as it essentially has the computational speed of decentralised control while maintaining the fidelity of a centralised controller.

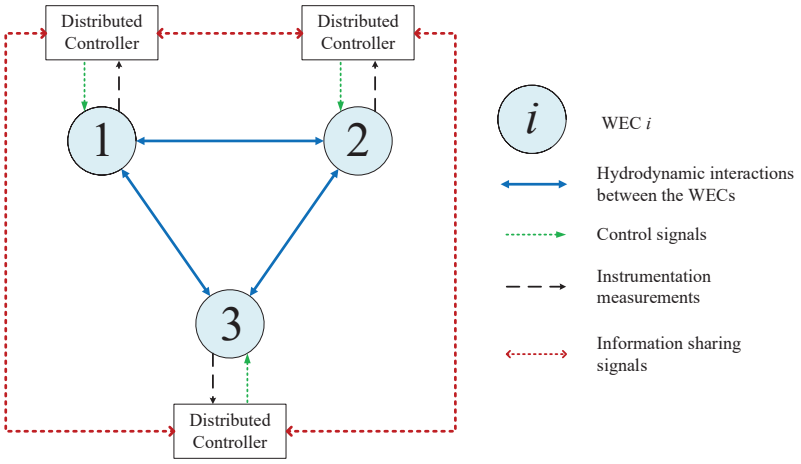

Figure 6.6: The layout of a distributed control algorithm controlling all three WEC that are in an equilateral triangle orientation. Each controller uses its local measurements from the PTOs and WECs, then distributes their optimum solutions to their neighbouring found after every solver iteration. After a certain number of iterations, the optimum solution is found and the control signals sent to the PTOs from the local controllers.

This chapter presents a comparison of the maximum electrical energy extraction of equally spaced point absorber arrays, utilising both centralised and decentralised MPC control (O'Sullivan & Lightbody 2017*a*). It focuses on the effect of layout, viscosity and constraints on the potential benefits of a centralised approach, hence providing the justification of developing a future distributed control algorithm. Finally, it provides a method for the improvement of electrical power quality through the optimisation process.

6.2 Modelling an Array of Grid Connected Point Absorbers

The wave to grid electrical system is shown in Fig. 6.7. The WEC is connected to a linear permanent magnet generator (LPMG) (Polinder et al. 2004), which is connected to the grid via back to back voltage source converters. The grid side converter is used

to control the DC link voltage and reactive power. The machine side converter is used to control the motion of the LPMG.

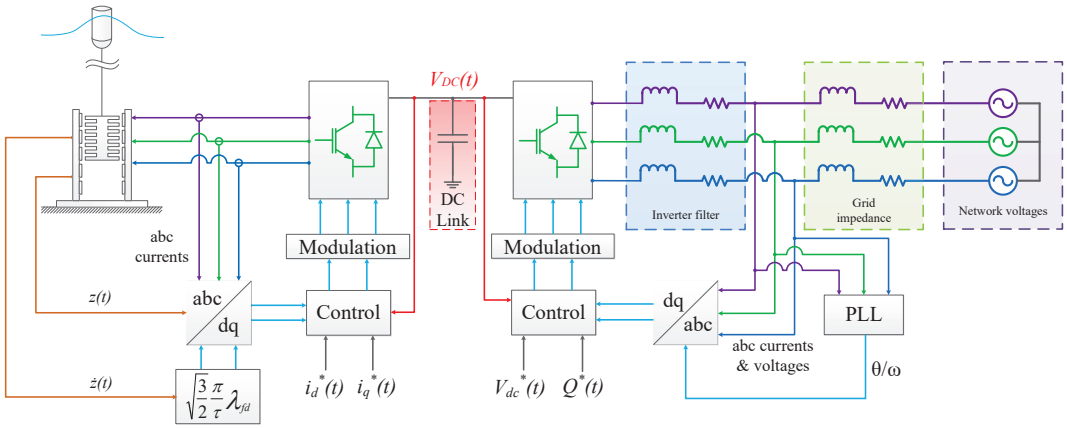

Figure 6.7: Schematic of the Wave to Grid electrical system which includes: a point absorber WEC connected to a LPMG, the machine side converter, the machine side controller using dq transformations, the DC-link capacitor, a grid side converter, grid side converter filters, grid impedance network, network voltages, the grid side controller utilising a dq transformation with a PLL.

6.2.1 Hydrodynamics

The two WEC array orientations analysed in this work are shown in Fig. 6.8. All WECs within the arrays have identical dimensions. The angle of unidirectional wave excitation penetration is θ and each WEC is equally separated from each other with a separation distance d. The WEC used in this research is a cylindrical point absorber

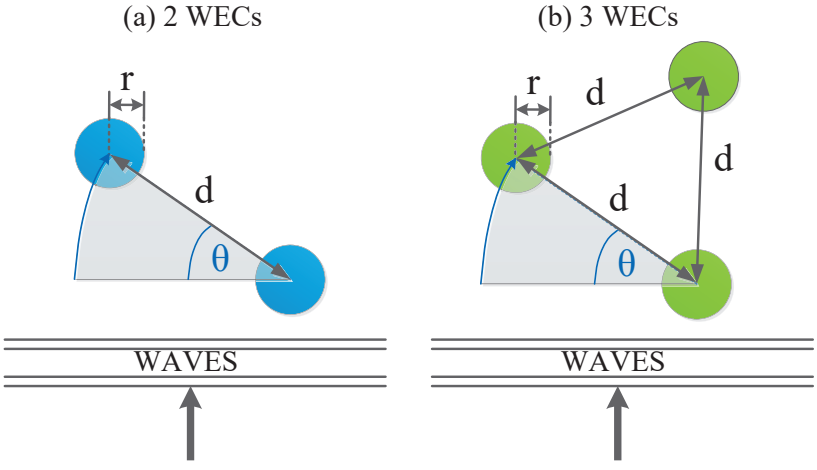

Figure 6.8: Top view of (a) a 2 WEC array, (b) a 3 WEC equilateral triangle array with the WEC radius r, the WEC separation distance d, the array orientation θ

with a semi-hemispherical bottom, modelled with a radius of $r = 5$ m and a draught of 10 m. Each WEC is restricted to move in the heave direction and its model is based on linear wave theory. The hydrodynamic model of the i^{th} WEC (6.1), consists of the hydrostatic force $F_{h_i}(t)$, the radiation force $F_{rad_i}(t)$, the excitation force $F_{e_i}(t)$, the controlled PTO force $F_{PTO_i}(t)$ and the non-linear viscous force $F_{v_i}(t)$,

$$M_i\ddot{z}_i(t) = F_{h_i}(t) + F_{rad_i}(t) + F_{e_i}(t) + F_{PTO_i}(t) + F_{v_i}(t). \tag{6.1}$$

The hydrodynamic model for a single device (6.1) is then further developed into (6.3) where the heave displacement of the i^{th} WEC is $z_i(t)$, the WEC velocity is $\dot{z}_i(t)$, the wave elevation is $\eta_i(t)$ and the wave velocity is $\dot{\eta}_i(t)$. The hydrostatic force $F_{h_i}(t)$ is a function of the displacement $z_i(t)$, where β is the linear hydrostatic spring constant. The radiation force $F_{rad_i}(t)$ is modelled (6.2) using the Cummins decomposition (Cummins 1962), where the radiation kernels $h_{r_{i,j}}(t)$ and the added mass at infinity frequency m_{μ_i} are found using WAMIT (Version 7) (Lee 1995).

$$F_{rad_i}(t) = \sum_{j=1}^{N_w} \left[-m_{\mu_{i,j}}\ddot{z}_j(t) + \int_0^t h_{r_{i,j}}(\tau)\dot{z}_j(t-\tau)d\tau \right]. \tag{6.2}$$

The non-linear viscous force $F_{v_i}(t)$ depends on the relative velocity between the WEC and wave and the PTO force $F_{PTO_i}(t)$ is manipulated by the control system,

$$\begin{aligned} M_i\ddot{z}_i(t) + \sum_{j=1}^{N_w}\left[m_{\mu_{i,j}}\ddot{z}_j(t)\right] + \overbrace{\sum_{j=1}^{N_w}\left[\int_0^t h_{r_{i,j}}(\tau)\dot{z}_j(t-\tau)d\tau\right]}^{F_{r_i}(t)} + \beta_i z_i(t) \\ + C_{vis_i}(t)\left(\dot{z}_i(t) - \dot{\eta}_i(t)\right) = F_{PTO_i}(t) + F_{e_i}(t). \end{aligned} \tag{6.3}$$

Here N_w is the number of WECs in the array. The excitation force $F_{e_i}(t)$ is a non-causal convolution integral of the wave elevation $\eta_i(t)$, where the excitation kernel $h_{e_i}(t)$ was found using WAMIT (Lee 1995),

$$F_{e_i}(t) = \int_{-\infty}^{t} h_{e_i}(\tau)\eta_i(t-\tau)d\tau. \tag{6.4}$$

The radiation force on the i^{th} WEC, $F_{r_i}(t)$, which is expressed as the sum of forces produced by the movement of the N_w devices in (6.3), can be realised as a multi-input-single-output state space subsystem (6.5) using the Hankel singular value decomposi-

tion (HSVD) method (Kung et al. 1983):

$$\begin{aligned} \dot{\boldsymbol{x}}_{\boldsymbol{r_j}}(t) &= \boldsymbol{A}_{\boldsymbol{r_j}}\boldsymbol{x}_{\boldsymbol{r_j}}(t) + \boldsymbol{B}_{\boldsymbol{r_j}}\dot{z}_j(t) \\ F_{r_i}(t) &= \sum_{j=1}^{N_w}\left(\boldsymbol{C}_{\boldsymbol{r_{i,j}}}\boldsymbol{x}_{\boldsymbol{r_j}}(t) + D_{r_{i,j}}\dot{z}_j(t)\right), \end{aligned} \tag{6.5}$$

where n is the radiation kernel order, $\boldsymbol{x}_{\boldsymbol{r_j}}(t) \in \mathbb{R}^{n\times 1}$, $\boldsymbol{A}_{\boldsymbol{r_j}} \in \mathbb{R}^{n\times n}$, $\boldsymbol{B}_{\boldsymbol{r_j}} \in \mathbb{R}^{n\times 1}$, $\boldsymbol{C}_{\boldsymbol{r_{i,j}}} \in \mathbb{R}^{1\times n}$, $D_{r_{i,j}} \in \mathbb{R}^1$.

The non-linear viscosity force $F_{v_i}(t)$, is based on the semi-empirical Morison equation (Morison et al. 1950),

$$F_{v_i}(t) = -C_{vis_i}(t)\left(\dot{z}_i(t) - \dot{\eta}_i(t)\right), \tag{6.6}$$

where,

$$C_{vis_i}(t) = \frac{1}{2}\rho C_{d_i} A \left|\dot{z}_i(t) - \dot{\eta}_i(t)\right|.$$

Here ρ is the density of water, C_{d_i} is the drag coefficient (Bhinder et al. 2011) and A_i is the sectional area of the i^{th} point absorber which is orthogonal to the direction of the force. Combining all WEC models, a global non-linear hydrodynamic system can be formed, which includes all the cross coupling radiation terms (6.7),

$$\frac{d}{dt}\mathbf{X}(t) = \mathbf{A_c}(t)\mathbf{X}(t) + \mathbf{B_c}\mathbf{U_q}(t) + \mathbf{F_c}\mathbf{V}(t) + \mathbf{E_c}(t)\dot{\mathbf{H}}(t), \tag{6.7}$$

where,

$$\mathbf{A_c}(t) = \boldsymbol{K_m}^{-1}\begin{bmatrix} A_{c,1,1}(t) & A_{c,1,2}(t) & \dots & A_{c,1,N_w}(t) \\ A_{c,2,1}(t) & A_{c,2,2}(t) & \dots & A_{c,2,N_w}(t) \\ \vdots & \vdots & \ddots & \vdots \\ A_{c,N_w,1}(t) & A_{c,N_w,2}(t) & \dots & A_{c,N_w,N_w}(t) \end{bmatrix} \in \mathbb{R}^{N_w(n+2)\times N_w(n+2)},$$

$$A_{c,i,j}(t) = \begin{cases} \begin{bmatrix} 0 & 1 & \mathbf{0} \\ -\beta_i & -(D_{r_{i,i}} + C_{vis_i}(t)) & -\boldsymbol{C}_{\boldsymbol{r_{i,i}}} \\ 0 & \boldsymbol{B}_{\boldsymbol{r_i}} & \boldsymbol{A}_{\boldsymbol{r_i}} \end{bmatrix}, & \text{if } i = j \\ \begin{bmatrix} 0 & 0 & \mathbf{0} \\ 0 & -D_{r_{i,j}} & -\boldsymbol{C}_{\boldsymbol{r_{i,j}}} \\ 0 & \boldsymbol{B}_{\boldsymbol{r_j}} & \boldsymbol{A}_{\boldsymbol{r_j}} \end{bmatrix}, & \text{if } i \neq j \end{cases} \in \mathbb{R}^{(n+2)\times(n+2)},$$

$$\mathbf{B_c} = \boldsymbol{K_m}^{-1} \begin{bmatrix} \boldsymbol{B_{c,1}} & \mathbf{0} & \dots & \mathbf{0} \\ \mathbf{0} & \boldsymbol{B_{c,2}} & \dots & \mathbf{0} \\ \vdots & \vdots & \ddots & \vdots \\ \mathbf{0} & \mathbf{0} & \dots & \boldsymbol{B_{c,N_w}} \end{bmatrix} \in \mathbb{R}^{N_w(n+2)\times N_w},$$

$$\mathbf{F_c} = \boldsymbol{K_m}^{-1} \begin{bmatrix} \boldsymbol{F_{c,1}} & \mathbf{0} & \dots & \mathbf{0} \\ \mathbf{0} & \boldsymbol{F_{c,2}} & \dots & \mathbf{0} \\ \vdots & \vdots & \ddots & \vdots \\ \mathbf{0} & \mathbf{0} & \dots & \boldsymbol{F_{c,N_w}} \end{bmatrix} \in \mathbb{R}^{N_w(n+2)\times N_w},$$

$$\mathbf{E_c}(t) = \boldsymbol{K_m}^{-1} \begin{bmatrix} \boldsymbol{E_{c,1}}(t) & \mathbf{0} & \dots & \mathbf{0} \\ \mathbf{0} & \boldsymbol{E_{c,2}}(t) & \dots & \mathbf{0} \\ \vdots & \vdots & \ddots & \vdots \\ \mathbf{0} & \mathbf{0} & \dots & \boldsymbol{E_{c,N_w}}(t) \end{bmatrix} \in \mathbb{R}^{N_w(n+2)\times N_w},$$

$$\boldsymbol{B_{c,i}} = \boldsymbol{F_{c,i}} = \boldsymbol{K_m}^{-1} \begin{bmatrix} 0 \\ (M_i + m_{\mu_i}) \\ \mathbf{0} \end{bmatrix} \quad \boldsymbol{E_{c,i}}(t) = \boldsymbol{K_m}^{-1} \begin{bmatrix} 0 \\ C_{vis_i}(t) \\ \mathbf{0} \end{bmatrix} \in \mathbb{R}^{(n+2)\times 1},$$

where,

$$\boldsymbol{K_m} = \begin{bmatrix} \boldsymbol{M_{a_{1,1}}} & \boldsymbol{M_{a_{1,2}}} & \dots & \boldsymbol{M_{a_{1,N_w}}} \\ \boldsymbol{M_{a_{2,1}}} & \boldsymbol{M_{a_{2,2}}} & \dots & \boldsymbol{M_{a_{2,N_w}}} \\ \vdots & \vdots & \ddots & \vdots \\ \boldsymbol{M_{a_{N_w,1}}} & \boldsymbol{M_{a_{N_w,2}}} & \dots & \boldsymbol{M_{a_{N_w,N_w}}} \end{bmatrix} \in \mathbb{R}^{N_w(n+2)\times N_w(n+2)} \tag{6.8}$$

$$\boldsymbol{M_{a_{i,j}}} = \begin{cases} \begin{bmatrix} 1 & 0 & \mathbf{0} \\ 0 & (M_i + m_{\mu_{i,i}}) & \mathbf{0} \\ \mathbf{0} & \mathbf{0} & \mathbf{I} \end{bmatrix}, & \text{if } i = j \\ \begin{bmatrix} 0 & 0 & \mathbf{0} \\ 0 & m_{\mu_{i,j}} & \mathbf{0} \\ \mathbf{0} & \mathbf{0} & \mathbf{0} \end{bmatrix}, & \text{if } i \neq j \end{cases} \in \mathbb{R}^{(n+2)\times(n+2)}$$

$$\mathbf{X}(t) = \begin{bmatrix} \boldsymbol{x_1(t)} \\ \vdots \\ \boldsymbol{x_{N_w}}(t) \end{bmatrix}, \mathbf{U_q}(t) = \begin{bmatrix} u_{q_1}(t) \\ \vdots \\ u_{q_{N_w}}(t) \end{bmatrix},$$
$$\mathbf{V}(t) = \begin{bmatrix} v_1(t) \\ \vdots \\ v_{N_w}(t) \end{bmatrix}, \dot{\mathbf{H}}(t) = \begin{bmatrix} \dot{\eta}_1(t) \\ \vdots \\ \dot{\eta}_{N_w}(t) \end{bmatrix},$$
$$\boldsymbol{x}_i(t) = \begin{bmatrix} z_i(t) \\ \dot{z}_i(t) \\ \boldsymbol{x_{ri}}(t) \end{bmatrix}.$$

Here $\boldsymbol{x}_i(t) \in \mathbb{R}^{(n+2)\times 1}$, $\mathbf{X}(t) \in \mathbb{R}^{N_w(n+2)\times 1}$ and $\{\mathbf{U_q}(t), \mathbf{V}(t), \dot{\mathbf{H}}(t)\} \in \mathbb{R}^{N_w \times 1}$ and the scaled forces, $u_{q_i}(t)$ and $v_i(t)$ are,

$$u_{q_i}(t) = \frac{F_{PTO_i}(t)}{M_i + m_{\mu_i}} \qquad v_i(t) = \frac{F_{e_i}(t)}{M_i + m_{\mu_i}} \tag{6.9}$$

6.3 Theoretical Maximum Power

In this section, a frequency domain algorithm producing optimum average electrical power from a hydrodynamically coupled WEC array is described. Initially, the entire hydrodynamic WEC array system (6.7) is representable in the frequency domain as (6.10),

$$j\omega \boldsymbol{K_m}(\omega)\dot{\mathbf{Z}}(\omega) + \mathbf{H_r}(\omega)\dot{\mathbf{Z}}(\omega) + \frac{\beta}{j\omega}\dot{\mathbf{Z}}(\omega) - \mathbf{F_{ex}}(\omega) = \mathbf{F_{PTO}}(\omega) \in \mathbb{C}^{N_w \times 1}, \tag{6.10}$$

where,

$$\mathbf{H_r}(\omega) = \begin{bmatrix} H_{r,11}(\omega) & H_{r,12}(\omega) & \dots & H_{r,1N}(\omega) \\ H_{r,21}(\omega) & H_{r,22}(\omega) & \dots & H_{r,2N}(\omega) \\ \vdots & \vdots & \ddots & \vdots \\ H_{r,N1}(\omega) & H_{r,N2}(\omega) & \dots & H_{r,NN}(\omega) \end{bmatrix} = \mathbf{H_{r,a}} + j\mathbf{H_{r,b}} \in \mathbb{C}^{N_w \times 1}, \tag{6.11}$$

$$\dot{\mathbf{Z}}(\omega) = \begin{bmatrix} \dot{Z}_1(\omega) \\ \dot{Z}_2(\omega) \\ \vdots \\ \dot{Z}_N(\omega) \end{bmatrix} = \dot{\mathbf{Z}}_\mathbf{a} + j\dot{\mathbf{Z}}_\mathbf{b} \in \mathbb{C}^{N_w \times N_w}, \tag{6.12}$$

$$\mathbf{F_{ex}}(\omega) = \begin{bmatrix} F_{ex,1}(\omega) \\ F_{ex,2}(\omega) \\ \vdots \\ F_{ex,N}(\omega) \end{bmatrix} = \mathbf{F_{ea}} + j\mathbf{F_{eb}} \in \mathbb{C}^{N_w \times 1}, \tag{6.13}$$

$$\mathbf{F_{PTO}}(\omega) = \begin{bmatrix} F_{PTO,1}(\omega) \\ F_{PTO,2}(\omega) \\ \vdots \\ F_{PTO,N}(\omega) \end{bmatrix} = -\left(\mathbf{F_a} + j\mathbf{F_b}\right) \in \mathbb{C}^{N_w \times 1}. \tag{6.14}$$

Transforming (6.10) into its complex form, showing the corresponding real and imaginary figures, (6.10) can be represented as (6.15),

$$\left(\mathbf{G} + j\mathbf{Q}\right)\left(\dot{\mathbf{Z}}_\mathbf{a} + j\dot{\mathbf{Z}}_\mathbf{b}\right) - \left(\mathbf{F_{ex,a}} + j\mathbf{F_{ex,b}}\right) = -\left(\mathbf{F_a} + j\mathbf{F_b}\right) \in \mathbb{C}^{N_w \times 1}, \tag{6.15}$$

where,

$$\left(\mathbf{G} + j\mathbf{Q}\right) = \left(\mathbf{H_{r,a}} + j\left(\omega \boldsymbol{K_m}(\omega) + \mathbf{H_{r,b}} - \frac{\beta}{\omega}\mathbf{I}\right)\right) \in \mathbb{C}^{N_w \times N_w}. \tag{6.16}$$

Decomposing the real and imaginary components of (6.15), the following can be transformed into matrix form,

$$\begin{bmatrix} \mathbf{F_a} \\ \mathbf{F_b} \end{bmatrix} = \begin{bmatrix} \mathbf{F_{ea}} \\ \mathbf{F_{eb}} \end{bmatrix} - \begin{bmatrix} \mathbf{G} & -\mathbf{Q} \\ \mathbf{Q} & \mathbf{G} \end{bmatrix} \begin{bmatrix} \dot{\mathbf{Z}}_\mathbf{a} \\ \dot{\mathbf{Z}}_\mathbf{b} \end{bmatrix} \in \mathbb{R}^{2N_w \times 1}. \tag{6.17}$$

The formulation of the average electrical power from first principles is shown in Appendix C, where the resulting average electrical power $\bar{P}$ is shown in (6.18),

$$\bar{P} = \frac{1}{2}\left[\begin{bmatrix} \dot{\mathbf{Z}}_\mathbf{a} \\ \dot{\mathbf{Z}}_\mathbf{b} \end{bmatrix}^T \begin{bmatrix} \mathbf{F_a} \\ \mathbf{F_b} \end{bmatrix} - \begin{bmatrix} \mathbf{F_a} \\ \mathbf{F_b} \end{bmatrix}^T \begin{bmatrix} \boldsymbol{\psi} & \mathbf{0} \\ \mathbf{0} & \boldsymbol{\psi} \end{bmatrix} \begin{bmatrix} \mathbf{F_a} \\ \mathbf{F_b} \end{bmatrix}\right] \in \mathbb{R}^{1\times 1}, \tag{6.18}$$

where,

$$\boldsymbol{\psi} = \frac{R}{\left(\frac{\pi}{\tau}\lambda'_{fd}\right)^2}\begin{bmatrix} 1 & 0 & \dots & 0 \\ 0 & 1 & \dots & 0 \\ \vdots & \vdots & \ddots & \vdots \\ 0 & 0 & \dots & 1 \end{bmatrix} \in \mathbb{R}^{N_w \times N_w}. \tag{6.19}$$

Substituting (6.17) into (6.18) yields (6.20),

$$\bar{P} = \frac{1}{2}\Bigg(-\begin{bmatrix} \dot{\mathbf{Z}}_\mathbf{a} \\ \dot{\mathbf{Z}}_\mathbf{b} \end{bmatrix}^T \left(\boldsymbol{\Phi} + \boldsymbol{\Phi}^\mathbf{T}\boldsymbol{\Lambda}\boldsymbol{\Phi}\right)\begin{bmatrix} \dot{\mathbf{Z}}_\mathbf{a} \\ \dot{\mathbf{Z}}_\mathbf{b} \end{bmatrix} + \begin{bmatrix} \dot{\mathbf{Z}}_\mathbf{a} \\ \dot{\mathbf{Z}}_\mathbf{b} \end{bmatrix}^T \left(2\boldsymbol{\Phi}^\mathbf{T}\boldsymbol{\Lambda} + \mathbf{I}\right)\begin{bmatrix} \mathbf{F}_\mathbf{ea} \\ \mathbf{F}_\mathbf{eb} \end{bmatrix} - \begin{bmatrix} \mathbf{F}_\mathbf{ea} \\ \mathbf{F}_\mathbf{eb} \end{bmatrix}^T \boldsymbol{\Lambda}\begin{bmatrix} \mathbf{F}_\mathbf{ea} \\ \mathbf{F}_\mathbf{eb} \end{bmatrix}\Bigg) \in \mathbb{R}^{1\times 1}, \tag{6.20}$$

where,

$$\boldsymbol{\Phi} = \begin{bmatrix} \mathbf{G} & -\mathbf{Q} \\ \mathbf{Q} & \mathbf{G} \end{bmatrix} \in \mathbb{R}^{2N_w \times 2N_w} \tag{6.21}$$

and

$$\boldsymbol{\Lambda} = \begin{bmatrix} \boldsymbol{\psi} & \mathbf{0} \\ \mathbf{0} & \boldsymbol{\psi} \end{bmatrix} \in \mathbb{R}^{2N_w \times 2N_w}. \tag{6.22}$$

Optimising (6.20), the optimum frequency domain velocities $\begin{bmatrix} \dot{\mathbf{Z}}^{\star T}_\mathbf{a} & \dot{\mathbf{Z}}^{\star T}_\mathbf{b} \end{bmatrix}^T$ become attainable,

$$\begin{bmatrix} \dot{\mathbf{Z}}_\mathbf{a} \\ \dot{\mathbf{Z}}_\mathbf{b} \end{bmatrix}^\star = \left(\boldsymbol{\Phi} + \boldsymbol{\Phi}^\mathbf{T}\boldsymbol{\Lambda}\boldsymbol{\Phi}\right)^{-1}\left(\boldsymbol{\Phi}^\mathbf{T}\boldsymbol{\Lambda} + \frac{1}{2}\mathbf{I}\right)\begin{bmatrix} \mathbf{F}_\mathbf{ea} \\ \mathbf{F}_\mathbf{eb} \end{bmatrix}. \tag{6.23}$$

Substituting the optimum velocities (6.23) into the average power equation (6.20), the optimum average power (6.24) is obtained, illustrating the maximum obtainable average electrical power from the WEC array,

$$\bar{P}^\star = \frac{1}{2}\Bigg(\begin{bmatrix} \mathbf{F}_\mathbf{ea} \\ \mathbf{F}_\mathbf{eb} \end{bmatrix}^T \Bigg(\left(\boldsymbol{\Phi}^\mathbf{T}\boldsymbol{\Lambda} + \frac{1}{2}\mathbf{I}\right)^T \left(\boldsymbol{\Phi}^T + \boldsymbol{\Phi}^\mathbf{T}\boldsymbol{\Lambda}\boldsymbol{\Phi}\right)^{-1}\left(\boldsymbol{\Phi}^\mathbf{T}\boldsymbol{\Lambda} + \frac{1}{2}\mathbf{I}\right) - \boldsymbol{\Lambda}\Bigg)\begin{bmatrix} \mathbf{F}_\mathbf{ea} \\ \mathbf{F}_\mathbf{eb} \end{bmatrix}\Bigg) \tag{6.24}$$

6.4 Control of the Array of Point Absorbers to Optimise Electrical Power

In this work, a cascade controller is used for each localised WEC system, as shown in Fig. 6.9. An economic model predictive control (MPC) controller is implemented on the outer slower loop, which maximises the average electrical power extracted from the system. Using the optimum LPMG force set point $u_{q_i}(k)$ provided from the outer loop, the faster inner loop produces this LPMG force utilising PI control. Here zero field weakening is assumed ($i_{d_i}(t) = 0$ A), (O'Sullivan & Lightbody 2017*a*).

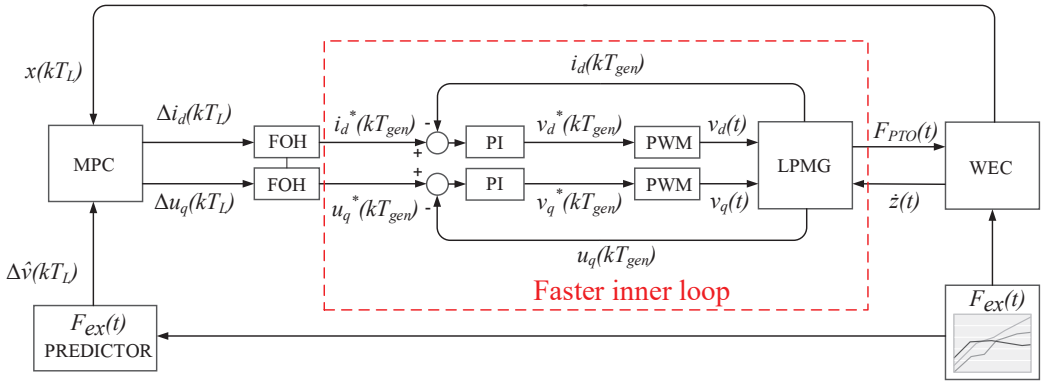

Figure 6.9: Cascade control scheme of slower MPC outer loop and faster LPMG PTO force controller.

6.4.1 The Cost Function for an Array

The purpose of the MPC presented in this work is to maximise the electrical power absorbed from the entire WEC array. The total average electrical power absorbed from the array can be expressed as (6.25),

$$P_{e_{tot}}(t) = \sum_{i=1}^{N_w} P_{e_i}(t). \tag{6.25}$$

Here each individual WEC average electrical power $P_{e_i}(t)$ can be determined as (6.26),

$$P_{e_i} = -\frac{1}{T}\int_{t=0}^{T} \left((M_i + m_{\mu_i})\, u_{q_i}(t)\dot{z}_i(t) + \frac{R}{\psi^2} u_{q_i}^2(t) \right) dt. \tag{6.26}$$

where as shown in (O'Sullivan & Lightbody 2017*a*),

$$\psi = \frac{\frac{\pi}{\tau}\lambda_{fd}^{'}}{(M_i + m_{\mu_i})}$$

Here τ is the pole pitch and $\lambda_{fd}^{'}$ is the scaled flux linkage of the LPMG. As in previous work (O'Sullivan & Lightbody 2017*a*), the outer MPC loop in the cascade control scheme sends optimal $u_{q_i}(t)$ ramp trajectories to the inner current control loop which operates at a much higher bandwidth. Since a first order hold (FOH) is utilised, $u_{q_i}(k)$ and $\dot{z}_i(k)$ are both piecewise linear between the outer-loop samples and the average electrical power for a single WEC (6.26) can be estimated in the discrete domain using trapezoidal integration. Maximising electrical power P_{e_i} for the i^{th} WEC is equivalent to minimising the cost function $J_i(k)$, (6.27),

$$\begin{aligned} J_i(k) = \frac{1}{2}u_{q_i}(k+N_p)\dot{z}_i(k+N_p) + \sum_{j=1}^{N_p} u_{q_i}(k+j)\dot{z}_i(k+j) \\ + \frac{R(M_i+m_{\mu_i})}{(\lambda_{fd}^{'}\frac{\pi}{\tau})^2}\left(\frac{1}{2}u_{q_i}^2(k+N_p) + \sum_{j=1}^{N_p} u_{q_i}^2(k+j)\right). \end{aligned} \tag{6.27}$$

Combining all N_w cost functions into a single cost function, a global cost function (6.28) is formed,

$$J_T(k) = \sum_{i=1}^{N_w} J_i(k). \tag{6.28}$$

Using optimisation algorithms such as quadratic programming (QP) over a prediction horizon N_p, the cost function (6.28) can be minimised.

6.4.2 Prediction Model for Centralised MPC

MPC requires a discrete time model of the array. To simplify the discretisation of the system, the viscosity term in (6.7) is initially ignored. Later in this work, the viscosity term will be reinstated into the control using non-linear model predictive control (NMPC), which was introduced in (O'Sullivan & Lightbody 2017*c*). The discrete state space model is,

$$\begin{aligned} \mathbf{X_f}(k+1) = \mathbf{A_f}\mathbf{X_f}(k) + \mathbf{B_f}\mathbf{\Delta U_q}(k+1) + \mathbf{F_f}\mathbf{\Delta V}(k+1) \\ \mathbf{Y_f}(k) = \mathbf{C_f}\mathbf{X_f}(k) \end{aligned} \tag{6.29}$$

$$\mathbf{X_f}(k) = \begin{bmatrix} \mathbf{X}(k) \\ \hdashline \mathbf{U_q}(k) \\ \mathbf{V}(k) \end{bmatrix} \in \mathbb{R}^{N_w(n+4)\times 1}$$

$$\mathbf{Y_f}(k) = \begin{bmatrix} z_1(k) \\ \dot{z}_1(k) \\ u_{q1}(k) \\ \hdashline \vdots \\ \hdashline \\ z_{N_w}(k) \\ \dot{z}_{N_w}(k) \\ u_{qN_w}(k) \end{bmatrix} \in \mathbb{R}^{3N_w\times 1}$$

$$\mathbf{A_f} = \begin{bmatrix} e^{\mathbf{A_c}T_L} & \mathbf{\Lambda} & \mathbf{\Lambda} \\ \hdashline \mathbf{0} & \mathbf{1} & \mathbf{0} \\ \mathbf{0} & \mathbf{0} & \mathbf{1} \end{bmatrix} \in \mathbb{R}^{N_w(n+4)\times N_w(n+4)}$$

$$\mathbf{B_f} = \begin{bmatrix} \mathbf{\Gamma} \\ \hdashline \mathbf{1} \\ \mathbf{0} \end{bmatrix} \mathbf{F_f} = \begin{bmatrix} \mathbf{\Gamma} \\ \hdashline \mathbf{0} \\ \mathbf{1} \end{bmatrix} \in \mathbb{R}^{N_w(n+4)\times N_w}.$$

Here $\mathbf{\Lambda} = \mathbf{A_c}^{-1}\left(e^{\mathbf{A_c}T_L} - I\right)\mathbf{B_c} \in \mathbb{R}^{N_w(n+2)\times N_w}$, $\mathbf{\Gamma} = \frac{1}{T_L}\mathbf{A_c}^{-1}\left(\mathbf{\Lambda} - T_L\mathbf{B_c}\right) \in \mathbb{R}^{N_w(n+2)\times N_w}$ and T_L is the outer sampling time.

Assuming that the future excitation wave forces are known over the prediction horizon, the output vector of the system can be predicted over the N_p step prediction horizon using (6.30),

$$\hat{\mathbf{Y}}_\mathbf{f}(k) = \mathbf{P}\mathbf{X_f}(k) + \mathbf{H_a}\mathbf{\Delta}\hat{\mathbf{U}}_\mathbf{q}(k) + \mathbf{H_w}\mathbf{\Delta}\hat{\mathbf{V}}(k), \tag{6.30}$$

where

$$\hat{\mathbf{Y}}_\mathbf{f}(k) = \begin{bmatrix} \mathbf{Y_f}(k+1|k) \\ \vdots \\ \vdots \\ \mathbf{Y_f}(k+N_p|k) \end{bmatrix} \in \mathbb{R}^{N_p(3N_w)\times 1} \tag{6.31}$$

and $\mathbf{P} \in \mathbb{R}^{N_p(3N_w)\times(n+4)N_w}$, $\mathbf{H_a} \in \mathbb{R}^{N_p(3N_w)\times N_p(N_w)}$, $\mathbf{H_w} \in \mathbb{R}^{N_p(3N_w)\times N_p(N_w)}$,$\mathbf{\Delta}\hat{\mathbf{U}}_\mathbf{q}(k)$ $\in \mathbb{R}^{N_p(N_w)\times 1}$, $\mathbf{\Delta}\hat{\mathbf{V}}(k) \in \mathbb{R}^{N_p(N_w)\times 1}$; a full description of the structure of these matrices is provided in previous chapters and in (O'Sullivan & Lightbody 2017*a*).

Using the output predictions (6.31), the cost function (6.27) can then be represented in matrix form (6.32),

$$J_T(k) = \frac{1}{2}\hat{\mathbf{Y}}_\mathbf{f}(k)^T \mathbf{Q_a} \hat{\mathbf{Y}}_\mathbf{f}(k), \tag{6.32}$$

where,

$$\mathbf{Q_a} = \begin{bmatrix} \mathbf{Q}_1 & \mathbf{0} & .. & \mathbf{0} \\ \mathbf{0} & \mathbf{Q}_2 & .. & \mathbf{0} \\ : & : & \ddots & : \\ \mathbf{0} & \mathbf{0} & \mathbf{0} & \mathbf{Q}_{N_w} \end{bmatrix} \in \mathbb{R}^{N_p(3N_w)\times N_p(3N_w)}.$$

Here $\mathbf{Q}_i \in \mathbb{R}^{3N_p \times 3N_p}$ and $\mathbf{M}_i \in \mathbb{R}^{3\times 3}$

$$\mathbf{Q}_i = \begin{bmatrix} \mathbf{M}_i & \mathbf{0} & .. & \mathbf{0} \\ \mathbf{0} & \mathbf{M}_i & .. & \mathbf{0} \\ : & : & \ddots & : \\ \mathbf{0} & \mathbf{0} & \mathbf{0} & \frac{1}{2}\mathbf{M}_i \end{bmatrix}, \ \mathbf{M}_i = \begin{bmatrix} 0 & 0 & 0 \\ 0 & 0 & 1 \\ 0 & 1 & 2G_i \end{bmatrix}$$

and

$$G_i = \frac{R(M_i + m_{\mu_i})}{(\lambda'_{fd}\frac{\pi}{\tau})^2}.$$

Neglecting terms that are independent of $\mathbf{\Delta U_q}(k)$, the expansion of (6.32) yields (6.33),

$$\begin{aligned} J_T = \frac{1}{2}\mathbf{\Delta \hat{U}_q}^T \mathbf{H_a}^T \mathbf{Q_a} \mathbf{H_a} \mathbf{\Delta \hat{U}_q} \\ + \mathbf{\Delta \hat{U}_q}^T \mathbf{H_a}^T \mathbf{Q_a} \left(\mathbf{P X_f} + \mathbf{H_w} \mathbf{\Delta \hat{V}} \right). \end{aligned} \tag{6.33}$$

Assuming that the cost function in (6.33) is semi-positive definite, Quadratic programming (QP) solvers, such as in MATLAB (R2016a) or AMPL (Version 1) (Hürlimann 1993), can be used to minimise the cost function across a prediction horizon, subject to constraints.

6.5 Results

6.5.1 Centralised Predictive Control of Wave Energy Arrays

The effects of incorporating linear constraints in the centralised MPC (6.33) is explored. The linear constraints include the heave displacement $\pm z_{max}$, the heave velocity $\pm \dot{z}_{max}$ and the scaled PTO force $\pm u_{q_{max}}$. Subsequently the effect of viscosity on the arrays interactions is then analysed using a non-linear MPC (NMPC) where the viscous force $F_v(t)$ was discussed in section 6.2.1. The structure and algorithm of this NMPC is thoroughly discussed in (O'Sullivan & Lightbody 2017*c*), where the predicted states over the prediction horizon of the NPMC are dependent on the previously predicted wave and WEC velocities. In this study, the cross-coupling added mass values (6.8) in the hydrodynamic system model (6.7) and the control model are excluded, since they complicate the modelling and they have little effect on the hydrodynamics. However, in previous work these cross-coupling added mass terms have been included (O'Sullivan & Lightbody 2018), where the results are identical.

6.5.1.1 The Effect of Constraints and Viscosity on the Sensitivity of the Array Power to Changes in Penetration Angle

In this section the unconstrained system was excited with 1 m high monochromatic waves with wave frequencies $\omega \in \{0.6, \dots 1.22\}$ rad/s and a range of penetration angles $\theta \in \{0, \dots 2\pi\}$ rad. Examples of the absorbed average electrical powers $\bar{P}$ are shown in Fig. 6.10, where the method for calculating optimum average electrical powers absorbed are from a fully coupled array using centralised optimum control is shown in Appendix C; in Fig. 6.10 the average powers from the two array orientations are tested at both $d = 25$ m and $d = 100$ m.

The power variance factor $\Delta P^2(\omega)$ is defined in (6.34),

$$\Delta P^2(\omega) = \frac{\sum_{\theta} \left[\bar{P}(\theta, \omega) - \bar{P}_\theta(\omega)\right]^2}{N_\theta}. \tag{6.34}$$

Here $\Delta P^2(\omega)$ is a measure of how much the average power varies with the wave penetration angle range θ, $\bar{P}_\theta(\omega)$ is the mean average power of the array across the θ range for excitation frequency ω and N_θ is the amount of angles considered.

The power variance factor $\Delta P^2(\omega)$ of an unconstrained two device array is shown in Fig. 6.11(a) and an unconstrained three device array in Fig. 6.11(b). The arrays are ex-

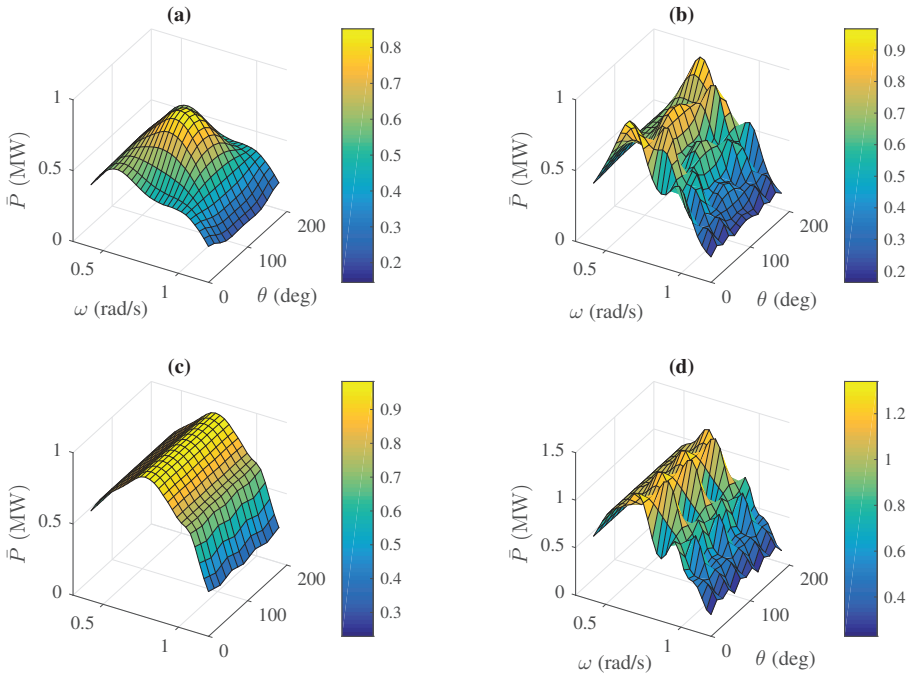

Figure 6.10: Average electrical power $\bar{P}$ extracted from an unconstrained, inviscid WEC array which are excited by monochromatic waves with a peak height of $\alpha = 1$ m, a range of frequencies ω and uniformly distributed wave penetration angles θ using centralised MPC of the array with (a) two devices with a separation distance of $d = 25$ m, (b) two devices a separation distance of $d = 100$ m, (c) three devices with a separation distance of $d = 25$ m and (d) three devices with a separation distance of $d = 100$ m

cited with 1 m high monochromatic waves with wave frequencies $\omega \in \{0.6, \ldots 1.22\}$ rad/s, penetration angles $\theta \in \{0, \ldots 2\pi\}$ rad and $d \in \{20, \ldots, 100\}$ m. The power variance factor of the average electrical power $\bar{P}$ is less for a three device array than it is for a two device array. Furthermore, the power variance factor at low separation distances is much less than the two device array, meaning that the average power from a three device array is more independent of the wave penetration angle θ.

An unconstrained inviscid system with an MPC, a constrained inviscid system with a MPC, and a constrained viscid system with a NMPC were excited with 1 m high monochromatic waves with wave frequencies $\omega \in \{0.6, \ldots 1.22\}$ rad/s. To simplify the analysis, the two device array orientation was chosen with a constant separation distance of $d = 25$m. In Fig. 6.12, the power variance factor $\Delta P^2(\omega)$ across the θ range ($\theta \in \{0, \ldots 2\pi\}$ rad) is shown for each frequency. The results in Fig. 6.12 show that when linear mechanical constraints are incorporated into the NMPC, which is implemented on a viscous system, the variance of the average power dramatically reduces; this results in an array with diminished constructive or indeed destructive

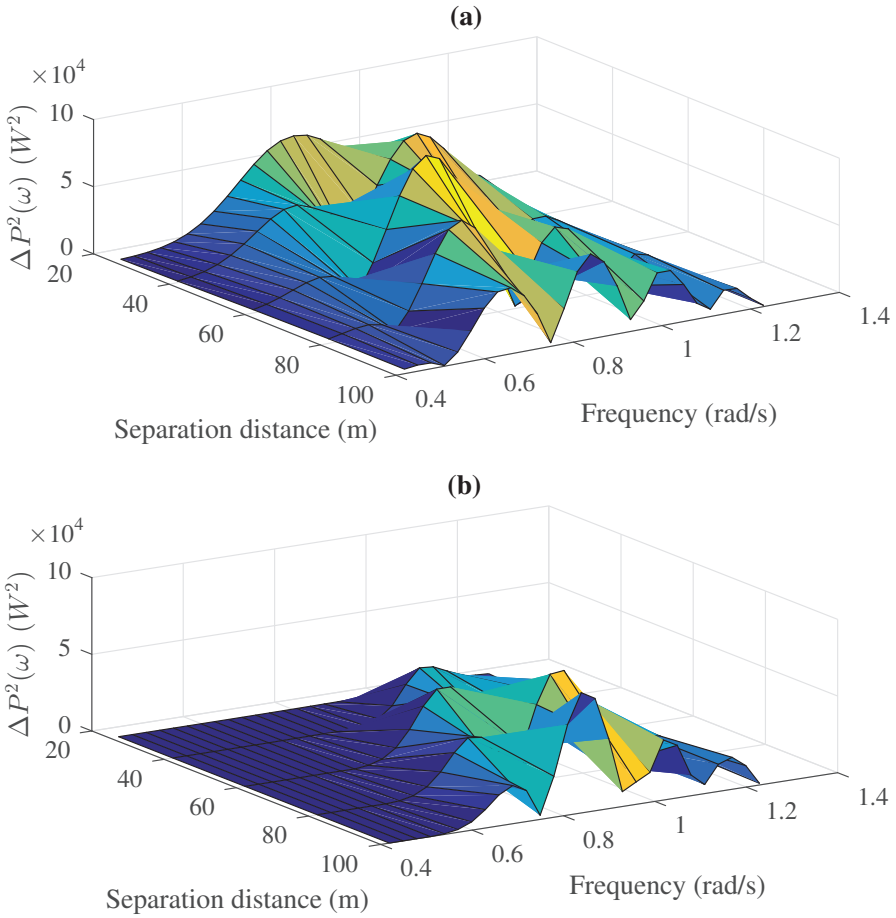

Figure 6.11: The power variance factor $\Delta P^2(\omega)$ of the average power $\bar{P}$ from a fully coupled two and three WEC array using 1 m high monochromatic waves with a range of separation distances d and excitation, frequencies and a uniformly weighted wave heights with (a) the power variance factor from a two device array, (b) the power variance factor from a three device array

interactions.

6.5.1.2 The Effect of Constraints and Viscosity on the q Factor of the Array

In this section the q factor (6.35) of the array is analysed, where the q factor is the ratio of the average power extracted from a coupled array $\bar{P}_c(\omega, \theta)$ to the average power extracted from an array of N_w isolated identical WECs each producing $\bar{P}_d(\omega, \theta)$.

$$q(\omega, \theta) = \frac{\bar{P}_c(\omega, \theta)}{N_w \bar{P}_d(\omega, \theta)} \tag{6.35}$$

The amplitude α of the monochromatic excitation ($0 < \alpha(\theta) \leq 1$ m) preferentially weights waves with penetration angles close to the optimal penetration angle θ^* for the

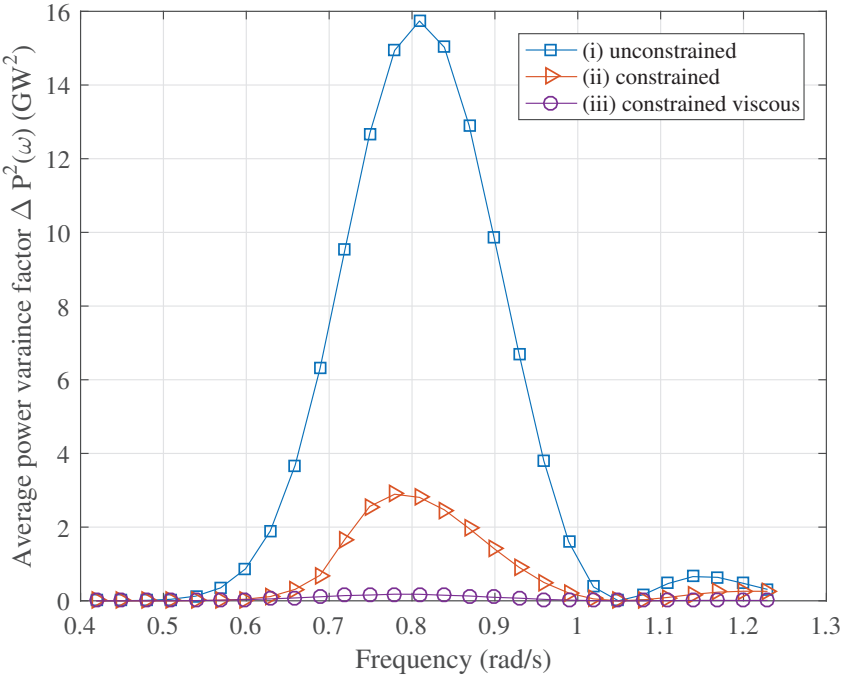

Figure 6.12: The power variance factor $\Delta P^2(\omega)$ of the average power $\bar{P}$ from a fully coupled two device WEC array receiving 1 m high monochromatic waves across a range of $\theta \in \{0, \ldots 2\pi\}$ at a constant separation distance of $d = 25$ m when (i) an unconstrained global MPC controller is used, (ii) a constrained global MPC controller is used and when (iii) a constrained non-linear global MPC controller is used which includes the effects of viscosity

array using (6.36) (Balitsky & Ringwood 2014),

$$\alpha(\theta) = \frac{2^{2s-1}}{\pi} \frac{\Gamma^2(s+1)}{\Gamma(2s+1)} \cos^{2s}\left(\frac{\theta - \theta^*}{2}\right), \tag{6.36}$$

where Γ is the weighted Gamma function and the s parameter determines the width of the weighted spectrum. Here $\theta^* = \pi/4$ rads for the array orientations in this work, $\omega \in \{0.6, \ldots 1.22\}$ rad/s, penetration angles $\theta \in \{0, \ldots 2\pi\}$ rad and $d \in \{20, \ldots, 100\}$ m.

Fig. 6.13 shows the mean q factor over the range of penetration angles ($\theta \in \{0, \ldots 2\pi\}$) with weighted monochromatic waves. When the q factor values from the unconstrained two device array Fig. 6.13(a) are compared against the q factor values from an unconstrained three device array Fig. 6.13(b), it is clearly shown in both data sets that as the separation distance increases, inter-device interactions decrease causing the q factor across the frequency range to approach unity. However, it is notable that at shorter separation distances, the q factor for the three device array varies more across the frequency range than the two device array.

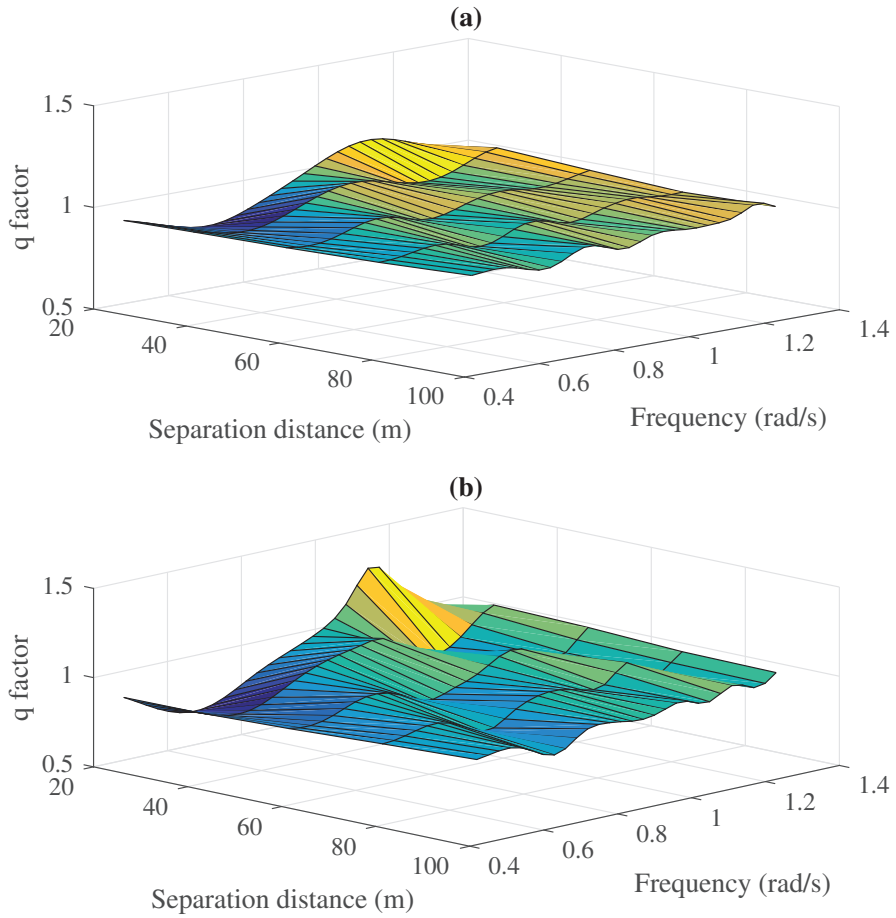

Figure 6.13: A comparison of the mean q factor across a θ range between a two and three unconstrained, inviscid WEC array using preferentially weighted $0 < \alpha(\theta) \leq 1$ m high monochromatic waves with a range of separation distances d, frequencies and a wave amplitude $0 < \alpha(\theta) \leq 1$ with (a) the q factor from a two device array, (b) the q factor from a three device array

An unconstrained inviscid system with an MPC, a constrained inviscid system with a MPC and a constrained viscid system with a NMPC were excited with 1 m high monochromatic waves. As in section 6.5.1.1, the two device array orientation was chosen with a constant separation distance of $d = 25$m to simplify the analysis. The frequencies $\omega \in \{0.6, \ldots 1.22\}$ rad/s and the penetration angle $\theta \in \{0, \ldots 2\pi\}$ rads were uniformly distributed. The results shown in Fig. 6.14 present the minimum, average and maximum q factor across the range of ω and θ values. It is evident that as the linear constraints are included into the MPC, the maximum and minimum q factor values each approach unity. As the viscosity force $F_v(t)$ is then included in the system and the linear constraints are included in the NMPC, the minimum and maximum q factors move even closer to unity. It is clearly shown in Fig. 6.14 that both the presence of constraints and viscosity lead to a reduction in the variability of the q factor in response to the penetration angle and frequency. This also signifies that the effects of constructive and destructive interactions are reduced.

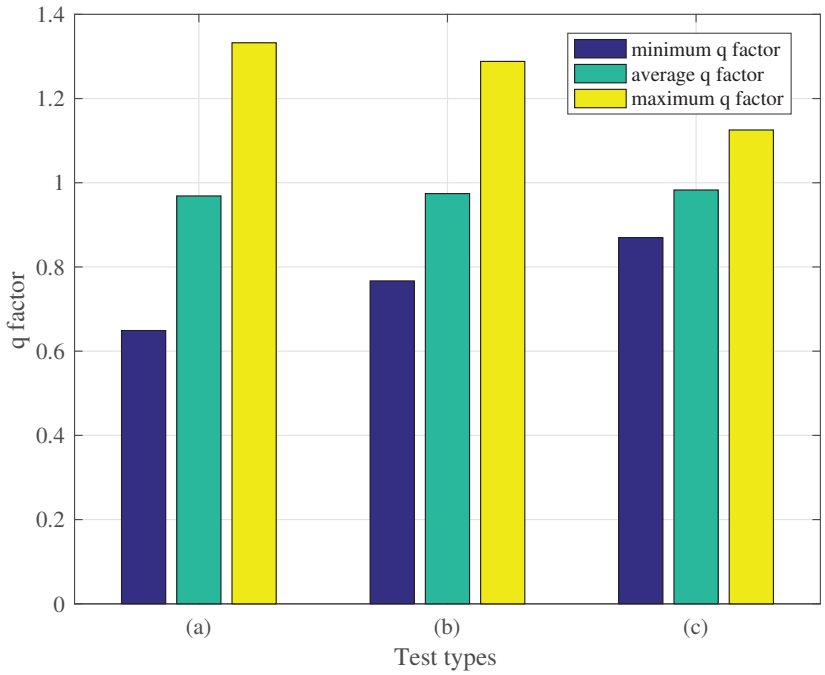

Figure 6.14: The q factor range (minimum, average, maximum) from a fully coupled two device WEC array receiving high monochromatic waves with a range of equally distributed wave penetration angles $\theta \in \{0, \ldots 2\pi\}$ rad and frequencies $\omega \in \{0.4, \ldots 1.22\}$ rad.s^{-1} at a constant separation distance of $d = 25$ m when (a) an unconstrained global MPC controller is used, (b) a constrained global MPC controller is used and when (c) a constrained non-linear global MPC controller is used which includes the effects of viscosity

6.5.2 Centralised vs Decentralised Predictive Control

Here the performance of a centralised MPC and a decentralised MPC are compared against each other for the extraction of electrical power from the two device array with a range of equally distributed wave penetration angles $\theta \in \{0, \ldots \pi\}$ rad and frequencies $\omega \in \{0.4, \ldots 1.22\}$ rad.s^{-1} at a constant separation distance of $d = 25$ m. Using 1 m high monochromatic waves the total electrical power extracted from the array using the decentralised MPC scheme P_{local} is compared with the total electrical power extracted using the centralised MPC, P_{global}. Fig. 6.15 shows the power ratio P_{local}/P_{global} of: (a), an inviscid unconstrained system using a linear MPC, (b) an inviscid constrained system using a linear MPC and (c), a viscid constrained system using a NMPC. From Fig. 6.15(a), the power ratio from an unconstrained inviscid system is shown to vary significantly P_{local}/P_{global} to as low as 0.83 with the average power ratio across the ω and θ range is 0.92. When comparing the results from Fig. 6.15(a) to the results shown in Fig. 6.15(b) and Fig. 6.15(c) it is clear that as the viscosity and linear constraints are included in the NMPC optimisation, both the minimum and

average power ratios converge towards unity, hence indicating that in the presence of constraints and viscosity, the independent decentralised MPC produces near identical results to the global centralised MPC.

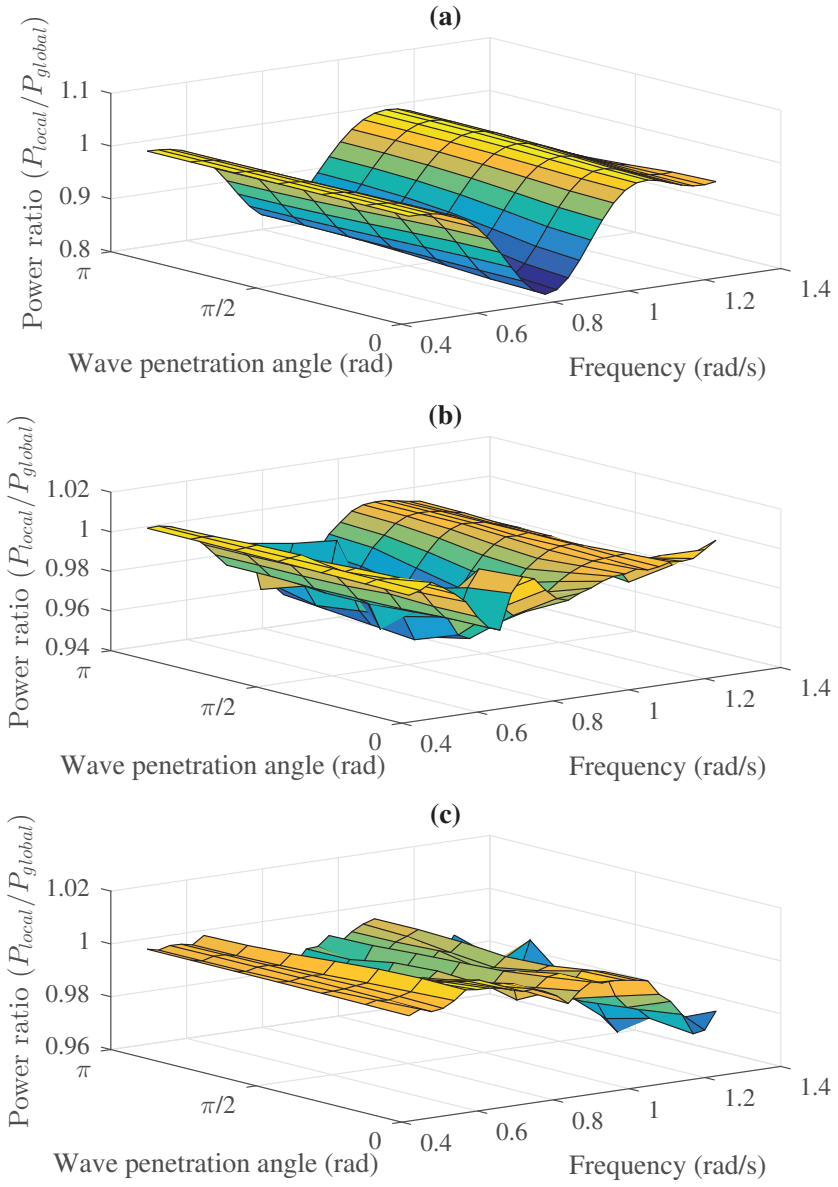

Figure 6.15: The average power ratio produced between the decentralised MPC P_{local} and the centralised MPC P_{global} for a fully coupled two device WEC array receiving 1 m high monochromatic waves with a range of equally distributed wave penetration angles $\theta \in \{0, \ldots \pi\}$ rad and frequencies $\omega \in \{0.4, \ldots 1.22\}$ rad.s^{-1} at a constant separation distance of $d = 25$ m when (a) the unconstrained MPC controllers are used, (b) the constrained MPC controllers are used and when (c) viscosity is included and the constrained non-linear MPC controller is used.

Both two device and three device arrays were then excited with an irregular wave obeying the Bretschneider spectrum. Three sea states are examined: ($T_p = 6$ s, $H_s = 1$ m), ($T_p = 7.8$ s, $H_s = 2$ m) and ($T_p = 9.6$ s, $H_s = 3$ m). The waves are unidirectional, with a penetration angle $\theta = \pi/4$ rad. Both viscosity and linear mechanical constraints are included. The non-linear NMPC is utilised. The performance of a centralised, and a decentralised NMPC are compared for the following ratios of separation distance to WEC radius, $d/r \in \{3, 5, 8, 12\}$. In the centralised NMPC, the full model of the array including the interactions between devices is used - the power extracted using this control is P_{global}. In the decentralised NMPC, the problem is broken down into N_w simpler independent control problems, one for each device, assuming that there is no interaction between the devices in the array - the power extracted from the array is P_{local}.

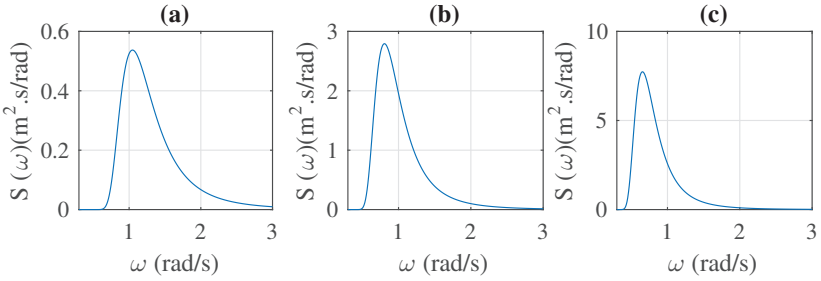

Figure 6.16: The Bretschneider spectrum distributions representing (a) sea state 1 ($T_p = 6$ s and $H_s = 1$ m), (b) sea state 2 ($T_p = 7.8$ s and $H_s = 2$ m) and (c) sea state 3 ($T_p = 9.6$ s and $H_s = 3$ m)

Fig. 6.17 shows the power ratio P_{local}/P_{global} for both a two device and a three device array, for the sea-states shown in Fig. 6.16 and how this depends on d/r. Indeed it is apparent that for reasonable device separation for both arrays, that there is little benefit to be obtained from using a centralised over a decentralised controller. For separation ratio $d/r > 5$ for the two device array and $d/r > 7$ for the three device array, the decentralised MPC extracts $> 99\%$ of the global optimum electrical power, over the three sea states.

6.5.3 Control of the Electrical Power Quality

Even though the maximisation of the average power from the WEC array is desirable, another primary problem which is frequently highlighted is the low average to peak power ratio from the extracted instantaneous power. Ideally, the instantaneous power exported from the WEC array onto the grid should be constant, especially at high power levels where high power fluctuations may cause stability problems in weak grids. The

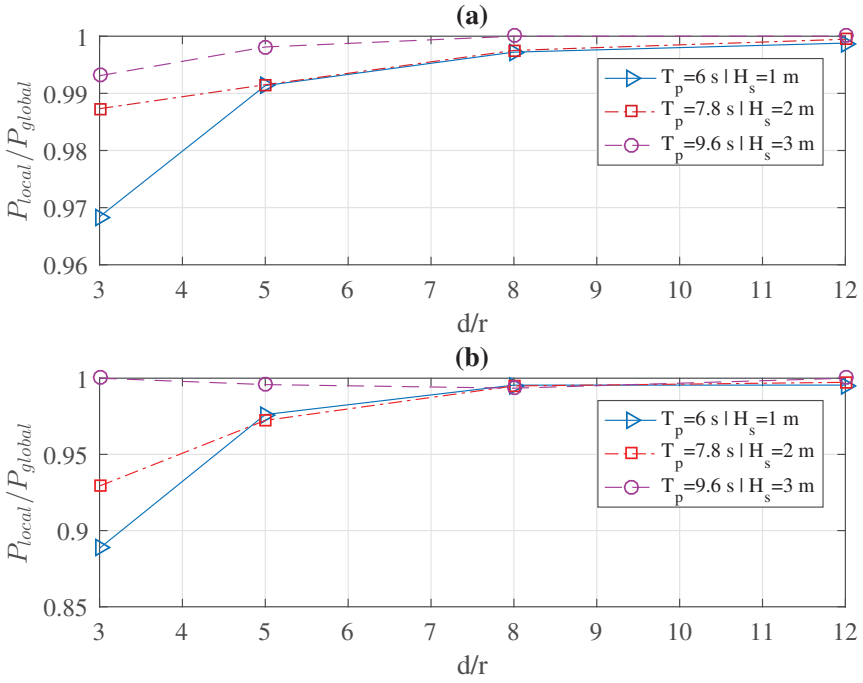

Figure 6.17: The average power ratio produced between the decentralised MPC P_{local} and the centralised MPC P_{global} for three unidirectional irregular sea states. The wave penetration angle is $\theta = \pi/4$ rad and the range of (separation/WEC radii) distances $d/r \in \{3, 5, 8, 12 \text{ m}\}$ where (a) two device array, (b) three device array

instantaneous power extracted from a wave energy device is generally an oscillatory waveform. Aggregating the power from multiple devices could decrease the variability of the power exported to the grid, due to the fact that the WEC devices each receive different excitation waves, hence each producing power waveforms which are out of phase.

In this section an upper instantaneous power limit P_{MAX} is incorporated into the centralised NMPC; this is compared with the results obtained when applying a local power constraint P_{MAX}/N_w to each individual device. Also incorporated in both the global and local power constrained NMPC is a move-blocking technique (O'Sullivan & Lightbody 2017*b*), which reduces the computational effort of the QP algorithm while maintaining a similar performance to an economic MPC with a full horizon; in this case the selected move-blocking horizon is $N_p = 40$. As shown in section 6.5.2, when an irregular excitation wave with sea state 3 ($T_p = 9.6$ s and $H_s = 3$ m) was implemented on the two arrays, the difference between the centralised control system and the decentralised control system was insignificant. In this analysis a three WEC array with a set wave penetration angle $\theta = \pi/4$ rad and separation distance of $d = 40$ m ($d/r = 8$) is chosen, as it is the threshold in Fig. 6.17(b) where the P_{local}/P_{global} ratio is effectively unity. The analysis consists of simulating the system under the same irregular

sea state waveforms with a range of different instantaneous power limits for the array $P_{MAX} \in \{0.25,\ 0.5,\ 0.75,\ 1,\ 1.5,\ 2,\ 3,\ 4,\ 5,\ 6\}$ MW.

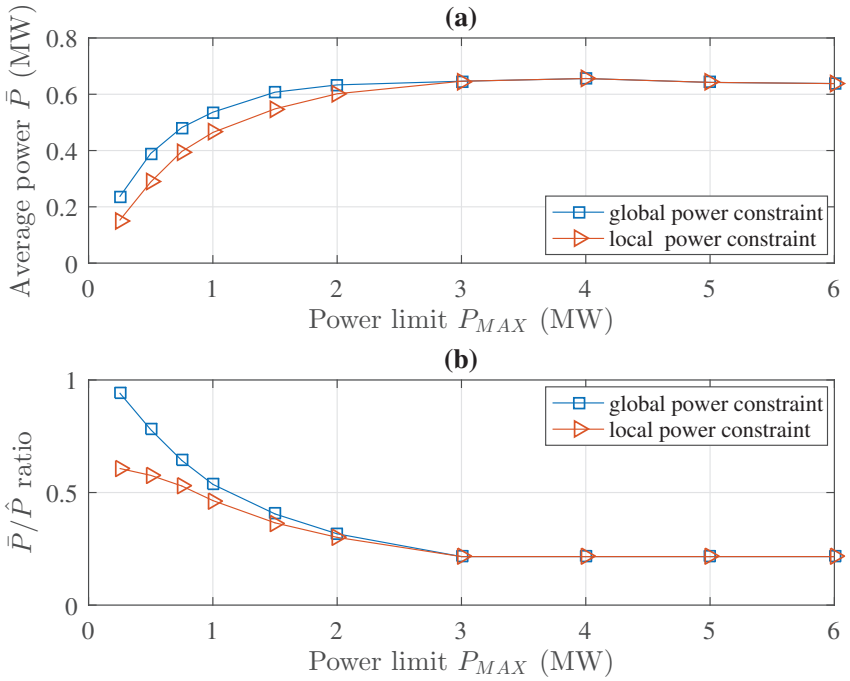

Figure 6.18: An analysis of the power extracted from a three device array with either a global power constraint or with a local power constraint. The array is excited with a unidirectional irregular sea state modelled using a Bretschneider spectrum with $H_s = 3$ m and $T_p = 9.6$ s (a) Average absorbed power $\bar{P}$ from the entire three WEC array, (b) the average to peak power ratio $\bar{P}/\hat{P}$ of the entire three WEC array

It is shown in Fig. 6.18(a) that as the array power limit P_{MAX} decreases, the average power $\bar{P}$ extracted decreases. It is noticeable that the average power from the global power limited system is greater than the average power using the local power constraint. From Fig. 6.18(b), it is important to note that for the global power constraint that the average to peak ratio $\bar{P}/\hat{P}$ when the power is constrained is superior to the value found with local device power limits.

For example, in Fig. 6.18(b) when the power limit is $P_{MAX} = 0.25$ MW, the global power limited system produces a $\bar{P}/\hat{P}$ ratio of 0.9427, which is an improvement from the system with the local power limits which produced $\bar{P}/\hat{P} = 0.6070$. The instantaneous waveforms of these electrical powers when the power limit is $P_{MAX} = 0.25$ MW are shown in Fig. 6.19. Here the individual device power waveforms from both the local and global cases are shown along with the overall array power waveform showing the aggregation of all the three WECs connected onto the same DC bus. In the case of the local power limited system, it is clear that each WEC is constrained to operate below a certain power limit (0.0833 MW), hence leading to

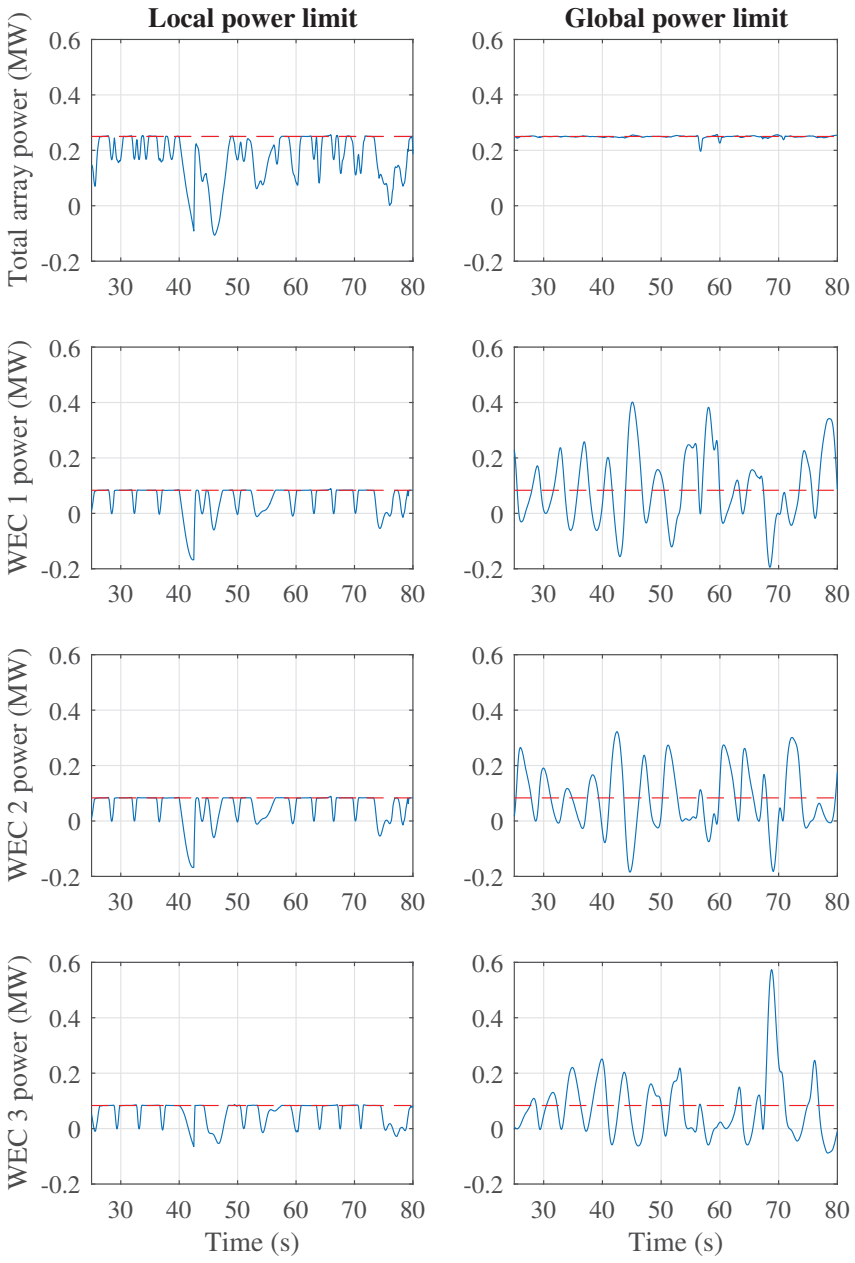

Figure 6.19: Example waveforms of the power extracted from a three device array with the **Local power limit** and the **Global power limit** for a unidirectional irregular sea state modelled using a Bretschneider spectrum with $H_s = 3$ m and $T_p = 9.6$ s; for both modes the total aggregated power from the array and their corresponding instantaneous power waveform from each device are shown.

the overall power limit constraint of the array ($3 \times 0.0833 = 0.25$ MW). The global power limited system on the other hand operates in a different manner, where the aggressiveness of the local power from each device is permitted to be more oscillatory as

long as the local linear constraints are upheld, hence explaining why the local power produced from each device breaches the local power limits but maintains the global power limit of the array. By choosing a moderate global power limit with the centralised NMPC, the average power may decrease, but this results in exceptional power quality that would significantly reduce the problems that would arise when exporting the power onto the grid.

When connected to a weak grid, instabilities can occur due to high instantaneous power fluctuations from connected energy sources. Now, the sea state energy is increased to a higher level (using a Bretschneider excitation wave with $H_s = 5$ m and $T_p = 11$ s). The comparison between the global and local power limited systems is shown in Fig. 6.20. As previously seen, the global power limited system produces higher

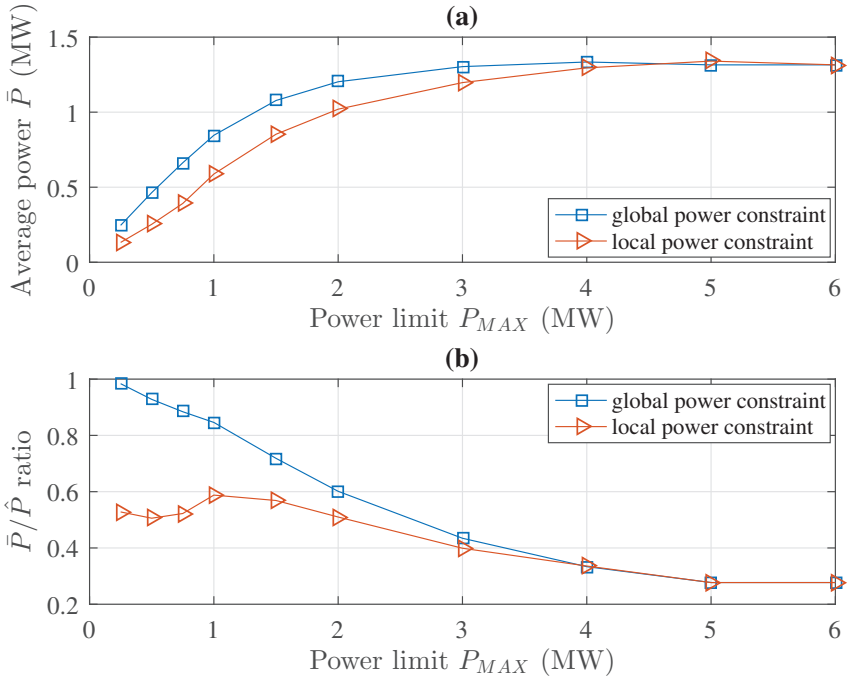

Figure 6.20: The effect of either a global power constraint or a local power constraint on the power extracted from a three device array excited with a Bretschneider excitation wave with $H_s = 5$ m and $T_p = 11$ s (a) the average absorbed power $\bar{P}$ from the entire three WEC array, (b) the average to peak power ratio $\bar{P}/\hat{P}$ of the entire three WEC array

average power $\bar{P}$ than the local power limited system for low values of the power limit P_{MAX}, as shown in Fig. 6.20(a). Examining the average to peak power ratio $\bar{P}/\hat{P}$ in Fig. 6.20(b), the benefits of choosing a global power limit over a local power limit is evident; especially for the lower power limit P_{MAX} range where the ratio $\bar{P}/\hat{P}$ is significantly better for the global (array) power constraint.

Examples of instantaneous powers produced from the global power limited system with different power limits P_{MAX} are shown in Fig. 6.21. It is clear that as the global power limit P_{MAX} decreases, the instantaneous power becomes more constant.

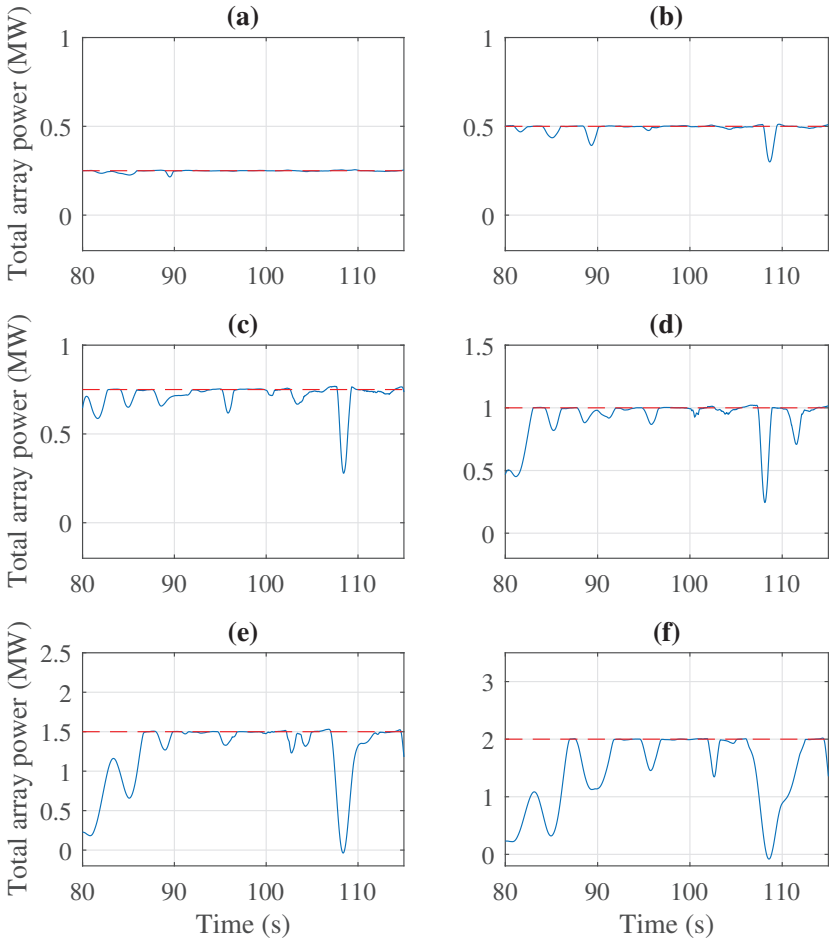

Figure 6.21: Waveforms of the aggregated instantaneous power from the three device array using a Bretschneider excitation wave with $H_s = 5$ m and $T_p = 11$ s and the **Global power limit** of (a) 0.25 MW, (b) 0.5 MW, (c) 0.75 MW, (d) 1 MW, (e) 1.5 MW, (f) 2 MW.

6.6 Conclusion

This chapter was based on the premise that there was a benefit to be obtained from the centralised optimal control of interacting WECs. First, it was shown that when linear mechanical constraints and viscous affects were included in the optimisation problem that the variability of the absorbed average power from monochromatic waves in response to changes in the penetration angle was reduced.

With the inclusion of the linear constraints and the viscous forces in the MPC optimisation, the difference between the performances of the decentralised and the centralised MPC reduced. By exciting the system with multiple sea states with a range of separation distances, a comparison of the average power values absorbed between the centralised and decentralised MPCs was then made. It was shown that in general, if the separation distance of the WEC devices was low and the sea state was un-energetic, then the difference between the global and local MPC performance was evident. This is due to the larger interaction when the WECs are closer together and the inactivity of the linear mechanical constraints.

It could be said that for a multi-body WEC system where the WECs are fixed to a common platform that there may be, the need for a centralised NMPC due to the small d/r ratio. However, it could also be said that for WEC arrays with large WECs, the d/r ratio would need to be over a certain threshold to allow for maintenance and to reduce the probability of device collision. Hence for large WECs in an array, there may be little benefit in implementing a centralised NPMC over the array for power maximisation.

Besides power maximisation, it is desirable that the control system can improve the average to peak power ratio and hence improve the power quality, the regulation of the DC-link and importantly lead to a reduction in the rating of the grid side converter. With the incorporation of an upper power limit on the power extracted either from each device, or from the complete array, it was shown that the average to peak power ratio could be increased by lowering the power constraint. The main highlight of this power quality analysis was the considerable difference in performance at lower power constraint levels when the power constraint was applied at the individual device level or for the whole array. It is important to note that tightening the global power constraints for an array allows the user to improve the quality of power exported to the grid, at the cost of curtailed power. This constraint could be set according to the prevailing grid conditions, to improve flicker levels for example. This work showed the benefit of centralised NMPC for power quality control.

References

Babarit, A., Hals, J., Muliawan, M. J., Kurniawan, A., Moan, T. & Krokstad, J. (2012), 'Numerical benchmarking study of a selection of wave energy converters', *Renewable Energy* **41**, 44–63.

Balitsky, P. & Ringwood, J. V. (2014), 'Control-Influenced Layout Optimization of Arrays of Wave Energy Converters', *33rd International Conference on Ocean, Offshore and Arctic Engineering* pp. 1–10.

Barcelli, G. & Ringwood, J. (2013), 'Constrained control of arrays of wave energy devices', *International Journal of Marine Energy* **3**, 53–69.

Bhinder, M. A., Babarit, A., Gentaz, L. & Ferrant, P. (2011), 'Assessment of Viscous Damping via 3D-CFD Modelling of a Floating Wave Energy Device', *In Proceedings of the 9th European Wave and Tidal Energy Conference (EWTEC)* pp. 1–6.

Cummins, W. E. (1962), 'The Impulse Response Function and Ship Motions', *Schiffstechnik* **9**, 101–109.

Garcia-Rosa, P. B., Bacelli, G. & Ringwood, J. V. (2015), 'Control-informed optimal array layout for wave farms', *IEEE Transactions on Sustainable Energy* **6**(2), 575–582.

Göteman, M., Engström, J., Eriksson, M. & Isberg, J. (2015), 'Optimizing wave energy parks with over 1000 interacting point-absorbers using an approximate analytical method', *International Journal of Marine Energy* **10**, 113–126.

Hürlimann, T. (1993), 'AMPL: A mathematical programming language', *OR Spektrum* **15**(1), 43–56.

Kung, S.-Y., Arun, K. S. & Rao, D. V. B. (1983), 'State-space and singular-value decomposition-based approximation methods for the harmonic retrieval problem', *JOSA* **73**(12), 1799–1811.

Lee, C.-H. (1995), *WAMIT Theory Manual*.

López, I., Andreu, J., Ceballos, S., de Alegr, I. M. & Kortabarria, I. (2013), 'Review of wave energy technologies and the necessary power-equipment', *Renewable and Sustainable Energy Reviews* **27**, 413–434.

Mc Namara, P., Negenborn, R. R., De Schutter, B. & Lightbody, G. (2013), 'Optimal coordination of a multiple HVDC link system using centralized and distributed control', *IEEE Transactions on Control Systems Technology* **21**(2), 302–314.

Morison, J. R., Johnson, J. W., Schaaf, S. A. & Others (1950), 'The force exerted by surface waves on piles', *Journal of Petroleum Technology* **2**(05), 149–154.

Oetinger, D., Magaña, M. E. & Sawodny, O. (2014*a*), 'Centralised model predictive controller design for wave energy converter arrays', *IET Renewable Power Generation* **9**(2), 142–153.

Oetinger, D., Magaña, M. E. & Sawodny, O. (2014*b*), 'Decentralized model predictive control for wave energy converter arrays', *IEEE Transactions on Sustainable Energy* **5**(4), 1099–1107.

O'Sullivan, A. C. & Lightbody, G. (2017*a*), 'Co-design of a wave energy converter using constrained predictive control', *Renewable Energy* **102**, 142–156.

O'Sullivan, A. C. & Lightbody, G. (2017*b*), 'The Effect of Model Inaccuracy and Move-blocking on the Performance of a Wave-to-wire Wave Energy Converter , under Economic Predictive Control', *The 12th European Wave and Tidal Energy Conference* (August), 1–10.

O'Sullivan, A. C. M. & Lightbody, G. (2017*c*), 'The Effect of Viscosity on the Maximisation of Electrical Power from a Wave Energy Converter under Predictive Control', *IFAC-PapersOnLine* **50**(1), 14698–14704.

O'Sullivan, A. C. M., Sheng, W & Lightbody, G. (2018), 'An Analysis of the Potential Benefits of Centralised Predictive Control for Optimal Electrical Power Generation from Wave Energy Arrays', *IEEE Transactions on Sustainable Energy*, Accepted, DOI: 10.1109/TSTE.2018.2812749.

Polinder, H., Damen, M. E. C. & Gardner, F. (2004), 'Linear PM Generator System for Wave Energy Conversion in the AWS', *IEEE Transactions on Energy Conversion* **19**(3), 583–589.

Sjolte, J., Tjensvoll, G. & Molinas, M. (2012), All-electric wave energy converter connected in array with common dc-link for improved power quality, *in* 'Power Elec-

tronics for Distributed Generation Systems (PEDG), 2012 3rd IEEE International Symposium on', IEEE, pp. 431–436.

Thorburn, K., Bernhoff, H. & Leijon, M. (2004), 'Wave energy transmission system concepts for linear generator arrays', *Ocean Engineering* **31**(11), 1339–1349.

Van Eeckhout, B., Van Hertem, D., Reza, M., Srivastava, K. & Belmans, R. (2010), 'Economic comparison of VSC HVDC and HVAC as transmission system for a 300 MW offshore wind farm', *International Transactions on Electrical Energy Systems* **20**(5), 661–671.

Chapter 7

Conclusion

7.1 Concluding Summary

In Chapter 1, the background literature was discussed, including environmental considerations, renewable energy types, WEC design, the history of classical and advanced control algorithm design and why the installation of WEC arrays may be beneficial.

In Chapter 2, the component mathematical models of a wave-to-grid system were developed. Initially, the hydrodynamics of a floating object was described using the Navier-Stokes equations. Assuming an inviscid, irrotational fluid and an incompressible incident flow, the Navier-Stokes equations were simplified to produce a potential flow model. Since a cylindrical point absorber WEC was used in this work, it was assumed that utilising a linear potential flow model was sufficient since the wetted surface area of the device is a linear function of displacement. Each component of the linear model was introduced, where WAMIT was used to produce the frequency and time domain data representing the excitation force and the radiation force kernels. The modelling of the excitation waves was based on sea spectrum analysis; here the Bretschneider spectrum was utilised throughout the thesis. Prony's exponential approximation was explained, where the SISO radiation kernel was found using the impulse response data produced using WAMIT. Kung's system realisation method was then introduced, where a SIMO radiation kernel model was utilised to model the radiation effects that are present between WECs in an array. Kung's method was shown to produce a system with better fidelity without the need for postprocessing SVD methods. The electrical system from wave-to-grid was then introduced, where LPMG modelling, Park's dq0 transformation, LPMG control and grid integration were described in detail. This section showed that there is a need for a smarter grid side DC-link

voltage controller since the dynamics of the grid side converter vary with the fluctuating power exported onto the grid; indeed, non-minimum phase behaviour can result if power flow is negative.

In Chapter 3, the optimisation of average electrical power from the LPMG coupled to a point absorber WEC was investigated. Optimal mechanical control based on reactive control, was shown to produce substantial extracted mechanical power, however, this performed poorly when a realistic PTO was included in the model. Model Predictive Control (MPC) was introduced, where the MPC was initially designed to maximise average mechanical power. By including resistive losses within the MPC's cost function, the average electrical power could now be optimised. The results demonstrated the importance of including the resistive losses in the cost function, where higher levels of average electrical power can be extracted when compared to the electrical power levels found using an MPC optimising mechanical power. Furthermore, it was shown that the use of a FOH instead of a ZOH in the outer control loop yields a significant increase in power quality.

Chapter 4 showed that introducing linear mechanical constraints into the MPC's algorithm maximised the average electrical power while obeying the physical restrictions of the system. The voltage restrictions from the DC-link and the machine side converter were then considered in the wave-to-wire system, where a non-linear voltage constraint was required in the controller's algorithm. It was shown that if the DC-link voltage is too low, the system becomes uncontrollable; too large and the power electronics become overrated. Field weakening was introduced to increase the feasibility of the system during periods of low DC-link voltage levels. Introducing field weakening extended the feasible region of the system; this allowed higher velocities, causing higher average electrical power levels. Negative electrical power flow is avoided when a uni-directional power flow constraint is incorporated into the control algorithm, hence, avoiding stability problems which may occur with the grid-side DC-link voltage controller.

In Chapter 5, a mismatch analysis was carried out, which investigated the resulting electrical power extracted from the WEC when the controller's internal hydrodynamic model was mismatched from the system model. System model uncertainty included the WEC mass, hydrostatic coefficient and the radiation kernel. The results showed that each mismatch introduced a power loss when compared to the power extracted from a fully matched system. However, these average power losses are acceptable in most cases. An LPV NPMC was then implemented in the simulation to tackle the non-linear viscosity effects; this control algorithm produced optimum results. A linear

MPC was then introduced to reduce the computational expense, where the non-linear viscous force in the control algorithm was approximated as a linear function. Tuning the constant viscous term $\tilde{C}_{vis}$ for each sea state, the resulting average power becomes comparable to the results obtained when the LPV NMPC was used. It was found that by introducing linear mechanical constraints into the control algorithm, the resulting powers became less sensitive to the choice of $\tilde{C}_{vis}$. Therefore, a constant $\tilde{C}_{vis}$ value could be set for all sea states, producing a computationally inexpensive control algorithm with performance very close to the full non-linear control algorithm. In order to further reduce the computational burden, a move blocking technique was incorporated into the control horizon, where the number of free control variables needed to be calculated was reduced. By using the move-blocking technique, the performance of the MPC could be maintained, while the QP computational time was reduced (e.g. for an MPC with linear mechanical constraints and non-linear constraints, with $N_c = 25$, the power ratio is unity while reducing the solve time by 90%).

In Chapter 6, it was shown that when linear mechanical constraints and viscous effects were included in the optimisation problem, the variability of the average absorbed power from monochromatic waves across a range of penetration angles reduced. Including the linear constraints and the viscous forces in the MPC optimisation, the decentralised MPC performance came close to that of the centralised MPC. The average power values absorbed between the centralised and decentralised MPCs were then compared against each other when a range of sea states were used. It was shown that during high sea states and with long separation distances, the performance of the decentralised MPC algorithm became close to identical to the performance of the centralised MPC algorithm. Hence, for large separation distances, a centralised MPC algorithm is no longer required. Incorporating an upper power limit in the centralised MPC algorithm, it was shown that an MPC with a global upper power constraint could produce higher levels of electrical power along with a better average to peak power ratio when compared to the results found from a centralised MPC with a local set of upper power constraints. It was shown that as the upper power limit was decreased, the control algorithm with the global power constraint outperformed the control algorithm with a set of local power constraints, with higher levels of average power and near unity average to peak power ratios.

7.2 Future Work

For the majority of the thesis, non-linear hydrodynamic effects were ignored. It was only when the non-linear viscosity phenomena was introduced into the linear model, that the resulting problems became apparent. Other non-linear hydrodynamic effects such as the Froude-Krylov forces could be introduced into the simulation model to fully assess the performance of the approximate linear system models used in controllers (Pe et al. 2015). When a high sea state overexcites the constrained system, it is expected that the effects of the Froude-Krylov non-linear forces on the average absorbed power would be minimal since the WEC would act as a wave follower, restrictively hold its cross-sectional area in the water due to the constrained control algorithm. However, in lower sea states the effect of the Froude-Krylov forces could become crucial, due to inactive constrained control algorithm, allowing the WEC to oscillate instead acting like a wave follower. Using CFD testing, the fidelity of the control system could be tested.

The robustness of the energy extraction system was previously covered in this thesis. However, the errors which can commonly occur in the excitation wave prediction were not examined. Assuming that the predicted values at the early stage of the prediction would have a high fidelity, the system constraints would be easily obeyed. However, as the prediction steps are extended into the future, the degradation of the wave prediction increases; potentially causing knock-on effects that degrade the extraction of average electrical power.

The advantages of utilising MPC are its ability to produce optimum results while incorporating linear and especially non-linear constraints, which prevent system damage while allowing maximum energy extraction. However, the main disadvantage of the advanced control algorithm is the computation time it takes to obtain these optimum solutions. Therefore, there may be a need to develop simplified algorithms which estimate the action of the MPC, without the computation expense included. Fuzzy logic control is one possible solution that could replace the MPC (Lee 1990). Using the MPC, which produces optimum results while incorporating system constraints, a data bank is formed. This large data set may allow the development of a fuzzy logic control that mimics the control action of the MPC, without the computation expense. Another replacement option is learning MPC (Rosolia & Borrelli 2017). A standard MPC bases its operation on present system measurements and future disturbances, hence the control system is ignorant of the possible repetitive patterns which may have occurred in the past. Learning MPC takes past measurements into consideration along with present

and predicted data, which allows the MPC optimisation time to reduce over time if the past control actions were periodically repetitive. In a steady sea state, there is a probability of a repetitive cyclic excitation action occurring over a period. Considering this repetitive nature, learning MPC can be developed to produce the same fidelity of the conventional MPC while reducing the computation time.

Using the information gained from the centralised and decentralised MPC comparison, it was also shown that with a reasonable separation distance between the WEC's, the difference in the amount of absorbed electrical power between the decentralised controlled system and the centralised system was minor. However, regarding power quality, there are benefits in utilising a centralised control. Utilising a centralised MPC with a global power constraint, much-improved power quality is achievable under certain circumstances (O'Sullivan & Lightbody 2017). However, with commercial WEC arrays, potentially with many WEC's within the array, there comes a point where the computation level needed to implement the centralised MPC algorithm becomes overwhelming and the control system becomes infeasible in a real-life application. Assuming sufficient WEC separation distances, the hydrodynamic interactions between the devices can be assumed negligible. With this assumption, a distributed MPC algorithm can be utilised to find close to optimum solutions, while reducing the computational cost. Distributed control involves localised control algorithms that solve their own individual optimisation problems (Mc Namara et al. 2013). After every iteration in each localised system, each local control system distributes its information to its neighbouring devices. After some iterations, the local control calculations converge to one optimum answer, which is equivalent to using centralised control.

By connecting the WEC array to a simulation grid, the effects of importing fluctuating power onto the DC-link can be examined (Dirscherl et al. 2017). It is here where the necessity of designing a suitable grid side DC-link voltage controller could be shown. By introducing the centralised or distributed MPC algorithms to control the WEC farm, the benefits of including a global power limit in the MPC on the operation of the DC-link voltage control will be highlighted. This will also demonstrate how the voltage flicker which occurs in the distributed network will be affected (Blavette 2015).

References

Blavette, A. (2015), 'Estimation method for evaluating the wave-induced flicker level emitted by a tidal energy farm', *Proceedings of the 11th European Wave and Tidal Energy Conference* (2), 1–7.

Dirscherl, C., Hackl, C. M. & Schechner, K. (2017), 'Modeling and control of modern wind turbine systems: An introduction', *CoRR* **abs/1703.0**.

Lee, C.-C. (1990), 'Fuzzy logic in control systems: fuzzy logic controller. I', *IEEE Transactions on systems, man, and cybernetics* **20**(2), 404–418.

Mc Namara, P., Negenborn, R. R., De Schutter, B. & Lightbody, G. (2013), 'Optimal coordination of a multiple HVDC link system using centralized and distributed control', *IEEE Transactions on Control Systems Technology* **21**(2), 302–314.

O'Sullivan, A. C. M. & Lightbody, G. (2017), 'The Effect of Viscosity on the Maximisation of Electrical Power from a Wave Energy Converter under Predictive Control', *IFAC-PapersOnLine* **50**(1), 14698–14704.

Pe, M., Giorgi, G. & Ringwood, J. V. (2015), 'A Review of Non-Linear Approaches for Wave Energy Converter Modelling', (1), 1–10.

Rosolia, U. & Borrelli, F. (2017), 'Learning Model Predictive Control for Iterative Tasks: A Computationally Efficient Approach for Linear System', *IFAC-PapersOnLine* **50**(1), 3142–3147.

Appendix A

Space Vector Pulse Width Modulation (SVM/SVPWM)

Fig. A.1 shows a block diagram for an LPMG, with inner digital current controller. Since the PTO force does not depend on $i_d(t)$, the D axis current is typically regulated to 0 A. A current set point is sent to the $i_q(t)$ control loop to produce the desired force. In this work a proportional-integral gain controller is used for both current control

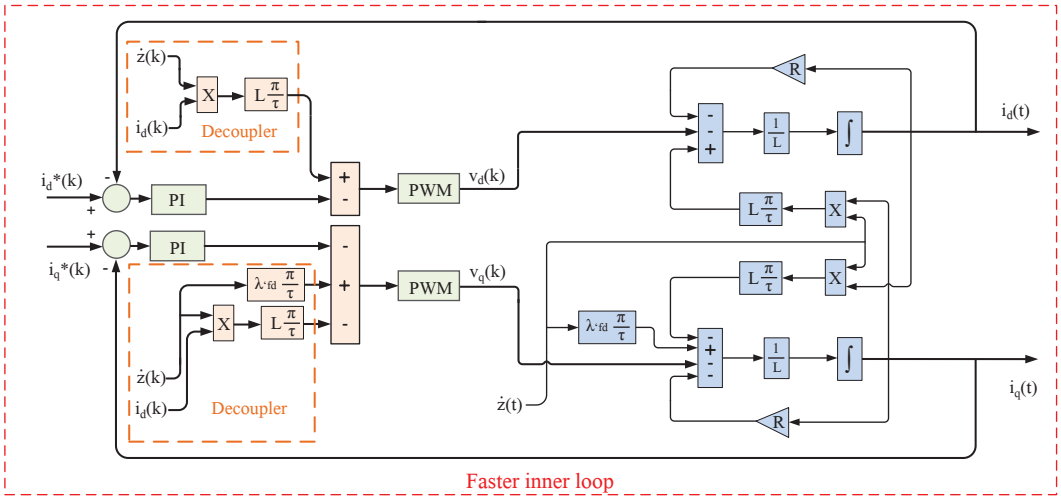

Figure A.1: A block diagram of the digital current control for the LPMG in the DQ domain.

loops. The output of each PI controller is then sent to the LPMGs terminals in the form of digital voltage zero order steps. To produce these continuous voltage $v_a(t)$, $v_b(t)$ and $v_c(t)$, pulse width modulation (PWM) (Holmes & Lipo 2003) signals are used where a set of IGBTs (Fig. A.2) are switched at a very high frequency to produce square waves with variable pulse widths, where the peak square wave amplitude is the constant $V_{DC}(t)$ value; when averaged out over the square waves period, it produces

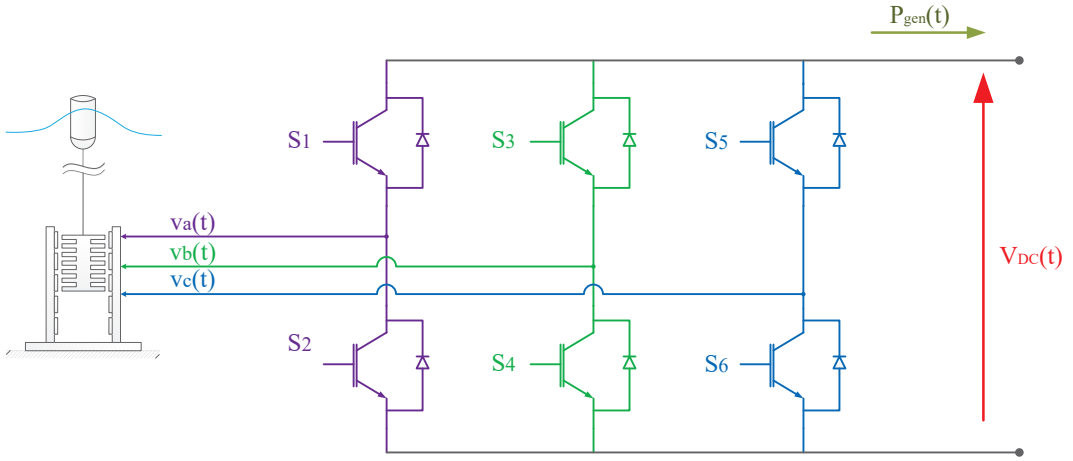

Figure A.2: A schematic of the machine side power inverter that utilises an array of parallel IGBTs which chop a constant voltage level $V_{DC}(t)$ into square waves with varying duty cycles, hence creating the controller voltages to produce the wanted PTO forces from the LPMG

the wanted $v_a(t)$, $v_b(t)$ and $v_c(t)$ values, as shown in Fig. A.3. For this three phase

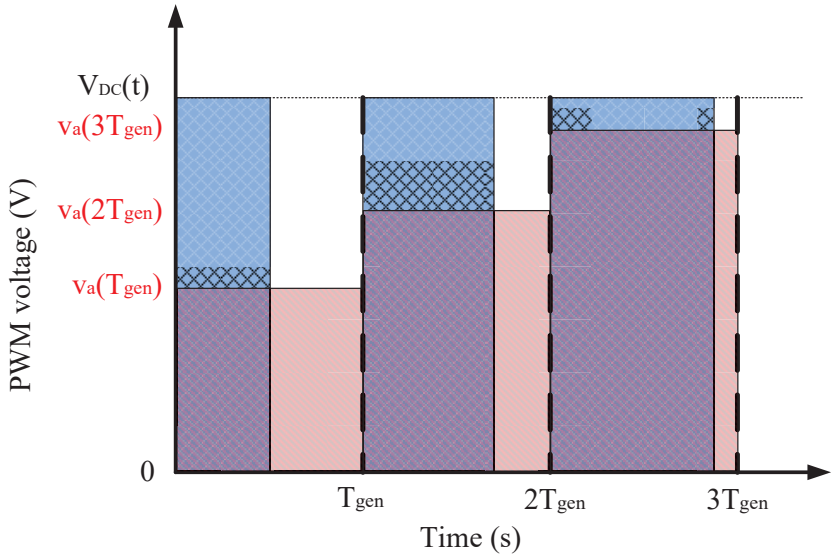

Figure A.3: The fundamental operation of a standard PWM system, where a square wave with a variable duty cycle is averaged out over a switching period T_{gen} to create an average voltage $v_a(T_{gen})$ over a switching period.

system, space vector modulation (SVM) is used (Habetler et al. 1992). SVM is a commonly used technique in three phase synchronous machine applications, especially when a dq0 transformation is used. The SVM method is preferred over the standard sinusoidal pulse width modulation (SPWM) because the SWM utilises more of the

available voltage across the inverters input terminals $V_{DC}(t)$ (Fig. A.4), causing a more efficient system. From Fig. A.2 it is shown that the switching on and off of the IGBTs can be represented as a set number of binary combinations that can be made, where the binary switching signals are denoted as S_1, S_3 and S_5; signals S_2, S_4 and S_6 are the corresponding inverted signals to S_1, S_2 and S_4 (i.e. $S_1 = 1, S_2 = 0$). With these binary signals, a table can be formed which shows all the possible binary states that can be formed, as shown in table A.1. When the three phase voltages $v_a(t)$, $v_b(t)$ and $v_c(t)$ are formed from the switching, they can be combined together to create a voltage space vector, where this table shows the space vector values for the different binary logic orientations.

Table A.1: Switching logic states creating the corresponding voltage space vector

$\vec{v_s}(t)$	S_1	S_3	S_5
0	0	0	0
$V_{dc}(t)e^{j0}$	0	0	1
$V_{dc}(t)e^{j2\pi/3}$	0	1	0
$V_{dc}(t)e^{j\pi/3}$	0	1	1
$V_{dc}(t)e^{j4\pi/3}$	1	0	0
$V_{dc}(t)e^{j5\pi/3}$	1	0	1
$V_{dc}(t)e^{j\pi/3}$	1	1	0
0	1	1	1

These space vector states that correspond to the set of binary logics can then be plotted on the $\alpha\beta$ axis, as shown in Fig. A.4. It is noticeable that if a a certain binary logic state is enabled for an entire switching time (e.g. $S_1 = 0$, $S_3 = 1$ and $S_5 = 1$), the corresponding voltage space vector will become $\vec{v_s}(t) = V_{DC}(t)e^{j\pi/3}$. However, to obtain a voltage space vector that is within one of the hexagons sections (between two switching logic states), there needs to be a distribution where an array of binary logic states are enabled at different parts of the switching period.

An example of this is shown in Fig. A.5, where the logic states ($\{S_1, S_3, S_5\} = \{0, 1, 0\}$ and $\{0, 1, 1\}$) are enabled for durations of the switching period to create an average space vector that is between the two switching logic states $\{S_1, S_3, S_5\} = \{0, 1, 0\}$ and $\{0, 1, 1\}$. The limitations to this SVM method (also known as SVPWM) is that the maximum voltage space vector magnitude depends on the angle of the space vector, where at sections in the hexagon the space vector voltage is limited to $|\vec{v_s}(t)| = (\sqrt{3}/2)V_{DC}(t)$. In this example, along with this thesis, the maximum voltage space vector is set as a constant for all angles, hence the circle with the diameter $(\sqrt{3}/2)V_{DC}(t)$, where in this example $V_{DC}(t) = 100$ V. Averaging the real and imagi-

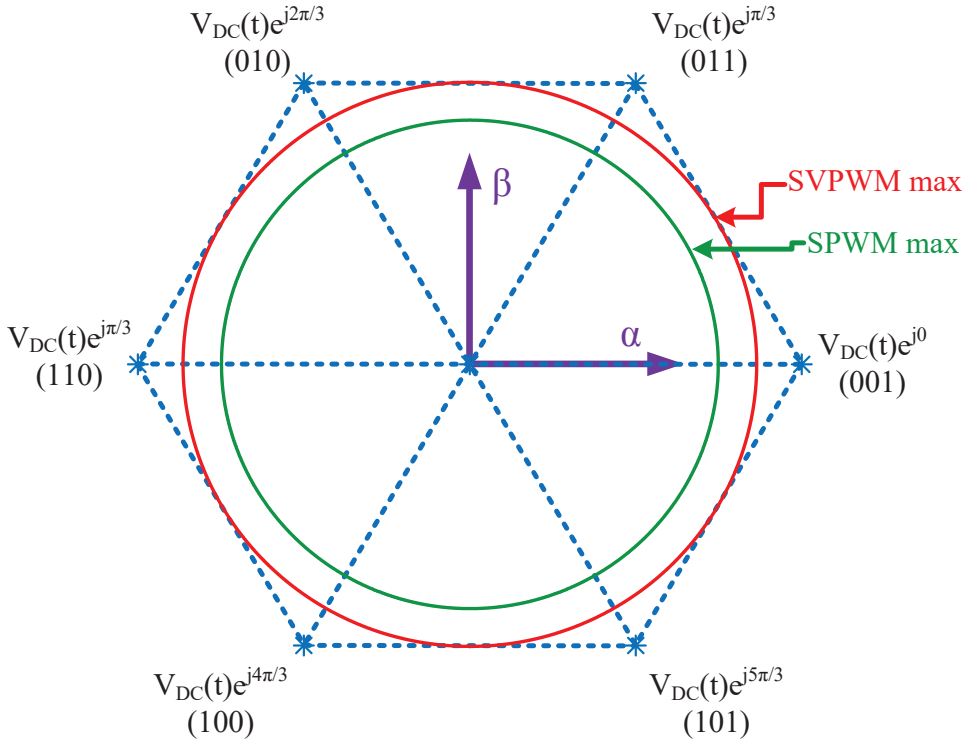

Figure A.4: The voltage space vector orientation with their corresponding switching binary logic states coinciding with the $\alpha\beta$ axis, along with the circular voltage limits of the SVPWM method and the limited SPWM method

nary voltage space vectors from Fig. A.5, it can be found that the average space vector for that switching time is $(\sqrt{3}/2)V_{DC}(t)$ with a phase of 1.2565 rad.

The voltage limits of the voltage space vector depends solely on the voltage $V_{DC}(t)$ that is across the IGBT terminals from Fig. A.2. This $V_{DC}(t)$ voltage level, which is across a bank of capacitors, is controlled by the IGBT grid side converter as shown in Fig. A.6, where the $V_{DC}(t)$ voltage level is controlled to be constant, hence decoupling the generation side from the grid side. How easily controllable the $V_{DC}(t)$ link is, depends on the power exported from the generation side $P_{gen}(t)$ onto the grid side and the weakness of the grid. The most common method is to treat the grid network as an ideal network where the voltages from the grid are assumed to be at their optimum values, as shown in Fig. A.6.

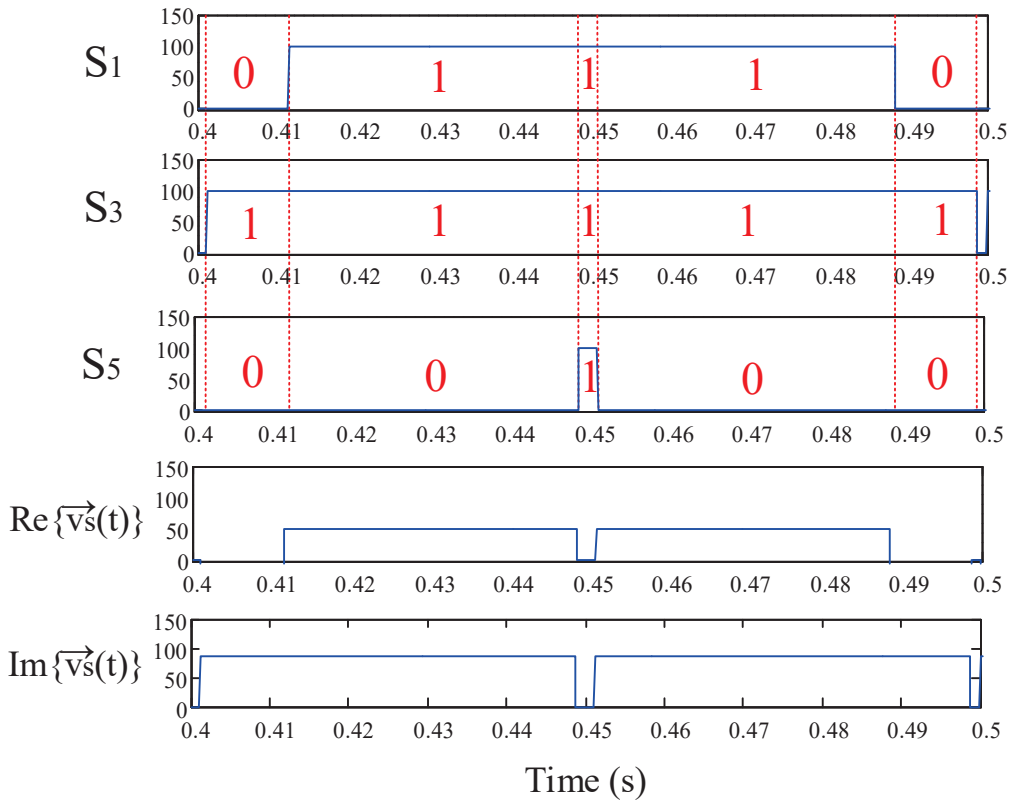

Figure A.5: An example over a single switching period (i.e. $T_{gen} = 0.1$) of the operation of the SVM method where the following switching binary logic pattern occurs: $\{S1, S3, S5\}$ $=\{0,0,0\}$, $\{0,1,0\}$, $\{0,1,1\}$, $\{1,1,1\}$, $\{0,1,1\}$, $\{0,1,1\}$, $\{0,1,0\}$. With this switching pattern the following real and imaginary space vector values are found; when averaged over the switching period, produces $\vec{v_s}(t) = 26.77 + \mathbf{i}82.36$, or $\vec{v_s}(t) = 86.6025\angle 71.99^o$

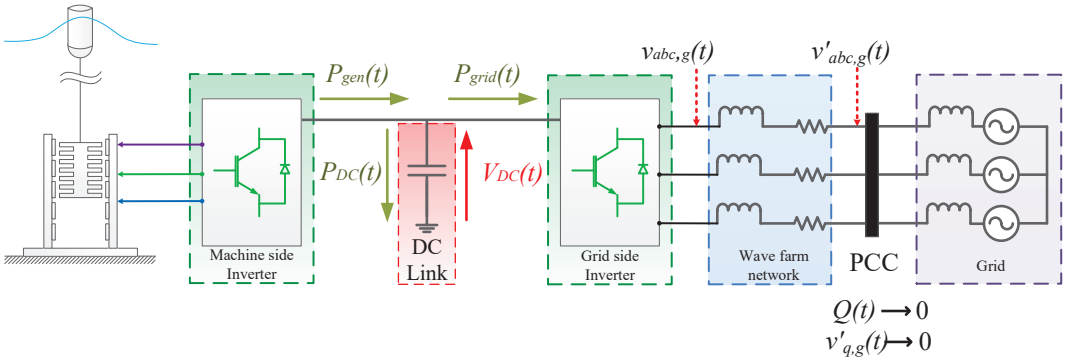

Figure A.6: A schematic of the overall system from wave to wire; starting from the WEC connected to the LPMG, which is controlled by the voltages generated from the machine side inverter that is limited by the voltage across the DC-link. The DC-link is controlled by the grid side inverter that interacts with (as in this case) an ideal grid by utilising the control voltages from the grid side converter which are filtered through an inverter filter.

Appendix B

Crowbar Protection System

In the thesis presented, the external PTO force exerted on the WEC is created by the LPMG. The force created from the LPMG is directly related to the $i_{dq0}(t)$ current, where the $i_{dq0}(t)$ current is controlled by varying the stator voltage via a VSC. The VSC can produce a stator voltage which is a proportion of the DC-link voltage $v_{dc}(t)$, where the maximum capable stator voltage is the DC-link voltage $v_{dc}(t)$.

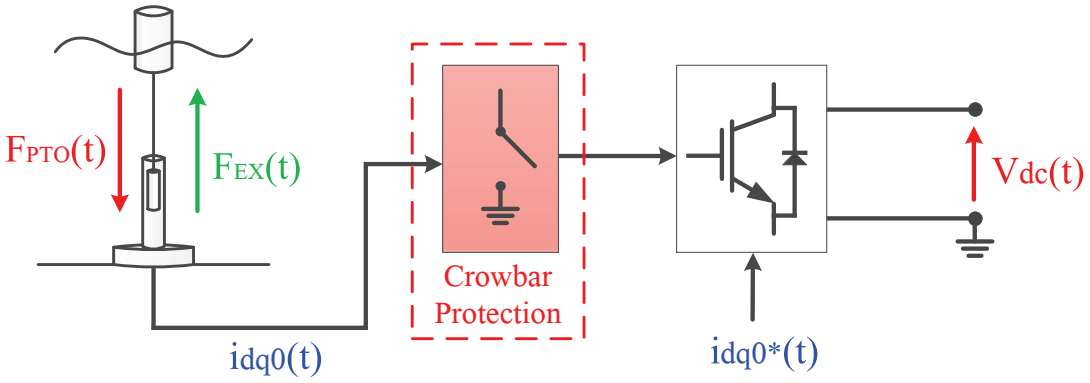

Figure B.1: System model with WEC, PTO, Crowbar, VSC and DC-link voltage

As excitation waves with large significant heights excite the WEC, feasibility problems may arise if the DC-link voltage is too low. To protect the VSC from high currents, a crowbar is inserted into the system and can be shown in Fig. B.1. A crowbar is a power electronics device which acts as a fail safe component (Morren & de Haan 2007), that is used, for example, during a grid-fault ride-through. As the currents rise beyond an acceptable point, the crowbar latches, which then causes a short circuit, allowing minimal current flow through the machine side VSC. When the crowbar is activated, the VSC is safe from permanent damages, however, the WEC is no longer under active control.

Appendix C

Electrical Optimum Solution for Array

The coupled hydrodynamic model of the WEC array is described as the following,

$$j\omega \boldsymbol{K_m}(\omega)\dot{\mathbf{Z}}(\omega) + \mathbf{H_r}(\omega)\dot{\mathbf{Z}}(\omega) + \frac{\beta}{j\omega}\dot{\mathbf{Z}}(\omega) - \mathbf{F_{ex}}(\omega) = \mathbf{F_{PTO}}(\omega) \tag{C.1}$$

where,

$$\mathbf{H_r}(\omega) = \begin{bmatrix} H_{r,11}(\omega) & H_{r,12}(\omega) & \dots & H_{r,1N}(\omega) \\ H_{r,21}(\omega) & H_{r,22}(\omega) & \dots & H_{r,2N}(\omega) \\ \vdots & \vdots & \ddots & \dots \\ H_{r,N1}(\omega) & H_{r,N2}(\omega) & \dots & H_{r,NN}(\omega) \end{bmatrix} \in \mathbb{C}^{N\times 1} \tag{C.2}$$

$$\dot{\mathbf{Z}}(\omega) = \begin{bmatrix} \dot{Z}_1(\omega) \\ \dot{Z}_2(\omega) \\ \vdots \\ \dot{Z}_N(\omega) \end{bmatrix} \in \mathbb{C}^{N\times N} \tag{C.3}$$

$$\mathbf{F_{ex}}(\omega) = \begin{bmatrix} F_{ex,1}(\omega) \\ F_{ex,2}(\omega) \\ \vdots \\ F_{ex,N}(\omega) \end{bmatrix} \in \mathbb{C}^{N\times 1} \tag{C.4}$$

$$\mathbf{F_{PTO}}(\omega) = \begin{bmatrix} F_{PTO,1}(\omega) \\ F_{PTO,2}(\omega) \\ \vdots \\ F_{PTO,N}(\omega) \end{bmatrix} \in \mathbb{C}^{N\times 1} \tag{C.5}$$

The vectors $\dot{\mathbf{Z}}(\omega)$, $\mathbf{H_r}(\omega)$, $\mathbf{F_{ex}}(\omega)$ and $\mathbf{F_{PTO}}(\omega)$ can be broken into real and imaginary components,

$$\dot{\mathbf{Z}}(\omega) = \dot{\mathbf{Z}}_\mathbf{a} + j\dot{\mathbf{Z}}_\mathbf{b} \tag{C.6}$$

$$\mathbf{H_r}(\omega) = \mathbf{H_{r,a}} + j\mathbf{H_{r,b}} \tag{C.7}$$

$$\mathbf{F_{ex}}(\omega) = \mathbf{F_{ea}} + j\mathbf{F_{eb}} \tag{C.8}$$

$$\mathbf{F_{PTO}}(\omega) = -\left(\mathbf{F_a} + j\mathbf{F_b}\right). \tag{C.9}$$

Substituting into (C.1) produces (C.10),

$$\begin{aligned} j\omega\boldsymbol{K}_m(\omega)\left(\dot{\mathbf{Z}}_\mathbf{a} + j\dot{\mathbf{Z}}_\mathbf{b}\right) + \left(\mathbf{H_{r,a}} + j\mathbf{H_{r,b}}\right)\left(\dot{\mathbf{Z}}_\mathbf{a} + j\dot{\mathbf{Z}}_\mathbf{b}\right) + \frac{\beta}{j\omega}\left(\dot{\mathbf{Z}}_\mathbf{a} + j\dot{\mathbf{Z}}_\mathbf{b}\right) \\ -\left(\mathbf{F_{ex,a}} + j\mathbf{F_{ex,b}}\right) = -\left(\mathbf{F_a} + j\mathbf{F_b}\right) \end{aligned} \tag{C.10}$$

$$\begin{aligned} \underbrace{\left(\mathbf{H_{r,a}} + j\left(\omega\boldsymbol{K}_m(\omega) + \mathbf{H_{r,b}} - \frac{\beta}{\omega}\mathbf{I}\right)\right)}_{\mathbf{G}+j\mathbf{Q}}\left(\dot{\mathbf{Z}}_\mathbf{a} + j\dot{\mathbf{Z}}_\mathbf{b}\right) - \left(\mathbf{F_{ex,a}} + j\mathbf{F_{ex,b}}\right) = \\ -\left(\mathbf{F_a} + j\mathbf{F_b}\right) \end{aligned} \tag{C.11}$$

The total electrical power absorbed from an array of point absorber WECs can be written as the following,

$$P(t) = \dot{\mathbf{Z}}(t)^T\mathbf{F_{PTO}}(t) - \mathbf{F_{PTO}}(t)^T\psi\mathbf{F_{PTO}}(t) \tag{C.12}$$

where

$$\psi = \frac{R}{\left(\frac{\pi}{\tau}\lambda'_{fd}\right)^2}\begin{bmatrix} 1 & 0 & \dots & 0 \\ 0 & 1 & \dots & 0 \\ \vdots & \vdots & \ddots & \vdots \\ 0 & 0 & \dots & 1 \end{bmatrix}. \tag{C.13}$$

All the continuous time velocity and PTO force signals are sinusoidals taking the assumption that the excitation force is monochromatic,

$$\mathbf{F_{PTO}}(t) = \left(\frac{\mathbf{F_{PTO}}(\omega)e^{j\theta} + \mathbf{F_{PTO}}^*(\omega)e^{j\theta}}{2}\right) \tag{C.14}$$

$$\dot{\mathbf{Z}}(t) = \left(\frac{\dot{\mathbf{Z}}(\omega)e^{j\theta} + \dot{\mathbf{Z}}^*(\omega)e^{j\theta}}{2}\right) \tag{C.15}$$

$$\begin{aligned} P(t) = \frac{1}{4}\left(\dot{\mathbf{Z}}(\omega)e^{j\theta} + \dot{\mathbf{Z}}^*(\omega)e^{j\theta}\right)^T \left(\mathbf{F_{PTO}}(\omega)e^{j\theta} + \mathbf{F_{PTO}}^*(\omega)e^{j\theta}\right) \\ -\frac{\psi}{4}\left(\mathbf{F_{PTO}}(\omega)e^{j\theta} + \mathbf{F_{PTO}}^*(\omega)e^{j\theta}\right)^T \left(\mathbf{F_{PTO}}(\omega)e^{j\theta} + \mathbf{F_{PTO}}^*(\omega)e^{j\theta}\right) \end{aligned} \tag{C.16}$$

where the average power $\bar{P}$ can be represented as the following,

$$\begin{aligned} \bar{P} = \frac{1}{4}\left(\dot{\mathbf{Z}}^T(\omega)\mathbf{F_{PTO}}^*(\omega) + \dot{\mathbf{Z}}^{*T}(\omega)\mathbf{F_{PTO}}(\omega)\right) \\ -\frac{\psi}{4}\left(\mathbf{F_{PTO}}^T(\omega)\mathbf{F_{PTO}}^*(\omega) + \mathbf{F_{PTO}}^{*T}(\omega)\mathbf{F_{PTO}}(\omega)\right) \end{aligned} \tag{C.17}$$

which when substituted into becomes,

$$\begin{aligned} \bar{P} = \frac{1}{4}\left(-\left(\dot{\mathbf{Z}}_\mathbf{a} + j\dot{\mathbf{Z}}_\mathbf{b}\right)^T (\mathbf{F_a} - j\mathbf{F_b}) - \left(\dot{\mathbf{Z}}_\mathbf{a} - j\dot{\mathbf{Z}}_\mathbf{b}\right)^T (\mathbf{F_a} + j\mathbf{F_b})\right) \\ -\frac{\psi}{4}\left((\mathbf{F_a} + j\mathbf{F_b})^T (\mathbf{F_a} - j\mathbf{F_b}) + (\mathbf{F_a} - j\mathbf{F_b})^T (\mathbf{F_a} + j\mathbf{F_b})\right) \end{aligned} \tag{C.18}$$

which then simplifies to,

$$\bar{P} = \frac{1}{2}\left[\dot{\mathbf{Z}}_\mathbf{a}^T\mathbf{F_a} + \dot{\mathbf{Z}}_\mathbf{b}^T\mathbf{F_b} - \psi\left(\mathbf{F_a}^T\mathbf{F_a} + \mathbf{F_b}^T\mathbf{F_b}\right)\right] \tag{C.19}$$

$$\bar{P} = \frac{1}{2}\left[\begin{bmatrix} \dot{\mathbf{Z}}_\mathbf{a} \\ \dot{\mathbf{Z}}_\mathbf{b} \end{bmatrix}^T \begin{bmatrix} \mathbf{F_a} \\ \mathbf{F_b} \end{bmatrix} - \begin{bmatrix} \mathbf{F_a} \\ \mathbf{F_b} \end{bmatrix}^T \begin{bmatrix} \boldsymbol{\psi} & 0 \\ 0 & \boldsymbol{\psi} \end{bmatrix} \begin{bmatrix} \mathbf{F_a} \\ \mathbf{F_b} \end{bmatrix}\right] \tag{C.20}$$

$$(\mathbf{G} + j\mathbf{Q})\left(\dot{\mathbf{Z}}_\mathbf{a} + j\dot{\mathbf{Z}}_\mathbf{b}\right) - (\mathbf{F_{ea}} + j\mathbf{F_{eb}}) = -(\mathbf{F_a} + j\mathbf{F_b}) \tag{C.21}$$

Separating the real and imaginary components of (C.21) then produces (C.22) and (C.23),

$$\mathbf{F_a} = -\mathbf{G}\dot{\mathbf{Z}}_\mathbf{a} + \mathbf{Q}\dot{\mathbf{Z}}_\mathbf{b} + \mathbf{F_{ea}} \tag{C.22}$$

$$\mathbf{F_b} = -\mathbf{G}\dot{\mathbf{Z}}_\mathbf{b} - \mathbf{Q}\dot{\mathbf{Z}}_\mathbf{a} + \mathbf{F_{eb}} \tag{C.23}$$

which can conveniently be put into the matrix form,

$$\begin{bmatrix} \mathbf{F_a} \\ \mathbf{F_b} \end{bmatrix} = \begin{bmatrix} \mathbf{F_{ea}} \\ \mathbf{F_{eb}} \end{bmatrix} - \begin{bmatrix} \mathbf{G} & -\mathbf{Q} \\ \mathbf{Q} & \mathbf{G} \end{bmatrix} \begin{bmatrix} \dot{\mathbf{Z}}_\mathbf{a} \\ \dot{\mathbf{Z}}_\mathbf{b} \end{bmatrix}. \tag{C.24}$$

Substituting (C.24) into (C.19) then produces (C.25),

$$\bar{P} = \frac{1}{2}\Bigg(- \begin{bmatrix} \dot{\mathbf{Z}}_{\mathbf{a}} \\ \dot{\mathbf{Z}}_{\mathbf{b}} \end{bmatrix}^T \left(\mathbf{\Phi} + \mathbf{\Phi^T \Lambda \Phi} \right) \begin{bmatrix} \dot{\mathbf{Z}}_{\mathbf{a}} \\ \dot{\mathbf{Z}}_{\mathbf{b}} \end{bmatrix} + \begin{bmatrix} \dot{\mathbf{Z}}_{\mathbf{a}} \\ \dot{\mathbf{Z}}_{\mathbf{b}} \end{bmatrix}^T \left(\mathbf{2\Phi^T \Lambda + I} \right) \begin{bmatrix} \mathbf{F_{ea}} \\ \mathbf{F_{eb}} \end{bmatrix} - \begin{bmatrix} \mathbf{F_{ea}} \\ \mathbf{F_{eb}} \end{bmatrix}^T \mathbf{\Lambda} \begin{bmatrix} \mathbf{F_{ea}} \\ \mathbf{F_{eb}} \end{bmatrix} \Bigg), \tag{C.25}$$

where

$$\mathbf{\Phi} = \begin{bmatrix} \mathbf{G} & -\mathbf{Q} \\ \mathbf{Q} & \mathbf{G} \end{bmatrix} \tag{C.26}$$

and

$$\mathbf{\Lambda} = \begin{bmatrix} \boldsymbol{\psi} & 0 \\ 0 & \boldsymbol{\psi} \end{bmatrix}. \tag{C.27}$$

Differentiating (C.25) in terms of $\left[\dot{\mathbf{Z}}_{\mathbf{a}}^T \; \dot{\mathbf{Z}}_{\mathbf{b}}^T\right]^T$,

$$\frac{\partial \bar{P}}{\partial \begin{bmatrix} \dot{\mathbf{Z}}_{\mathbf{a}} \\ \dot{\mathbf{Z}}_{\mathbf{b}} \end{bmatrix}} = \frac{1}{2}\Bigg(-2 \left(\mathbf{\Phi} + \mathbf{\Phi^T \Lambda \Phi} \right) \begin{bmatrix} \dot{\mathbf{Z}}_{\mathbf{a}} \\ \dot{\mathbf{Z}}_{\mathbf{b}} \end{bmatrix} + \left(\mathbf{2\Phi^T \Lambda + I} \right) \begin{bmatrix} \mathbf{F_{ea}} \\ \mathbf{F_{eb}} \end{bmatrix} \Bigg), \tag{C.28}$$

the optimum velocities $\begin{bmatrix} \dot{\mathbf{Z}}_{\mathbf{a}} \\ \dot{\mathbf{Z}}_{\mathbf{b}} \end{bmatrix}^\star$ can be found by setting (C.28)$= 0$ producing (C.29),

$$\begin{bmatrix} \dot{\mathbf{Z}}_{\mathbf{a}} \\ \dot{\mathbf{Z}}_{\mathbf{b}} \end{bmatrix}^\star = \left(\mathbf{\Phi} + \mathbf{\Phi^T \Lambda \Phi} \right)^{-1} \left(\mathbf{\Phi^T \Lambda} + \frac{1}{2}\mathbf{I} \right) \begin{bmatrix} \mathbf{F_{ea}} \\ \mathbf{F_{eb}} \end{bmatrix}. \tag{C.29}$$

Substituting the optimum velocities (C.29) into the average power equation (C.28), the optimum average power (C.30) is found,

$$\bar{P}^\star = \frac{1}{2}\Bigg(\begin{bmatrix} \mathbf{F_{ea}} \\ \mathbf{F_{eb}} \end{bmatrix}^T \Bigg(\left(\mathbf{\Phi^T \Lambda} + \frac{1}{2}\mathbf{I} \right)^T \left(\mathbf{\Phi}^T + \mathbf{\Phi^T \Lambda \Phi} \right)^{-1} \left(\mathbf{\Phi^T \Lambda} + \frac{1}{2}\mathbf{I} \right) - \mathbf{\Lambda} \Bigg) \begin{bmatrix} \mathbf{F_{ea}} \\ \mathbf{F_{eb}} \end{bmatrix} \Bigg) \tag{C.30}$$

References

Habetler, T. G., Profumo, F., Pastorelli, M. & Tolbert, L. M. (1992), 'Direct torque control of induction machines using space vector modulation', *IEEE Transactions on Industry Applications* **28**(5), 1045–1053.

Holmes, D. G. & Lipo, T. A. (2003), *Pulse width modulation for power converters: principles and practice*, Vol. 18, John Wiley & Sons.

Morren, J. & de Haan, S. W. H. (2007), 'Short-Circuit Current of Wind Turbines With Doubly Fed Induction Generator', *IEEE Transactions on Energy Conversion* **22**(1), 174–180.